The thermal stability of bulk nanocrystalline steels

Christopher Neil Hulme-Smith

Peterhouse

University of Cambridge

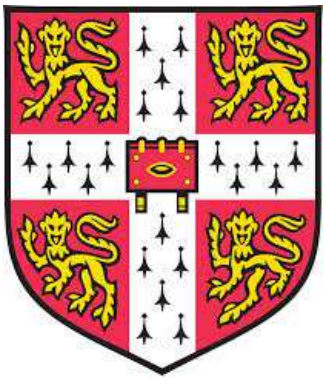

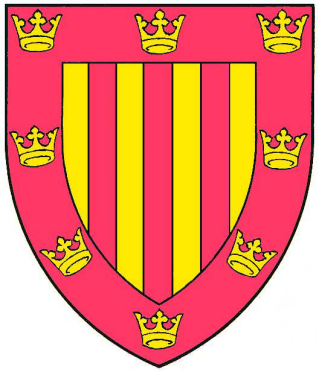

A dissertation submitted for the degree of Doctor of Philosophy

June 2016

Cambridge, U. K.

The thermal stability of bulk nanocrystalline steels

Christopher Neil Hulme-Smith

Abstract

Nanocrystalline bainite, commonly known as "superbainite", is a novel class of steel that utilises careful alloy design to reduce the bainite transformation temperature to below 300 °C. This results in grains that are tens of nanometres in width, which make steel strong and tough. The structure can be produced in large volumes without the need for rapid cooling or severe deformation.

The presence of austenite in nanocrystalline bainite is largely responsible for the toughness. Unfortunately, the austenite is metastable and previous work has shown that it decomposes into cementite and ferrite upon heating. This decomposition makes the material weak and brittle.

The present work aims to develop new alloys that form nanocrystalline bainite, but which are able to survive heating. Previous work has shown that cementite precipitation is the first stage in the decomposition process and so the first alloys developed aimed to suppress cementite precipitation. This resulted in a noticeable improvement in thermal stability, although the austenite does eventually decompose at higher temperatures.

Subsequent work led to an alloy which was designed not to resist cementite precipitation, but to tolerate it without the associated loss of austenite. This was achieved by the addition of large quantities of nickel to stabilise the austenite even if its carbon content is depleted. This alloy is able to survive exposure to elevated temperatures with the majority of austenite being retained.

The thermal stability of the alloys was assessed using time-resolved synchrotron

X-ray diffractometry at both the Deutsches Elektronen Synchrotron (DESY) and Diamond Light Source. The high-quality data that were collected allowed the symmetry of the ferrite lattice to be investigated and it was found that the lattice was best-described using a body-centred tetragonal crystal structure. This is the first evidence of its kind.

Mechanical properties were investigated in the as-transformed condition at ambient temperature and at a temperature representative of aeronautic applications. The alloys developed in this project have comparable strength, toughness and fatigue performance to existing nanocrystalline bainitic steels. Mechanical properties were also measured after heating at 480 °C for 8 d and this was found to reduce strength and toughness, consistent with the measured loss of austenite.

Declaration

This thesis is submitted for the degree of Doctor of Philosophy at the University of Cambridge. The research was conducted under the academic supervision of Professor H. K. D. H. Bhadeshia in the Phase Transformations and Complex Properties Research Group of the Department of Materials Science and Metallurgy and under the industrial supervision of Mr Martin Rawson and Dr Paul Hill of Rolls-Royce plc between 2011 and 2015.

I declare that all of the enclosed work is original, except where explicitly acknowledged and referenced. I declare that I have not submitted this thesis, or any part thereof, for any award, degree, diploma or any other qualification at any other institution. To the best of my knowledge, no substantially similar thesis has been submitted to any institution for any reason whatsoever.

I declare that this thesis does not exceed the prescribed limit of 60,000 words.

Aspects of this work have been published in the following academic papers or presented at the following academic conferences:

Section 4.3: Hulme-Smith, C. N., Lonardelli, I., Peet, M. J., Dippel, A. C. & Bhadeshia, H. K. D. H. Enhanced thermal stability in nanostructured bainitic steel. *Scripta Materialia*, 69:191–194, 2013.

Section 8 C. N. Hulme-Smith, Improving the Thermal Stability of Bulk Nanocrys-

talline Steel, presented at *Solid State Transformations in Inorganic Materials*, Whistler, B. C., Canada, 2015

Section 10.2: C. N. Hulme-Smith, I. Lonardelli, A. C. Dippel, & H. K. D. H. Bhadeshia. Experimental evidence for non-cubic bainitic ferrite. *Scripta Materialia*, 69:409–412, 2013.

Section 10.3: C. N. Hulme-Smith, M. J. Peet, I. Lonardelli, A. C. Dippel, & H. K. D. H. Bhadeshia. Further evidence of tetragonality in bainitic ferrite. *Materials Science and Technology*, 3:254–256, 2015.

Christopher Neil Hulme-Smith
Cambridge, U.K., June 2016

Micrographs sourced from the DoITPoMS Micrograph Library are distributed under a "Creative Commons Attribute–NonCommerical–ShareAlike 2.0 UK: England and Wales licence (CC BY-NC-SA 2.0 UK)"[1]. All such micrographs are used here under the terms of the said licence and may be reused from this document with no need for explicit permission. Any reuse requires citation to this document or (if taken from elsewhere) the source of the image and must be made freely available in any new work under the said-same licence. No commercial use is permitted under this licence. All micrographs were adapted by converting to grayscale (if required), optimising contrast and brightness and the addition of a new scale bar.

Parts of this research were carried out at the light source Petra III at DESY, a member of the Helmholtz Association (HGF). I would like to thank both Alexander Schökel and Dr Ann-Christin Dippell and her colleagues for assistance in using beamline P02.1.

I thank Diamond Light Source for access to beamline I12 (proposal EE9880) that contributed to the results presented here. In particular, I would like to thank Dr Michael Drakopoulos and Dr Robert Atwood for their assistance in preparation for and during the beamtime.

I would like to thank ISIS for access to the HRPD beamline and to Dr Aziz Daoud-Aladine for his assistance in performing the neutron diffraction experiment there.

[1]Full details available at `http://creativecommons.org/licenses/by-nc-sa/2.0/uk/`

Acknowledgements

I would like to thank my parents for their endless encouragement and many sacrifices over the years to help get me where I am. I am forever in your debt.

I will be eternally grateful to my beautiful wife, Rebecka, for all the support, practical help, tolerance and patience over the four years of this project and especially for not complaining when I talked materials!

I would like to thank everyone who has contributed to this project. In particular I would like to thank Professor Harshad Kumar Dharamshi Hansraj Bhadeshia for all his frequent and vital advice, ideas, encouragement and patience. Sincere thanks also to Rolls-Royce plc and the Engineering and Physical Sciences Research Council for funding this project, and in particular to Dr Paul Hill and Mr Martin Rawson at Rolls-Royce plc for their technical input. I would also like to thank Dr Steve Ooi and Dr Mathew Peet for their tireless assistance on both theoretical and practical matters. I would also like to express my gratitude to Dr Ivan Lonardelli for introducing me to high energy diffraction experiments.

I must give special mention to those without whom this project would have been much more difficult, all of whom have my heartfelt gratitude: Mr Dave Saul and Mr Frank Clarke for their help and advice on metallographic preparation and for keeping a well-equipped teaching lab, Mr Andrew Moss and Mrs Mary Vickers for getting me started with with X-ray diffractometry, Mr Simon Griggs for his help with scanning electron microscopy, Mr Dave Nicol for assistance with trasmission electron microscopy and Drs Ed Pickering, James Nygaard, Tim Ramjaun, Wilberth Solano, Lucy Fielding, Yan Pei and Hector Pous-Romero who, along with the rest of the Phase Transformations and Complex Properties Research Group,

made my lab and office a delightful place to work, and who have all been happy to let me bounce ideas off them.

Sherlock Holmes in the works of Sir Arthur Conan Doyle:

"It is an old maxim of mine that when you have excluded the impossible, whatever remains, however improbable, must be the truth.", in *The Adventure of the Beryl Coronet*

"I make a point of never having any prejudices, and of following docilely where the facts may lead me.", in *The Reigate Squires*

"It is a capital mistake to theorise in advance of the facts. Insensibly one begins to twist facts to suit theories, instead of theories to suit facts.", in *A Scandal in Bohemia*

"Data! Data! Data!" he cried impatiently. I can't make bricks without clay.", *The Adventure of the Copper Beeches*

John Fitzgerald Kennedy:

"We choose to go to the moon in this decade and do the other things, not because they are easy, but because they are hard, because that goal serves to organize and measure the best of our energies and skills, becuase that challenge is one we are willing to accept, one we are unwilling to postpone, and one which we intend to win, and the others, too."

"Do not pray for easy lives. Pray to be stronger men."

"Things do not hapen. Things are made to happen."

"The goal of education is the advancement of knowledge and the dissemination of truth."

"Man is still the most extraordinary computer of all."

Nomenclature

Ae_3	the highest temperature at which ferrite is thermodynamically stable at equilibrium
AFM	atomic force microscopy
APT	atom probe tomography
α	ferrite
α'	martensite, martensitic ferrite
α_a	acicular ferrite
α_i	idiomorphic ferrite
α_{lb}	lower bainite
α_{ub}	upper bainite
α_w	Widmanstätten ferrite
BCC	body-centred cubic
BCO	body-centred orthorhombic
BCT	body-centred tetragonal
B_s	bainite start tempeature
β-NiAl	nickel aluminide, NiAl
CCT	continuous cooling transformation diagram

d	grain size
δ	delta (high temperature) ferrite
EDM	electrical discharge machining
ESR	electro slag remelting
ε	total strain
ε_{e}	elastic component of strain
ε_{p}	plastic component of strain
ε	epsilon carbide, $Fe_{2.4}C$
FCC	face-centred cubic
G_{N}	universal nucleation function
γ	austenite
γ'	austenite existing in equilibrium with other products following the transformation of austenite of a different composition
γ_{p}	plastic shear strain
γ_{r}	retained austenite
η	eta carbide, Fe_2C
IPS	invariant plane strain
$\bar{L}$	mean lineal intercept

M_f	martensite finish tempeature
M_s	martensite start tempeature
R_exp	expected R-factor
R_wp	weighted profile R-factor
SEM	scanning electron microscopy
σ_UTS	ultimate tensile strength
σ_y	yield stress
$\sigma_{\mathrm{y},0}$	yield stress of large-grained sample of material
T_0	the temperature at which austenite and ferrite of the same composition have the same Gibbs free energy
T_0'	the temperature at which austenite and ferrite of the same composition have the same Gibbs free energy if the stored strain energy is taken into account
TEM	transmission electron microscopy
TTT	time-temperature transformation
θ	cementite, Fe_3C
τ_y	shear yield stress
VAR	vacuum arc remelting
VIM	vacuum induction melting
W_s	Widmanstätten start temperature

XRD	X-ray diffraction
x_{T_0}	carbon content of austenite and ferrite of the same composition and Gibbs free energy at a specified temperature
$x_{T_0'}$	carbon content of austenite and ferrite of the same composition and Gibbs free energy at a specified temeprature if the stored strain energy is taken into account

Contents

Chapter 1

Introduction

Nanocrystalline bainitic steels are a recent development in steel metallurgy, produced via the bainite transformation at temperatures in the range 150 °C–300 °C. The resultant material contains very fine mixtures of alternating platelets of bainitic ferrite, typically ~ 100 nm wide and *films* of retained austenite, ~ 50 nm wide, together with larger *blocks* of retained austenite, usually several micrometres in size.

These low-temperature bainitic steels exhibit impressive combinations of strength and toughness. Most steels with very fine grain structures are produced either by rapid cooling or by severe plastic deformation, so there is a restriction on the size and shape of the product that can be produced. Nanocrystalline bainitic steels require neither rapid cooling nor plastic deformation and still form nanometre-scale grains associated with an exceptionally high density of interfaces, which is unique in steel metallurgy. This allows very large pieces of material to be produced with extremely fine grain sizes. No exotic alloying elements are required to form nanocrystalline bainite and extreme processing is unnecessary, making the production of large quantities of high-strength and tough steel very economical. The result of the combination of low cost, ease of production and excellent mechanical properties has seen the commercial development of nanocrystalline bainitic steels as armour [1].

Strong and tough materials are in high demand in many sectors, especially where mass must be minimised, for example to improve fuel efficiency in auto-

motive and aerospace applications [2, page 230] [3, page 12]. One potential area of use for nanocrystalline bainitic steels is as components in gas turbine engines, replacing other ferrous alloys that are either more expensive or possess inferior mechanical properties which necessitate more material, and hence more mass, to be used in the component. Use in such applications requires the material to perform for extended periods of time at somewhat elevated temperatures. Existing nanocrystalline steels are not thermally stable and this makes them unsuitable for use at elevated temperatures and prevents any high temperature treatment after the bainite transformation, such as galvanising or dip-coating.

The work described in this dissertation documents the design and testing of novel nanocrystalline steel compositions that are more resistant to thermal decomposition, while maintaining the good mechanical properties and simple processing.

It has been proposed that bainitic ferrite may form with a body-centred tetragonal lattice if it is forced to contain more carbon than is soluble in a body-centred cubic lattice, much in the way as has been documented for martensite. Work presented in this dissertation also investigates this using precise neutron and synchrotron X-ray diffraction measurements of transformed nanocrystalline steel. Should bainitic ferrite indeed possess non-cubic symmetry, there could be a significant effect on the thermodynamic properties of the ferritic phase and, hence, on thermal stability.

The scientific background to the thermal stability of nanocrystalline steels and the phenomenon of non-cubic bainitic ferrite is presented in Chapter 2 and a summary of the design tools used in this project is given in Chapter 3. A study of a nanocrystalline steel specifically designed to withstand thermal exposure is described in Chapter 4. Chapters 5 and 6 report design of novel compositions expected to exhibit improved thermal stability. As-transformed microstructures are investigated with optical, scanning electron and transmission electron microscopy to show the as-transformed microstructures. X-ray diffractometry results are also presented to corroborate the microscopy. Two alloys were selected for detailed study and the transformation kinetics of these alloys are presented in Chapter 7. An assessment of the thermal stability of the chosen alloys using time-resolved

synchrotron X-ray and neutron diffraction results is presented in Chapter 8. A range of mechanical tests was then performed to determine the properties of these alloys as presented in Chapter 9. Experiments to investigate the phenomenon of non-cubic bainitic ferrite are presented in Chapter 10.

Chapter 2

Scientific background

2.1 Solid state transformations in steel

Careful control of processing conditions can lead to an extraordinarily wide variety of physical properties in steels. Along with low production costs compared to alternative metals, this is the main factor that makes steel so widely used: in 2014, 1.65 billion tonnes of steel was produced [4]. This is ten times as much by weight as all other metals combined [5, figure 2]. The mass of steel produced worldwide has more than doubled in fifteen years and is still on an upward trend. Despite its popular image as symbolising the consumption of resources, steel requires relatively little energy to be produced: $6\,\mathrm{kWh\,kg^{-1}}$, comparable to wood (5) and glass (7), and significantly less than aluminium (40) or the polymer PET (30) [6, page 88]. Any development that improves the mechanical properties of steel without prohibitively increasing costs would allow a reduction in steel consumption and would result in a significant environmental and economic benefit. Should steel be developed such that it is usable at under extreme conditions, more expensive and energy-intensive materials may be replaced with steel, again aiding economy and the environment.

When assessing phase transformations in steel, there are strong effects of alloying additions and temperature on the stable phases. Phase diagrams detailing the behaviour of the iron–carbon system are given in figure 2.1. In steel processing,

it is common for the steel to be heated close to, or in excess of, 1000 ℃. At these temperatures, many steels consist of austenite, a face-centred cubic phase usually given the symbol γ. When this steel is cooled to ambient temperature, various phase changes occur. At temperatures typically up to 900 ℃, a body-centred cubic phase known as ferrite is stable. This phase is given the symbol α. The method of transformation from austenite to ferrite is one of the most critical factors governing the mechanical properties of any steel. The temperatures at which phase changes occur and the identity of the phases that form depend both on the composition of the steel, any deformation that the steel has been subjected to — the dislocation density and distribution — and the temperatures that the steel is exposed to: the steel's thermal history. For simplicity, only the iron-carbon system will be considered in this section and the effects of strain will be neglected.

2.1.1 Reconstructive transformations

If heat treatments are long and at sufficiently high temperatures, thermodynamic equilibrium may be achieved and phase changes take place by reconstructive mechanisms where all elements are able to partition to minimise the Gibbs free energy of the system. When this occurs in the absence of applied stresses, ferrite is usually found to consist of equiaxed grains. Those grains nucleate on heterogeneous nucleation sites such as austenite grain boundaries (*allotriomorphs*) or on inclusions (*idiomorphs*). Examples of these structures are given in figure 2.2. In the case of allotriomorphs, initial growth is along austenite grain boundaries as these are easy diffusion paths and allow more rapid partitioning of alloying elements. The shape of allotriomorphs bear no relation to the crystal structure of the growing phase, but reflect the easy paths for growth. Over time, these grains of ferrite impinge and form a conventional grain structure. Idiomorphs have no easy diffusion paths and grow with crystal facets during transformation, reflecting the underlying crystal structure of the new phase [11, page 42]. As is shown by figure 2.1, ferrite has a very low solubility for carbon when in equilibrium with austenite or cementite, so there are almost always carbon-rich precipitates in steels. At equilibrium, these precipitates will be graphite [12, page 39], however, kinetic limitations

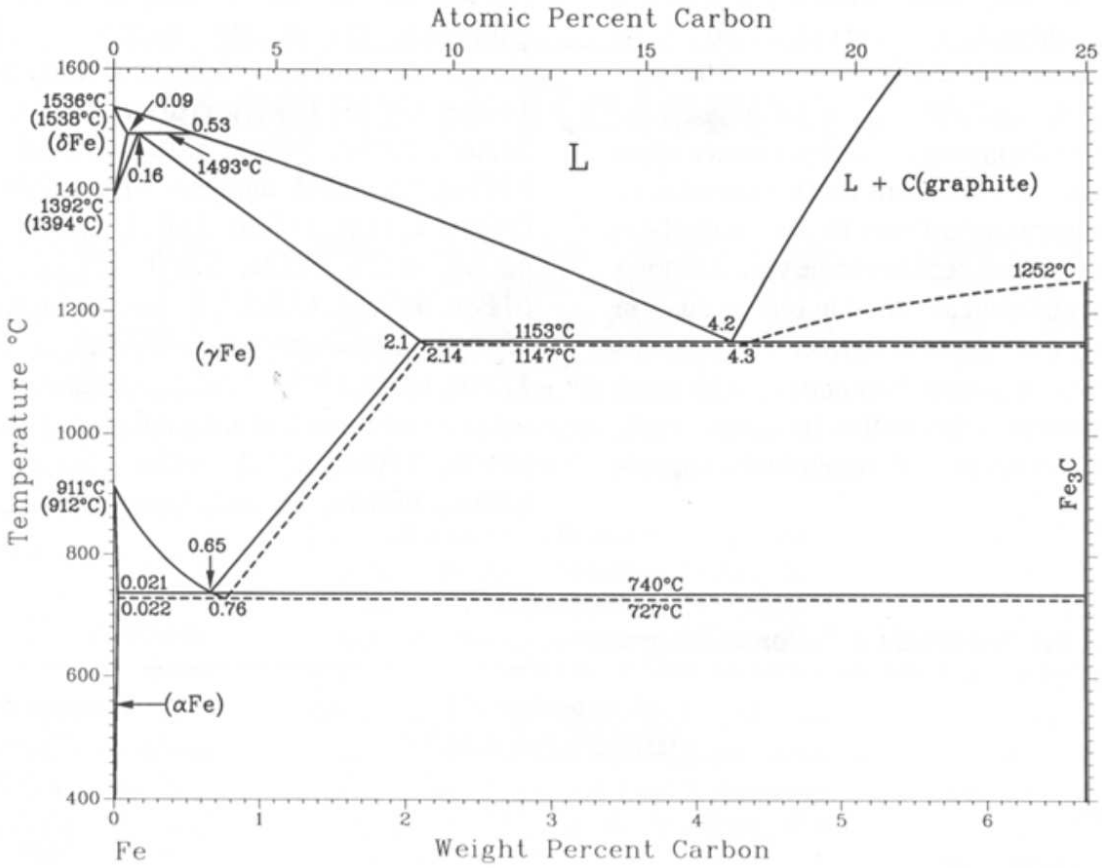

Figure 2.1: Iron–carbon phase diagram [7]. Solid lines represent results of calculations by Ohtani et al. [8] and dashed lines are earlier results obtained by Chipman [9]. See [8] for full explanation. Reproduced from [10] with permission of ASM International.

restrict the formation of graphite and carbides tend to form instead. For this reason, iron–carbon phase diagrams, such as those in figure 2.1 show cementite — the most thermodynamically stable carbide in the iron–carbon system, with the composition Fe_3C, sometimes given the symbol θ — rather than graphite as the most carbon-rich phase. It is, however, possible to form graphite in iron-carbon systems, most notably in grey cast irons, but also in some steels at sufficiently high temperatures and with a composition that is not conducive to cementite formation. Both steels and grey cast iron rely on alloying elements that are insoluble in cementite (that is have a high chemical potential when forced to occupy an iron site in the cementite lattice, such as aluminium [13, page 243], nickel and silicon [13, page 244] and consequently promote the formation of other phases) to form graphite. Anexample of cementit in plain-carobn steel is given in figure 2.3(a), while figure 2.3(b) shows an example of graphite in a silicon-rich cast iron. The removal of silicon can lead to enhanced strength and toughness in steel. This is discussed in more detail in section 2.3.8.

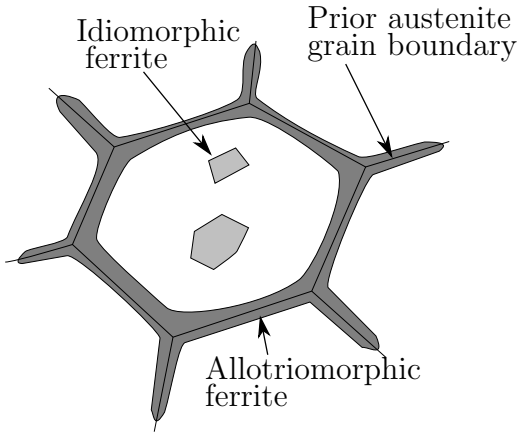

Figure 2.2: Schematic representation of allotriomorphic and idiomorphic ferrite.

When significant amounts of alloying elements are present, these may be accommodated in iron-rich carbides, may be rejected from iron carbides or may form carbides without iron. With sufficient temperature and time, these carbides form as large precipitates in such a shape as to minimise the total interfacial energy of the system. Just as in other alloy systems, when iron carbide precipitates are

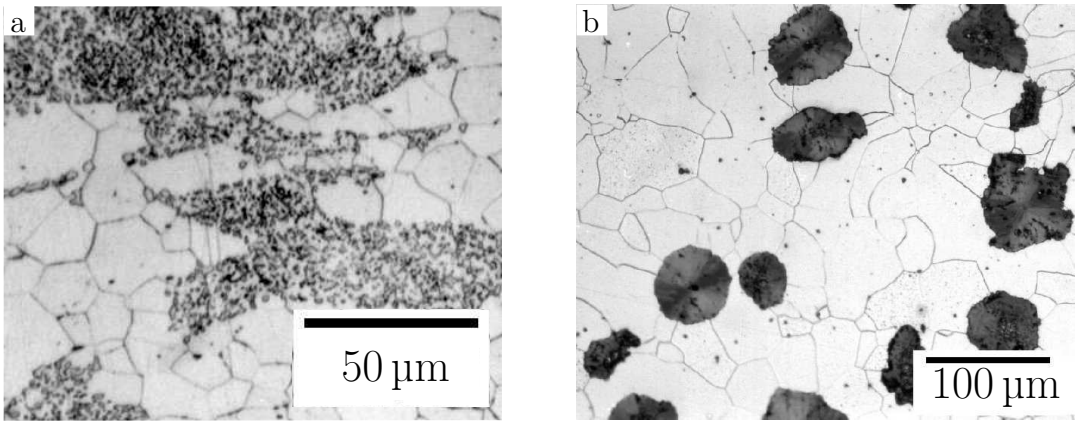

Figure 2.3: (a) spheroidal cementite (dark spots) in ferrite matrix in Fe–0.3 wt% C, adapted from [14, micrograph 242]; (b) spheroidal graphite in ferrite matrix in Fe–3.2 C–2.5 Si–0.05 Mg (wt%), adapted from [14, micrograph 781].

small, they tend to form with some well-defined orientation between their crystal and that of the matrix from which they have grown. This reduces the interface energy at the expense of restricting the shape of the precipitate to allow for atomic correspondence across the interface and possibly introducing strain, required to cause the atomic spacings to match across the interface. This matching of atomic spacings is called *coherency*. As precipitates grow, any strain energy caused by coherency at the precipitate/matrix interface will increase, and the restrictions on shape may become prohibitive. Large precipitates are, therefore, likely to exhibit semi-coherent (only match some atomic spacings) or incoherent (match no spacings) interfaces.

Reconstructive transformations tend to be observed when steel is at elevated temperatures for extended periods of time. While there are examples of practices where this occurs, a wide range industrial processes involve forming steel at high temperatures and then allowing the steel to cool at a rate which does not allow full equilibrium to be reached. In this case, some other transformation will occur that does not represent the lowest attainable energy state of the material, but which is able to take place in the time allowed. In other words, the transformation

products are metastable. During service at elevated temperatures, the microstructure may change to a more thermodynamically stable state. This will result in a corresponding change in mechanical properties during service and may lead to the steel being unsuitable for the purpose it was designed for.

2.1.2 The eutectoid transformation: pearlite

One of the key features of the iron–carbon system is the eutectoid point at 727 °C and 0.76 wt% carbon (figure 2.1). As a eutectoid transformation, one solid phase — in this case, austenite — transforms simultaneously into two others. For iron–carbon these product phases are ferrite and cementite. In order to produce two phases from one solid parent phase, the growth mechanism involves a common growth interface for both product phases with diffusion occurring parallel to the growth interface, as shown in figure 2.4. This results in a microstructure known as pearlite where many alternating regions of ferrite and cementite form from a single pair of nucleation sites. In section, the morphology resembles a lamellar structure, such as is shown in figure 2.5.

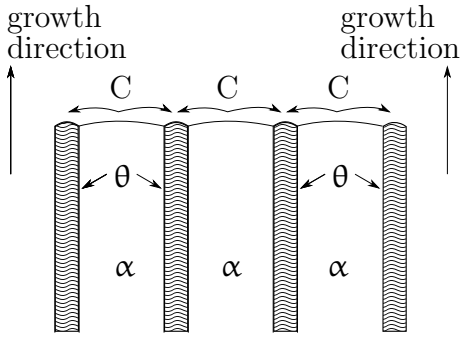

Figure 2.4: Schematic representation of the growth direction and diffusion directions during the pearlite transformation

A more physically accurate description is that the pearlite consists of two interpenetrating crystals. In other words, in each individual region of pearlite formed from one nucleation site (termed a 'colony' of pearlite), all of the 'lamellae' of ferrite are in fact one branched crystal, as are the 'lamellae' of cementite. Within one phase in one colony it is possible to trace a path from each lamella to each

other lamella in without crossing a grain boundary [15].

The ferrite and cementite form from the austenite after a diffusive redistribution and rearrangement of atoms. There is therefore no relationship between the crystals of the parent austenite and those of the product phases. One consequence of having interpenetrating crystals is that there is a large interfacial area per unit volume. It is therefore likely that the interface will be such as to minimise interfacial energy and thereby minimise the energy of the system. This is achieved by there being some correspondence between the crystals of the product phases, which requires a well-defined relationship between the crystallographic orientations. The relationship between the two crystals is known as an *orientation relation*. There are three common orientation relations found in pearlite, the first of which is named after Pitsch and Petch (equations 2.1–2.3) [16, 17], the second named after Bagaryatski (equations 2.4–2.6) [18] and the third after Isaichev (equations 2.7 and 2.8) [19].

$$(001)_\theta \parallel (\bar{5}2\bar{1})_\alpha \tag{2.1}$$

$$(010)_\theta \ \text{2-3}\,^\circ \text{from}\ [11\bar{3}]_\alpha \tag{2.2}$$

$$(100)_\theta \ \text{2-3}\,^\circ \text{from}\ [131]_\alpha \tag{2.3}$$

$$(100)_\theta \parallel (0\bar{1}1)_\alpha \tag{2.4}$$

$$(010)_\theta \parallel (1\bar{1}1)_\alpha \tag{2.5}$$

$$(001)_\theta \parallel (211)_\alpha \tag{2.6}$$

$$[010]_\theta \parallel [111]_\alpha \tag{2.7}$$

$$(101)_\theta \parallel (11\bar{2})_\alpha \tag{2.8}$$

Although this reduces the energy contribution from the interfaces within the lamellar structure, the system energy may still be lowered if the lamellae break up

and the (minority) cementite regions change their shape to reduce the total interfacial area in the microstructure. This is an example of a material changing its microstructure during exposure to elevated temperature and is known as *spheroidisation* [20, 21]. Figure 2.3(a) is an example of spheroidal cementite, formed from pearlite when heated close to the eutectoid temperature. Due to the change in microstructure, the mechanical properties of the steel change [22] and in this case, the steel becomes softer once spheroidisation begins and continues to soften as the spheroidised particles coarsen.

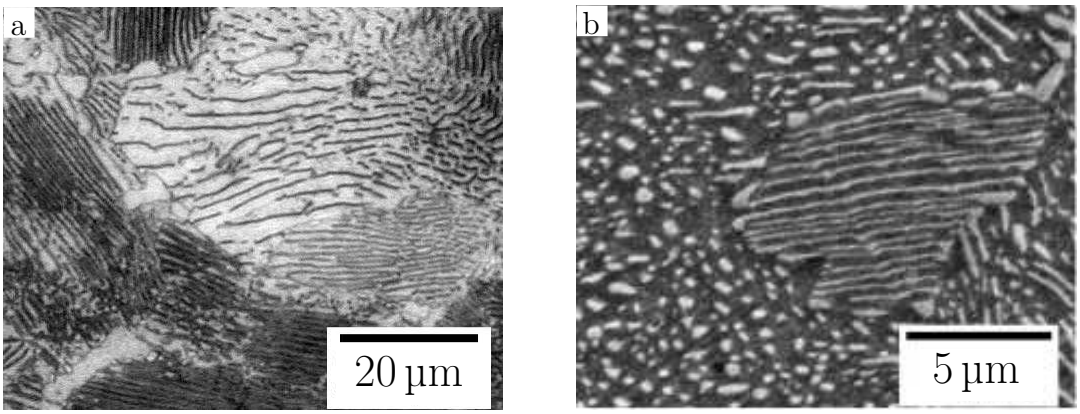

Figure 2.5: Micrographs showing the possible morphologies of pearlite, (a) optical micrograph with dark cementite adapted from [14, micrograph 15] and (b) with cementite bright, adapted from [14, micrograph 20]. The inversion of the shading is a result of the differing imaging techniques.

2.1.3 Shear transformations

The austenite to ferrite shear transformation

Under conditions where diffusion is not possible, for example, at low temperatures, or not sufficiently rapid, for example during rapid straining, phase changes may occur via a mechanism that involves the coordinated movement of atoms without the need for any diffusion at all. The austenite to ferrite transformation can

proceed via a mechanism known as the Bain strain. It is possible to describe a face-centred cubic crystal as a body-centred tetragonal lattice, as shown in figure 2.6, where all atoms form two unit cells of the face-centred cubic crystal and one unit cell of the equivalent body-centred tetragonal crystal is denoted by the black atoms. An expansion of around 12% in the tetragonal a and b directions together with a contraction of 17% in the common c direction could form a body-centred cubic crystal [12, page 103].

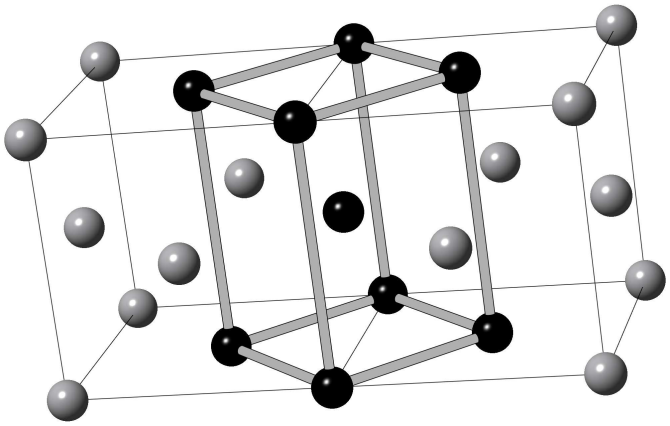

Figure 2.6: The body-centred tetragonal lattice (black) that is equivalent to the face-centred cubic lattice (all atoms) and that may be transformed to a body-centred cubic lattice by the Bain strain

While capable of generating the correct crystal structure, the Bain strain is not able to produce either the observed orientation relationships or the correct shape of ferrite that is observed experimentally. The Bain strain on its own suggests that $\langle 001 \rangle$ of the austenite and ferrite are parallel and that the parent $\langle 110 \rangle$ is parallel to the product $\langle 110 \rangle$. In reality, the orientation has irrational Miller indices and brings the closest-packed planes and directions of both parent and product crystals into approximate coincidence.

It is also necessary that there is a high degree of atomic correspondence across the interface, otherwise diffusive rearrangement of atoms would be necessary. There is no possible plane that allows face-centred cubic and body-centred cubic lattices with lattice parameters typical of steels to form a coherent and strain-free

interface. The highest coherency that is possible is if one direction is left undistorted and unrotated across the interface. In other words, there is an *invariant line* at the interface.

The Bain strain may be modified to produce an invariant line if a rigid-body rotation is performed on the crystal after the Bain strain has been applied [1]. This may equivalently be achieved by applying two invariant plane strains on non-parallel planes, such as transforming figure 2.7(a) to figure 2.7(c). The invariant line is then the direction common to both invariant planes.

This still does not address the problem of the incorrect shape of the product crystal, which is shown schematically in figure 2.7(c). The observed macroscopic interfacial plane is called the *habit plane*. This may be explained if there is some lattice-invariant deformation within the parent crystal, such as twinning (figure 2.7(d)) or dislocation motion (figure 2.7(e)). The deformation shifts the interface so that it appears, at least macroscopically, to obey the observed habit plane. On a local (atomic) level, the habit plane can still be that predicted by the Bain strain, but the plane that describes the average interface is that observed in practice. It is this plastic deformation that results in irrational Miller indices in the macroscopic habit planes of many displacive transformations in steel. Generally speaking, dislocations are favoured since the stored energy required to accommodate the transformation strain of the Bain strain is significantly less than that stored by twinning: 20 J, compared to 100 J [23]. However, twins may form if the transformation is rapid as a twinned interface is more glissile than an interface heavily populated by dislocations.

This transformation mechanism has been measured to impart a shear strain in the habit plane of between 0.22 and 0.45, depending on the transformation product [11, page 47]. An accompanying dilatational strain of ~ 0.03 is observed, reflecting the lower packing efficiency of ferrite. The shear strain, which can be either elastic or plastic, depending on the transformation conditions, results in a large stored energy of transformation once it has been accommodated.

[1] in practice all of these operations happen together at the transfer interface

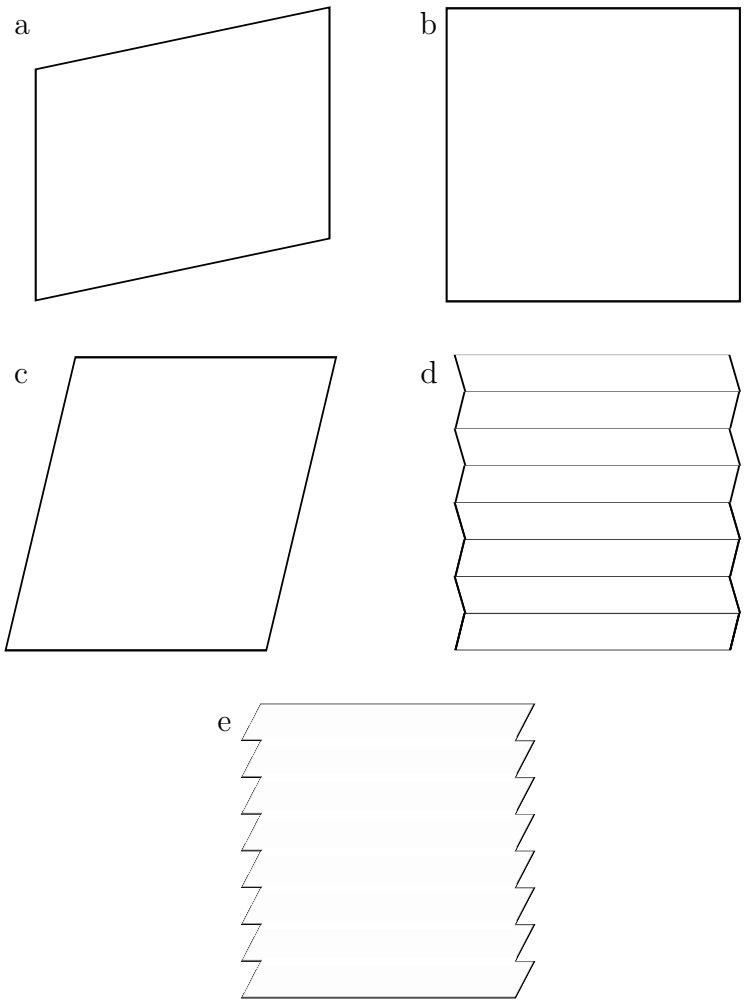

Figure 2.7: Schematic of the Bain strain [12, adapted]. (a) starting austenite. A single shear generates (b) which is the correct shape but the wrong crystal structure. A second shear generates the correct crystal structure (BCC), but has the wrong shape. Macroscopic deformation that does not change the crystal structure can regenerate the correct shape, e.g. twinning (d) or slip (e). All figures represent the same amount of material.

Widmanstätten ferrite

Once ferrite allotriomorphs form and populate the prior austenite grain boundaries, the austenite to ferrite transformation can only increase if the ferrite is able to grow into the body of the austenite grain. As indicated by the iron–carbon phase diagram (figure 2.1), ferrite and austenite coexist over a range of temperatures. The highest temperature at which α-ferrite (i.e. not δ-ferrite) may exist in equilibrium with austenite is known as the Ae_3 temperature [12, page 40]. At temperatures close to Ae_3, there is little driving force for the transformation of austenite to ferrite, given the symbol $\Delta G^{\gamma\rightarrow\left(\gamma'+\alpha\right)}$. Since the system is at a temperature only slightly below the equilibrium, it is said to have a low *undercooling*. Although diffusive rearrangement of atoms may occur after extended periods of time, the first transformation to occur is one that does not require bulk redistribution of all atoms. Secondary Widmanstätten ferrite, α_{w}, grows as fine plate-like structures from grain boundary allotriomorphs. An example is shown in figure 2.8. Primary Widmanstätten ferrite is also possible, nucleating directly on prior austenite grain boundaries if allotriomorphs are absent.

There is little driving force for the change of crystal structure and so the transformation must proceed in such a way as to minimise the amount of energy consumed during the transformation. Potential sinks for energy include high-energy interfaces, elastic and plastic transformation strains in either or both of the parent and product phases, trapping of atoms in the product phase (atoms occupying sites in the product crystal, despite their chemical potential being higher in the product phase than the parent phase). Together, these energy penalties associated with the transformation mechanics are referred to as *stored energy*. In the case of Widmanstätten ferrite, the stored energy is approximately $50\,\mathrm{J\,mol^{-1}}$ [24].

Since Widmanstätten ferrite is formed via a displacive mechanism, it may be expected that there will inevitably be some trapping of atoms in the product phase. Examination of the iron–carbon phase diagram shows that there is very little solubility of carbon in ferrite. This may be explained by looking at the chemical potential of carbon in austenite and ferrite, as shown in figure 2.9. By definition, the Gibbs' free energy of a system if the sum of the total chemical potential of all

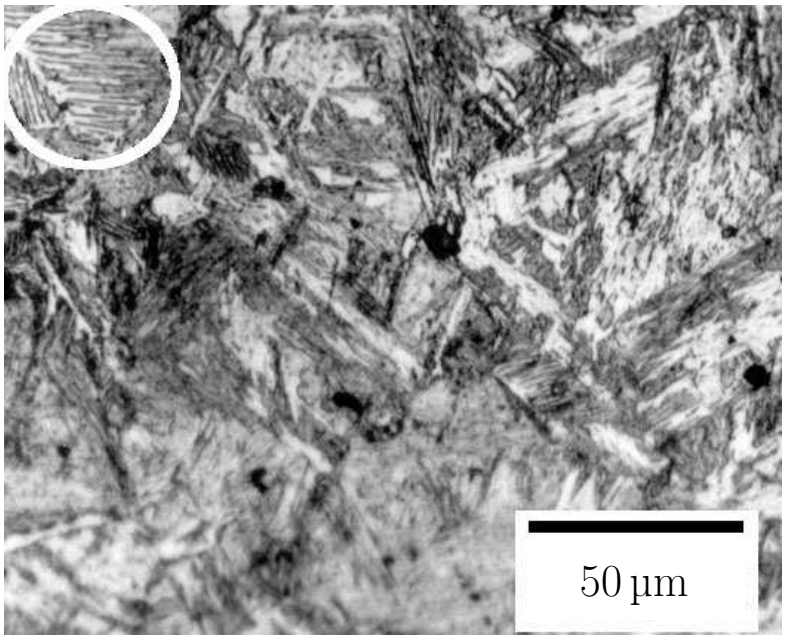

Figure 2.8: Example of Widmanstätten ferrite (circled) growing from allotriomorphs in a "slow-quenched" Fe–0.55 wt%/,C steel[14, micrograph 308, adapted]

species in all phases, $G = \sum_{i,j} \mu_{i,j} x_{i,j}$, where $\mu_{i,j}$ is the molar chemical potential of the i^{th} component in the j^{th} phase and $x_{i,j}$ is the number of moles of the i^{th} component in the j_{th} phase. The greater chemical potential of carbon in ferrite would result in a large increase in free energy of the system, should carbon be forced in to the ferrite. For this reason, carbon may not be present when the crystal structure changes and instead diffuses immediately ahead of the austenite/ferrite interface — the formation of Widmanstätten ferrite proceeds under *paraequilibrium*. The diffusion of carbon ahead of the growth interface is the rate-limiting step in the growth process and is also required for nucleation of Widmanstätten ferrite [24]. This contributes to the slow rate of formation of Widmanstätten ferrite.

While the partitioning of carbon reduces the free energy of the system compared to the case of a completely diffusionless transformation, partitioning of every species in the system — i.e. an equilibrium transformation — would further reduce the free energy of the product. However, the low driving force for the formation of Widmanstätten ferrite is due to there being little difference in chemical potential

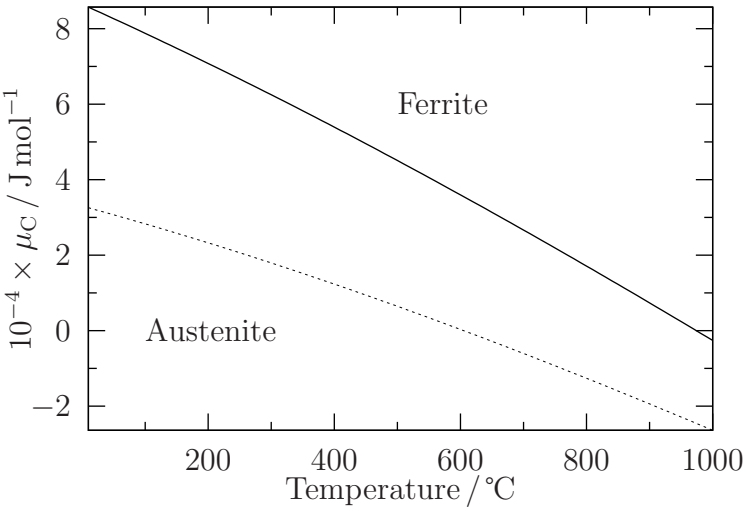

Figure 2.9: Calculated chemical potential of carbon in austenite and ferrite in Fe–1.0 wt% C as a function of temperature [25, 26]

for each species between austenite and ferrite. Diffusion occurs down gradients of chemical potential and so a shallow chemical potential gradient will result in slow diffusion. Since the partitioning of substitutional solutes is very slow, the growth of Widmanstätten ferrite proceeds via the paraequilibrium mechanism whereby only interstitial solutes partition and achieve a common chemical potential in both the product and parent phases. Substitutional solutes exist in the same quantities in both phases, but will exhibit different chemical potentials.

Another factor that restricts the rate of formation of Widmanstätten ferrite, also related to the need to minimise stored energy, is the slow rate of nucleation. Since the crystal structure does not have time to change via a diffusive process, it must do so by a displacive mechanism. As discussed in section 2.1.3, this necessarily imparts a large shear stress in the untransformed region around the product crystal. This strain energy must be minimised to allow the transformation to proceed at low undercoolings. This is achieved by nucleating two ferrite plates next to each other which grow with antiparallel strains such that very little strain is imparted in the untransformed material [27]. The boundary between the two adjacent grains comprises a low-misorientation boundary. Any strain that is im-

parted into the lattice is accommodated to minimise the overall energy stored due to deformation [28]. This is shown schematically in figure 2.10.

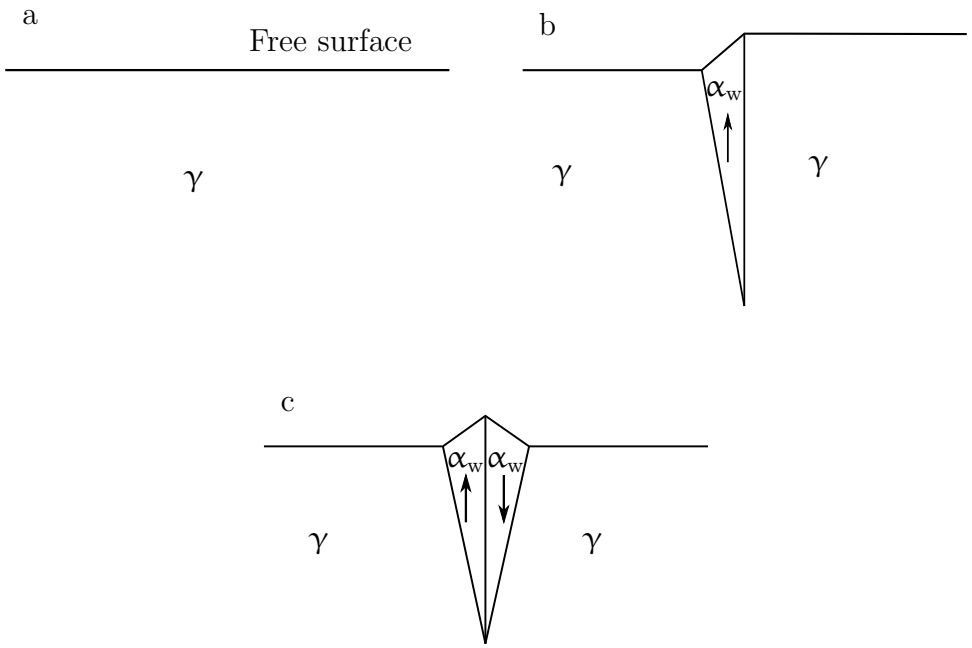

Figure 2.10: Nucleation of Widmanstätten ferrite. Arrows indicate the shear strain caused by the transformation. (a) before nucleation; (b) deformation if one ferrite plate forms and (c) deformation if two ferrite plates nucleate back-to-back.

The habit plane between austenite and Widmanstätten ferrite is approximately $\{558\}_\gamma$ [11, page 511]. The necessity to nucleate two plates adjacent to each other forces the interfaces to consist of two variants of the $\{558\}_\gamma$. This results in the angle between the habit planes being sharp (approximately 23°).

Martensite

In contrast to Widmanstätten ferrite, martensite tends to form when a large driving force is present and when other transformations are not able to occur sufficiently rapidly. The transformation is completely diffusionless at all stages and

there is sufficient driving force for carbon to be trapped in the ferrite. Martensite consists of lenticular grains of ferrite in a matrix of austenite. As will be discussed in detail in section 2.4, in interstitial-containing alloys, the phase produced by the martensitic transformation will be body-centred tetragonal. In interstitial-free alloys, such as Fe–30 wt% Ni, the martensite will be body-centred cubic [29] unless the substitution atoms order. The presence of carbon impedes dislocation motion due to the formation of Cottrell atmospheres and the lower symmetry of the BCT crystal results in fewer slip systems, further impeding dislocation motion. This makes this type of steel strong, since dislocations do not move easily, but brittle since little plastic work may be done before failure occurs [12, page 26]. Tempering the steel allows carbon to leave solution in the martensite, either by precipitating as carbides or by diffusing into another phase. This raises the toughness and ductility of the steel at the expense of reducing the yield strength.

Since no diffusion whatsoever is required for martensite to form, the transformation can be extremely rapid, limited only by the rate at which atoms can move in a disciplined manner. This may approximate to the speed of sound in the metal. Such rapid transformations can result in audible sounds [30–32].

Due to the low temperatures at which martensite forms the yield strength of the parent austenite is higher than during other transformations and a significant proportion of the transformation strain is accommodated elastically. Typically, this stored energy is of the order of $600\,\mathrm{J\,mol^{-1}}$. Contributions due to the interfaces in transformation twins are of the order of $100\,\mathrm{J\,mol^{-1}}$. Some plastic relaxation may occur during the transformation, but the total energy of the resulting dislocations is an order of magnitude less than the twinning and elastic strain energies. The interface energy between the parent austenite and the martensitic ferrite is typically $1\,\mathrm{J\,mol^{-1}}$, which is significantly smaller than the strain energies but is significant, especially during nucleation [33, page 10]. Given the much larger strain energies involved in the transformation, martensite plates tend to form with small ratios of thickness to length, i.e. a small *aspect ratio* (figure 2.11(a)). Plates form in a zig-zag pattern which represents an array in which each plate accommodates the shape change of adjacent plates (figure 2.11(b)).

Since martensite forms by a displacive mechanism, there is a well-defined orientation relationship between the parent and product phases. In the Kurdjumov-Sachs relationship [34], where the close-packed planes of the austenite and ferrite are parallel, as are a pair of close-packed directions within those planes. The other close-packed direction is slightly misaligned with the corresponding direction in the austenite:

$$\{011\}_{\alpha} \parallel \{111\}_{\gamma} \tag{2.9}$$

$$\langle 11\bar{1}\rangle_{\alpha} \parallel \langle 10\bar{1}\rangle_{\gamma} \tag{2.10}$$

The Nishiyama-Wasserman orientation [35, 36], is rotated relative to the Kurdjumov-Sachs orientation by 5.25° about the normal to the parallel, close-packed planes. This results in both close-packed directions being misaligned by half the angle of that in Kurdjumov-Sachs. In the Greninger-Troiano relation [37], the close-packed planes are misaligned by 2.7° and the close-packed directions lie 0.2° apart. All of these orientation relations are idealisations and the true orientation relation is irrational.

Martensite will only form in a given steel below a certain temperature known as the martensite-start temperature, M_{s}. Below this temperature, it does so rapidly depending on the available thermodynamic driving force. If there is only just enough driving force to start the martensite transformation, the transformation will stop with only a small amount of martensite in the steel. This is because strain accumulates in the parent austenite and the volume available for new martensite grains to form is limited by the presence of existing ones. Holding at a particular temperature for a long time will not alter the fraction of martensite formed, only reducing the temperature may do this. Below some temperature, no further martensite formation occurs. This temperature is known as the martensite-finish temperature, M_{f}.

Bainite

Martensite forms at large undercoolings where there exists a large driving force that can overcome the nucleation barrier. Equilibrium microstructures exhibit very

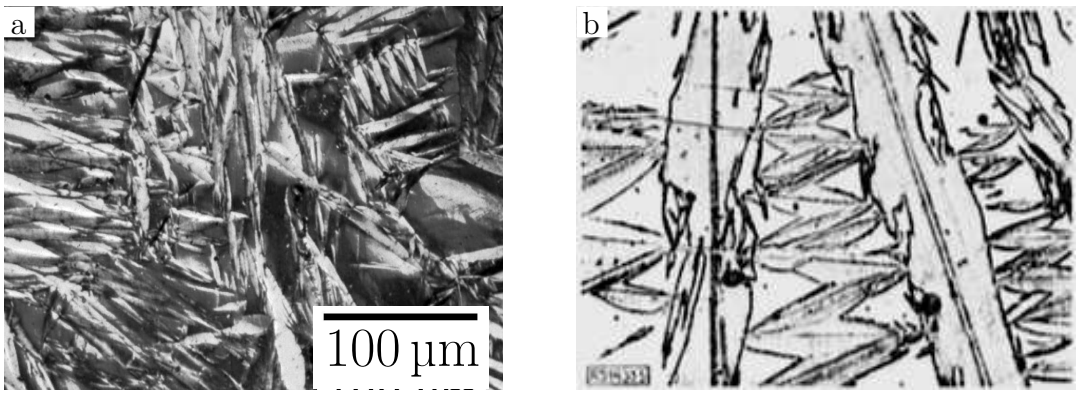

Figure 2.11: Optical micrographs of martensite, (a) Fe–30 wt% Ni–0.4 wt% C. Adapted from [14, micrograph 846]; (b) zig-zag arrangement of martensite in Fe–29 wt% Ni [32] (no scale bar provided).

small stored energies, mainly due to the formation of interfaces. One intermediate case is Widmanstätten ferrite (section 2.1.3). Another is bainite.

Bainite forms at temperatures too high to sustain diffusionless nucleation but only forms at temperatures below which there is sufficient driving force to overcome the stored energy contributions, which have been quantified to be $400\,\mathrm{J\,mol^{-1}}$ [38]. The temperature at which bainite first forms is referred to as the bainite-start temperature, B_s.

2.2 The bainitic microstructure

First identified by Davenport and Bain in 1930 [39], bainite results from the transformation proceeding at temperatures too low to allow a reconstructive transformation but too high to drive the diffusionless martensitic transformation.

Even 85 years after the discovery of bainite at the time of writing, the exact nature of the bainite transformation is the subject of continued debate, with two alternative models proposed. The first is that proposed by an international committee in 1912 [40], developed by Bain for martensite [41] and applied to bainite by Hehemann and others [40]. This theory asserts that bainite nucleates displacively

under paraequilibrium conditions and then grows, like martensite, by a diffusionless mechanism, but that carbon partitions after the phase change has occurred to reduce the stored energy of transformation relative to that of martensite under the same conditions. Small regions of austenite transform to lenticular plates of ferrite known as *sub-units*. Many sub-units are formed together to form a *packet*. The second model has been supported by Hultgren [42] and later by Aaronson [43] and Hillert [44] and asserts that bainite grows by a ledge-propagation mechanism that is rate-limited by the diffusion of carbon ahead of the transformation interface and that both nucleation and growth take place under paraequilibrium conditions, as for Widmanstätten ferrite.

Evidence in support of the diffusionless hypothesis includes:

- introduction of surface relief, measured using atomic force microscopy (AFM), that was consistent with an invariant plane strain (IPS), characteristic of the shear operations seen in the Bain strain [45];

- the accumulation of high dislocation density in the material, observed in transmission electron microscopy (TEM), atom probe tomography (APT) and dilatometry, consistent with the plastic accommodation of transformation strains arising from a displacive transformation [46–49];

- the synchrotron X-ray diffraction (XRD) experiments of Stone et al. [50], which investigated the bainite transformation *in-situ* and in real time, revealing:

  - the accumulation of non-uniform stresses after the bainite transformation, characteristic of displacive transformation strains;

  - the lack of austenite heterogeneity at any stage prior to the bainite transformation in a synchrotron study, precluding carbon redistribution ahead of the transformation;

  - the evolution of a second austenite peak simultaneous with or a short time after the formation of bainitic ferrite. This is consistent with

the formation of a population of carbon-enriched austenite as carbon partitions from supersaturated ferrite;

- the derivation of a consistent kinetic theory that has been able to accurately predict transformation behaviour of bainitic steels [51];
- XRD and APT experiments that have shown carbon content in bainitic ferrite limited to the level consistent with diffusionless growth [47, 48, 52–57];
- a plethora of data showing bainitic ferrite carbon contents above that expected under paraequilibrium conditions, in particular atom probe measurements showing Cottrell atmospheres and carbon supersaturation in bainitic ferrite after and during the early stages of the bainite transformation [54];
- high-precision measurement showing no substitutional solute partitioning after the formation of bainite.

Evidence in favour of the paraequilibrium ledge-growth mechanism includes:

- directly-observed growth velocities that are more typical of diffusion velocities rather than displacive transformation velocities [58–60];
- scanning tunnelling microscope and AFM measurements showing surface relief more consistent with ledgewise growth rather than IPS [61, 62];
- the analogous microstructures of bainite and that formed during solidification of cast iron (referred to as ledeburite) and the fact that the latter certainly occurs via a carbon-diffusion-controlled ledge growth mechanism [63].

Most of the evidence of low growth rates presented to support the ledgewise growth mechanism is based on optical microscopy and can be equally-well explained by slow nucleation and fast growth of bainitic ferrite sub-units. Hu et al. [60] used laser scanning confocal microscopy to isolate an individual ferrite sub-unit, and measured its growth rate to be $5.1\,\mu m\,s^{-1}$, however, this is based on only three frames taken over 5 seconds and the growth velocity is not constant during even this short time. It is also not certain that the plate was growing parallel to

the surface. The samples used by Hu et al., were 10 mm thick and it is possible that the plate of bainitic ferrite used for the measurement was growing at some angle to the polished surface, meaning that only a component of its growth velocity was measured. This issue was noted by Quidort and Brechet [59], who restricted analysis to only the longest laths to ensure the maximum growth velocity was obtained. Quidort and Brechet [59] combined micrographs and dilatometry to derive the length of the ferrite 'laths' and time for which the material transformed, respectively. Yada et al. [58] used hot stage microscopy with *in-situ* transformation, however it is likely that the optical technique used was not able to resolve individual sub-units and so the measurement was for the growth of a packet. A similar study by Kang et al. [64] observed growth of bainite sub-units using hot-stage TEM and concluded that growth occurred by shear and not ledgewise growth.

While the overall surface relief of both the bainite 'plate' and the 'sub-subunit' measured by Fang et al. [61] are described as 'tent shaped' and consistent with a ledgewise growth mechanism, the actual shape is similar to that observed by Swallow and Bhadeshia [45]. The only difference between the two studies is that Fang et al. [61] attributes each 'tent shaped' region to ferrite only, with no austenite inside their (lower) 'bainite plate'. This 'plate' consists of 'sub-subunits' that exhibit a similar surface relief to that measured in subunits by Swallow and Bhadeshia [45]. This does not, therefore, provide diagnostic evidence for ledgewise growth of bainite.

The similarity in morphology between ledeburite, Widmanstätten ferrite and bainite are intriguing, the most likely explanation is coincidence. Ledeburite forms during a solidification reaction, and the presence of liquid relieves any transformation strain during the solidification of the primary phase. There is no reason why a solid-state reaction would necessarily appear the same if it proceeds by a similar mechanism, as strain energy could lead to a different morphology. Furthermore, even if one concludes that the microstructures do look similar, there is no physical evidence that the same mechanisms governed the reactions, as is claimed by Borgenstam et al. [63].

On the balance of the evidence listed, it seems clear that the diffusionless

growth mechanism is correct and this mechanism is therefore used when designing new compositions.

In the type of steel relevant to the present work, bainite consists of alternating regions of transformed ferrite and untransformed austenite. Nucleation is on austenite grain boundaries and grows into the austenite grain [38, 65]. At low magnifications, it appears as though there is a modulated (layered) microstructure, such as that shown in figure 2.12(a). At high magnifications it becomes possible to resolve the features in figure 2.12(b). These features reveal that bainite grows in *packets*, where clusters of platelets with similar orientations grow with untransformed austenite between them. This is analogous to lath martensite [66]. Each platelets grows to a limited size since defects created by the plastic accommodation of the shape change render the interface immobile. The transformation propagates due the nucleation of new platelets in close proximity. Each ferrite grain produces a strain field around it, which leads to more favourable nucleation sites near its tip. The growth of each bainitic ferrite platelet — known as a *sub-unit* when it forms a constituent of a packet — is driven by the thermodynamic driving force for the diffusionless transformation of austenite to ferrite (shown in figure 2.13) and is resisted by the creation of an austenite/ferrite interface and the requirement to accommodate the transformation strain in the parent lattice.

2.2.1 Plastic accommodation of displacements

The formation of bainite causes a change in the shape of the transformed region, consisting of a shear of approximately 0.22–0.26 [45, 68, 69]. At the temperature at which bainite forms, the austenite is relatively weak and this large deformation causes plastic relaxation in the adjacent parent austenite [70]. The resulting dislocation debris accommodates [71] and hinders the progress of the transformation, although the relaxation greatly reduces the overall stored strain energy due to the displacements.

Continued transformation causes further deformation and an accumulation of dislocation density in the parent austenite around the transforming region. Thus, the parent austenite in the vicinity of the bainitic ferrite is work hardened and

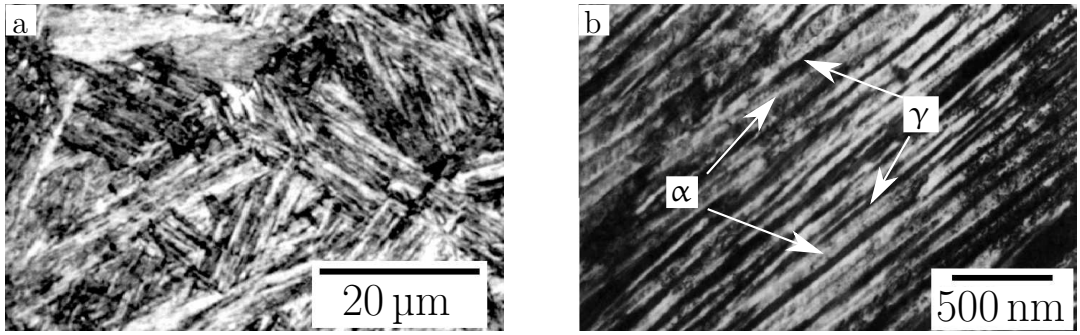

Figure 2.12: Micrographs showing bainite at different scales. (a) optical micrograph showing bainite packets. Optical microscopy cannot resolve individual ferrite sub-units and retained austenite films. (b) transmission electron micrograph of the interior of a bainite packet, showing retained austenite films and ferrite sub-units. Both adapted from [67].

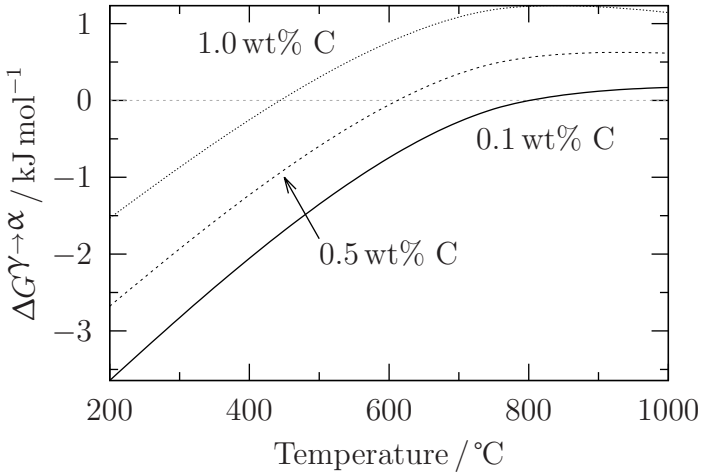

Figure 2.13: Molar driving force for the transformation from austenite to ferrite at a fixed composition, $\Delta G^{\gamma\to\alpha}$ as a function of temperature for Fe–0.1 wt% C, Fe–0.5 wt% C and Fe–1.0 wt% C [25, 26]

eventually stifles the growth of the bainitic ferrite. The transformation continues by the nucleation of new platelets at the tip of the stifled plate, where the carbon enrichment is minimal due to the small volume of the adjacent ferrite and the elastic strains favour the formation of a new platelet in the same orientation with intervening *films* of austenite, forming a packet. If there is sufficient retained austenite, the "films" are connected in three dimensions and are said to *percolate*.

2.2.2 Destination of carbon

Carbon is relatively mobile at the temperatures at which the bainite grows. The carbon in the bainitic ferrite can either precipitate as carbides or partition into the untransformed austenite and then precipitate. The latter occurs at relatively high temperatures, leading to an *upper bainitic* microstructure and is given the symbol α_{ub} (figure 2.14(b)). At lower temperatures, not all of the carbon is able to escape the ferrite. The carbon that is able to leave the ferrite precipitates at the austenite/ferrite boundaries, whereas that remaining in the ferrite precipitates as fine cementite with a long axis approximately 60° to the main growth direction of the ferrite sub-unit [11, 72, 73] (figure 2.14(a)). This is known as *lower bainite* and is denoted as α_{lb}. In the presence of sufficient quantities of elements that are insoluble in cementite, especially silicon, no cementite precipitates and all the carbon escapes to defects or into solid solution in the austenite. This is known as *carbide-free bainite*. The formation of carbide-free bainite is shown schematically in figure 2.15.

Bainitic ferrite ultimately contains less than the bulk content of carbon and so carbon must have been redistributed within the timescale of the transformation — one point, at least, in which both the Zener and Hultgren models agree. Bainitic ferrite is also usually found to be carbon-supersaturated after the transformation has stopped — i.e. it contains more than the maximum amount of carbon permitted by equilibrium with cementite, as described by the maximum extent ferrite phase field of the iron–carbon phase diagram (at room temperature, this is approximately 0.02 wt% [75]). The austenite that remains untransformed at any stage is enriched in carbon, above the bulk carbon content. The austenite may be

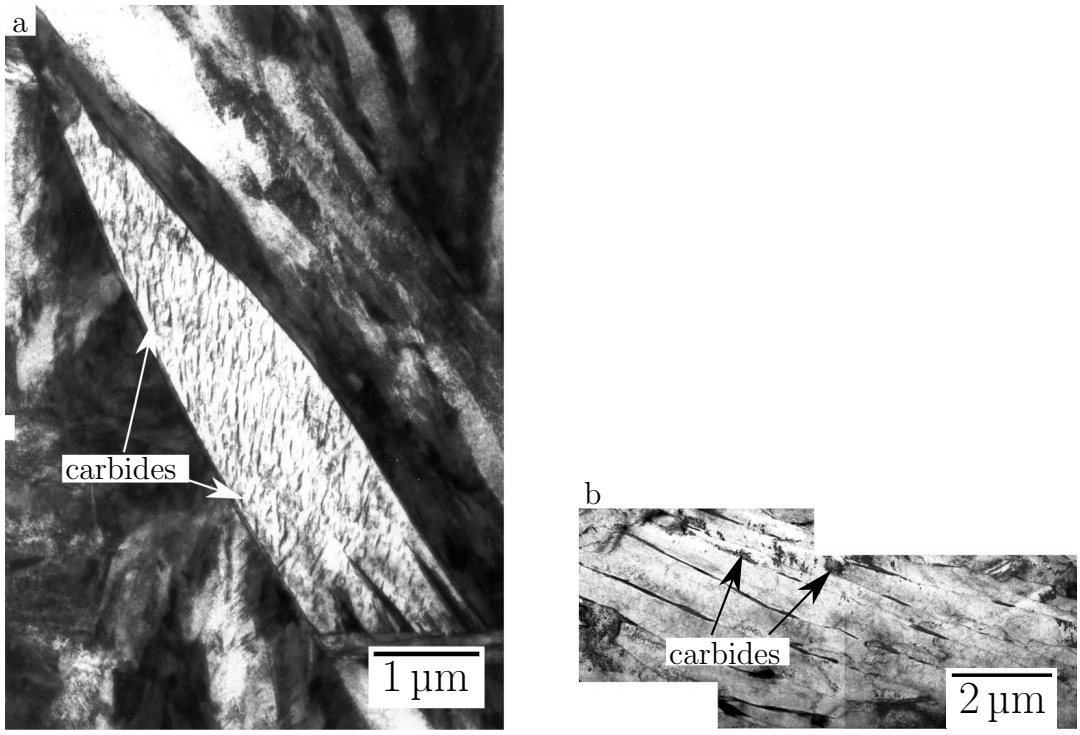

Figure 2.14: Transmission electron micrograph showing carbide precipitation in (a) [74, adapted] upper and (b) lower bainite [69, adapted]

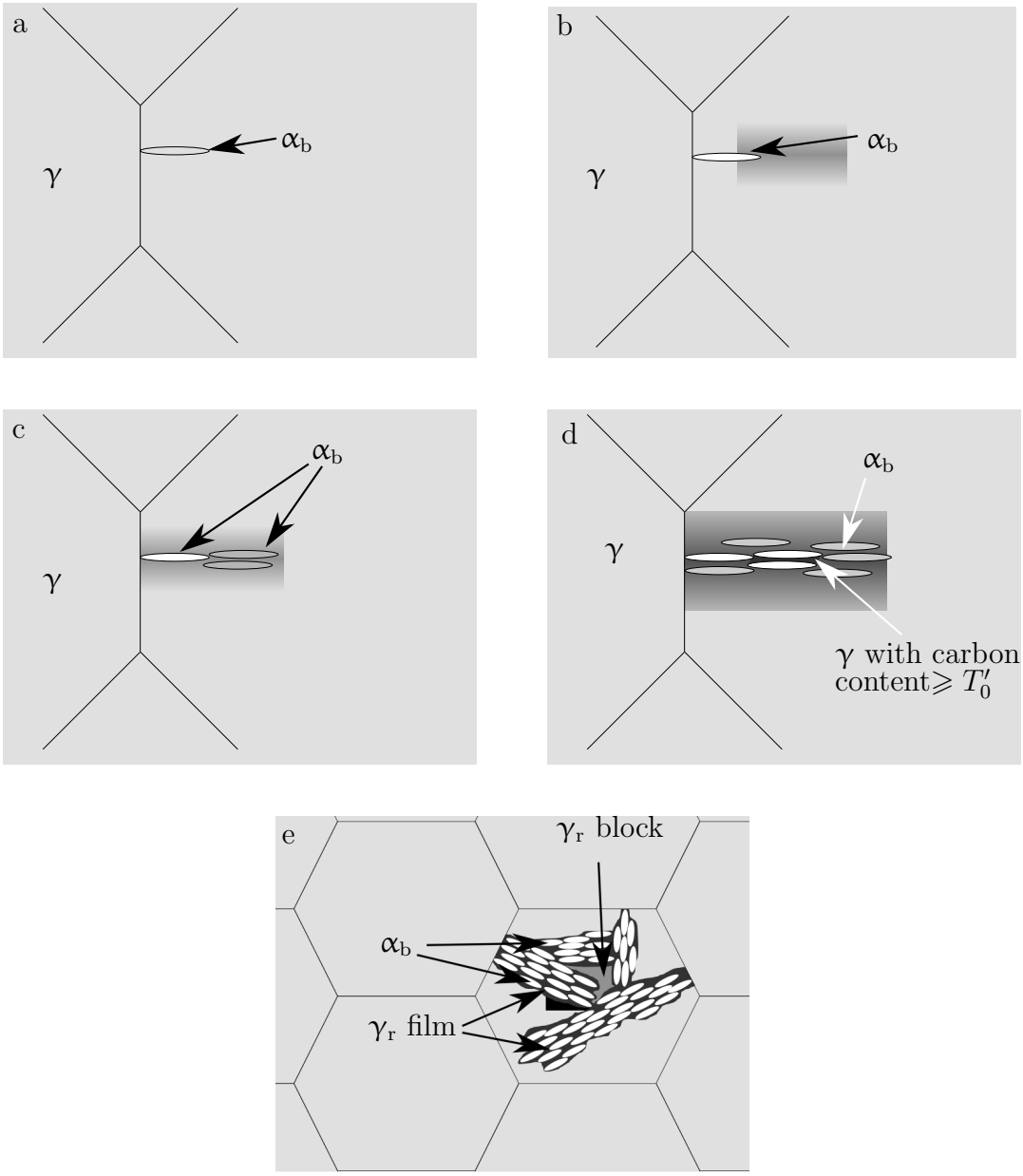

Figure 2.15: Schematic depiction of the formation of carbide-free bainite. White indicates no carbon content, black represents x_{T_0}. (a) nucleation of the first ferrite sub-unit. Ferrite inherits the carbon content of the parent austenite but then carbon partitions back into austenite (b). (c) this localised carbon enrichment together with work hardening stifles the sub-unit but more nucleate to (d) form a packet. (e) the convergence of packets leads to the formation of blocky austenite.

thermodynamically stable with respect to ferrite if a sufficiently high carbon content is reached. Indeed, austenite remains in the microstructure once the bainite reaction stops and is said to be *retained*. The transformation products expected at equilibrium are predicted by the iron–carbon phase diagram and under conditions that produce bainite these are often ferrite and cementite. Since the bainite transformation produces transformation products other than those predicted at equilibrium, it is said to be an *incomplete reaction* [38, 43, 76, 77].

Since bainitic ferrite inherits the composition of the parent austenite, the austenite should continue to transform and produce more bainitic ferrite at a fixed temperature until it reaches the point at which its carbon content is high enough for it to have the same free energy as ferrite of the same composition. The locus of compositions and temperatures at which both austenite and ferrite of the same composition have the same free energy is known as the T_0 line and may be plotted on the phase diagram. The temperature at which austenite and ferrite of the same composition have the same free energy is termed the T_0 temperature and the carbon content required for austenite and ferrite of the same composition to have the same free energy at a particular temperature is x_{T_0}.

In practice, the conditions under which austenite and ferrite have the same free energy do not define whether or not bainitic ferrite may form from austenite. Instead, the conditions under which sufficient driving force exists to overcome the stored energy of the bainite transformation define whether austenite will transform to bainitic ferrite. The equivalent of the T_0 line that accounts for this stored energy is known as the T_0' line. The equivalent to x_{T_0} that accounts for stored energy is $x_{T_0'}$. Since on the T_0' line the free energy of austenite is greater than that of ferrite of the same composition, the T_0' line lies below the T_0 line.

The T_0 and T_0' lines in a Fe–x C–1.0 Mn (wt%) steel are given in figure 2.16(a) and the relationship between the T_0 line and the equilibrium austenite and ferrite phase fields is given in figure 2.16(b). Experimental observations have shown that the carbon content of the retained austenite follows the T_0' line [11, figure 5.5b].

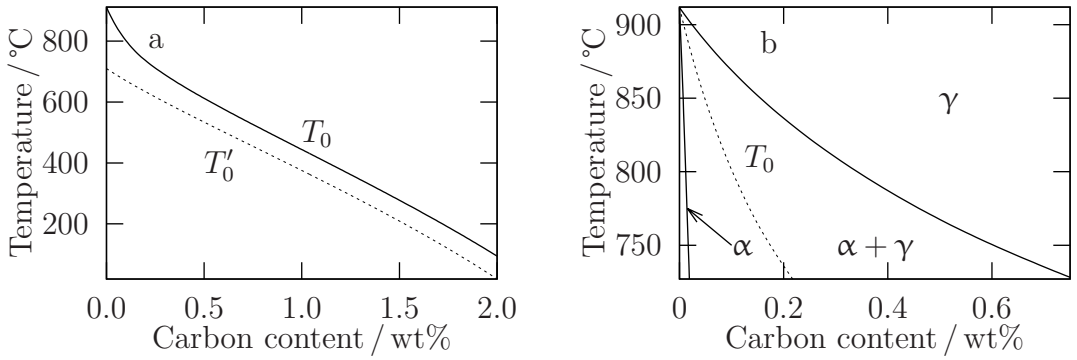

Figure 2.16: (a) T_0 and T_0' lines; (b) the T_0 line in the equilibrium phase diagram calculated using the modelling software MatCalc [78] for Fe–x C.

2.2.3 Mechanical properties of bainite

The two phase structure of bainite gives bainitic steel properties of both the constituent phases: hardness and strength from ferrite and toughness and ductility from austenite [11, page 303]. The presence of austenite allows carbon to partition away from ferrite to occupy regular octahedral interstices. This leads only to an isotropic volume expansion that interacts weakly with dislocations [79, 80]. For this reason, bainite is generally found to be less hard than carbon-rich martensite. Lower bainite, with a dispersion of fine cementite particles embedded within the ferrite, has a higher hardness and tensile strength than upper and carbide-free bainite. Upon heating, cementite also precipitates from the carbon-rich austenite, which then transforms to martensite upon cooling. This helps to counteract the coarsening of any carbides and any grain growth that occurs during tempering of bainite, resulting in little change in hardness and yield strength during tempering. The yield strength of bainite is also affected by the high dislocation density that results from the shear transformation, which leads to work hardening and which exists in both the austenite and ferrite constituents.

Austenite is also able to transform under applied stress to martensite in an effect called ***tr****ansformation* ***i****nduced* ***p****lasticity* (TRIP) [81–84]. This resulting plastic work is a mechanism for absorbing energy during failure, raising toughness

and elongation. Since bainite can contain a significant fraction of austenite, the TRIP effect may be exploited to enhance toughness.

2.3 Enhancing the mechanical properties of bainite

2.3.1 Strengthening mechanisms in steels

There is always a desire to produce steels which have a higher yield strength and toughness. Stronger steel in principle allows the same function to be fulfilled with less material. However, adequate toughness is required to avoid catastrophic brittle fracture in service. Strength relies on hindering the motion of dislocations which in turn limits ductility and, hence, toughness. Such mechanisms include interstitial and substitutional solution strengthening, precipitate hardening, dispersion strengthening, order hardening and work hardening. These mechanisms are summarised in Bhadeshia and Honeycombe [12, chapter 2].

Toughening steel requires that more energy is absorbed during fracture. One way to do this is to increase the size of the plastic zone ahead of a crack tip, which requires a lower yield strength. Clearly if there is a lower yield stress, there will be a larger plastic zone ahead of a given crack tip under a given far-field stress. It is therefore clear that strengthening mechanisms that rely solely on hindering dislocation motion will necessarily diminish toughness. While it is possible to increase toughness in composite materials using techniques such as crack bridging or crack deflection, these materials are usually anisotropic and are susceptible to fibre buckling under compressive loading. This makes such of materials less desirable in those engineering applications where multiaxial and compressive stress states are possible. Metallic materials perform well under compressive loading and — with the exception of some highly-specialised applications such as single crystal gas turbine blades and materials that possess crystallographic texture — exhibit isotropic mechanical properties.

One mechanism that allows strength to be raised without compromising tough-

ness is grain refinement [85]. Ordinary dislocations do not alter the crystal structure during slip as their Burgers vectors are also lattice vectors. Slip displacements are therefore difficult to propagate across crystallographic discontinuities such as grain boundaries. They must accommodate each other and annihalate or *pile-up* ensues at obstacles [86]. The resulting stress field eventually triggers a dislocation in an adjacent grain, thus propagating slip and causing macroscopic yielding. The shear stress projected by a dislocation pile-up is inversely proportional to the square root of the length of the pile-up [87, 88]. In small grains, the length of the pile-up is constrained by the size of the grain, leading to the Hall-Petch relationship, given as equation 2.11, where $\sigma_{\mathrm{y},0}$ is the yield stress in a large-grained sample of the material and k is a material-dependent parameter [87, 89]. Although dislocations are constrained at low stresses, general dislocation glide can occur at high stresses once it becomes possible to form new dislocations across grain boundaries and so ductility is not adversely affected. The resulting increase in work done enhances toughness. Strength and toughness therefore increase simultaneously.

$$\sigma_{\mathrm{y}} = \sigma_{\mathrm{y},0} + \frac{k}{\sqrt{d}} \tag{2.11}$$

In the Hall-Petch mechanism, dislocations are able to form with relative ease, but are unable to glide beyond the confines of the grain in which they were created. Once the grain size reaches a certain lower limit, dislocation formation itself is limiting and leads to a yield strength given by equation 2.12, where k' is $115\,\mathrm{Pa\,m^{-1}}$ and $\bar{L}$ is the *mean lineal intercept* of the grains [90–92], which is equivalent to twice the actual grain size for plate-shaped grains [93, table 4.1].

$$\sigma_{\mathrm{y}} = \sigma_{\mathrm{y},0} + \frac{k'}{\bar{L}} \tag{2.12}$$

Grain refinement can be achieved by rapid cooling [94] of small samples (i.e. components are restricted to wires or thin plates). Extreme deformation can also lead to refined grains. For example, equal channel angular extrusion induces large plastic strains and redundant work, while maintaining the cross-section of the

workpiece. This is achieved by forcing the steel through a die which contains a large-angle vertex, as shown schematically in figure 2.17. The process can be repeated multiple times to increase the total strain [95–97]. Clearly, to retain the plastic strain, the work must be done cold to prevent recovery and the die must be sufficiently robust to cope with the trauma. This, combined with the need to develop sufficient pressures, makes equal channel angular extrusion an expensive process, and limits the size of workpiece. A variant of this technique is to deform austenite while hot to induce dynamic recrystallisation, promoting a grain size of the order of a micrometre. This and other deformation techniques are outlined in Beladi et al. [98, table 2]. Martensitic steel, when cold-rolled has a structure of dislocation cells give a greater density of interfaces and improving the mechanical properties accordingly, in a similar manner to equal channel angular extrusion [99–102]. Of the techniques outlined in Beladi et al. [98], the cold working of martensite was shown to achieve the finest grain size, as low as 200 nm. Such cold-rolled martensitic steels, for example, those studied by Tsuji et al. [100], were able to achieve an ultimate tensile strength of 1.5 GPa and 8% uniform elongation, significantly stronger than the as-quenched state (1100 MPa) with little loss of uniform elongation (10%, reduced to 8%), albeit with minimal uniform elongation. Tempering the cold-rolled structure was able to significantly enhance ductility, with up to 8% uniform elongation achieved, but at the cost of almost halving the ultimate tensile strength.

Bainite, unlike the martensite/ferrite steels studied in references [99–102], has ductile austenite together with the hard ferrite, and so should be able to exhibit much better uniform ductility than nanostructured martensitic steels, while still benefiting from the strengthening provided by grain refinement. During deformation, the austenite gradually transforms to martensite via the TRIP effect. Theoretically, ductility should continue until less than 10% by volume of austenite remains, at which point, stress will focus on the more brittle ferrite — the so-called percolation threshold [103–105].

The challenge of forming bainite with nanometre-scale grain size may be tackled by considering the growth mechanism of bainite. As noted in section 2.2.1, the

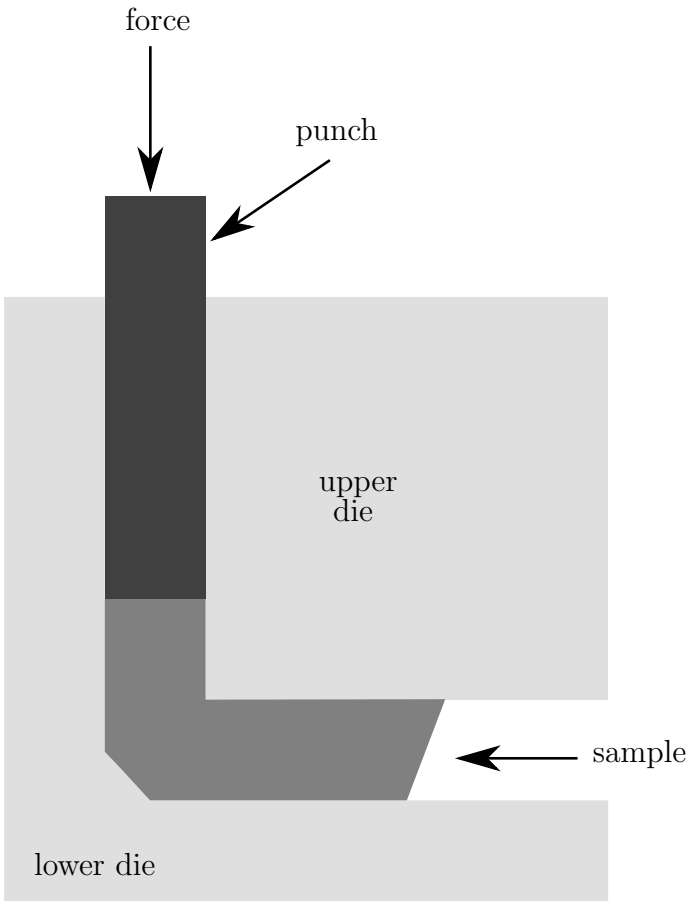

Figure 2.17: Schematic of equal-channel angular extrusion [after 97, figure 5]

fact that bainite grows at temperatures above those of martensite, and at a much slower rate allows plastic relaxation of the transformation strains. It should thus be possible to control the size of individual ferrite sub-units by controlling the available thermodynamic driving force and the yield stress of the parent austenite. Once the work required to shear the parent austenite by the amount required to allow an incremental growth of a given ferrite sub-unit exceeds the total free energy released by that increment of transformation, the growth of that sub-unit will cease, as described in section 2.2.

2.3.2 Bulk nanocrystalline steels

A recent development in steel metallurgy is a new class of steels called *nanostructured bainitic steels*. Careful alloy design is used to control the austenite to ferrite driving force to suppress the bainite transformation to temperatures lower than those normally associated with bainite while simultaneously suppressing the martensite transformation to even lower temperatures so that bainite is allowed to form. So far, the bainite transformation has been allowed to proceed at temperatures as low as 125 °C [47, 67, 106]. The result is a mixture of austenite and ferrite with extremely fine effective grain size. Typically in nanocrystalline bainite, the bainitic ferrite forms with a width of the order of 50 nm and retained austenite films remain with width which is typically tens of nanometres wide [1, 67, 107, 108]. Blocks of retained austenite remain, albeit $\sim 1\,\mu m$ wide. All of these dimensions represent an order of magnitude decrease compared to the values typically observed in regular bainite formed at temperatures more traditionally associated with bainite formation.

In order to form bainite, there must be sufficient driving force for the diffusionless transformation of austenite to ferrite, but not sufficient to allow martensite to form. This requires the addition of a significant quantity of austenite stabilisers, such as manganese, nickel and carbon. The addition of carbon is crucial as it is the post-transformation partitioning of carbon from ferrite to austenite that allows some austenite to become thermodynamically stable. In order to form nanostructured bainite, the amount of carbon added is typically around 1 wt% [67, 75, 107].

This suppresses the martensite transformation to below 200 °C, allowing the bainite transformation to proceed at temperatures at which it is not usually able to, providing rapid work hardening and leading to grain refinement.

Although there are a large number of combinations of alloying additions that may be used to form bulk nanocrystalline bainite, the alloys that are presented in the literature generally contain 0.8–1 wt% carbon, 1.5–2 wt% silicon, and one or more of: up to 2.5 wt% manganese, up to 4 wt% nickel, up to 1.5 wt% chromium, up to 0.2 wt% vanadium and microalloying additions of niobium. There are also instances of compositions falling outside these limits [57, 67, 107, 109–112].

2.3.3 Alloy design

The ultimate goal of bulk nanocrystalline bainite alloy design is to:

- stifle sub-unit growth to limit the size of the bainitic ferrite and retained austenite to provide strength;
- retain sufficient austenite for the alloy to be ductile and provide toughness;
- allow the transformation to finish within a reasonable time period;
- avoid the need for rapid cooling;
- avoid increasing the cost of the alloy;
- produce an alloy which can withstand exposure to high temperatures.

If the bainite transformation temperature is reduced, dislocation glide is more difficult and the dislocation density rises faster for a given amount of transformation [113]. Therefore, at lower bainite transformation temperatures, not only does the parent austenite become inherently stronger [70], but the work hardening rate will increase [113]. Both of these effects will raise the free energy change required for the transformation front to advance.

The shear measured during the formation of nanostructured bainite has been reported to be as high as 0.46 [114] similar to Widmanstätten ferrite [27], but

greater than bainite formed at higher temperatures. This explains the slender plates obtained since the strain energy scales proportionally to the plate aspect ratio. The stored energy due to the shear deformation is approximately equal to the product of the aspect ratio of the plate, the shear modulus and the square of the magnitude of the total deformation. In their experiments, Peet and Bhadeshia determined the stored energy due to shear to be approximately $340\,\mathrm{J\,mol^{-1}}$ — very similar to the total stored energy of regular bainite ($400\,\mathrm{J\,mol^{-1}}$) [115].

While dislocation density increases faster as temperature decreases, which leads to an expected refinement of the ferrite sub-units, the magnitude of the transformation driving force also increases, as demonstrated in figure 2.13. This will lead to larger ferrite grains, as more work may be done to deform the austenite before the driving force is no longer sufficient to continue the deformation, however, experimental findings indicate that grain size is refined as transformation temperature is decreased. This implies that the stored energy of transformation increases faster than the driving force for bainite formation as the transformation temperature is reduced in this range.

2.3.4 Thermal Stability of Bulk Nanocrystalline Steel

It has been noted that the bainite reaction does not represent a thermodynamic equilibrium, but occurs due to limited atomic mobility at low temperatures. Therefore, with sufficient time, a bainitic material exposed to elevated temperatures may undergo microstructural changes that compromise properties, in particular the precipitation of carbides from the carbon-enriched austenite [116]. Once carbides have begun to form, carbon will leave solid solution to feed the growth of the precipitates. The austenite then transforms to ferrite. This transformation may occur at the tempering temperature or upon subsequent cooling to ambient temperature, depending on the composition of the steel. The formation of crack-nucleating carbide particles and the loss of the ductile austenite from bainite renders it brittle and weak.

Tempering carbides

Cementite, in the absence of graphite, usually represents the equilibrium phase for carbon in contact with ferrite. Its unit cell is shown in figure 2.18(a). Under certain conditions, it is possible to identify other *transition* carbides that precipitate before cementite, as they are easier to nucleate [117]. Transition carbides do not represent the lowest energy species during tempering, and only form when atomic mobility is sluggish enough to make nucleation difficult, regarded to be below 200 °C. Above this temperature, and in the absence of other effects that prevent it, cementite precipitates.

Carbides rich in substitutional solutes may also form during tempering, such as those containing niobium [118–124], tungsten [125], titanium [118, 126, 127], molybdenum [128–130], vanadium [126, 131, 132] and chromium [118, 126, 133], if the tempering temperature is sufficiently high for these substitutional solutes to diffuse [12, table 1.4]. This limited supply of constituent atoms makes alloy carbides fine, which means that they tend tend to form coherent interfaces. The fine size also makes them unlikely to fracture during deformation, unlike relatively coarse cementite particles. Since the growth of these carbides requires the long-range diffusion of substitutional atoms, they will only extremely slowly coarsen, making them suitable for the vast majority of combustion-type applications for which steel is a potential candidate material. Various decomposition products in martensitic steels are given in Saha Podder [134, table 2.1].

2.3.5 Mechanism of decomposition in bainite

Here, *decomposition* of the bainitic microstructure refers to the change of retained austenite into cementite and ferrite. The bainite reaction may be summarised by equations 2.13 and 2.14, where it should be remembered that α_b is likely to be supersaturated in carbon, with respect to cementite [52–54]. This carbon-enriched austenite is denoted as γ'. Austenite that survives the transformation is referred to as *retained* and is given the symbol γ_r. γ_r is richer in carbon than the starting bulk composition and is also likely to contain more carbon than is stable

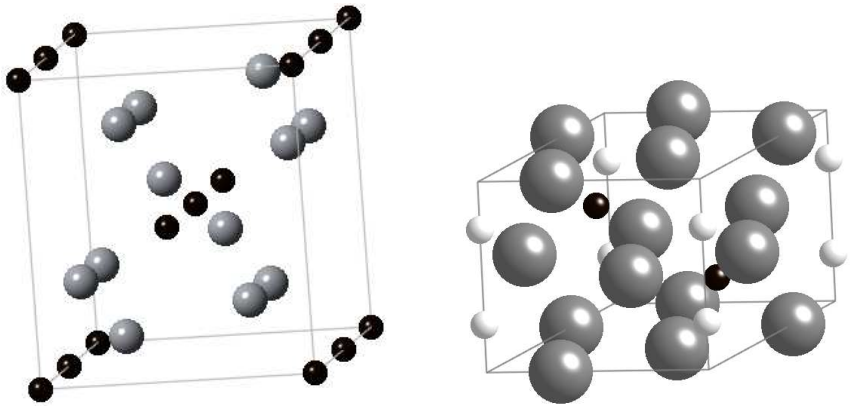

Figure 2.18: Unit cells of tempering carbides. Left: cementite — black atoms are carbon, grey atoms are iron. [135–138]; right: ε-carbide. Large, grey atoms are iron; small, black atoms are carbon sites that are fully occupied and small, light grey atoms are carbon sites with an average occupancy of 6.25% [139].

in solution when in contact with cementite. Some of the carbon-enriched austenite may transform into martensite upon cooling from the transformation temperature.

$$\gamma \rightarrow \alpha_{\mathrm{b}} + \gamma' \tag{2.13}$$

$$\rightarrow \alpha_{\mathrm{b}} + \gamma_{\mathrm{r}} \tag{2.14}$$

During low-temperature tempering of bainite, the predominant method of decomposition is carbide precipitation in the bainitic ferrite where the driving force for precipitation is largest [134]. In steels with a high dislocation density, more carbon is accommodated in Cottrell atmospheres and is not available for initial carbide precipitation [140, figure 8]. In this case, there is a lower driving force for carbide precipitation and cementite is more likely to precipitate directly, as described later by equations 2.15–2.16. Conversely, with only moderate dislocation density, cementite precipitation occurs via the transition carbide, ε, a hexagonal carbide identified by Jack [117, 141] with the formula $Fe_{2.4}C$. The unit cell of ε is given in figure 2.18(b). Cementite then nucleates either independently or on the surface of ε particles and consumes ε as it grows, as described later in

equations 2.17–2.18 and [19, 142, 143].

There is also a range of orthorhombic carbides that are able to form and have been reported in tempered bainite. These are summarised in Saha Podder [134, table 2.2]. One significant orthorhombic carbide is denoted at eta-carbide (η), which was first isolated by Hirotsu and Nagakura [144]. η has the formula Fe_2C and has been found in retained austenite after tempering. This carbide was found by Jha and Mishra [142] to act as a second transition carbide to allow epsilon to be converted into cementite in low carbon steel. However, Kim et al. [145] have shown that it is extremely difficult for η to form, due to it having a large positive enthalpy of formation. Only specific conditions will allow η to form, for example, there being very favourable interfacial conditions to allow the overall free energy change from ε to be negative.

In retained austenite, the driving force for carbide precipitation is lower and so cementite nucleates directly, but only at temperatures in excess of 200 °C [134, table 2.1]. The precipitation of carbides within retained austenite depletes it of carbon and it can undergo subsequent transformation to ferrite at the tempering temperature or to martensite upon cooling to ambient temperature.

$$\alpha_b + \gamma_r \rightarrow \alpha_b + \theta_{in\,\alpha_b} + \gamma_r \tag{2.15}$$

$$\rightarrow \alpha_b + \theta_{in\,\alpha_b} + \gamma \tag{2.16}$$

$$\alpha_b + \gamma_{ret} \rightarrow \alpha_b + \varepsilon_{in\,\alpha_b} + \gamma_r \tag{2.17}$$

$$\rightarrow \alpha_b + \theta_{in\,\alpha_b} + \theta_{\text{between ferrite plates}} + \alpha' \tag{2.18}$$

$$\alpha_b + \gamma_r \rightarrow \alpha_b + \theta + \gamma_{\text{carbon depleted}} \tag{2.19}$$

$$\rightarrow \alpha_b + \theta + \alpha \tag{2.20}$$

The temperatures at which cementite nucleation can occur in ferrite are typically those that are used in the bainite transformation and this is the reason that

lower bainite can form. In the case of upper bainite, carbon diffuses to the austenite/ferrite interface, where it can precipitates to form a cementite film. As noted in section 2.2.2, the addition of silicon that suppresses or retards cementite formation can stifle these decomposition processes and lead to the formation of carbide-free bainite. Heating of the as-decomposed microstructure can lead to "stage two" of tempering and cause cementite to precipitate in the austenite at temperatures in the range 200 ℃–300 ℃ [134, table 2.1].

Andrews [19] noted that, if the Pitsch orientation relationship between austenite and cementite is accepted, and any ferrite produced has the conventional orientation relation with cementite, the ferrite and austenite necessarily have a Kurdjumov-Sachs relation between them, as would normally be expected. Apart from the widely-published Pitsch relation, [146], Thompson and Howell [147] observed another orientation relation in a high-carbon alloy, similar to existing bulk nanocrystalline bainitic alloys. During the early stages of tempering, carbides have been observed in plate-like clusters, similar to the Guinier-Preston zones in aluminium-copper alloys, [148]. Guinier-Preston zones provide a low activation-energy route for the formation of Al_2Cu precipitates in an aluminium matrix, [149], and these carbon clusters may be performing the same rôle in the formation of Fe_3C precipitates in steels. Speich & Leslie proposed a high-silicon carbide as a transition state between ε-carbide and cementite, [150]. They named this γ-carbide.

Although retained austenite films are rich in carbon (section 2.2.2), which suggests that they are more prone to thermal decomposition, the decomposition of blocky austenite is more problematic. This is because decomposed blocks represent a large volume of brittle material and martensite plates are more likely to develop in blocky austenite than in the restricted volume of an austenite film. One simple way to mitigate this problem is to reduce the transformation temperature, as this will increase the amount of carbon required to stabilise austenite with respect to ferrite (increase x_{T_0}) and lead to a higher fraction of bainite forming. This will subdivide existing austenite blocks as the later stages of the transformation proceed [151, 152]. Unfortunately, as will be explained in section 2.3.7, there is a

limit to the extent to which transformation temperatures may be lowered. Such a method would also rob the steel of the ability to undergo TRIP during deformation. There is an optimum carbon content to maximise the energy absorbed during TRIP: too low and the transformation occurs readily, too high and little of the austenite transforms [148]. A more suitable solution would be to ensure that no decomposition occurs once bainite has formed.

Saha-Podder studied the tempering behaviour of austenite retained in bainite [134, section 5]. He showed in his figure 5.4 that the austenite blocks show optical signs of decomposition, whereas films do not and that this change is associated with softening of the sample ([134, figure 6]). These observations were attributed to the transformation of carbon-rich retained austenite to ferrite and cementite. In a sample tempered and then subsequently cooled, untempered martensite formed upon cooling. Transmission electron micrographs of film austenite showed evidence of cementite precipitation, and, during *in-situ* TEM observations, the progressive loss of austenite from the α/γ boundary during prolonged tempering. This decomposition was followed by the onset of recovery, and occurred by movement of the α/γ interface.

Saha-Podder's dilatometric analysis [134] showed that the first process during exposure to elevated temperatures was the tempering of martensite present in the as-transformed microstructure, leading to an initial volume contraction. Subsequently, volumetric expansion occurred as the retained austenite decomposed to cementite and martensite.

Saha-Podder also conducted synchrotron X-ray diffraction studies of bainite with *in-situ* heating [134, chapter 7]. He showed that film austenite decomposes faster than blocky austenite, supporting the contention that it is carbon precipitation that dominates the decomposition process. Due to its higher carbon content, film austenite is more stable with respect to ferrite (or martensite) than blocky austenite, but less so with respect to a mixture of either cementite and austenite or ε and austenite, as suggested in figure 2.19(a).

Such decomposition processes have been observed in bulk nanocrystalline bainite, which would be expected to be vulnerable to tempering due to the high

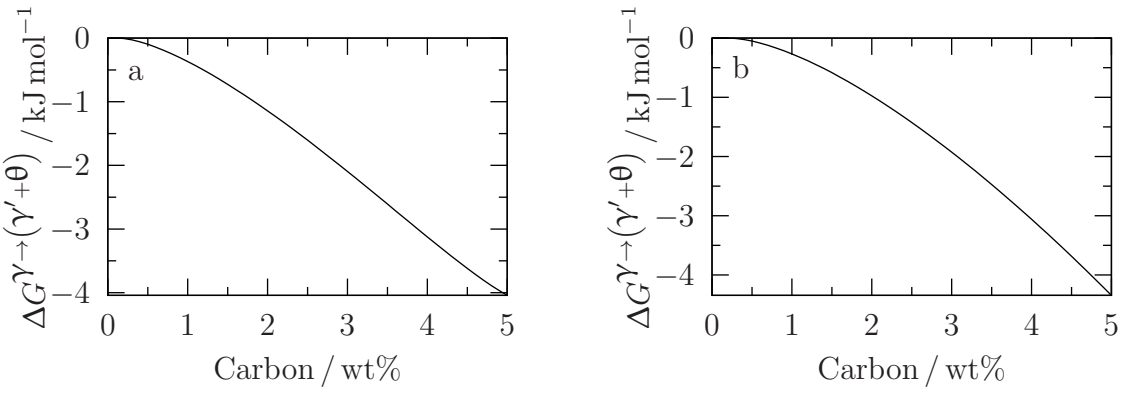

Figure 2.19: Driving force for decomposition of austenite to an equilibrium mixture of austenite and cementite at 450 °C [25, 26]. (a) Fe–x C–3.0 Mn–2.3 Si (wt%) as investigated by Saha Podder [134]; (b) Fe–x C.

carbon contents used (see section 2.3.4). However, Caballero et al. [67] showed that bulk nanocrystalline steels were surprisingly resistant to tempering, resisting a change in hardness up to 550 °C when heated for one hour.

2.3.6 Effects of alloying additions on decomposition

The thermodynamic driving force for the decomposition of a metastable mixture of bainitic ferrite and retained austenite will be affected by the presence of alloying additions. This can be exploited to control the decomposition process.

Carbon

As may be seen in figure 2.19, the higher the carbon content, the greater the driving force for the decomposition of austenite to an equilibrium mixture of cementite and austenite. This suggests that reducing the carbon content of the retained austenite — in practice, the T_0' composition — is likely to lead to an increase in thermal stability. A reduction in carbon may only be achieved by the addition of elements that reduce the driving force for the transformation of austenite to ferrite. This must be done to avoid the martensitic transformation occurring at temperatures

higher than those necessary for the formation of nanocrystalline bainite. Carbon cannot be eliminated entirely [1] as it is required for the formation of bainite — without it, martensite formation would occur directly once the temperature was low enough for the diffusionless transformation to occur (section 2.3.7). Such elements are shown, together with their effects on the driving force for the austenite to ferrite transformation, in [12, figure 4.3b].

Nitrogen

An alternative to using carbon is to add nitrogen to the steel, also an austenite stabiliser [12, figure 4.3b] and is an interstitial alloying element, that partitions away from ferrite during transformation from austenite [153–155]. This may be advantageous as the precipitation behaviour of iron nitrides is different to that of iron carbides, however, the precipitate with the lowest nitrogen content, known as γ' and with the chemical formula Fe_4N is hard and brittle [156] and is observed to form along with ferrite when nitrogen-rich austenite decomposes [153, 154]. The iron–nitrogen phase diagram is given in figure 2.20. Additionally, to introduce a significant amount of nitrogen into steel, powder metallurgy must be used, with associated cost implications.

Silicon

Of the elements used to suppress cementite, silicon is the one that has received the most attention. It has been known to promote the formation of graphite in preference to graphite in cast irons [13, 78, 158] by donating electron density to iron atoms and preventing them from interacting with clusters of carbon atoms, which then precipitate out as graphite [159, page 77].

The mechanism by which silicon suppresses the fraction of cementite has been discussed [150, 160–164]. Owen [160] suggested that silicon may partition ahead of a growing carbide which cannot accommodate it in its lattice, leading to an accumulation of silicon ahead of the growth interface. Concurrently, silicon raises the activity of carbon in austenite, which slows the diffusive flux of carbon towards the carbide since diffusion occurs down gradients of chemical potential. In order for

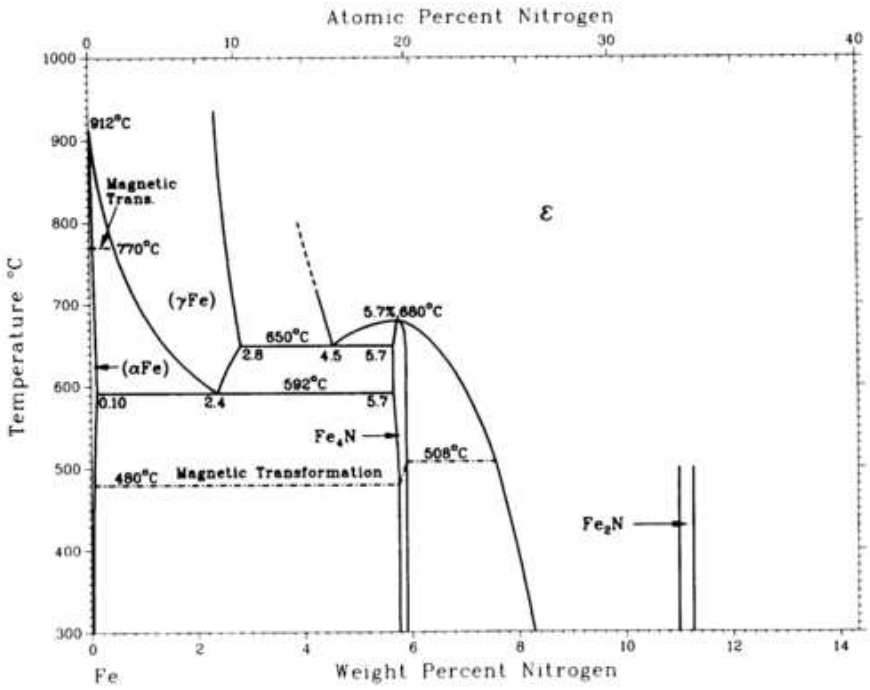

Figure 2.20: Iron–nitrogen equilibrium phase diagram [157]. Reproduced from [10] with permission of ASM International.

growth of the particle to continue, silicon must diffuse away from the interface so that the slower silicon diffusion, rather than carbon diffusion, becomes the limiting factor.

It is assumed that cementite initially forms under paraequilibrium conditions, i.e. without the partitioning of substitutional alloying elements, including silicon [165–167]. This has been observed independently by Babu et al. [168] and Caballero et al. [169] using atom probe tomography, where there was a similar silicon content both inside and around a cementite precipitate (shown in [169, figure 8]). Babu et al. [168] showed that prolonged tempering leads to a reduction of silicon content in the cementite. The thermodynamic effects of incorporating silicon into the cementite lattice were investigated by Bhadeshia et al. [170] and from first principles by Jang et al. [171]. They found that replacing one iron atom with silicon atom in the least unfavourable lattice site raised the enthalpy of formation of cementite from approximately $20\,\mathrm{kJ\,mol^{-1}}$ to $120\,\mathrm{kJ\,mol^{-1}}$, giving a thermodynamic basis for the suppression of cementite due to silicon, as the driving force for cementite precipitation is greatly reduced [78]. Conversely, Jang et al. [172] calculated that silicon can stimulate precipitation of ε in place of silicon, but concluded from *ab-initio* calculations that this effect was not thermodynamic in origin, but leads to a contraction of the c lattice parameter of ε, increasing the coherency with ferrite. Kim et al. [145] performed similar *ab-initio* calculations to Jang et al. [171] and their results are summarised in table 2.1. This was supported by calculation of the driving force of cementite precipitation and misfits by Kim et al. [143]. This effect is specific to ferrite, since the orientation relationship will be different in austenite. There is experimental evidence of ε forming in austenite [142, 173, 174], although as Jang et al. [172] note, this appears to contradict thermodynamic calculations [175]. Overall, there is no definitive evidence that adding silicon will result in increased ε precipitation.

Silicon is also an effective strengthener of ferrite [13, page 244] and austenite [176]. However, adding silicon in excess of $4\,\mathrm{wt\%}$ is known to embrittle ferrite. Silicon additions also reduce the density of steel, allowing a given component to be made with a lower overall mass [177]. Silicon also promotes the formation of

Carbide	Fe,M / C	ΔH / kJ (atom-mole)$^{-1}$	ΔH with the substitution by an impurity atom
Zener-ordered J-model $Fe_{16}C_2$	8	+5.80	—
Zener-ordered T-model $Fe_{16}C_2$	8	+5.78	—
Zener-ordered J-model $Fe_{16}C_4$	4	+24.18	—
Zener-ordered T-model $Fe_{16}C_4$	4	+23.98	—
Cementite θ -Fe_3C	3	+5.38	+7.70 (Si) +4.73 (Al) +5.07 (Mn)
Hexagonal ϵ -Fe_3C	3	+5.3	+11.38 (Si)
Hägg carbide χ -Fe_5C_2	2.5	+152.6	—
Hexagonal ϵ -$Fe_{2.4}C$	2.4	+6.23	+11.38 (Si) +4.98 (Al) 4.40 (Mn)
Hexagonal ϵ -Fe_2C	2	+7.00	+20.33 (Si)
Orthorhombic η -Fe_2C	2	+126.1	—
Anti-Perovskite κ-carbide Al(Fe_2Mn)C	4	−28.2 −27.9	— —
Cubic $Cr_{23}C_6$ carbide	3.83 ($=\frac{23}{6}$)	−8.61 −10.98 −8.75	−10.43 (Fe) — −10.65 (Fe)

Table 2.1: Calculated formation enthalpy per atom-mole (ΔH) in units of kJ/atom-mole of the considered carbides. ΔH values with the substitution of an impurity atom into an 'M' site are also given. After [145].

red scale, a product of hot rolling formed from fine grains of haematite (Fe_2O_3). During hot rolling, any FeO remaining on the steel surface oxidises to Fe_2O_3. FeO is usually removed prior to rolling, but the presence of silicon forms a eutectic melt between the FeO and Fe_2SiO_4 that penetrates grain boundaries near the surface and greatly increases the adhesion of the FeO to the steel surface. This makes descaling extremely difficult. At best this red scale is unsightly, at worst it may be incorporated into the steel during rolling and act as an initiation site for failure in service.

Aluminium

The rôle of aluminium in bulk nanocrystalline bainite is twofold. It accelerates the formation of bainite by altering the relative thermodynamic stabilities of austenite and ferrite [50, 92, 108, 178, 179]. There is, therefore, an increase in both B_s and M_s. This can lead to the coarsening of the microstructure. Excessive amounts of aluminium can also stabilise ferrite at all temperatures at which the material is solid [177].

Like silicon, aluminium is also a potent cementite suppressor, [13, 116, 180–182]. Leslie and Rauch [183] deduced that aluminium increases the energy of formation of a cementite lattice when forced onto the iron sites, but, unlike silicon, aluminium reduces the activity of carbon in austenite, so the diffusion of carbon towards growing cementite particles is not slowed by the addition of aluminium. Leslie and Rauch [183] also found that cementite can grow by paraequilibrium in the presence of aluminium. This will reduce the driving force for cementite formation and in some cases may suppress cementite entirely. When there is still a driving force for cementite precipitation with aluminium in its lattice, the presence of aluminium will slow the precipitation of cementite. At higher temperatures aluminium can partition away from cementite and the slow diffusion of aluminium will limit the rate of cementite formation.

Aluminium has a strong affinity for oxygen [13, page 242], and during casting, alumina particles may block the nozzles – vacuum induction melting, vacuum arc remelting and/or electro slag remelting can be used to avoid this, albeit at

increased production cost.

Manganese

Manganese is usually added to steels in order to increase hardenability by delaying reconstructive transformations [13, page 242], [12, figure 4.7] (originally published in [184]) [179, 185–188]. It suppresses both B_s and M_s [13, page 243] — it is an austenite stabiliser [12, figure 4.3b].

Manganese forms a carbide that is isostructural with cementite, Mn_3C, which favours cementite precipitation [13, page 242]; indeed Speich and Leslie [150] reported that manganese was more soluble in cementite than in ferrite. Leslie and Rauch [183] deduced that manganese reduces carbon activity both in ferrite and in cementite and lowers the isothermal tempering temperature required to precipitate cementite from a supersaturated solid solution, consistent with manganese increasing the thermodynamic stability of cementite and not partitioning away. Conversely, Pacyna et al. [189] determined that during continuous heating of samples quenched from the austenitic state, manganese was reported to delay the precipitation of cementite, and that cementite was the only carbide found. This may be understood as manganese reducing the diffusivity of carbon in austenite, consistent with the effect of manganese on austenitised alloys.

Manganese is also added to steels in small quantities to remove sulphur [188]. Sulphur — present as impurities in the coke used to produce iron in the blast furnace — contributes to a eutectic (Fe/FeS) that forms at grain boundaries when the steel is hot. This is termed *hot shortening.* and leads to decohesion of grains during rolling, producing cracks [190]. During low temperature machining, manganese sulphide improves machinability [13, page 242] [190]. Manganese is also added to increase yield strength and ultimate tensile strength [191].

Nickel

Nickel improves hardenability [13, page 244] [134, 152, 192], suppresses B_s and M_s [12, figure 4.3b] [134, 152, 188, 192, 193] and enhances toughness [194, 195], although this has been disputed by Keehan et al. [196] and Caballero et al. [197]

in the case of bainitic steels containing more than 1.5 wt% manganese, but does enhance solid solution strengthening [196, 198]. Nickel is generally not found in large quantities in carbides [13, page 58] and may contribute to thermal stability, although evidence from Saha Podder [134] suggests that nickel-containing steels may be less resistant to cementite precipitation than manganese-containing equivalents.

Thermodynamic modelling has shown that the ratio of iron atoms to solute atoms in cementite in equilibrium with austenite is much higher for nickel than the equivalent content of manganese (figure 2.21)

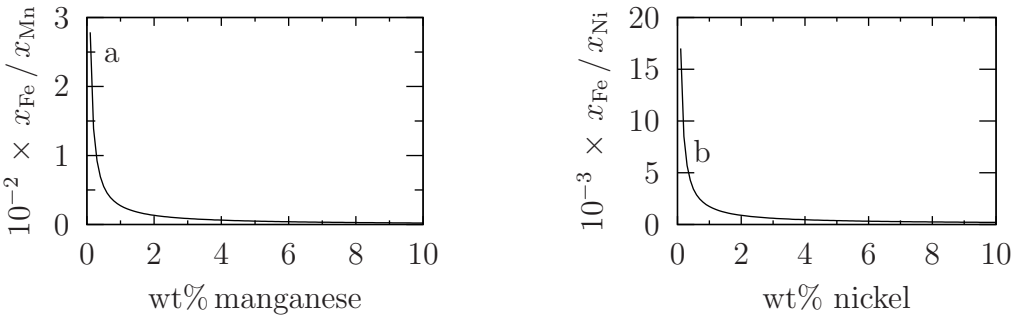

Figure 2.21: Ratio of molar fractions of iron and substitutional alloying addition in cementite under equilibrium conditions at 450 °C in (a) a manganese-containing steel and (b) a steel containing nickel [26, 199]

Cobalt

Cobalt is used to accelerate the bainite transformation by increasing the driving force for the transformation of austenite to ferrite [1, 50, 57, 75, 92, 104, 108, 110, 111, 179–181, 187, 192, 200–207]. It is an expensive solute [104, 180, 186, 205] and so its use should be minimised as far as possible to maximise commercial appeal. Although cobalt is not found enriched within carbides Bain and Paxton [13, page 58], it has just as much affinity for carbon as iron [13, page 243] and so will not contribute to thermal stability. Aluminium may be used in place of cobalt to accelerate the bainite transformation at much lower cost and has the added benefit of retarding cementite precipitation

Chromium

Chromium enhances hardenability and, as would be expected, also suppresses both M_s and B_s [107, 179, 182, 204, 207–209]. It is a well-known corrosion inhibitor, even when present only in solid solution. Chromium has an affinity for carbon and indeed it is the formation of carbides at grain boundaries that can lead to sensitisation, that is, chromium depletion in the vicinity of grain boundary carbides, producing sites anodic relative to their surroundings. Chromium may enter a range of iron and alloy carbides [210] including cementite [211] and is therefore unlikely to suppress the decomposition of retained austenite during tempering.

Molybdenum

Molybdenum helps to tie up residual phosphorus and hence prevent temper embrittlement and provides strong hardenability when in solid solution [13, page 244]. Molybdenum has a strong affinity for carbon, although its carbides generally grow extremely slowly, as they are limited by the availability of the comparatively slow-diffusing molybdenum atom, rather than carbon. Molybdenum is also used, as is boron, in small quantities to suppress allotriomorphic ferrite [12, page 148]. Molybdenum is found to significantly strengthen ferrite when in solid solution [207, 212].

2.3.7 Transformation temperature and time

Whether or not a given phase is able to grow is dependent on there being sufficient thermodynamic driving force to overcome all sources of stored energy, such that the overall free energy change of transformation is negative. There must also be sufficient driving force to allow nucleation of the product phase. It is possible to define a *universal nucleation function*, G_N [115], which describes the free energy change required for a displacive transformation to nucleate at a detectable rate and is a function of temperature alone. Since bainite nucleates via a paraequilibrium mechanism, it is required that the free energy change for the paraequilibrium, $\Delta G_{\text{para}}^{\gamma\rightarrow\alpha}$ must exceed this universal nucleation function. These two conditions,

represented by equations, which must be satisfied simultaneously for bainite to grow, are:

$$\Delta G^{\gamma\to\alpha} < -|\Delta G_{\text{stored}}| \tag{2.21}$$

$$\Delta G^{\gamma\to\gamma'+\alpha}_{\text{para}} < -|\Delta G_{\text{N}}| \tag{2.22}$$

It is crucial to suppress the martensite start temperature to below the temperature required to form bainite. This may be achieved by reducing the austenite to ferrite driving force at all temperatures to avoid the driving force exceeding the stored energy of the martensite formation. There are several factors that can control the magnitude of the stored energy of the martensite transformation: austenite grain size [213–216], strength of the parent austenite [215] and carbon content. The first of these controls both the availability of nucleation sites and the maximum size of individual martensite plates — if this is to low, surface energy and will make the martensite transformation unfavourable. The second factor influences how much work must be done to allow the transformation shear. The carbon content is vital as carbon is trapped in the martensite, significantly raising the energy of the system. It is, of course, possible to control the thermodynamic driving force for the austenite to ferrite transformation by altering the composition of the steel to raise or lower the M_{s} temperature.

Since the bainite transformation is similar to the martensite transformation, the same factors influence it. Just as the martensite transformation must be suppressed, the onset of the bainite transformation must be shifted to a lower temperature to avoid the formation of bainite at high temperatures at which large grains of bainitic ferrite will form. It is possible to suppress both the martensite and bainite start temperatures using the same substitutional elements, notably nickel and manganese [13, page 242], [12, figure 4.3b]. Unfortunately, use of large quantities of these elements results in a convergence of martensite and bainite start temperatures [1, figure 10a]. The only elements able to suppress both M_{s} and B_{s} while maintaining a useful gap between the two are interstitial elements: carbon (Bhadeshia [1, figure 10b]) and nitrogen [180]. This is because they reduce the

driving force for the austenite to ferrite transformation (hence the suppression of both M_s and B_s) and behave differently in the two transformations — they remain trapped in ferrite in the martensitic case and partition after the formation of ferrite in the bainite transformation.

One further complication is that while the nanostructured bainite system is capable of forming grains whose size is of the order of 10 nm, the process can take a significant amount of time, with the bainite evolving for several days before the retained austenite is enriched to the T_0' composition. Adding large quantities of elements capable of suppressing M_s and B_s will necessarily reduce the austenite to ferrite driving force and, hence, make nucleation of bainite sub-units less likely. Indeed, Bhadeshia [1] calculated that Fe–1.0 C–2.0 Si–3.0 Mn (wt%) would take one year to begin to transform, based on earlier thermodynamic modelling [217]. The data in Bhadeshia [1, figure 10b] are reproduced here as figure 2.22.

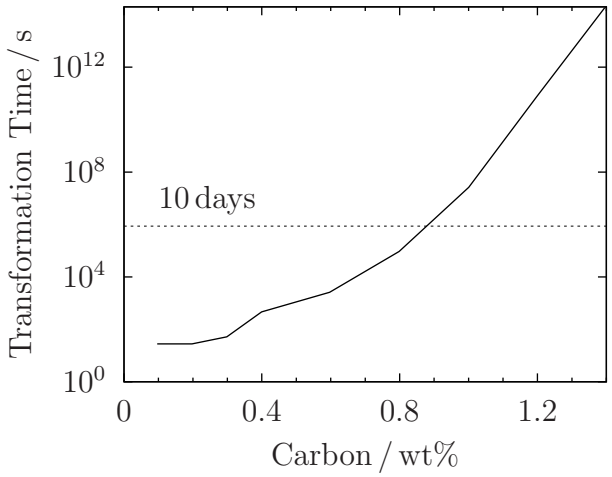

Figure 2.22: Calculated time required for bainite transformation to start in Fe–1.0 C–2.0 Si–3.0 Mn (wt%). After [1, figure 10b].

Studies have found that introducing defects after austenitisation leads to the bainite reaction speeding up. However, this effect is limited and the introduction of too many defects resulted in the bainite reaction actually being stifled and slowed [218, 219]. Gong et al. [219] also noted that deformation prior to the bainite reaction reduced the number of variants of ferrite, which was theorised to be due to

the preferential nucleation of certain variants, triggered by the action of particular slip systems during the deformation and the associated change in the ability of the austenite to shear in given directions. One further effect was the reduction in elongation of the bainitic sheaves. The same authors have found that ausforming only has an appreciable effect at low temperatures where planar dislocations form on active slip planes and lead to strong variant selection [220], while quoting Shirzadi et al. [221] that ausforming at higher temperatures does neither. Zhang et al. [222] showed that ausforming was able to suppress M_{s}, reduce the incubation time for bainite formation and refine the bainite laths. One consequence of the low rate of the bainite reaction is that the release of latent heat will not lead to a rise in temperature — so-called *recalescence* is avoided — and so the fine plate size may be maintained throughout the transformation. By suppressing the bainite transformation temperature, a higher amount of enrichment may occur before the $x_{T_0'}$ carbon content is reached and so a greater fraction of the steel will transform to ferrite, raising strength and hardness.

2.3.8 Mechanical properties of nanostructured bainite

The strength of steel may be estimated by considering the contributions to yield stress provided by all mechanisms that inhibit dislocations. The most general expression for strength is given in equation 2.23 [223, adapted], where σ_0 is the intrinsic yield strength of iron, approximately equal to the Peierls stress, $\Delta\sigma_{\mathrm{ss}}$ is the contribution of solid solution strengthening to the yield stress, $\Delta\sigma_{\mathrm{p}}$ is the amount of strengthening provided by precipitates and dispersion particles, $\Delta\sigma_{\mathrm{d}}$ is the contribution of work hardening (dislocation density), $\Delta\sigma_{\mathrm{sg}}$ is the effect of sub-grain structures, $\Delta\sigma_{\mathrm{t}}$ is the effect of texture and $\Delta\sigma_{\mathrm{gr}}$ is the effect of grain refinement.

$$\sigma_{\mathrm{y}} \approx \sigma_0 + \Delta\sigma_{\mathrm{ss}} + \Delta\sigma_{\mathrm{p}} + \Delta\sigma_{\mathrm{d}} + \Delta\sigma_{\mathrm{sg}} + \Delta\sigma_{\mathrm{t}} + \Delta\sigma_{\mathrm{gr}} \tag{2.23}$$

Nanostructured bainite differs from regular carbide-free bainite only in the scale of the transformed plates. Both the alternating austenitic and ferritic films and

the untransformed austenite blocks are refined by an order of magnitude when the transformation temperature is suppressed. Impressive combinations of strength and toughness have been achieved simultaneously, summarised in table 2.2. These compare favourably with other microstructures of steel, as is shown in figure 2.23, especially when it is noted that the cost of bulk nanocrystalline steels is a little over 1% of maraging steels of comparable mechanical properties [12, 109].

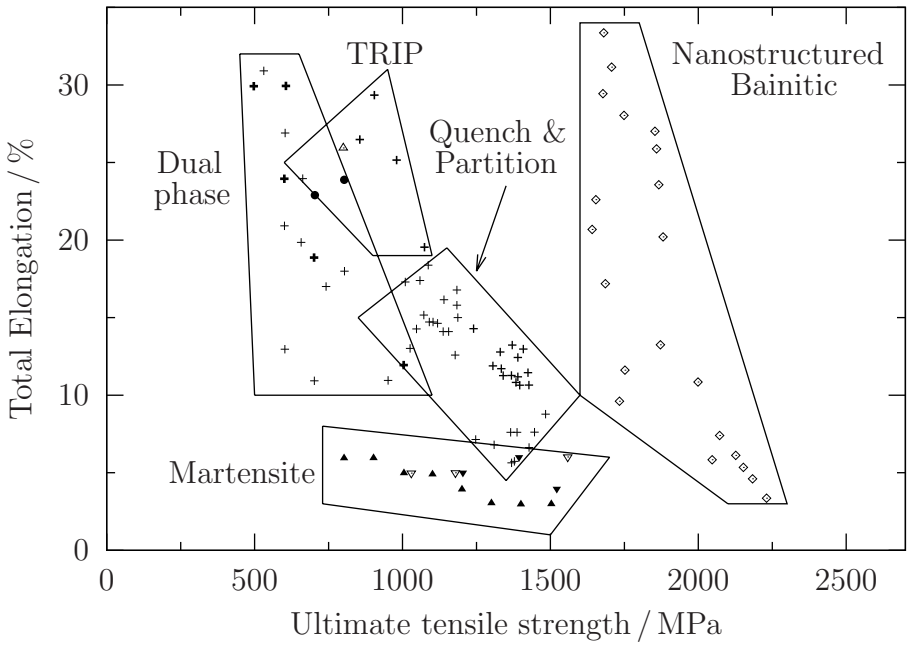

Figure 2.23: Mechanical properties of nanostructured bainite and other types of steel. Adapted, with author's permission, from [104]; original data from [207, 227].

The strengthening effect of dislocation density in bulk nanocrystalline steel was quoted by García-Mateo and Caballero [111] as being $7.34 \times 10^{-6} \rho^{0.5}$ MPa, where ρ is the dislocation density expressed in m^{-2}. Takahashi and Bhadeshia [228] derived that the dislocation density after the bainite transformation is a function of temperature alone and is given by $\log(\rho \,/\, \mathrm{m}^{-2}) = (9.2840 + 6880.73 T^{-1} - (1.780360 \times 10^6)\, T^{-2})$, where T is the transformation temperature expressed in Kelvin [228]. The Langford model of grain refinement strengthening is given by $115 \bar{L}^{-1}$ MPa where $\bar{L}$ is the mean lineal intercept of the grains in micrometres. These conditions, substi-

σ_y / GPa	σ_{UTS} / GPa	K_{IC} / MPa m$^{1/2}$	Charpy toughness / J	Reference
1.68	2.00		4	[67, 75, 104]
1.53	1.93		6	
1.4	2.2	32		[104, 111]
1.35	1.9	35		
1.3	1.7	50		
1.4	2.15	32		
1.5	1.95	38		
1.3	1.8	45		
1.4	2.2	32		
1.35	1.9	35		
1.3	1.7	50		
1.4	1.6	30.0*	2.3	[224]
1.6	1.8	32.3*	2.4	
2.2	2.5	4.6		
1.4	1.6	31*		
1.4	2.2	24		[187]
1.5	2.1	38		
1.2	1.7	42		
1.2	1.8	36		[197]
1.2	1.6	36		
1.2	1.7	44		
1.3	1.7	38		
1.2	1.7	40		
1.4	1.9	24		
1.6	2.0	15		[225]
1.2	2.3	5		
1.5	2.0	17		
1.3	1.8	24		
	2.3	30		[226]

Table 2.2: Strength, fracture toughness and Charpy impact energy for bulk nanocrystalline bainitic steels. K_{IC} measurements marked with an asterisk (*) did not meet validity specifications and are therefore K_Q. Data are only included from sources where strength and toughness or impact energy data were available for the same material.

tuted in to equation 2.23 along with the intrinsic yield stress of iron ($\sim 40\,\mathrm{MPa}$) [223, 229] result in equation 2.24 for the expected yield strength of nanostructured bainite. Since nanostructured bainite is expected to have neither precipitates, texture, nor sub-grain structure, the terms $\Delta\sigma_\mathrm{p}$, $\Delta\sigma_\mathrm{t}$ and $\Delta\sigma_\mathrm{sg}$ are 0. In their studies, García-Mateo and Caballero [111] deduced that the approximate strengthening contribution from dislocations in their bulk nanocrystalline bainite is around 200–300 MPa. The contribution of solid solution strengthening has been assessed in ferrite by Pickering [230] and is summarised in equation 2.25, where w_i represents the weight percentage of the element i in the alloy [230, 231]. It was found that nickel and aluminium provide negligible strengthening effects and chromium actually weakens the ferrite. All other alloying additions investigated increased the yield strength, with the strongest effect for small atoms that generate the strongest strain fields when incorporated in the lattice, especially the interstitial-occupying carbon and nitrogen.

$$\sigma_\mathrm{y} \approx 40 + 7.34\times10^{-6}\times10^{\left(4.642+3440T^{-1}-890180T^{-2}\right)} + \frac{115}{\bar{L}} + \Delta\sigma_\mathrm{ss}\,\mathrm{MPa} \tag{2.24}$$

$$\begin{aligned}\Delta\sigma_\mathrm{ss} \approx {} & 5544\,(w_\mathrm{C}+w_\mathrm{N}) + 678w_\mathrm{P} + 83w_\mathrm{Si} + 39_\mathrm{Cu} + 32w_\mathrm{Mn} + \\ & 11w_\mathrm{Mo} - 31w_\mathrm{Cr}\,\mathrm{MPa}\end{aligned} \tag{2.25}$$

Equation 2.25 was derived by Pickering [230] for ferrite, but the principle of equation 2.23 can be applied to any microstructure if correct data are used in each individual term. Young and Bhadeshia [176] considered the individual terms and extended the analysis to mixed microstructures of bainite embedded in a matrix of martensite. While this situation differs from the alloys considered here, which contain predominantly bainite mixed with retained austenite, the principle that mixed microstructures may be modelled is still sound.

Singh and Bhadeshia [232] used neural network analysis to derive the expected plate thickness as a function of input parameters including transformation temperature, chemical driving force and austenite strength. The latter was found to be the most significant in determining the thickness of individual sub-units (see [232, figure 8]) and can be estimated using an empirical expression over a specified

temperature range, given in equation 2.26 [232].

$$\begin{aligned}\sigma_{\mathrm{y}}^{\gamma} = 15.4 \\ &\times \left(1 - 2.6 \times 10^{-3}\,(T-25) + 4.7 \times 10^{-6}\,(T-25)^2 - 3.26 \times 10^{-8}\,(T-25)^3\right) \\ &\times \left(4.4 + 23 w_{\mathrm{C}} + 1.3 w_{\mathrm{Si}} + 0.24 w_{\mathrm{Cr}} + 0.94 w_{\mathrm{Mo}} + 32 w_{\mathrm{N}}\right)\ \mathrm{MPa}\end{aligned} \tag{2.26}$$

Taking a typical composition of bulk nanocrystalline bainite of Fe–0.8 C–1.6 Si–2 Mn–0.25 Mo–1 Cr–1.5 Co [111] gives a solid solution strengthening contribution of ≈ 170 MPa if carbon is neglected (a necessary approximation since the amount of carbon in solid solution in the ferrite is likely to be somewhat less than the bulk content and is very difficult to determine), a dislocation density of around $10^{16}\,\mathrm{m}^{-2}$ forming after transformation at 250 °C, giving a strengthening contribution from dislocations of 700 MPa and a grain size of 150 nm — equivalent to grain refinement strengthening of 770 MPa — gives an estimated strength of the ferrite of 1680 MPa. This is of the same order as was measured for the overall alloy in García-Mateo and Caballero [111] and is indicative of the importance of grain size in determining the strength of the final alloy.

2.3.9 Commercialisation of bulk nanocrystalline bainite

Despite being a recent innovation in steel metallurgy, bulk nanocrystalline bainite has already been put into commercial production [1, 233, 234]. Its use has allowed a high-performance armour to be produced with lower mass and cost than both alumina or titanium alternatives.

Caballero and co-workers have been developing a commercial design concept based on bulk nanocrystalline steel which they call *NANOBAIN* [109]. The first generation of steels was focused solely on forming bainite at the lowest possible temperature. The second generation was designed to transform more rapidly, to make the material less expensive to process and increase the commercially attractiveness. A minimum hardenability was also imposed to allow large sections to

be made where cooling rates are limited. It was imposed that a cooling rate of $1.5\,\mathrm{K\,s^{-1}}$ was the maximum permitted to form any pearlite or ferrite.

2.4 Non-cubic bainitic ferrite

As noted in section 2.2, bainite forms via a displacive mechanism, with carbon partitioning from ferrite after transformation. Carbon occupies octahedral interstices when dissolved in iron. In austenite there are twelve such interstices per unit cell, as may be seen in figure 2.24, where there is one octahedron at the body centre and one at each of the twelve edge centres. Each of the edge centres is shared between four unit cells, making a total of four octahedra per unit cell, or one per iron atom in the face-centred cubic crystal. By contrast, figure 2.25(a) shown that there is one octahedron at each of the six face centres in the body-centred cubic crystal and since each of these if shared between two unit cells, these sites contribute three octahedra to each cell. In addition, there is another identical octahedron at each edge centre, adding $12 \times {}^1\!/_4 = 3$ octahedra to each unit cell, to give six overall. There are only two atoms per unit cell in the body-centred cubic arrangement, so there are three octahedra per iron atom. That is three times as many octahedra per atom in ferrite than in austenite.

It is also important to note that while the octahedral interstices in a face-centred crystal are regular (i.e. all atoms forming the octahedron are equidistant to the centre of the interstice), those in a body-centred cubic crystal are irregular, with two coordinating atoms a distance of ${}^a\!/_2$ from the centre of the interstice and the other four being $\sqrt{2}$ times further away. The presence of carbon in any interstice will create a local compressive strain field. In the case of a regular interstice, the strain field will be isotropic and only consist of dilatational components. In the case of an irregular interstice, the strain field is anisotropic and a significant amount of tetragonal strain develops. Not only is this the reason that carbon is able to strengthen ferrite significantly more than it does austenite [235] — the shear components of the strain field around a filled irregular interstitial site are able to interact with the shear components of all dislocations and pin them much

more strongly than is possible if only dilatational strains are present to interact, as is the case in austenite — it imparts a significant energy penalty on the system. The overall energy may be relieved if the lattice expands parallel to one crystallographic axis, relative to the other two, to elongate the octahedra and make them regular, such as is shown in figure 2.25(b). This reduces the symmetry of the lattice, destroying the triads along the ⟨111⟩ directions. The crystal may no longer be considered cubic. The highest symmetry element is a tetrad parallel to [001] (where the z-axis is defined as that which has undergone the expansion relative to the other two perpendicular directions. The crystal is therefore tetragonal and still has a lattice point in the body centre, making it body-centred tetragonal, with space group I 4/m m m. Ferrite has a space group of I 4 3 2.

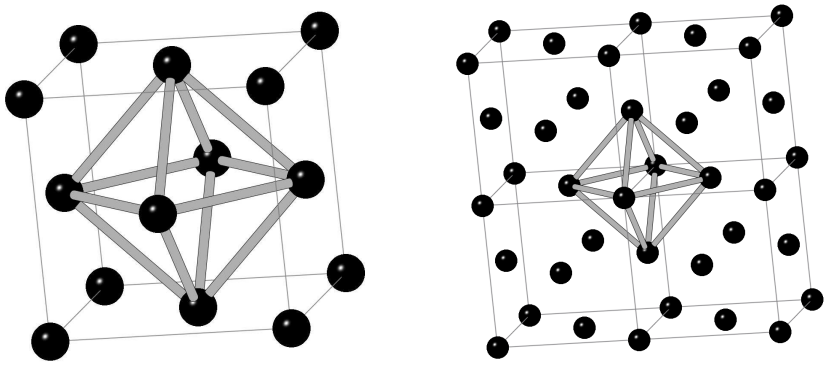

Figure 2.24: Octahedral interstices in a face-centred cubic crystal. Left: at the body centre and right: at the edge-centres. After Cohen [236, figure 7].

The presence of carbon in ferrite has long been known in martensite [236, figure 5] and studies of the effects of carbon on the lattice parameters of martensitic ferrite have led to equation 2.27, where a and c are the tetragonal lattice parameters and w_{C} is the amount of carbon in solid solution in the martensitic ferrite, expressed in weight percent. The thermodynamic reasons for such a reduction in symmetry were investigated by Jang et al. [237] and it was found that while the maximum solubility of carbon in an equilibrium mixture of body-centred cubic ferrite and austenite is from the iron–carbon phase diagram (see figure 2.1), this

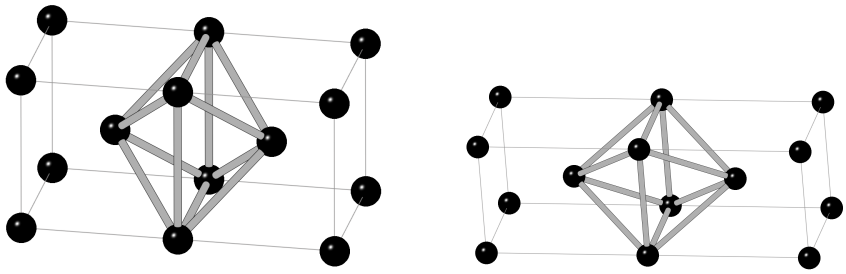

Figure 2.25: Octahedral interstices in a body-centred cubic crystal. Left: distorted octahedra at the face-centres and right: regular octahedron in a distorted BCC (equivalent to BCT) lattice. After Cohen [236, figure 8].

may be increased to 0.4 wt% carbon at 450 °C if the ferrite is allowed to adopt a body-centred tetragonal lattice, as this reduces the energy of the system. While such a reduction in symmetry is commonly observed in steels, where there is a significant amount of carbon present, it is by no means a necessity of the martensitic transformation. Indeed, Fe–30wt% Ni undergoes a martensitic transformation to form body centred cubic martensite, as can many other non-ferrous, or even non-metallic, systems [238].

$$\frac{c}{a} = 1 + 0.045 w_\mathrm{c} \tag{2.27}$$

It must be considered that the loss of symmetry in ferrite is dependent on carbon being in solid solution and not at dislocation cores, grain boundaries, pores, particle boundaries and any other sinks. According to the formula $x \sim \sqrt{Dt}$, where x is diffusion distance, D is the diffusivity and t is a time, the time required for carbon to diffuse far enough to escape a typical supersaturated ferrite plate is $\sim$ 10 days, based on the a diffusivity of $10^{-20}\,\mathrm{m^2\,s^{-1}}$ at 200 °C [239, figure 9] and a required diffusion distance of 100 nm. The bainite transformation at 200 °C typically requires 30 days to stop, yet despite there being ample time for carbon to leave ferrite, carbon supersaturation has been detected directly using atom probe tomography [47, 48, 52, 53, 56, 57, 76, 169, 240]. Although some of the ferrite may be assigned to defects [47, 53], studies have confirmed that carbon does enter

supersaturated solid solution far from defects [47, 52, 169] and should be expected to promote tetragonality.

Chapter 3

Design of novel alloys

3.1 Design tools

3.1.1 mucg83

"mucg83" is a powerful yet simple-to-use FORTRAN program [241]. The only input is a composition as both thermodynamic data and algorithms are built into the program. mucg83 predicts M_s, W_s and two values for B_s: one assuming that nucleation is limiting and another that growth is limiting. Other thermodynamic and kinetic parameters are calculated, such as the time required to detect the onset of shear and diffusional transformations. Time-temperature transformation (TTT) curves may therefore be estimated [77] as may T_0 curves. Full details may be found on the mucg83 page of Materials Algorithm Project website [241].

Predictions are made based on the driving force for the transformation from austenite to ferrite as a function of temperature and composition. Zener ordering is taken into account [217]. The program uses polynomial equations fitted to experimental thermodynamic data to calculate the interaction parameters of carbon in ferrite and austenite. Chemical potentials are calculated, leading to a variety of driving forces for transformation, depending on the mechanism involved [1] [38, 217, 242–246]. This allows mucg83 to perform all calculations internally,

[1] "mucg" is a portmanteau of mu (μ, chemical potential), C for carbon and G for gamma (γ,

i.e. using numbers contained within the source code and not from any external thermodynamic database or software. While this means that mucg83 can be run on systems without access to commercial databases such as those used by MTData [199], MatCalc [247] or ThermoCalc [248, 249], it does limit the calculations to prescribed alloying elements and compositions, as given in table 3.1.

Element	C	Si	Mn	Ni	Mo	Cr	V	Co	Cu	Al	W
Minimum / wt%	0.001	0.0	0.0	0.0	0.0	0.0	0.0	0.0	0.0	0.0	0.0
Maximum / wt%	2.0	2.5	3.5	3.5	1.5	3.5	1.5	4.0	4.0	2.0	4.0

Table 3.1: Solutes considered in mucg83 and their composition limits [241]

mucg83 does not account for grain size, however similar related programs do. Another variant, mucg46, does include a term accounting for grain size, but does not include the effects of aluminium on the driving force. Since aluminium is used in bulk nanocrystalline bainite to suppress cementite and accelerate the bainite transformation, mucg83 is preferred in the current work. Existing bulk nanocrystalline bainitic alloys generally fall within the limits in table 3.1 and so confident predictions of their transformation behaviour may be made using mucg83. There are numerous examples of the successful use of the mucg range of programs in the design of bulk nanocrystalline bainitic alloys [77, 104, 182, 205, 250–252]. Novel alloys, however, may have compositions outside the permitted range. Should mucg83 prove unsuitable, predictions may still be made using thermodynamic databases, which are not as restricted in composition as mucg83.

During the initial stages of alloy design, a modification was made to mucg83 that called the program repeatedly with varying composition to examine the effect of changing the concentration of a selected solute. Carbon is the strongest suppressor of B_s, followed by manganese and then nickel [253, figure 2]. Conversely, aluminium and silicon raise B_s, as they increase the driving force for the transformation of austenite to ferrite [253, figure 2]. mucg83 predicts that chromium will suppress the bainite transformation. This apparently contradicts Andrews

austenite). 83 is the version number.

[253, figure 2] and the documented effects of chromium on the equilibrium stability of austenite, for example Bhadeshia and Honeycombe [12, figure 4.4b], but agrees with published findings on the bainite transformation, where chromium is added to increase hardenability [108, 111, 152, 179, 204]. This is because the effect of chromium on the transformation of austenite to an equilibrium mixture of austenite and ferrite ($\gamma \rightarrow \gamma' + \alpha$) is different to the case where it does not partition between product phases, such as in the bainite transformation.

An example of a T_0 calculation using mucg83 is given in figure 3.2. Chromium shifts the T_0 line to lower carbon content, implying that the driving force for displacive transformation diminishes as chromium is added. This is consistent with the results in figure 3.1 that chromium suppresses the bainite transformation to lower temperatures.

mucg83 contains two polynomial equations to determine the driving force for the diffusionless transformation of austenite to ferrite in different temperature ranges. The change from one equation to the other results in a discontinuity in the calculated transformation time around 600 °C (e.g. figure 5.2). This is an artefact of the calculation and does not represent a physical discontinuity in expected transformation time.

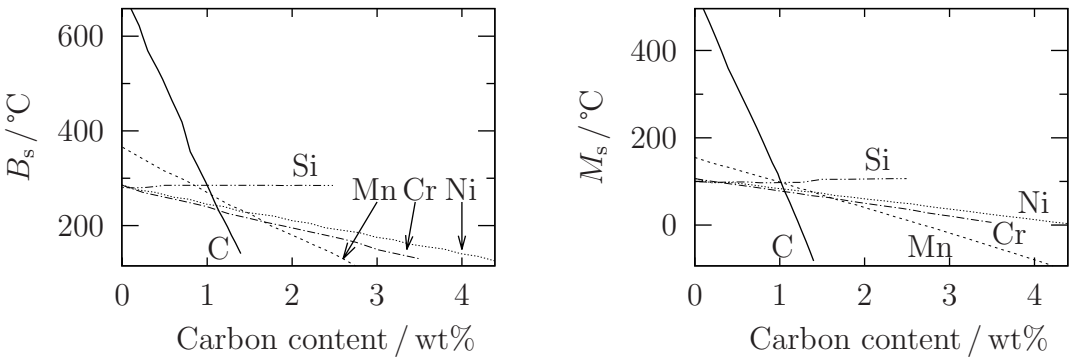

Figure 3.1: Transition temperatures for Fe–1.0 C–1.25 Mn–2.5 Si–1.0 Al–0.1 V (wt%) calculated using mucg83 [241] with indicated solute incremented.

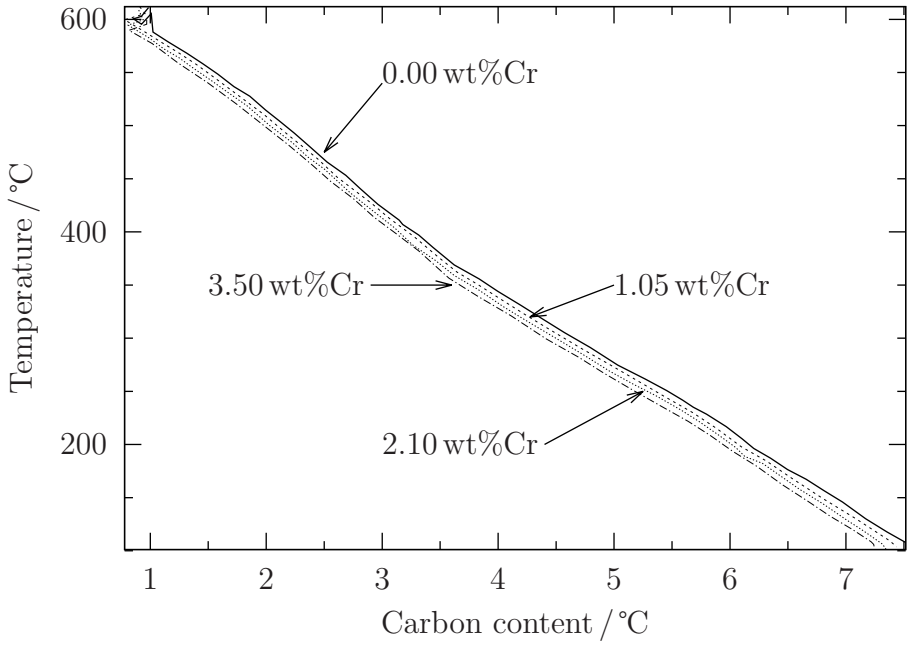

Figure 3.2: T_0 line for Fe–x C–1.25 Mn–2.5 Si–1.0 Al–0.1 V–Cr (wt%) calculated using mucg83 [241].

3.1.2 Thermodynamic modelling software

MTData is a thermodynamic software simulation package written by the National Physical Laboratory, Teddington, U.K. It is described in detail in Davies et al. [199]. The version used here is version 4.73 for Linux. Various thermodynamic databases were used in the current project and the database used is specified for each result:

- National Physical Laboratory PLUS database, version 3.02 [254]
- Scientific Group Thermodynamic Europe (SGTE) database, version 4.2 [26]
- TCAB thermodynamic database for steels (TCFE), version 1.0 for MTData (equivalent to version 5.0 for ThermoCalc) [255]

Although MTData was the thermodynamic software used most extensively, ThermoCalc versions 3.0 with the TCFE thermodynamic database version 6.0 [248, 249] was made available during the project. An upgrade to version 2015a for Mac with the TCFE database version 7.0 was obtained towards the end of the project. MatCalc version 5.43 was also used for a limited number of calculations to verify the findings of the other commercial software packages. The MatCalc Fe database version 0.017 was used for all MatCalc calculations.

Many thermodynamic quantities may be predicted, including Gibbs energy of phases or mixtures of phases, chemical potential, equilibrium compositions and fractions of phases in material with a user-specified composition. Both composition and temperature may be specified by the user and one quantity may be varied over a range to see its effect on the thermodynamic quantities in question. It is also possible to select which phases are to be considered and to specify constraints, such as paraequilibrium of specific components to reflect particular physical processes.

It is possible to write programs that interact with MTData to perform large numbers of calculations without user input. In this project, such programs are written in Fortran 77.

All three software packages use similar databases and each varies the compositions and relative fractions of each phase to find the global minimum Gibbs

energy of the system, subject to the constraints set by the user. MTData uses an algorithm called *Multiphase* that uses the National Physical Laboratory (NPL) Numerical Optimisation Subroutine Library (NOSL) to perform a nonlinear optimisation, subject to linear constraints set by the user, to find the Gibbs energy minimum [199]. ThermoCalc uses a technique known as *global minimisation*, which forms an array of conditions within the limits set by the user to find the approximate energy minimum and then uses standard function minimisation algorithms to find the minimum accurately [256, sections 8.1 and 8.4.9]. MatCalc utilises the well-known concept of Lagrange multipliers to find the Gibbs energy minimum, subject to the constraints defined by the user [257].

3.1.3 MTTTData

MTTTData is a FORTRAN program similar to mucg83, but which uses MTData to provide thermodynamic data which is used to find M_s, B_s, W_s and kinetic data for the transformation of austenite to ferrite to overcome the compositional limitations of mucg83. The methodology of MTTTData is schematically represented in figure 3.3. The National Physical Laboratory's "PLUS" database, version 3.02 is used. Yang and Bhadeshia [258] also used MTTTData to help design low carbon bulk nanocrystalline bainite. Thermodynamic data are retrieved from a thermodynamic database and kinetic predictions are made according to [217].

In this study, the resistance of alloys to thermal decomposition into carbides, especially cementite, is of particular interest. It is therefore desirable to calculate the equilibrium between retained austenite and cementite, which corresponds to the $\gamma \,/\, (\gamma + \theta)$ phase boundary. A slight adaptation of the source code provided on the Materials Algorithm Project website[2] allows MTTTData to calculate the driving force for the decomposition of retained austenite and an equilibrium mixture of austenite and cementite. During trials of this modification, it was found that those elements noted for being insoluble in cementite — silicon, aluminium and copper — were never present in cementite. Many thermodynamic databases do not allow these elements to exist in cementite. Any attempt to force these

[2] `http://www.msm.cam.ac.uk/map/steel/programs/MTTTDATA.html`

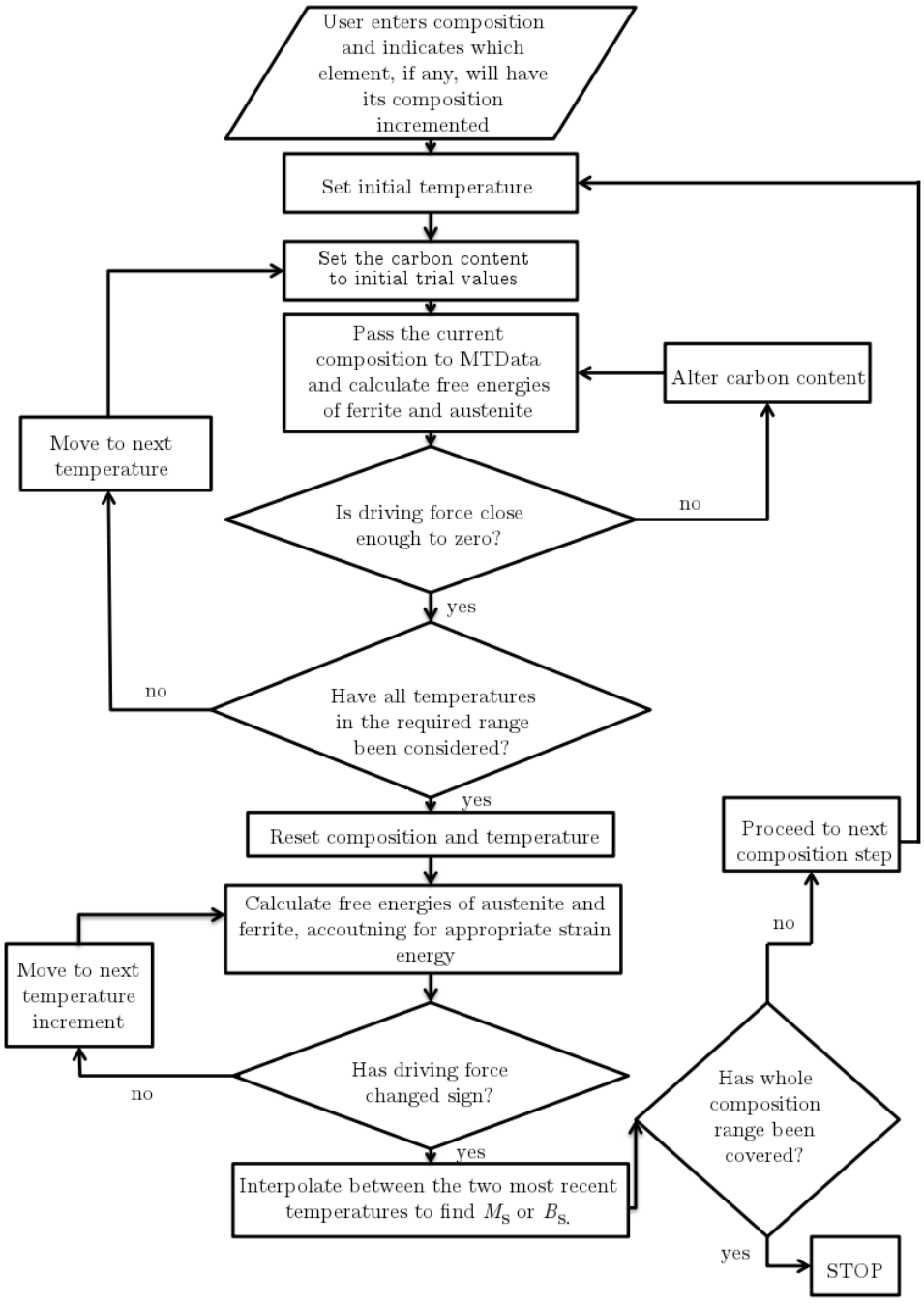

Figure 3.3: Flowchart of MTTTData functionality

elements to exist in cementite, for example by specifying paraequilibrium or by calculating the thermodynamic properties of cementite alone, caused the thermodynamic simulations to fail as there are no appropriate data for the modelling software to assess [145]. The latest thermodynamic databases, for example TCFE version 7 do include the effects of silicon on cementite, although there is not yet any independent assessment of the accuracy. An example of the kinetic predictions of MTTTData is given in figure 3.4. While the effects of chromium and nickel have been correctly predicted, there is a discrepancy for Fe–0.3 wt% C curve, where the transformation start time is predicted to be shorter for the diffusional transformation than the shear transformation at B_s.

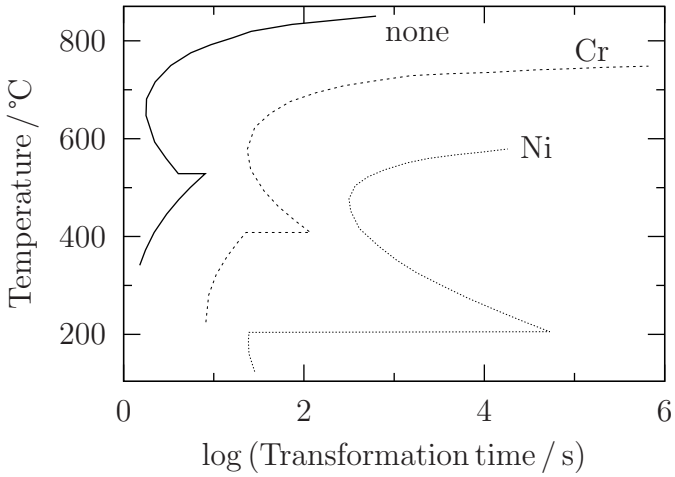

Figure 3.4: TTT curves for Fe–0.3 wt% C with 5 wt% of the labelled solute calculated using MTTTData [199, 254, 259].

MTTTData is able to predict the effects of nickel on the T_0 and T_0' lines, as shown in figure 3.5. Both lines are suppressed to lower temperatures, as is expected. It has also been possible to calculate the equilibrium line between retained austenite and the equilibrium mixture of austenite and cementite. An alloy that is thermodynamically stable with respect to cementite precipitation in retained austenite will have $x_{T_0'}$ to the left of the $\gamma \,/\, (\gamma + \theta)$ equilibrium line. It is therefore desirable to move the $\gamma \,/\, (\gamma + \theta)$ equilibrium line to higher carbon contents and to shift the T_0' line to lower carbon contents.

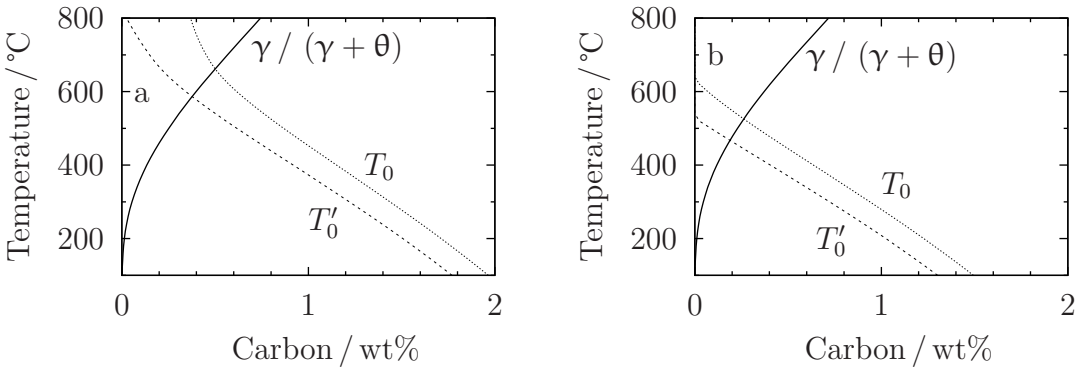

Figure 3.5: T_0, T'_0 and cementite stability data for Fe–1.0 C–1.25Mn–x Ni–1.0 Al–4.5 Si–0.1 V (wt%) with (a) $x = 0$ and (b) $x = 4$, calculated using MTTTData [199, 254, 259].

MTTTData was also adapted to select one element which could have its composition altered between two user-specified limits. The predictions of bainite start temperature as a function of composition is given in figure 3.6.

3.1.4 Genetic algorithm

In order to obtain an optimum composition, a systematic exploration of composition space is necessary. However, the number of calculations required makes this impractical. For example, a ten solute system with 50 possible concentrations of each solute would require $\sim 10^{17}$ sets of calculations. The bainite and martensite start temperatures must be calculated, in addition to an assessment of thermal stability via the driving force for retained austenite to precipitate cementite. Supposing that each composition needs fifty calculations to assess its suitability, $\sim 5 \times 10^{18}$ calculations must be performed. Assuming one million calculations may be performed every second, the requires calculations would take approximately 160 years.

Genetic algorithms have therefore been utilised [177, 188, 260–262]. Initial compositions are either specified or selected randomly as the first *generation*, as-

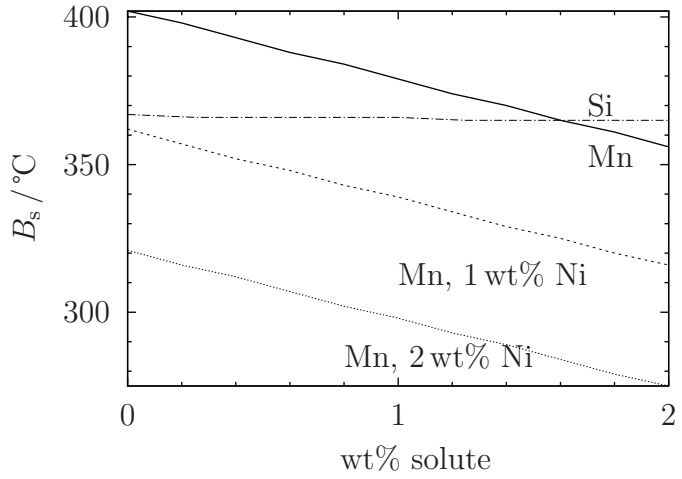

Figure 3.6: B_s temperatures for Fe–1.0 C–1.25Mn–1.0 Al–4.5 Si–0.1 V (wt%) with the concentration of labelled solute given by the x-axis, calculated using MTTT-Data [199, 254, 259].

sessed for suitability using an algebraic expression to derive a measure of suitability for each phenotype. This is known as a *fitness factor*. Figure 3.7 shows the calculation sequence used to derive the fitness factor for a given phenotype. Each individual composition is known as a *phenotype*. *Parents* are then chosen from the current generation, with the probability of selection proportional to each phenotype's fitness factor. The information from a set of parents is stored as a series of binary numbers and is combined in a process known as *crossover* to produce *daughter* phenotypes, with the total number of phenotypes equal in each generation. Each daughter composition is then allowed to *mutate*: the composition is given the opportunity to change randomly (figure 3.8). Each phenotype of the new generation is then assessed for fitness and the cycle repeats. Since the likelihood of each individual phenotype passing its genetic information to the next generation is based on its suitability, the overall suitability of the phenotypes increases with each successive generation and the possibility of mutation prevents the model becoming stuck at a local maximum. Once the best fitness factor stops increasing, the algorithm stops. Figure 3.9 shows the overall methodology of the genetic algorithm developed here.

In the current study, the first generation was randomly assigned. In order to increase the randomness of the generated numbers, a *shuffle procedure* [263, page 272] is used: one hundred pseudorandom numbers are produced and one of these is selected for use and then replaced in the pool of available numbers. Crossover was performed using the three-parent method whereby three parents are selected at random and whichever of 0 or 1 is the majority in each binary digit is passed to the daughter (table 3.2).

Phenotype	Binary Digit								Decimal
Parent 1	1	1	1	1	0	0	0	0	240
Parent 2	1	1	0	0	1	0	1	0	202
Parent 3	1	0	1	0	1	1	0	0	172
Daughter	1	1	1	0	1	0	0	0	232

Table 3.2: All possible outcomes of three-parent crossover

The probability of mutation must be set high enough to prevent the algorithm becoming stuck at a local maximum but not so high as to prevent the algorithm running indefinitely. Over many generations, several instances of the same composition occur, so that mutation often leaves at least one of these unchanged and the others regain their former composition during crossover to the next generation, allowing the algorithm to stop.

Changing the fitness factor may lead to a different solution, and randomness implies different results even if the same fitness factor is used. The fitness factor, f_{fit} (equation 3.1) is chosen subjectively to promote:

- a large temperature range between B_{s} and M_{s}
- $M_{\text{s}} \leq 200\,^{\circ}\text{C}$ (473.15 K)
- the $\gamma/\gamma{+}\theta$ equilibrium line at a specified temperature to be at least 3 wt% carbon and as large as possible

$$f_{\text{fit}} = \frac{(B_{\text{s}} - M_{\text{s}})^3 \times \left(c^{\gamma/(\gamma+\theta)} - 0.03\right)^3}{\left(1 + (M_{\text{s}} - 473.15)^2\right)^{-\frac{1}{4}}} \tag{3.1}$$

The form of f_{fit} is largely determined by the goals set for the algorithm. The exact values used in the expression of the fitness factor are subjective and may be adjusted to promote one characteristic over another. For example, in equation 3.1, the difference between B_{s} and M_{s} has been cubed to increase in importance of this quantity. It was decided that any negative fitness factors are set to 1. This greatly reduces the chances of such a parent producing daughters, but does not make it impossible.

After extensive trials, it was decided that genetic algorithms could not be used in this project. The lack of data available at the time of the trials meant that was not possible to assess the thermodynamic effects of silicon, aluminium and copper on the precipitation of cementite. In addition, it was not possible to avoid the model becoming stuck in a loop whereby successive generations failed to improve. It may be possible to overcome both these deficiencies with different thermodynamic databases and further optimisation of the algorithm. However, this was not considered practical in the timescale of this project.

3.1.5 Artificial neural network

Artificial neural networks permit the estimation of an output as a function of input variables using non-linear regression. No explicit knowledge is required of the mechanisms involved, and under the Bayesian framework used, there is no *a priori* need to specify the number of data required. The method allows interactions between inputs. The method developed by MacKay [264–266] used Bayesian statistics to handle noise and modelling uncertainties. If two models are similarly able to make predictions, the simplest one is favoured, as is explained in Peet [267]. Each neural network model captures the accuracy of its predictions based on the distribution of the input data. Where there are large numbers of closely-grouped

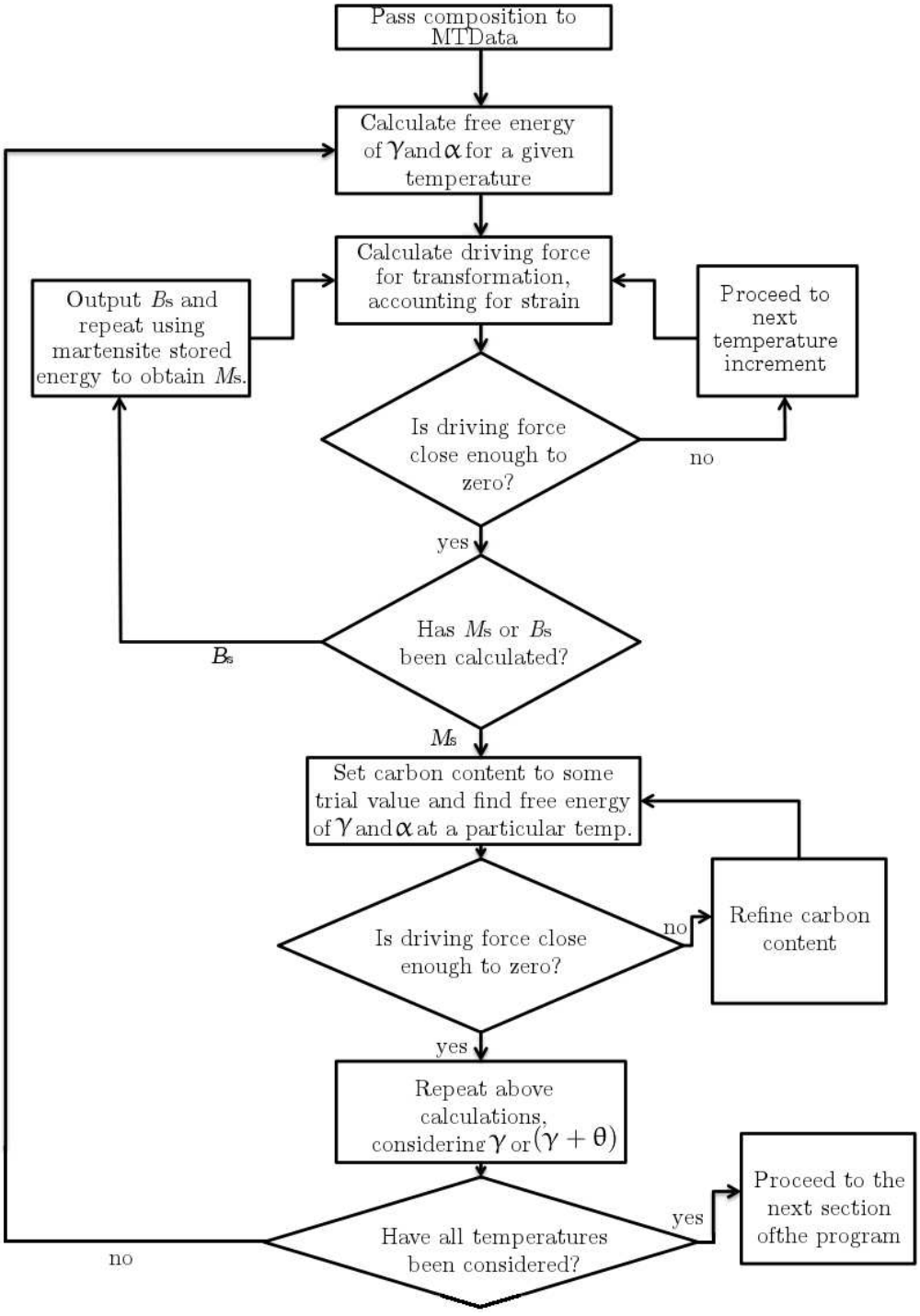

Figure 3.7: Flowchart for the calculations involved in the genetic algorithm

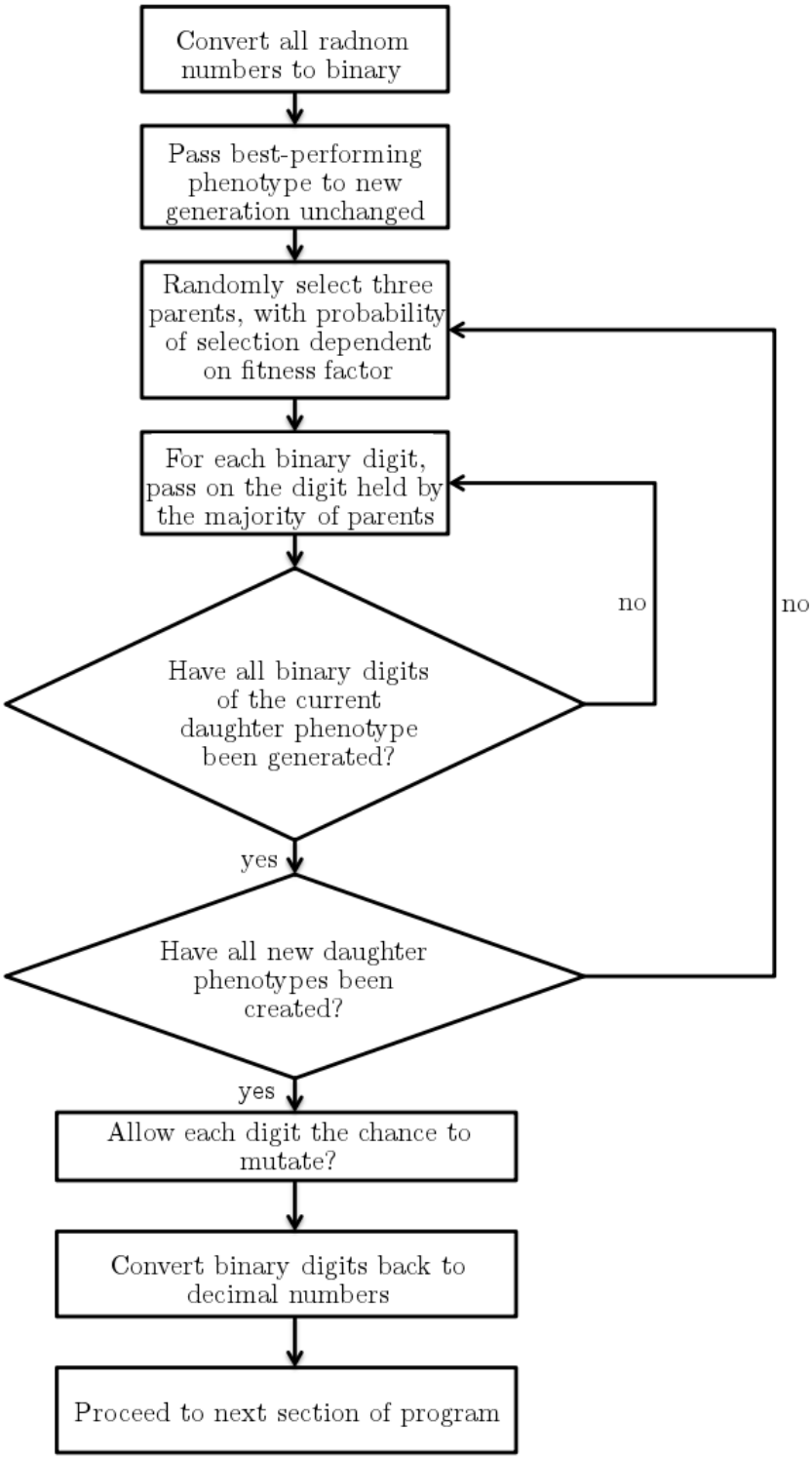

Figure 3.8: Flowchart for the production of a new generation in the genetic algorithm

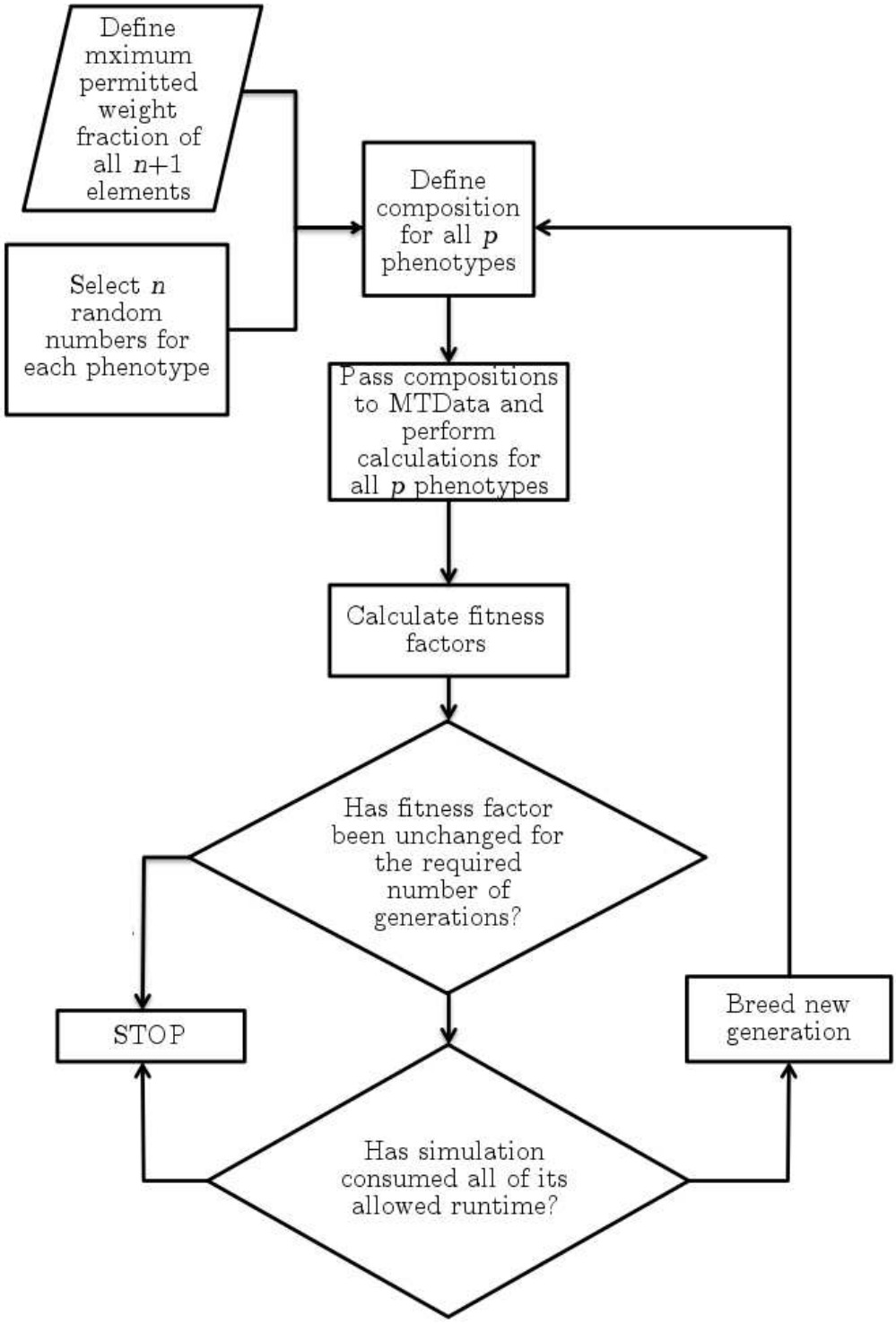

Figure 3.9: Flowchart for the genetic algorithm written as part of this study

inputs, the quantified errors tend to be small and where data are few and diverse the quantified error is large.

For each set of inputs, each variable, x_j, is weighted by some factor, wij, and the sum of all input variables is found. A constant, θ_i is then added and the hyperbolic tangent of the results found, as specified in equations 3.2. This generates an *hidden unit*. All hidden units are weighted by some new factor, w_i and summed to give the output, y, as in equation 3.3. To simplify the refinement of the weights, inputs may be normalised using equation 3.4 [267]. This was done in the present study. It is possible to use multiple hidden layers to form a more complex model, where each hidden unit acts as an input for the next group, but this was not considered in the present study as the available software (Neuromat ModelManager [268]) did not have this capability. It is also possible to combine several different models into a *committee* to reduce the uncertainty in any predictions. This was used in the current study where a committee was predicted to reduce uncertainty over a single model.

$$h_i = \tanh\left(\sum_j w_{ij}x_j + \theta_i\right) \tag{3.2}$$

$$y = \sum_i w_i h_i + \theta \tag{3.3}$$

$$x_j = \frac{x - \min}{x_{\max} - x_{\min}} - 0.5 \tag{3.4}$$

The neural network used in this study was designed to find M_s for candidate alloys and is based on an available M_s database [269].

Artificial neural networks have been used successfully to predict phase fractions [261], M_s [270] and B_s [271] temperatures, the onset of austenite formation during heating [272], transformation kinetics [192, 209], σ_UTS [192, 273], Charpy transition temperatures [274], Vickers hardness [275], fracture toughness [276], lattice parameters [277] and many other properties. As long as sufficient data may be accumulated and the relationship between inputs and outputs are represented by a continuous, non-periodic mathematical function, there is no restriction on what may be modelled using a neural network. While a database has been published

for martensite start temperatures, that for B_s [271] has not been made publicly available.

Chapter 4

The first thermally-stabilised bulk nanocrystalline steel

Initial work on the design of a thermally-stable bulk nanocrystalline bainitic alloy (table 4.1) was conducted by Dr Mathew Peet. Alloy 1 was designed to demonstrate that a large quantity of silicon is effective at suppressing cementite precipitation from austenite.

	C	Mn	Al	Si	Mo
Alloy 1	1.037	1.97	1.43	3.89	0.24

Table 4.1: Composition of Alloy 1 (wt%)

The equilibrium calculation in figure 4.1, performed on the thermodynamic modelling software "MTData" [199, 254] indicates that Alloy 1 should never be fully austenitic. All thermodynamic databases were found to produce similar results. This is contradicted by experimental observations that Alloy 1 heated to 1050 ℃ forms homogeneous microstructures, which could only form from a fully austenitic alloy [278]. 1050 ℃ is therefore chosen as the austenitisation temperature. Retrospective thermodynamic modelling using the modelling software "ThermoCalc" [248, 249] predicted that Alloy 1 will fully austenitise (figure 4.2). ThermoCalc was not available during the design of Alloy 1. Cementite is predicted to

be absent under equilibrium above 1020 °C.

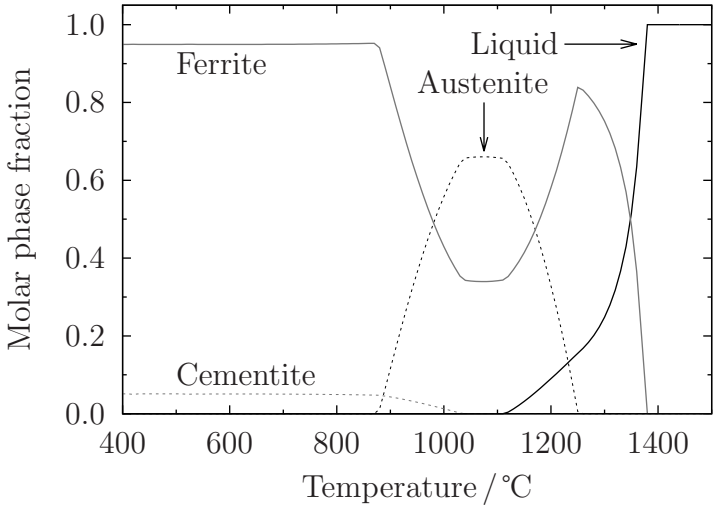

Figure 4.1: Phase fractions in Alloy 1 calculated using the thermodynamic modelling software MTData [199] using the SGTE thermodynamic database, version 4.2 [26].

Apart from its high silicon content, Alloy 1 lies within the composition limits of the thermodynamic and kinetic modelling program "mucg83" [241] (cf. table 3.1). However, other modelling suggests that silicon only has a weak effect on the thermodynamics of the austenite to ferrite transformation, as is shown in figures 4.3, 3.1(a), 3.1(b), 3.6 and Andrews [253, figure 2]. mucg83 may therefore be used to make thermodynamic predictions. The predicted T_0, T_0' and TTT curves for Alloy 1 are given in figures 4.4(a) and 4.4(b), respectively. The equivalent predictions made using "MTTTData" are given in figure 4.5 [199, 254, 259].

mucg83 predicts that M_s of Alloy 8 is (75 °C). MTTTData is unable to predict a martensite-start temperature for Alloy 1, although the program only considers temperatures of ≥ 100 °C, so is reasonable to conclude that M_s is likely to be lower than this. An artificial neural network [268, 269] was used to derive a final prediction of M_s, which was 140 ± 100 °C. The significant uncertainty in the data reflects the extreme composition being modelled: out of 1100 alloys assessed in Sourmail and García-Mateo [269] only four have more aluminium than Alloy 1 and

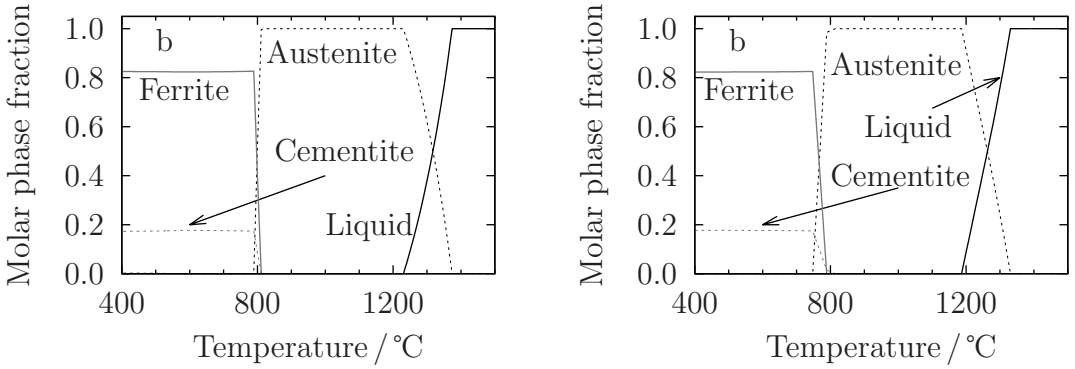

Figure 4.2: Phase fractions in Alloy 1, calculated using (a) ThermoCalc [248] and (b) MatCalc [247]. The two pieces of software give very similar results so there may be reasonable confidence that they are correct, despite their disagreement with MTData (cf. figure 4.1)

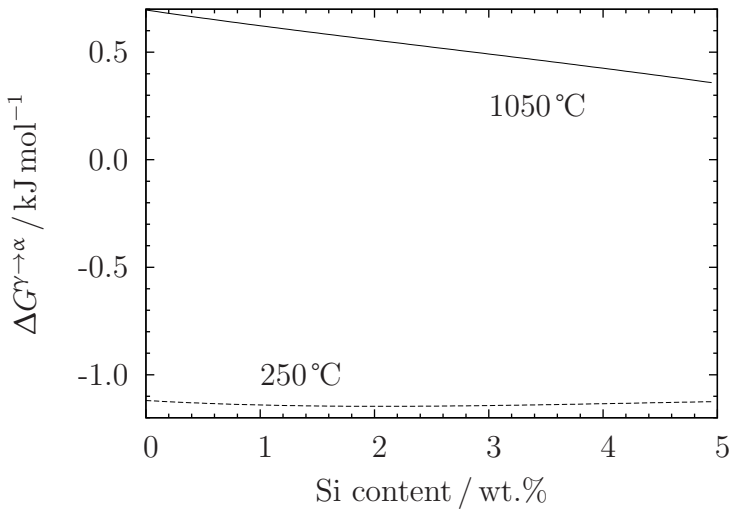

Figure 4.3: Austenite to ferrite driving force, $\Delta G^{\gamma\to\alpha}$, in a Fe–1.0 C–2.0 Mn–$x$ Si–1.4 Al–0.25 Mo (wt%) steel.

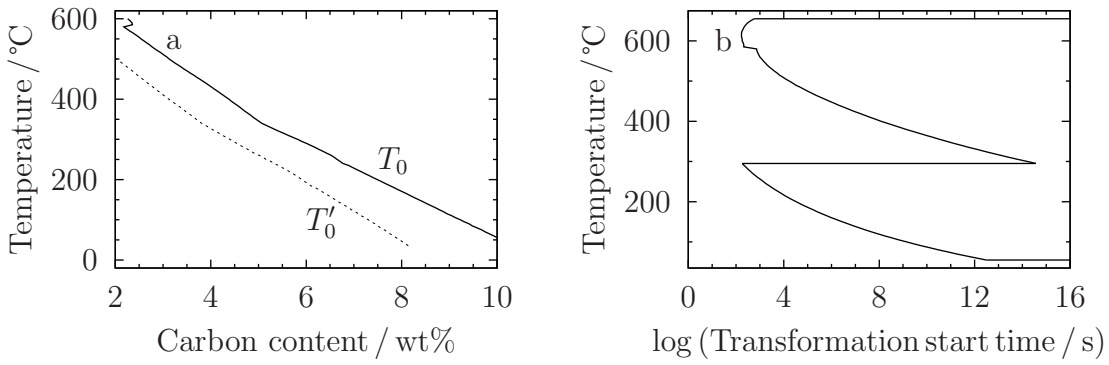

Figure 4.4: (a) T_0 and T_0' line and (b) TTT curve of Alloy 1 calculated using mucg83 [241].

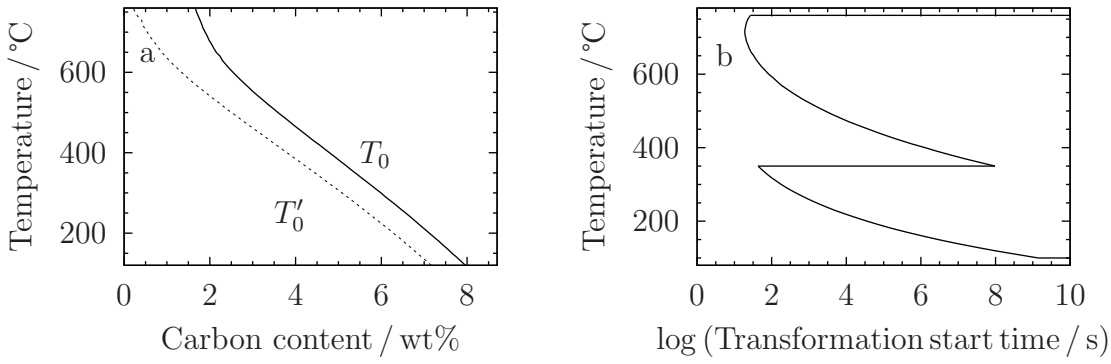

Figure 4.5: (a) T_0 and T_0' line and (b) TTT curve of Alloy 1 calculated using MTTTData [199, 254, 259]

none has as much silicon. This lack of data leads to a large uncertainty under the Bayesian framework (section 3.1.5). To date, no experiments have been performed to measure the M_s of Alloy 1 and there was insufficient material available to make such a measurement here.

MTTTData predicts B_s to be 350 °C, which is ideal for bulk nanocrystalline bainite as no coarse bainite will form at higher temperatures, but it is possible to form nanostructured bainite above M_s. MTTTData calculates that B_s is 300 °C. The predicted transformation kinetics (figure 4.4(b) and 4.5(b)) show that Alloy 1 exhibits sufficient hardenability for easy processing in bulk, with a pearlite nose at approximately 700 °C and 30 s. The bainite transformation is predicted to start after 3 min at 300 °C and 10 h at 200 °C. mucg83 makes remarkably similar predictions: 2.5 min and 9.2 h, respectively.

Using a mass-balance of carbon and assuming austenite has the T_0' carbon content and ferrite contains no carbon, bainite formed at at 250 °C contains 82 wt% ferrite. The equivalent prediction made by mucg is for 80 wt% bainitic ferrite. This is, of course, a lower bound estimate, as carbon can precipitate as carbides or sink to defects in either phase rather than enter solid solution in the austenite. Furthermore, ferrite is not necessarily carbon-free. This will be explored in detail in section 10.

Given the excellent agreement between mucg83 and MTTTData, heat treatments may be designed with high confidence to produce bulk nanocrystalline bainite in Alloy 1.

4.1 Initial transformation experiments

An initial set of experiments was performed to assess the transformation of Alloy 1 to bainite. These results were then used to produce material for synchrotron X-ray diffraction experiments.

Rods 3 mm in diameter and approximately 30 mm in length were prepared and sealed in quartz ampoules that were filled with argon to prevent oxidation and decarburisation. Samples were austenitised at 1050 °C for 30 min and were then

transferred to a pre-calibrated, high-precision oven capable of maintaining temperature to ±0.1 ℃ [279], verified using an independent, calibrated thermocouple. Following austenitisation, samples were removed from their ampoule to accelerate cooling and avoid reconstructive transformations and were left to transform to bainite according to table 4.2. After transformation, samples were water-quenched to ambient temperature. A typical heat treatment for transformation is illustrated in figure 4.6.

Temperature / ℃	200	250	300
Time / h	240	72	24

Table 4.2: Initial transformation conditions for Alloy 1.

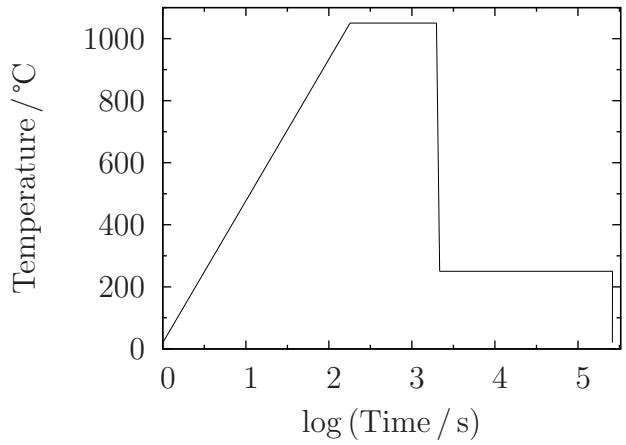

Figure 4.6: Schematic heat treatment of Alloy 1, transformation at 250 ℃.

Samples of the as-transformed material were sectioned using an abrasive cutting wheel and were hot-mounted in phenolic mounting resin at 180 ℃ for 8 min. They were then ground using silicon carbide paper and polished using first 6 µm and then 1 µm diamond paste with a water-based lubricant. After polishing, the samples were etched using a 2 vol.% nital (nitric acid in methanol) solution, for optical microscopy.

Samples that were examined using scanning electron microscopy (SEM) were prepared as for optical microscopy and examined using a JEOL-6340F cold field-emission scanning electron microscope in secondary electron mode with a 20 keV accelerating voltage. The image analysis software "ImageJ" [280] was used to optimise contrast and brightness.

For transmission electron microscopy (TEM) using a JEOL 200CX microscope, discs 500 µm thick were stuck onto an aluminium stub using thermoplastic resin and ground on fine silicon carbide paper to a thickness of ≈ 100 µm. After washing in acetone they were then ground by hand to a thickness of 50 µm using 2500 grit silicon carbide paper. They were then electropolished using a Struers Tenupol-5 twin-jet electropolisher set to a potential of 20 V and a solution consisting of 5 vol% perchloric acid, 20 vol% glycerol and 75 vol% ethanol.

Samples of Alloy 1 transformed at 250 °C exhibited bulk nanocrystalline bainite and it was thus established that 3 d was sufficient for the final microstructure to develop (figures 4.7). Quenching the sample directly form 1050 °C to ambient temperature in water resulted in a mixture of martensite and a small amount of retained austenite, with a hardness of 660 ± 30 HV2. Allowing the material to transform to bainite reduces its hardness to 500 ± 12 HV2.

It is evident from figure 4.7 that Alloy 1 forms a homogeneous microstructure, rather than a mixture of δ-ferrite and bainite. This proves that the sample is fully austenitic at 1050 °C, despite the results of thermodynamic modelling using MTData (figure 4.1. Subsequent modelling using alternative commercial software (ThermoCalc [248] and MatCalc) indicated that Alloy 1 should be fully austenitic at 1050 °C (figure 4.2). The reasons for the erroneous results in MTData were not investigated, and all subsequent heat treatments used an austenitisation temperature of 1050 °C.

4.2 Initial tempering experiments

Samples of Alloy 1, transformed to bainite at 250 °C, were exposed to temperatures of 400 °C, 450 °C and 500 °C for a variety of times to assess the thermal stability

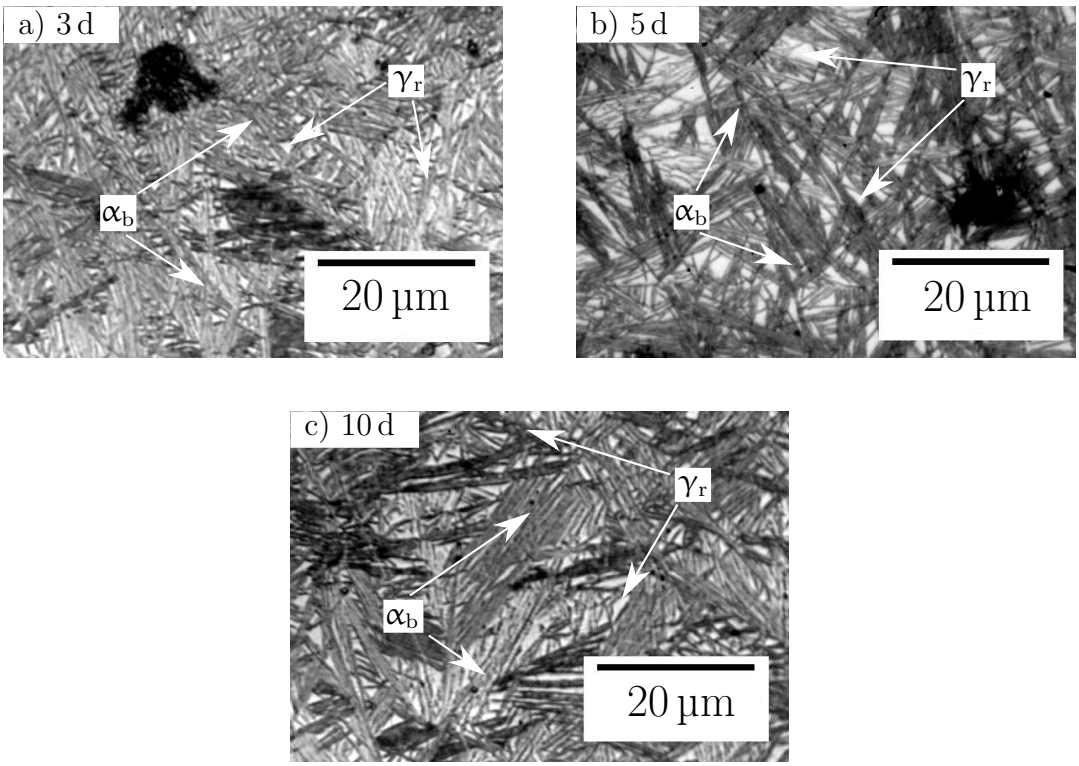

Figure 4.7: Alloy 1 transformed for the times indicated. It is evident that 3 d is sufficient to form the maximum possible fraction of bainite.

of the nanocrystalline bainite. The findings were then used to inform synchrotron X-ray diffraction experiments.

4.2.1 Tempering at 400 °C

Exposure at 400 °C had little visible effect when observed using optical microscopy, even after 30 d, as is shown in figures 4.8(a) and 4.8(b). However, microhardness increased from 470 ± 40 HV2 to 550 ± 30 HV2 (figure 4.9). This implies that some change has occurred, however, no change could be detected using optical or scanning electron microscopy. Samples were prepared for TEM, but no informative images were obtained. There was insufficient material to repeat the TEM experiments, but decomposition was investigated thoroughly using synchrotron X-ray diffraction (section 4.3).

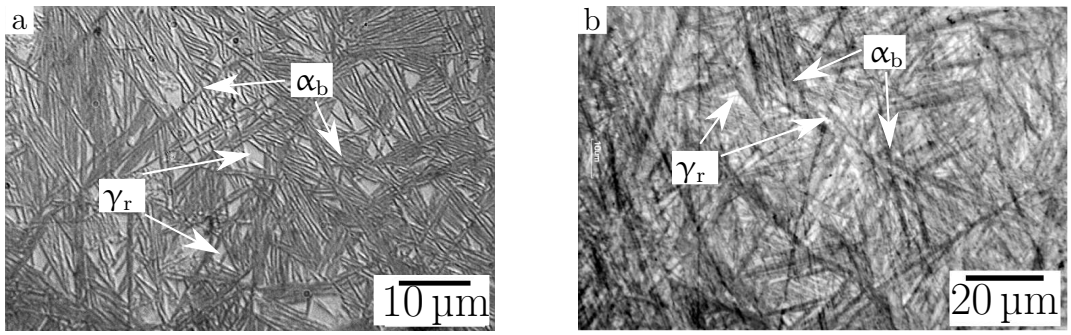

Figure 4.8: Alloy 1 tempered at 400 °C for (a) 10 d and (b) 30 d. Tempering for has little visible effect on the structure.

One possible explanation of the observations is the precipitation of very fine carbides that have not depleted the austenite of carbon sufficiently to cause it to transform to ferrite. It is also possible that tempering has allowed carbon to sink to dislocations, which will form Cottrell atmospheres and strengthen the steel. However, comparing a reported value for carbon diffusivity in austenite at 250 °C ([12, table 1.4]) and the expected separation of dislocations [49] ($5 \times 10^{-15}\,\mathrm{cm^2\,s^{-1}}$ and 100 nm, respectively), it is evident that there is ample time during the bainite transformation for carbon to sink to dislocations. Decomposition of retained

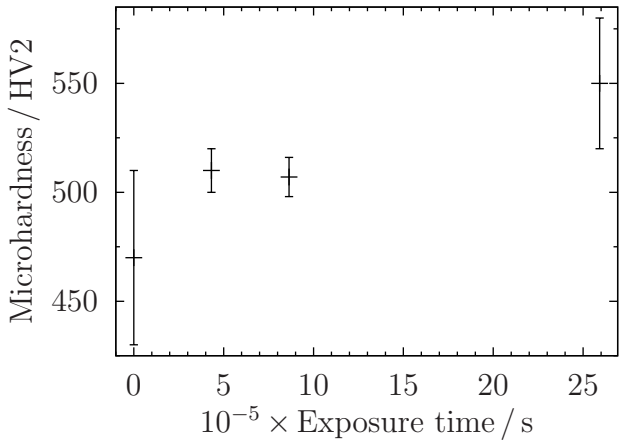

Figure 4.9: Microhardness of Alloy 1 subjected to tempering at 400 °C for the times indicated. Exposure for 4×10^5 s (5 d) is sufficient to cause a significant change in hardness, presumably due to a change in structure.

austenite will lead to an expansion of the bainitic ferrite grains, which have been shown to be ≈ 30% stronger and harder than the retained austenite [281, table 6]. The decomposition of austenite to ferrite will therefore inevitably lead to an increase in hardness.

The large time necessary for significant hardening during tempering at 400 °C prohibits investigation during synchrotron experiments, which are limited to 4 d.

4.2.2 Tempering at 450 °C

Increasing the tempering temperature to 450 °C for 24 h has little effect on the optical micrographs of Alloy 1 (figures 4.10(a)–4.11(a)), but there is a significant change after 72 h of tempering. The slender packets visible in figure 4.11(a) have disappeared. Only the large retained austenite blocks have survived. This is consistent with the mechanism of decomposition deduced by Saha Podder [134]. Blocky retained austenite has a lower carbon content than the films, making them less susceptible to thermal decomposition. After 24 h, the hardness peaks (figure 4.12), after which no further change occurs.

Since hardness peaks within 24 h during tempering at 450 °C, this is a suitable

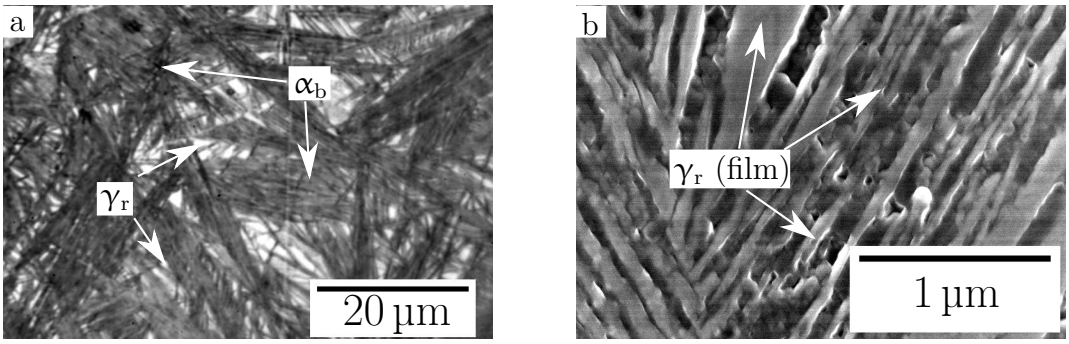

Figure 4.10: Alloy 1 tempered at 450 ℃ for 6 h. Austenite films have survived the tempering.

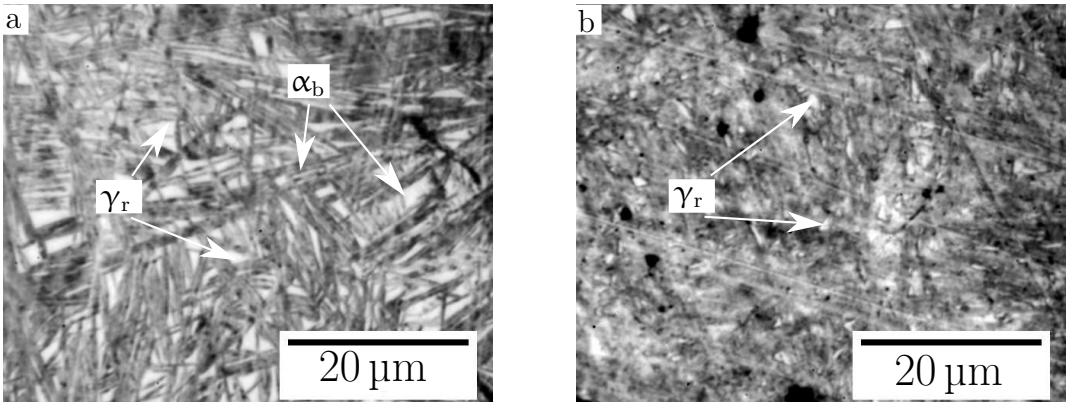

Figure 4.11: Alloy 1 tempered at 450 ℃ for (a) 1 d and (b) 3 d. After 3 d there is a visible change in structure, presumably due to thermal decomposition.

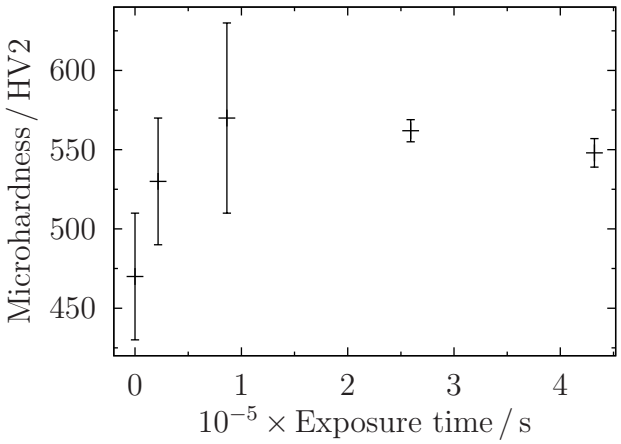

Figure 4.12: Alloy 1 tempered at 450 °C.

temperature for investigation during synchrotron experiments.

4.2.3 Tempering at 500 °C

Tempering at 500 °C for 24 h appears to have caused film austenite to decompose, leaving only blocky austenite intact (figure 4.13(a) cf. figure 4.11(b)). SEM (figure 4.13(b)) shows that the films break into smaller austenitic regions while the austenite blocks are apparently intact. The increase in hardness (figure 4.14) is consistent with the loss of austenite and the production of carbides, which pin dislocations and ferrite. This is consistent with other work on bulk nanocrystalline steel [116, 134, 282].

Increasing the tempering temperature from 400 °C to 500 °C changes the self-diffusivity of iron in austenite from $10^{-22}\,\mathrm{m^2 s^{-1}}$ to $10^{-19}\,\mathrm{m^2 s^{-1}}$ [283] and, hence, the random walk diffusion distance in 24 h increases from from 7 nm to 160 nm, sufficient to allow precipitation. These distances are similar for all substitutional elements.

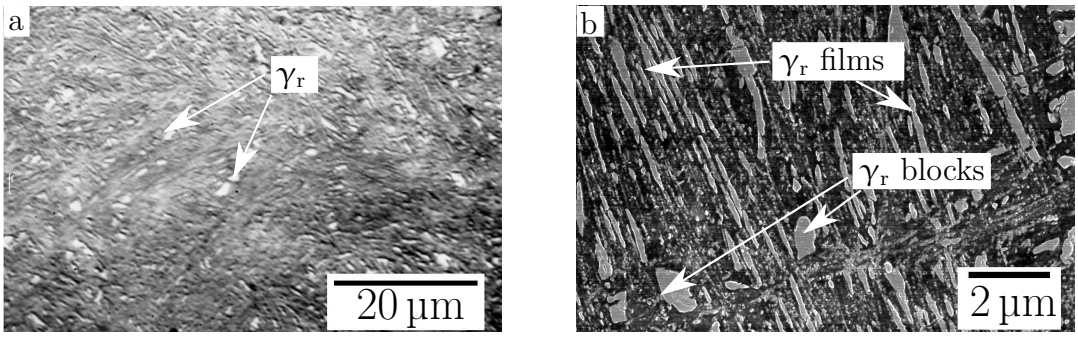

Figure 4.13: Alloy 1 tempered at 500 ℃ for 24 h. The structure is radically changed, with austenite films breaking up.

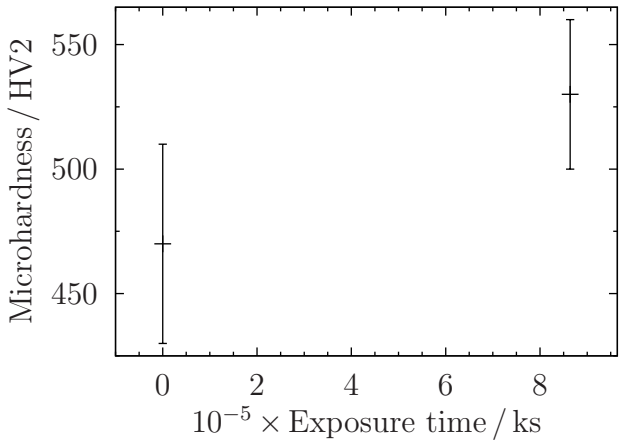

Figure 4.14: Alloy 1 tempered at 500 ℃.

4.3 Synchrotron study of Alloy 1 stability

Experiments were conducted on beamline P02.1 at the Deutsches Elektronen-Synchrotron (DESY) in Hamburg, Germany on Alloy 1 transformed at 200 °C, 250 °C and 300 °C. Samples were machined to 2 mm diameter rods that were held in the X-ray beam using a bespoke holder. Machining can potentially induce the transformation of retained austenite, but no deformed layer was detected beyond a depth of 5 µm from the surface. Since the synchrotron X-rays used here penetrate 2 mm of steel, any deformation in this surface layer will produce negligible effects.

The X-ray wavelength was 0.2069 Å, monochromated using diffraction from diamond and silicon {111} planes. Data were gathered in a transmission geometry using a flat-plate PerkinElmer XRD1621 2D area detector with a pixel size of 200 µm × 200 µm and a total of 2048 × 2048 pixels (≡ 40.96 cm × 40.96 cm). The detector was placed normal to the incident beam, which was collimated to a size of 1.2 mm × 1.0 mm. The distance from the centre of the sample to the detector was set to a nominal 1300 mm, calculated to permit the detection of three complete diffraction rings (figure 4.15), sufficient for Rietveld analysis. The sample-to-detector distance was later derived to be approximately 1323 mm. Data were recorded at 1 Hz and every 30 datasets were binned to give an effective temporal resolution of 2 min^{-1}. Heating was performed using a hot gas blower that was fed with nitrogen, with sample temperatures measured using a thermocouple spot-welded onto the sample surface close to the region that was exposed to the X-rays. The hot air blower setpoint was adjusted manually to achieve the desired temperatures. Isothermal treatment temperatures are detailed in table 4.3. An equipment schematic is given in figure 4.16.

The detector had 16 bit dynamic range, allowing any detection count rate between 0 s^{-1} and 65535 s^{-1}. Data were recorded as TIFF files and were investigated using the software known as MAUD (Materials Analysis Using Diffraction) [284]. The sample-detector distance, beam centre and detector tilts were refined and fixed using silicon and ceria NIST reference powders. The background signal, incident X-ray intensity, beam centre, detector tilts, austenite volume fraction and the lattice parameters, crystallite sizes and isotropic microstrains of both phases were

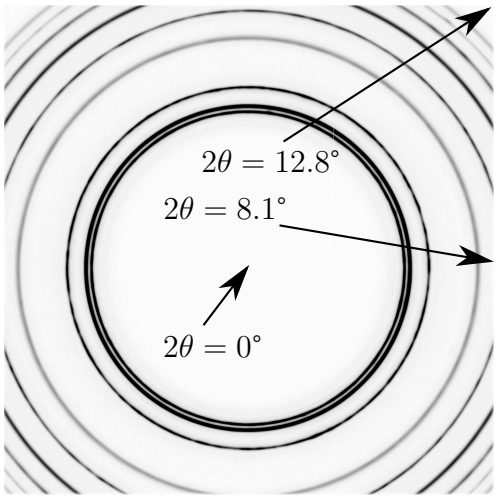

Figure 4.15: Example of data recorded during stability experiments on Alloy 1 at DESY. The data are for an as-transformed carbide-free bainitic sample. The image is approximately 40 cm square at the X-ray detector.

Alloy	Austenitisation		Transformation	
	Temp / ℃	Time / h	Temp / ℃	Time / h
Alloy 1	1050	0.5	250	72
			200	240
			250	72
			300	24
Alloy 2	1200	0.5	215	240

Table 4.3: Heat treatments of all samples used in synchrotron experiments

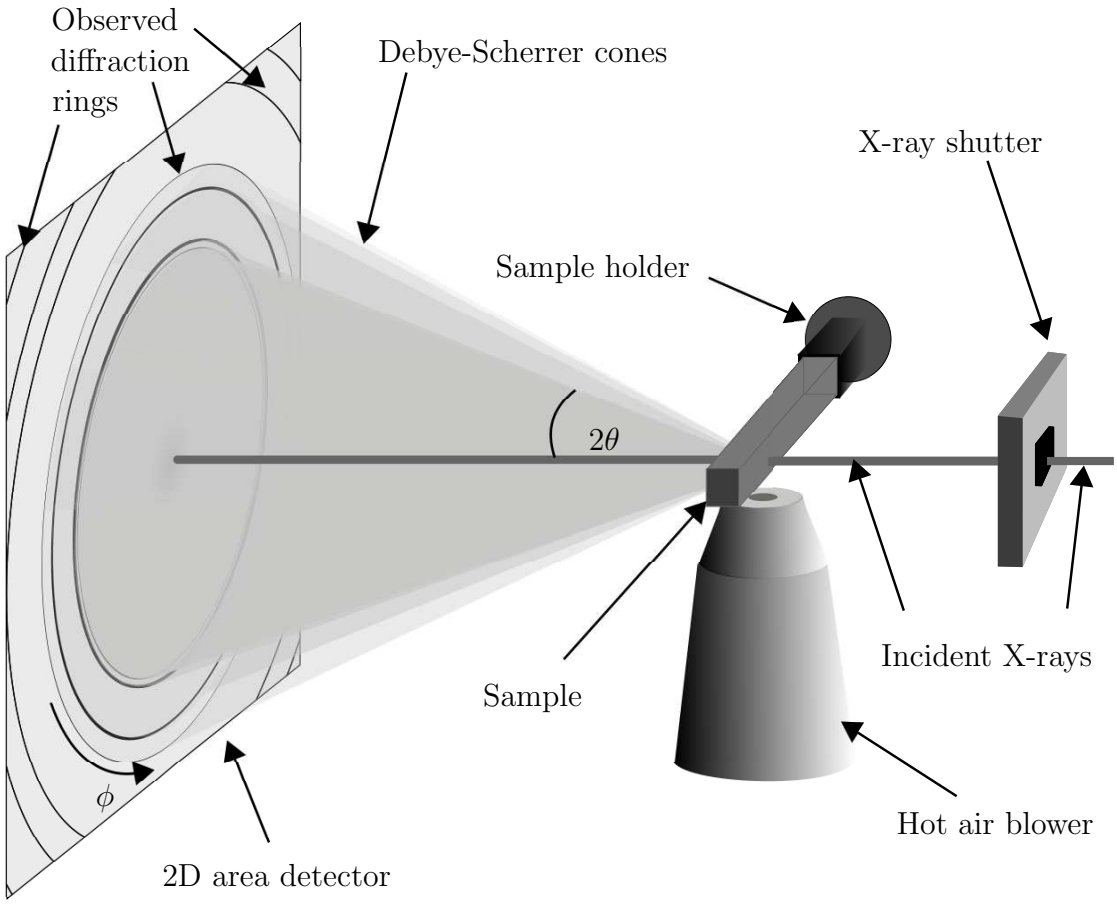

Figure 4.16: Experimental geometry for experiments at DESY

refined using the Rietveld method [285] using the guidelines set out by McCusker et al. [286] to achieve the best possible fit. The volume fraction of ferrite was dependent on that of austenite and is therefore not a refined variable.

Analysis was conducted using scripts written in Python at each stage to allow the hundreds of images captured during each experiment to be analysed efficiently. The images were first integrated using the image analysis software Fit2D to produce Fit2D "spreadsheet" format files. These files were then converted into the native file format of MAUD. Rietveld refinement was performed using the "Quantitative Analysis" wizard in MAUD. For each dataset, the first file was analysed manually to provide the best possible fit. This was the starting point for the automated analysis of all subsequent files from that experiment.

A previously-designed bulk nanocrystalline alloy was also investigated to provide a reference for the performance of Alloy 1. This alloy (Alloy 2) has the composition given in table 4.4. Alloy 2 was not designed to resist thermal decomposition, so it was expected that it will decompose more readily than Alloy 1.

	C	Mn	Al	Si	Mo	Co	Cr	others
Alloy 2	0.84	2.26	0.25	1.78	0.044	1.55	1.47	0.11 Cu, 0.11 V, 0.021 Nb

Table 4.4: Composition of Alloy 2 (wt%)

4.3.1 Continuous heating experiments

One sample of each of Alloy 1 transformed at 250 °C and Alloy 2, transformed at 240 °C (previously shown to form bulk nanocrystalline bainite [278]) was heated at 5 °C s^{-1} from ambient temperature to 650 °C. Results of Rietveld refinement are given in figure 4.17. The data show that the austenite in Alloy 2 begins to decompose at around 400 °C, consistent with continuous heating dilatometry experiments on conventional bulk nanocrystalline bainitic alloys [287]. Alloy 1 survives with no detectable change in phase fraction until the material reaches 600 °C. Figure 4.19 reveals that the minimum observed diffraction angle of the

austenite 111 peak, corresponding to the maximum observed lattice parameter, occurs at 520 °C in Alloy 1 and at 400 °C in Alloy 2. The significance of this is that the lattice parameter will expand due to thermal expansion as the alloy is heated, but will contract if carbon is lost from solid solution. The fact that Alloy 1 is able to retain its carbon to a higher temperature is consistent with its enhanced thermal stability.

The increased stability of austenite in Alloy 1 is due its large silicon and aluminium contents. The carbon and manganese contents of the two alloys are similar. The presence of cobalt in Alloy 2 is not likely to affect carbide precipitation (figure 4.18). The presence of chromium, vanadium and niobium in Alloy 2 is also unlikely to lead to a significant amount of carbide formation at 400 °C since the growth of such carbides is limited by the diffusivity of the substitutional solute, which is extremely slow at the temperatures stated. It is considered that such alloy carbides do not form significant quantities below 500 °C. Thus, the design philosophy of Alloy 1 is validated. Adding alloying elements insoluble in cementite can delay the decomposition of austenite in bulk nanocrystalline bainite.

After the austenite volume fraction begins to decrease, each sample developed many new, small diffraction peaks. It was then generally not possible to get a stable fit during Rietveld refinement, as they are small compared to those from ferrite and overlap the tail of the 110_α peak. Since there are no cementite-insoluble solutes in Alloy 2, the new peaks are likely to be cementite. detailed study on the phase(s) responsible for the new peaks revealed that cementite matched almost all the peaks that were not attributable to ferrite or austenite (figure 4.20). Of those peaks remaining, most could be attributed to haematite, Fe_2O_3. The samples were visibly oxidised after the heat treatment, with a well-adhered, gold-coloured layer, consistent with haematite.

Several strong cementite peaks overlap the austenite 111_γ peak (figure 4.20). This led to erroneous results, as the emergence of the 211_θ and 102_θ peaks is interpreted by the software as an increase in austenite content. For this reason, only the initial decomposition stage of the experiments was examined, as the 111_γ peak is still more intense than the cementite peaks and the volume fraction may

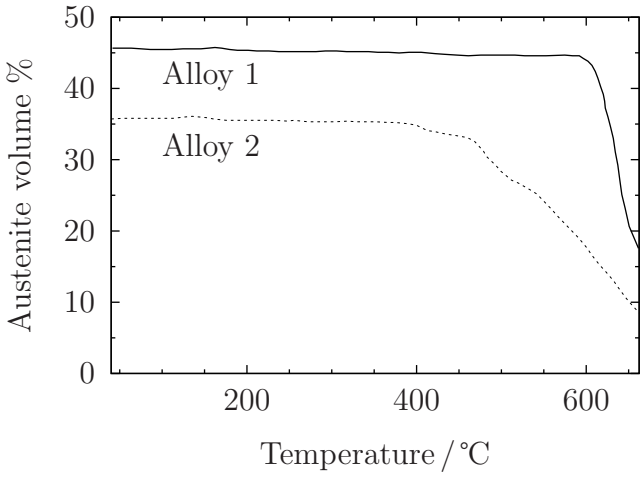

Figure 4.17: Synchrotron X-ray diffractometry results for Alloy 1 and Alloy 2 during continuous heating at $5\,^{\circ}\mathrm{C\,s^{-1}}$. The austenite in Alloy 1, which is designed to resist thermal decomposition, survives to higher temperatures than the conventional Alloy 2.

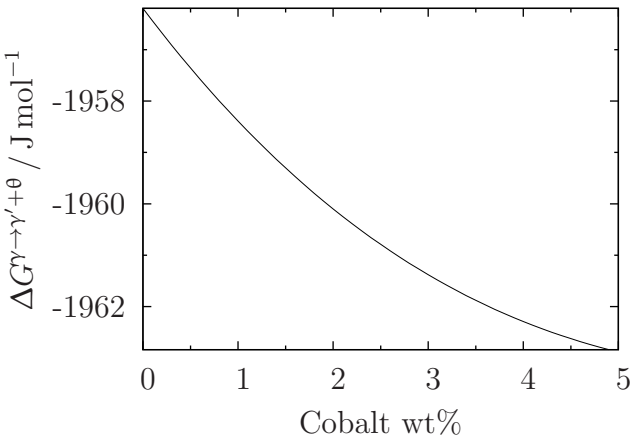

Figure 4.18: Driving force for the equilibrium decomposition of austenite in Fe–4.0 C–x Co (wt%) to carbon-depleted austenite and cementite [26, 199]. The addition of cobalt has a negligible effect.

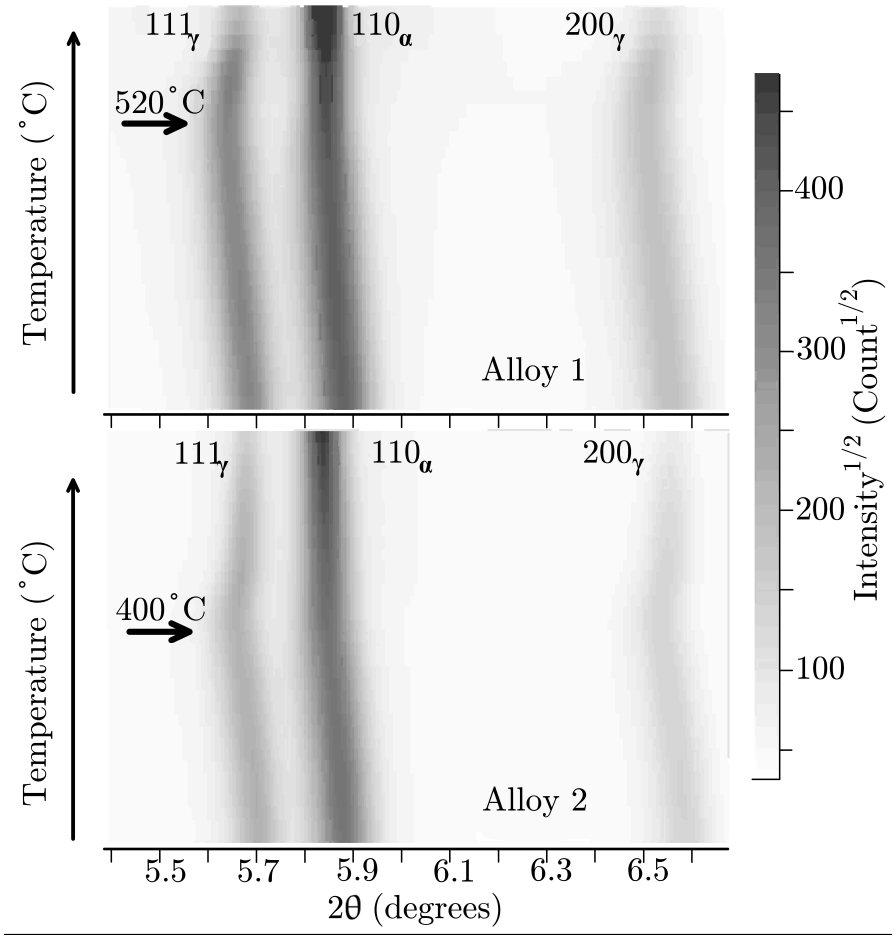

Figure 4.19: Diffraction data during *in-situ* heating of Alloy 1 and Alloy 2. Arrows indicate temperature at the time of minimum detected diffraction angle (maximum lattice parameter) of the austenite 111 peak. Reproduced with permission of Elsevier B. V.

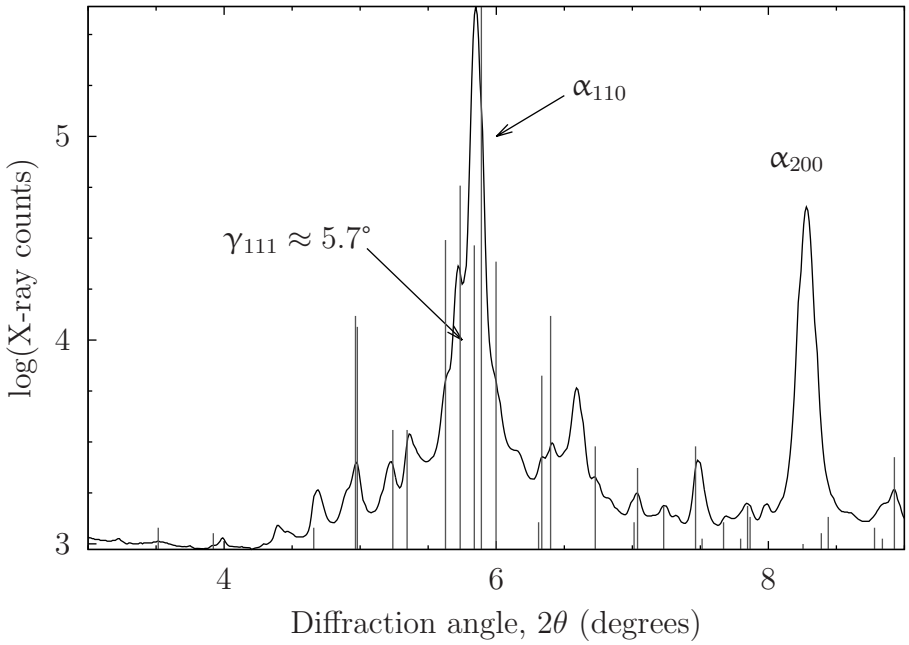

Figure 4.20: Diffractogram of thermally-exposed Alloy 2 recorded at DESY with calculated cementite peaks overlaid. The observed peaks are well-matched by a theoretical cementite pattern. The heights of the calculated peaks are relative to the most intense peak.

be derived reliably. The first stages of decomposition also represent the time of most interest of the experiments — once the austenite begins to decompose, the mechanical properties of the sample are expected to deteriorate.

The small peaks that emerge in Alloy 1 do not match with cementite (figure 4.21). This is consistent with the large contents of silicon and aluminium. No satisfactory match could be made between the observed data and predicted carbide peaks. The carbides investigated were: cementite, ε, κ, Hägg (M_5C_2), $M_{23}C_6$, Mo_2C, M_7C_3, M_6C and SiC. Predicted peaks for graphite, diamond and carbon clusters were also tested. All crystallographic data were retrieved from the Crystallographic Open Database [136, 137] and the lattice parameters of each phase were varied in an attempt to match the observed peaks. Electron diffraction was performed, but was not successful and insufficient material was available to make new attempts. The identification of the phase(s) responsible for the peaks would provide valuable information for the future improvement of this class of alloys and should be a priority in future work.

Further study of Alloy 1

A subsequent experiment was conducted on a sample of Alloy 1, subjected to XRD with *in-situ* heating at $5\,^{\circ}\mathrm{C\,s^{-1}}$to $670\,^{\circ}\mathrm{C}$, where it was held for approximately half an hour and then cooled in air. Figure 4.22 shows that the austenite lattice parameter initially increases, due to thermal expansion (the thermal expansion coefficient is $\approx 3 \times 10^{-5}\,\mathrm{K^{-1}}$, close to values reported in literature [116, 181, 288–290]). After 6200 s the lattice parameter of austenite suddenly decreases and $\sim$ 100 seconds later, its volume fraction of austenite reduces. Beyond 8000 s, the refinement becomes unstable, but the overall trend is the continued decrease in austenite volume fraction down from around 50 vol.% to below 20 vol.%. These unstable refinements show an apparent increase in austenite volume fraction. Subsequent examination of the raw data revealed this was due to the overlap of carbide peaks with the austenite 111 peak described in figure 4.20. Austenite volume fraction decreases with prolonged tempering, as expected.

Ferrite exhibits an expansivity of $\approx 2\times10^{-5}\,\mathrm{K^{-1}}$, consistent with literature [116,

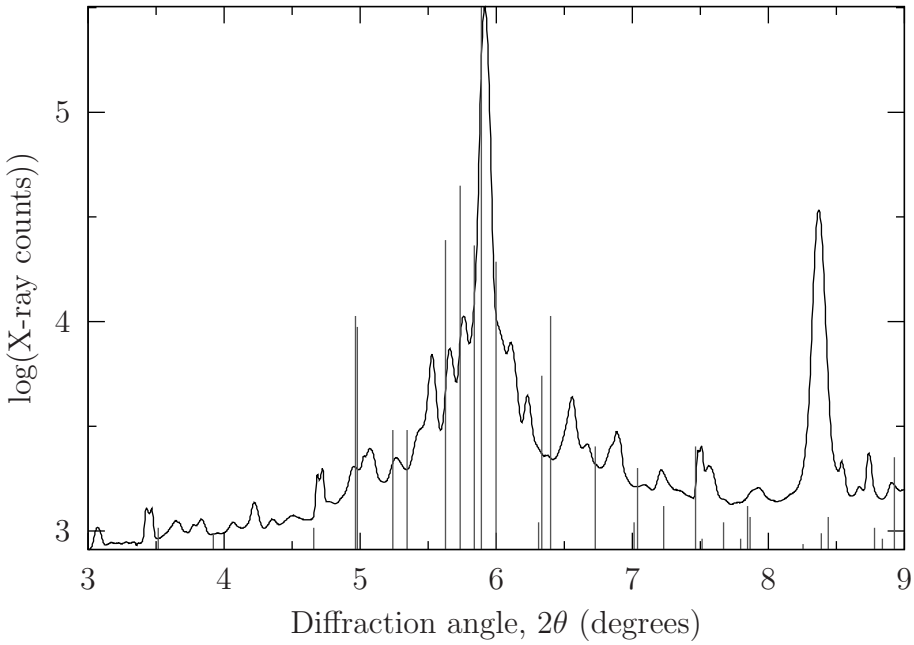

Figure 4.21: XRD data of Alloy 1 transformed at 300℃ and tempered at 500℃. A calculated cementite pattern does not match the observed diffraction peaks, suggesting that cementite is not the carbide that forms during tempering.

181, 290]. The lattice parameter then decreases slightly as soon as the austenite begins to decompose, which may be confirmed using figure 4.22(c). The lattice parameter remains almost constant during the hold at 670 °C and then contracts upon cooling.

These findings support the earlier work on low-strength bainite Saha Podder and Bhadeshia [116] that carbide precipitation and corresponding depletion of carbon in austenite is the initiating stage of retained austenite decomposition. The loss of carbon leads to the contraction in lattice parameter and it is soon after precipitation that the measured austenite volume fraction decreases.

4.3.2 Isothermal experiments

Samples of Alloy 1 were isothermally transformed at 200 °C, 250 °C or 300 °C and tempered at either 450 °C or 500 °C in order to assess the stability of retained austenite. A lower transformation temperature is associated with a higher carbon content in the retained austenite, increasing susceptibility to carbide precipitation.

Holding at 500 °C

Samples transformed at 200 °C, 250 °C and 300 °C were heated as rapidly as was possible to 500 °C which represents an extreme operating temperature in some aeronautical engineering applications or during processes such as galvanisation [291, 292].

Figure 4.23 shows that transformation at 200 °C both has the least retained austenite than the other samples and decomposes more rapidly, due to the greater driving force for carbide precipitation. The relative thermal stability of the austenite is also in the order expected, however, the sample transformed at 250 °C appears to start with an austenite lattice parameter larger than both other samples. This is because there was a delay in collecting data from that experiment, also indicated by the short time between the start of the experiment and the peak lattice parameter. Austenite eventually decomposes completely from all three samples.

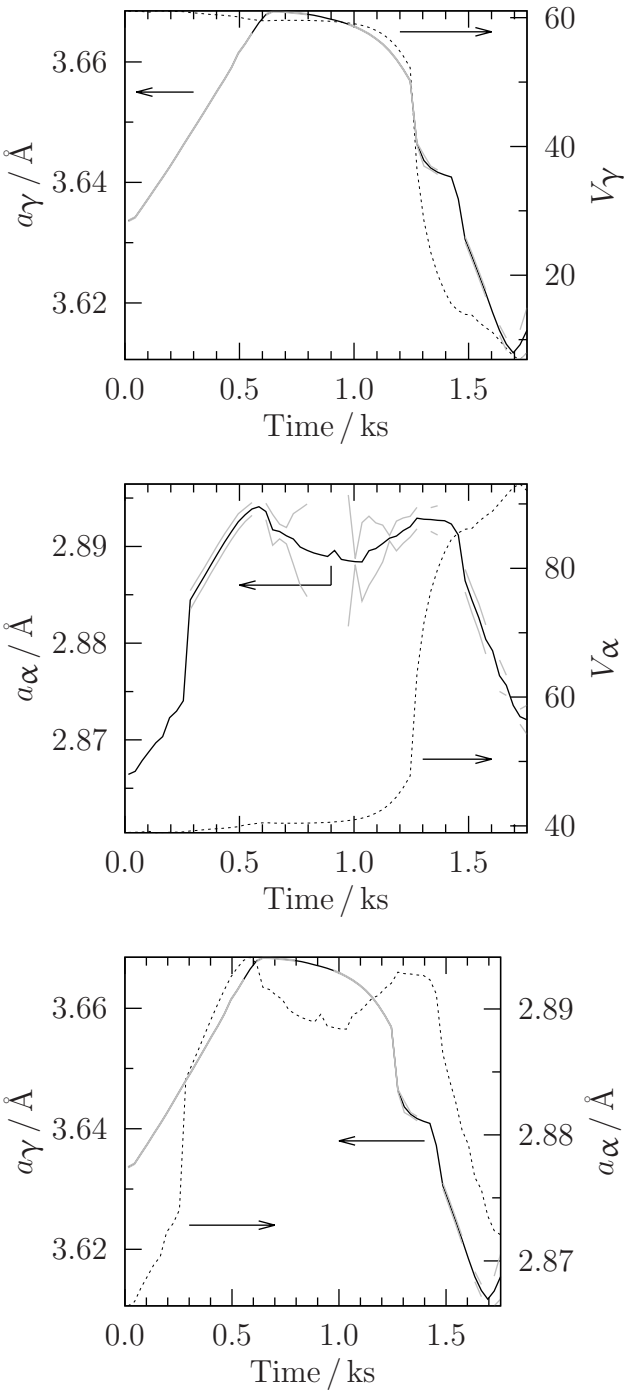

Figure 4.22: Lattice parameters and volume fraction of austenite and ferrite in Alloy 1 transformed to bainite at 300 °C and subjected to synchrotron XRD during continuous heating at 5 °C s^{-1}, assessed using Rietveld refinement. Austenite eventually decomposes and transforms to ferrite. Grey lines represent the assessed values ± one standard error. When errors are extremely small, the grey lines overlie the data. When one or more variables in the refinement could not be assessed, no error could be derived.

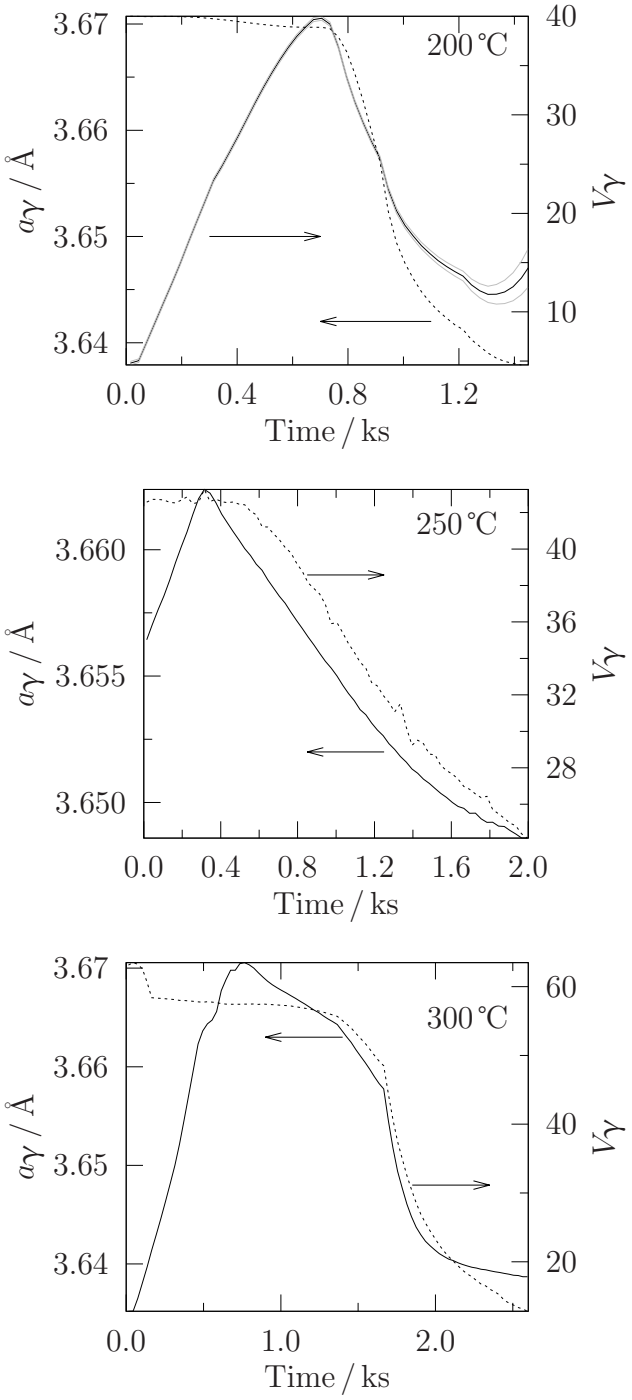

Figure 4.23: Lattice parameters and volume fraction of austenite and ferrite in Alloy 1 transformed to bainite at the temperature indicated and subjected to synchrotron XRD during isothermal tempering at 500 °C, assessed using Rietveld refinement.

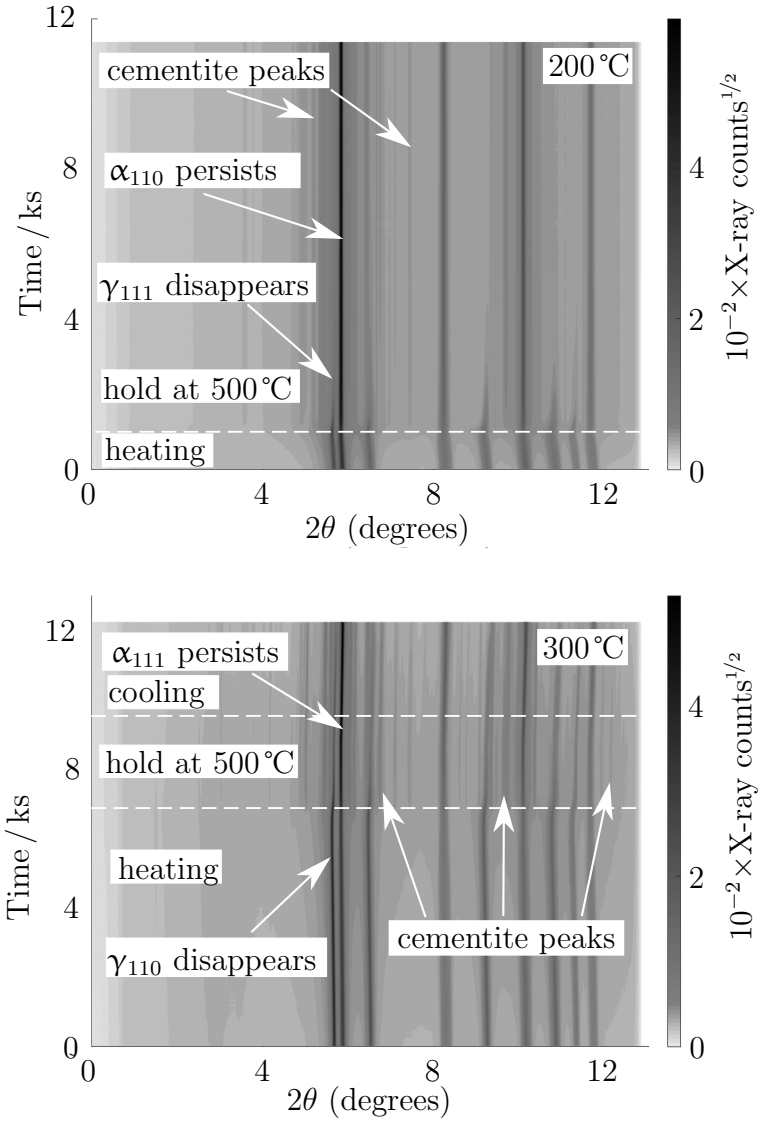

Figure 4.24: Synchrotron XRD data recorded from Alloy 1 transformed at the temperatures indicated during *in-situ* tempering at 500 °C. The square root of the number of observed counts is shown to allow small peaks to be observed.

Holding at 450 °C

Samples originally transformed at 250 °C and 300 °C were then tempered at 450 °C, where the decomposition of retained austenite is expected to be slower. This is clearly shown by comparing figures 4.23 and 4.25: reducing the tempering temperature by 50 °C leads to the decomposition becoming ten times slower. In the case of the sample transformed at 300 °C, decomposition barely begins in the six hours of the experiment. Due to restrictions on the available beamtime, data acquisition had to be terminated before the decomposition was complete.

As at 500 °C the austenite in the sample transformed at 250 °C decomposed more rapidly and had larger initial lattice parameters, consistent with a higher carbon content.

The results of the experiments involving tempering at 450 °C are presented in figure 4.26. It is noticeable that the austenite peaks persist to the end of the data collection, unlike the data in figure 4.24. There are also no visible peaks corresponding to precipitate phases, also unlike the 500 °C tempering experiments (section 4.3.2). This is consistent with the fact that decomposition had not reached an advanced stage during tempering at 450 °C.

4.4 Conclusions

Incorporation of elements that are insoluble in cementite, namely silicon and aluminium has been shown to retard the precipitation of cementite during the tempering of bulk nanocrystalline steel. Alloy design that incorporates a greater content of these elements stabilises the microstructure of bulk nanocrystalline steel during exposure to elevated temperatures. The presence of cementite-insoluble elements appears to lead to the precipitation of phases that are not readily identified from the XRD. Some work is needed to identify the new phase(s) and would be highly valuable to understand the decomposition mechanism in Alloy 1. Further refinement of the alloy composition has the potential to further improve thermal stability.

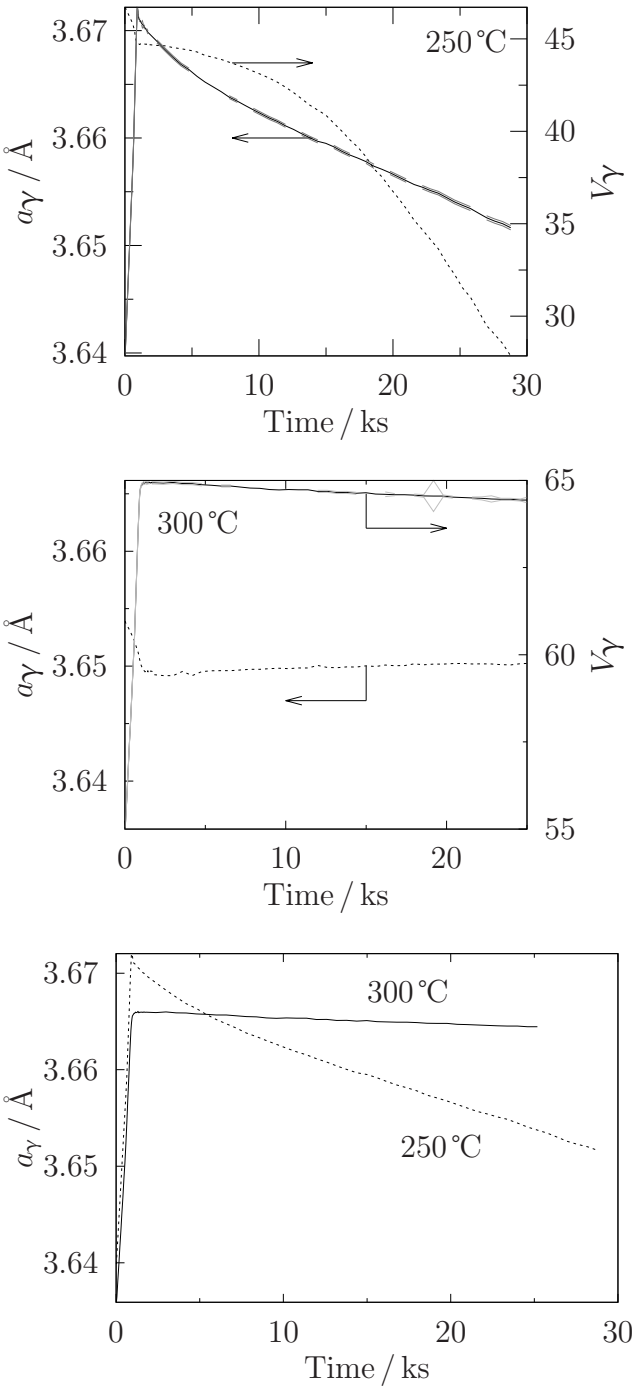

Figure 4.25: Comparison of austenite lattice parameters and volume fractions of Alloy 1 transformed at (a) 250 ℃ and (b)300 ℃ and tempered at 450 ℃; (c) austenite lattice parameters from (a) and (b).

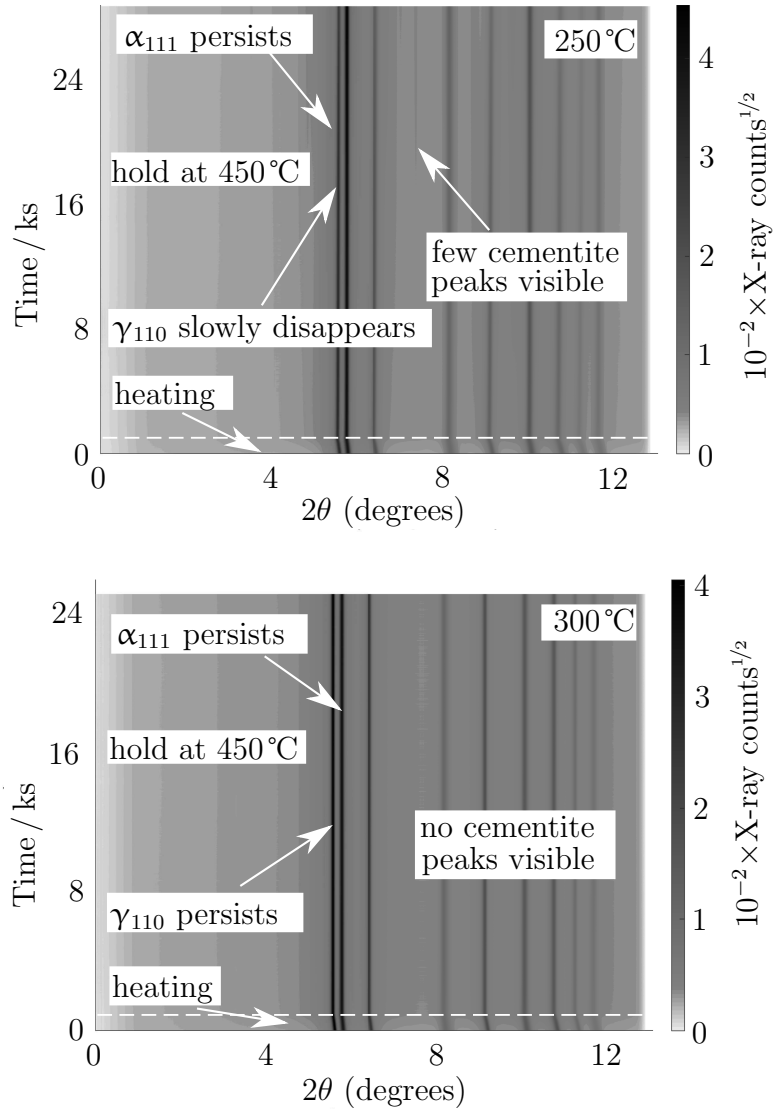

Figure 4.26: Synchrotron XRD data recorded from Alloy 1 transformed at the temperatures indicated during *in-situ* tempering at 450 °C. The square root of the number of observed counts is shown to allow small peaks to be observed.

Chapter 5

Improving thermal stability

Following the success of Alloy 1 in delaying the thermal decomposition of nanocrystalline bainite to higher temperatures than those previously observed, further alloys were designed to attempt to further improve thermal stability. This chapter documents the design process of five new alloys and the microstructures obtained from experimental melts made to those compositions. The design concepts of the novel alloys are summarised in table 5.1 and are discussed in more depth in section 5.1. The resulting microstructures are then given and discussed in section 5.2.3.

Designation	Design concept
Alloy 3	Variant of Alloy 1 that includes nickel in place of manganese.
Alloy 4	Variant of Alloy 3 with an increased level of aluminium.
Alloy 5	Variant of Alloy 4 with an even higher aluminium content.
Alloy 6	Variant of Alloy 4 incorporating copper.
Alloy 7	Variant of Alloy 5 incorporating copper.

Table 5.1: Summary of design concepts for the new generation of alloys. All the concepts are discussed in section 5.1

5.1 Alloy design concepts

In this section general design concepts for the current generation of alloys are explained and then each alloy is discussed in turn. The composition of each alloy is given in the relevant section and all the designed compositions are summarised in table 5.2.

It was decided to reduce the carbon content of the new alloys. This is expected to reduce the driving force for the precipitation of cementite (figure 5.1). Some carbon is, however, essential to avoid the convergence of B_s and M_s (section 2.3.7 and [1, figure 10a]). It was also considered desirable to include as many atoms as possible that are detrimental to cementite precipitation. It was noted both in literature (section 2.3.6) and during calculations performed during the design of the current alloys that silicon, aluminium and copper exhibit very limited solubility in cementite. Alloy 1 already includes a high level of silicon, so it was decided to investigate the possibility of increasing the amount of aluminium and copper in the new alloys. Manganese is also considered to be favourable for cementite precipitation as a mixed $(\mathrm{Fe},\mathrm{Mn})_3\,\mathrm{C}$ carbide is able to form (section 2.3.6). The manganese is included as an austenite stabiliser to both suppress the transformations to ferrite to low temperatures to allow nanostructured bainite to form and to provide hardenability and avoid reconstructive transformations. After carbon and manganese, nickel is the most powerful austenite stabiliser [12, figure 4.3] and has no affinity for carbide formation [13, page 244]. Nickel is also expected to provide hardenability to the alloy (figure 5.2).

The decrease in carbon content and the replacement of manganese with nickel are expected to lead to a reduction in solution strengthening (equation 2.26 [232] and equation 2.25). This inherent strength of both austenite and ferrite will diminish in the new alloys and allow larger bainite sub-units to form during transformation (section 2.2.1). The new alloys are therefore expected to be weaker than those produced previously, but this can be tolerated in order to gain greater thermal stability. Small amounts of manganese (0.2 wt% and molybdenum 0.3 wt% were added to tie up sulphur and phosphorus impurities, respectively. To simplify design, it was decided that these levels of manganese and sulphur would be kept

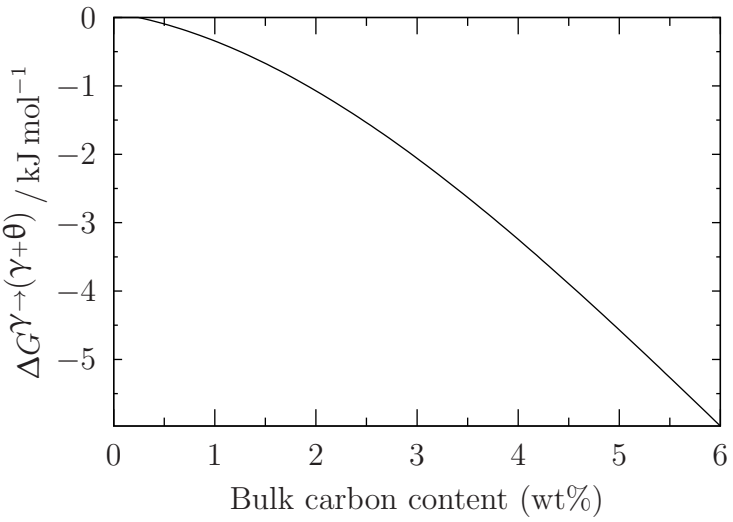

Figure 5.1: Driving force for the precipitation of cementite in austenite in Fe–x wt% C at 400 °C calculated using MatCalc thermodynamic modelling software [247, 293]. Decreasing the carbon content is calculated [116] to reduce the driving force for the nucleation of cementite in austenite, which is the limiting step in thermal decomposition of nanocrystalline steels [116, 134].

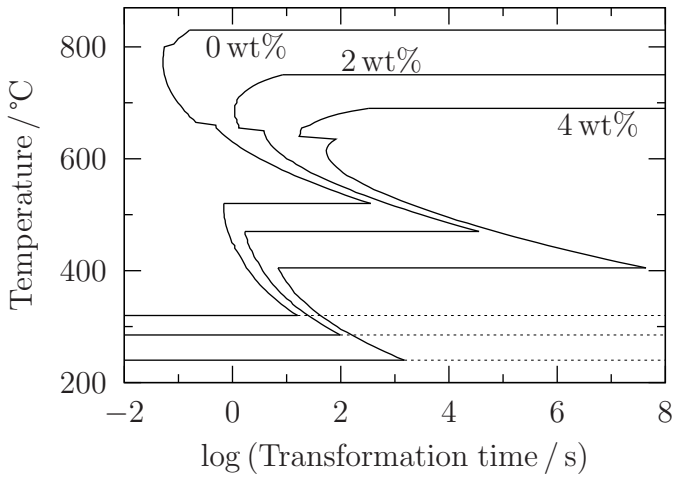

Figure 5.2: TTT curves calculated using mucg83 [241] for Fe–0.7 C–4.0 Si–1.4 Al–0.2 Mo–y Ni (wt%). The nickel content is indicated on each curve. It is possible to derive sufficient hardenability to avoid reconstructive transformations using nickel.

constant for all the current generation of alloys.

In order to form the correct structure, there are several criteria that must be satisfied and which were considered during the design procedure:

- it must be possible to fully austenitise the alloy;
- the martensite-start temperature should be below 200 °C to allow the formation of low-temperature bainite;
- the bainite start temperature should be above 300 °C to ensure that a substantial amount of bainitic ferrite may be formed in a practicable time.

M_s predictions for each alloy were made using a purpose-built artificial neural network (section 3.1.5) and by the program "mucg83" [241]. TTT curves, including an assessment of B_s, were calculated using a bespoke version of the program "MTTTData" [199, 254, 259]. MTTTData also provided a prediction of the T_0 and T_0' lines. At this preliminary stage of the alloy design process no attempt was made to verify either the exact value of M_s or the transformation kinetics of any of the alloys. Equilibrium phase fractions were calculated over a range of temperatures using the commercial thermodynamic modelling software "Thermo-Calc" [248, 249].

5.1.1 Alloy 3

The first alloy produced was a variant of Alloy 1, with nickel substituted for manganese and a corresponding reduction in carbon content to maintain constant martensite- and bainite-start temperatures. The hardenability is expected to be reduced without manganese [13, page 242], but may be compensated by nickel (figure 5.2). Aluminium is retained in order to accelerate the bainite transformation at approximately the same level as in Alloy 1 at 1.4 wt%. Several trial iterations of compositions resulted in a carbon content of 0.7 wt% and a nickel content of 3.3 wt%. Figure 5.3 shows that the alloy has sufficient hardenability to avoid reconstructive transformations.

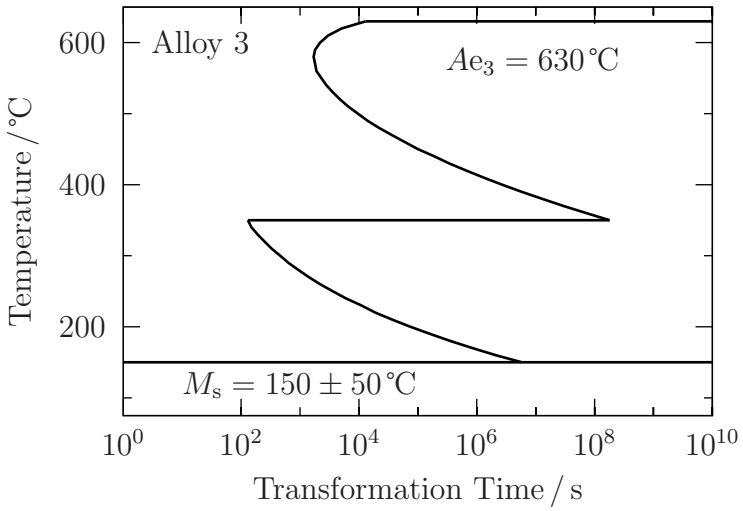

Figure 5.3: Calculated TTT diagram for Alloy 3 [199, 254, 259]. The results suggest that reconstructive transformations could be avoided using the designed composition.

The M_s predicted by the ANN is appropriate at 40±60 ℃. MTTTData predicts a value of 150 ℃. However, mucg predicts that $M_s = 266\,℃$. The alloy falls within the specified limits of applicability for mucg (table 3.1) and no reason could be found for this discrepancy. The M_s is therefore best determined experimentally, as described in section 7.2.1.

The alloy is expected to be fully austenitised between 900 ℃ and 1275 ℃ (figure 5.4). It generally is desirable to minimise the austenite grain size to help accelerate the bainite transformation [51, 115]. To minimise grain growth, austenitisation was initially carried out at 900 ℃, the lowest temperature at which the alloy is calculated to be fully austenitised.

5.1.2 Alloy 4

Another derivative of Alloy 1 containing a higher concentration of aluminium while maintaining a temperature range over which the alloy may be fully austenitised (figure 5.6). The tendency for aluminium to stabilise ferrite (figure 5.5) can be

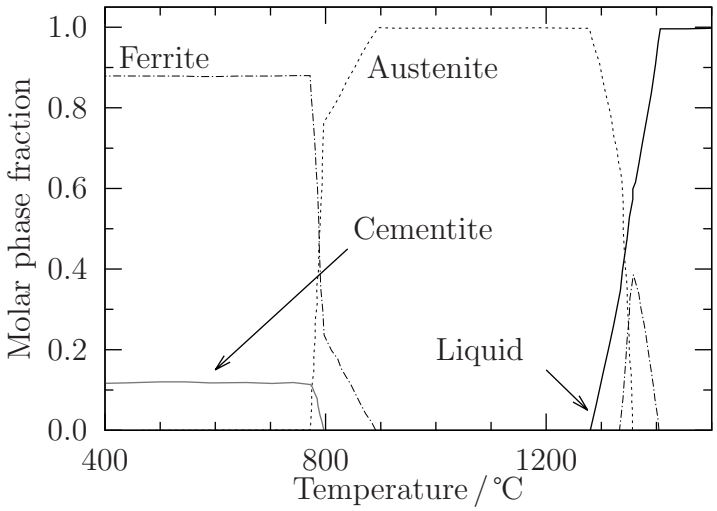

Figure 5.4: Calculated equilibrium phase fractions for Alloy 3 calculated using Thermo-Calc software [248, 249]. The alloy is predicted to be completely austenitic over a practicable temperature range and is expected to exhibit sufficient hardenability to avoid reconstructive transformations.

countered with solutes such as nickel [12, page 74]. The carbon content of Alloy 3 was retained to provide a large window between B_s and M_s. The manganese and molybdenum concentrations are too low to affect phase transformations and were kept constant. The increased aluminium content is intended to suppress the formation of cementite. After several iterations of modelling, a composition of 0.7 C–4.5 Ni–2.0 Al–2.0 Si–0.25 Mo–0.3 Mn (wt%) was derived.

Modelling using Thermo-Calc indicated that Alloy 4 is fully austenite between 800 °C and 1320 °C (figure 5.6) and the predicted B_s of 300 °C (from MTTTData) and M_s of 110 ± 40 °C (predicted using ANN) also meet the design goals.

5.1.3 Alloy 5

The concept of increasing the aluminium concentration to 2 wt% to improve the thermal stability of nanostructured bainite was extended to produce Alloy 5. The aluminium content was increased to 3 wt% and it was calculated using Thermo-

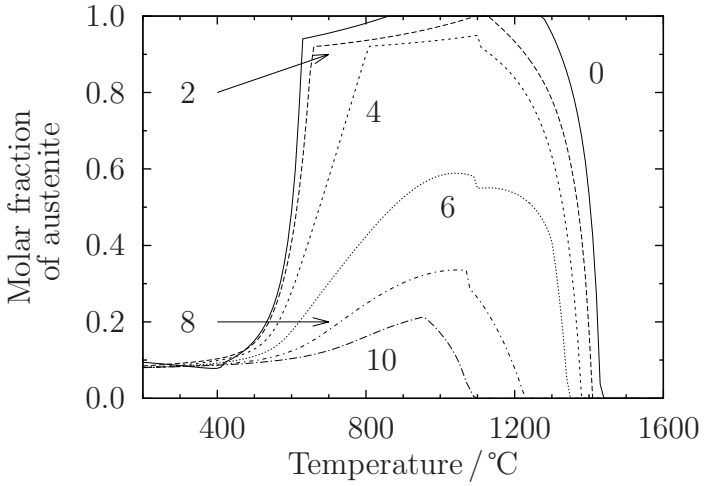

Figure 5.5: Phase fraction of austenite in the system Fe–1.0 C–10.0 Ni–x Al [26, 199].

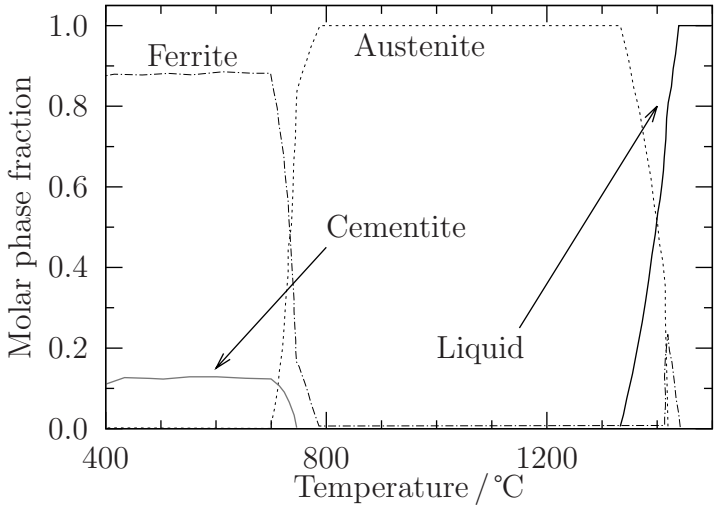

Figure 5.6: Calculated equilibrium phase fractions for Alloy 4 calculated using Thermo-Calc software [248, 249]. The alloy is predicted to be completely austenitic between 790 °C and 1300 °C.

Calc that the nickel content would then need to be raised to 7.5 wt% to retain the ability to fully austenitise the alloy over a similar temperature range to Alloy 4. The contents of all other elements were left unchanged.

Calculations made using Thermo-Calc [248, 249] show that Alloy 5 may be transformed completely to austenite between 740 °C and 1320 °C, as required (figure 5.7). M_s, predicted using an ANN is also appropriate to meet the design goals at -60 ± 70 °C.

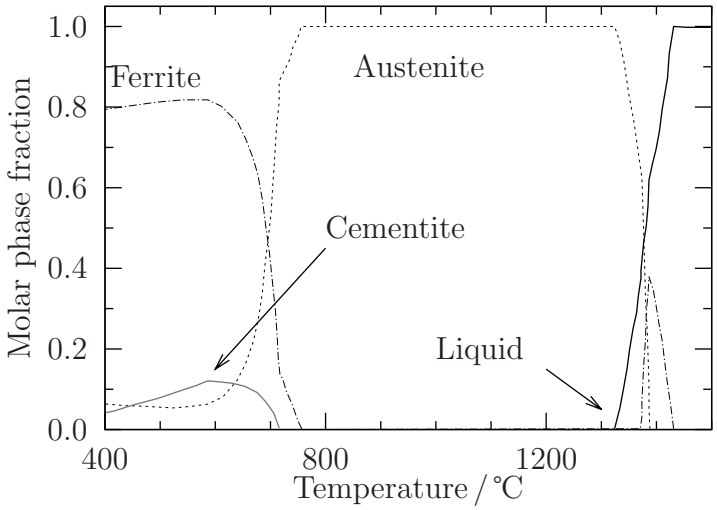

Figure 5.7: Calculated equilibrium phase fractions for Alloy 5 calculated using Thermo-Calc software [248, 249]. The alloy is predicted to be completely austenitic between 740 °C and 1320 °C.

5.1.4 Alloy 6 and Alloy 7

There is a lack of available thermodynamic data for copper in cementite. Wasynczuk et al. [294] found that in Fe–1.49 C–4.90 Cu (wt%), cementite contained ε copper precipitates, but no such precipitates were present in the martensite next to the cementite. The copper in a given cementite grain nearly all precipitates with in identical crystallographic orientation to the parent austenite from which the cementite formed, indicating precipitation of copper from cementite at the cemen-

tite/austenite interface. This, in turn, suggests that copper left solution before cementite formed and was never incorporated into the cementite lattice. It is possible therefore that if copper is unable to partition, it can suppress cementite.

Copper is also an austenite stabiliser [12, figure 4.3b] and suppresses B_s and M_s when in solution in austenite. Copper has a relatively low solubility in ferrite, so may in contribute to precipitation hardening [295]. Copper may also cause *hot shortening*, in which its segregation to grain boundaries may lead to localised melting and cracking. Nickel ameliorates this problem, provided there is at least half as much nickel as copper [296]. Calculations indicate that with 2 wt% copper, the nickel concentration may be reduced by 0.5 wt% to maintain values of B_s and M_s in an otherwise identical alloy. Predictions of temperatures over which the alloy may be fully austenitised, B_s, M_s and transformation kinetics are only affected slightly by the substitution of 0.5 wt% Ni with 2.0 wt% Cu (tables 5.2 and 5.3). Making this substitution in Alloy 4 leads to Alloy 6 and doing so in Alloy 5 leads to Alloy 7. The concentrations of other elements were left unchanged. The predicted equilibrium phase fractions indicate a suitable temperature range over which both Alloy 6 and Alloy 7 are fully austenitic (figures 5.8 and 5.9).

5.1.5 Summary of novel alloy designs

The designed compositions of all five current alloys are given in table 5.2.

5.2 Experimental casts

60 g casts (ellipsoidal cross section, 14 mm × 9 mm and 100 mm long) were made by arc melting of powders under vacuum and heat treated to verify austenitisation and their suitability to transform to bainite. A cast of nominally pure titanium was melted before each batch of alloys to getter any residual oxygen.

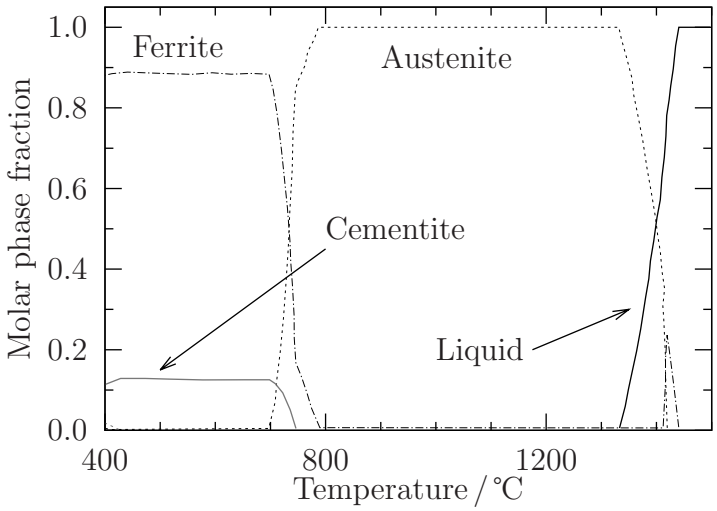

Figure 5.8: Calculated equilibrium phase fractions for Alloy 6 calculated using Thermo-Calc software [248, 249]. The alloy is predicted to be completely austenitic between 790 ℃ and 1320 ℃.

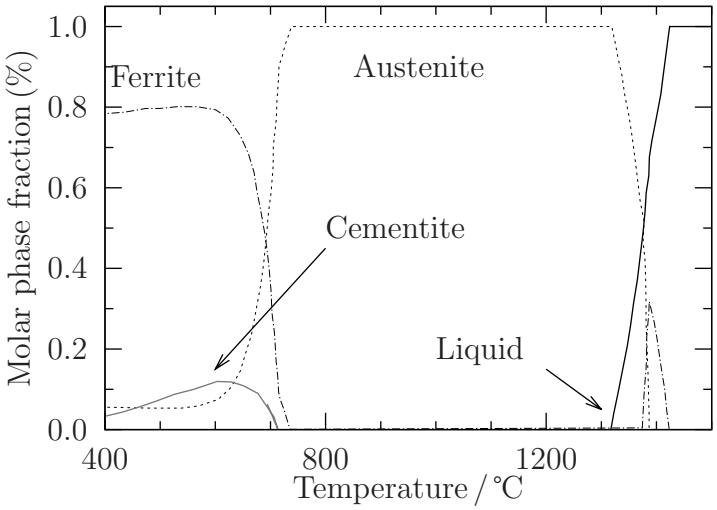

Figure 5.9: Calculated equilibrium phase fractions for Alloy 7 calculated using Thermo-Calc software [248, 249]. The alloy is predicted to be completely austenitic between 760 ℃ and 1330 ℃.

Alloy	C	Ni	Al	Si	Mo	Mn	Cu	B_s / °C	M_s / °C
Alloy 3	0.7	3.3	1.4	4.0	0.25	0.2	0.00	350	160 ± 50
Alloy 4	0.7	4.5	2.0	2.0	0.25	0.2	0.00	300	110 ± 40
Alloy 5	0.7	7.5	3.0	2.0	0.25	0.2	0.00	40	-60 ± 70
Alloy 6	0.7	4.0	2.0	2.0	0.25	0.2	2.00	250	130 ± 50
Alloy 7	0.7	7.0	3.0	2.0	0.25	0.2	2.00	0	-50 ± 80

Table 5.2: Design compositions of new generation of alloys, B_s modelled using MTTTData [199, 254, 259] and M_s predicted by an artificial neural network [268, 269].

Alloy	M_s / °C	B_s / °C	Austenitisation temp. / °C		Pearlite nose	
			Min	Max	time / ks	Temp. / °C
Alloy 3	40 ± 60	350	900	1275	1.7	580
Alloy 4	110 ± 40	300	790	1300	14	530
Alloy 5	-60 ± 70	100	740	1320	7.8×10^4	420
Alloy 6	130 ± 50	230	790	1330	30	530
Alloy 7	-50 ± 80	100	760	1320	2.5×10^5	410

Table 5.3: Calculated properties of new alloys: M_s, calculated using an artificial neural network (ANN), austenitisation temperature range calculated using Thermo-Calc [248, 249], B_s and transformation kinetics calculated using the program MTTTData [199, 254, 259]. All alloys may be fully austenitised over a wide temperature range and are predicted to be thermodynamically capable of producing bainite. All alloys are calculated to exhibit sufficient hardenability to avoid reconstructive transformations.

5.2.1 Measured composition

A sample of each alloy was sent to Inspiratech 2000 Ltd. (Rugby, U. K.) to determine the composition. Carbon was measured using combustion and gas chromatography. Other elements were identified and measured using X-ray fluorescence spectroscopy. However, the aluminium content of the current alloys could not be measured by Inspiratech, so energy dispersive X-ray spectroscopy (EDX) on a FEI Nova NanoSEM scanning electron microscope was used to estimate its concentration (table 5.4).

All alloys contain less carbon than was specified in the design. Due to an oversight during production no sample other than Alloy 3 contained more than trace amounts of molybdenum.

	C	Ni	Al	Si	Mo	Cu
Alloy 3	0.622	3.98 ± 0.12	1.20 ± 0.07	3.34 ± 0.15	0.32 ± 0.02	not detected
Alloy 4	0.544	4.30 ± 0.14	1.67 ± 0.10	1.50 ± 0.09	not detected	not detected
Alloy 5	0.522	7.47 ± 0.23	2.24 ± 0.13	1.26 ± 0.08	0.05 ± 0.03	not detected
Alloy 6	0.572	4.71 ± 0.13	1.65 ± 0.09	1.45 ± 0.07	0.05 ± 0.03	2.45 ± 0.08
Alloy 7	0.420	6.74 ± 0.21	2.31 ± 0.13	1.47 ± 0.09	0.05 ± 0.03	2.18 ± 0.09

Table 5.4: Experimentally measured composition (wt%) of new generation of alloys. The measurements of carbon and tungsten were assessed by Inspiratech 2000 Ltd. (Rugby, U.K.); all other elements assessed using EDX.

5.2.2 Homogenisation of novel alloys

After sealing in glass ampoules filled with argon to prevent oxidation and decarburisation, each sample was homogenised at 1250 °C, close to the highest temperature consistent with complete austenitisation across all the alloys, for 72 h. The present heat treatment parameters were based on the expected time for diffusion to occur over the length of an austenite grain [297].

Sections of each cast were protected in ampoules and separately austenitised at the temperatures listed in table 5.5. The lowest possible austenitisation temperature was chosen according to phase fraction modelling to ensure the finest possible austenite grain size. Samples were then transferred to an oven set at $250 \pm 1\,^{\circ}\mathrm{C}$. The ampoules were then broken to allow the samples to cool rapidly.

	Alloy 3	Alloy 4	Alloy 6	Alloy 5	Alloy 7
Austenitisation temp./℃	950	1150	1150	1100	1050

Table 5.5: Austenitisation temperatures for novel alloys, chosen to be the lowest temperature at which the alloy is calculated to be fully austenitic using Thermo-Calc [248, 249].

Figure 5.10 indicates that, following the homogenisation treatment, all the alloys have uniform microstructures.

5.2.3 Phase transformations of novel alloys

Alloy 3 transformed at 250 °C for 3 d did not lead to the expected bainitic structure (figure 5.11). Instead, it appears that the sample has not been fully austenitised. Large regions of ferrite have formed along with regions of bainitic ferrite that developed from the austenite.

The phase fractions of Alloy 3 were recalculated as a function of temperature using MTData [199, 255] than figure 5.4. The new results are given in figure 5.12(a). Austenitisation is not predicted to occur until the sample is heated above 1050 °C, compared to the 950 °C calculated during design of Alloy 3. Austenitisation at 1100 °C and isothermal transformation at 250 °C for 3 d produced a predominantly bainitic structure (figure 5.12(b)).

Calculations were also repeated for Alloy 4–Alloy 7 using MTData and there were no significant differences to the results obtained from Thermo-Calc.

After austenitisation at 1150 °C and transformation at 250 °C, Alloy 4 forms a small amount of allotriomorphic ferrite (figure 5.13(a)), although the majority

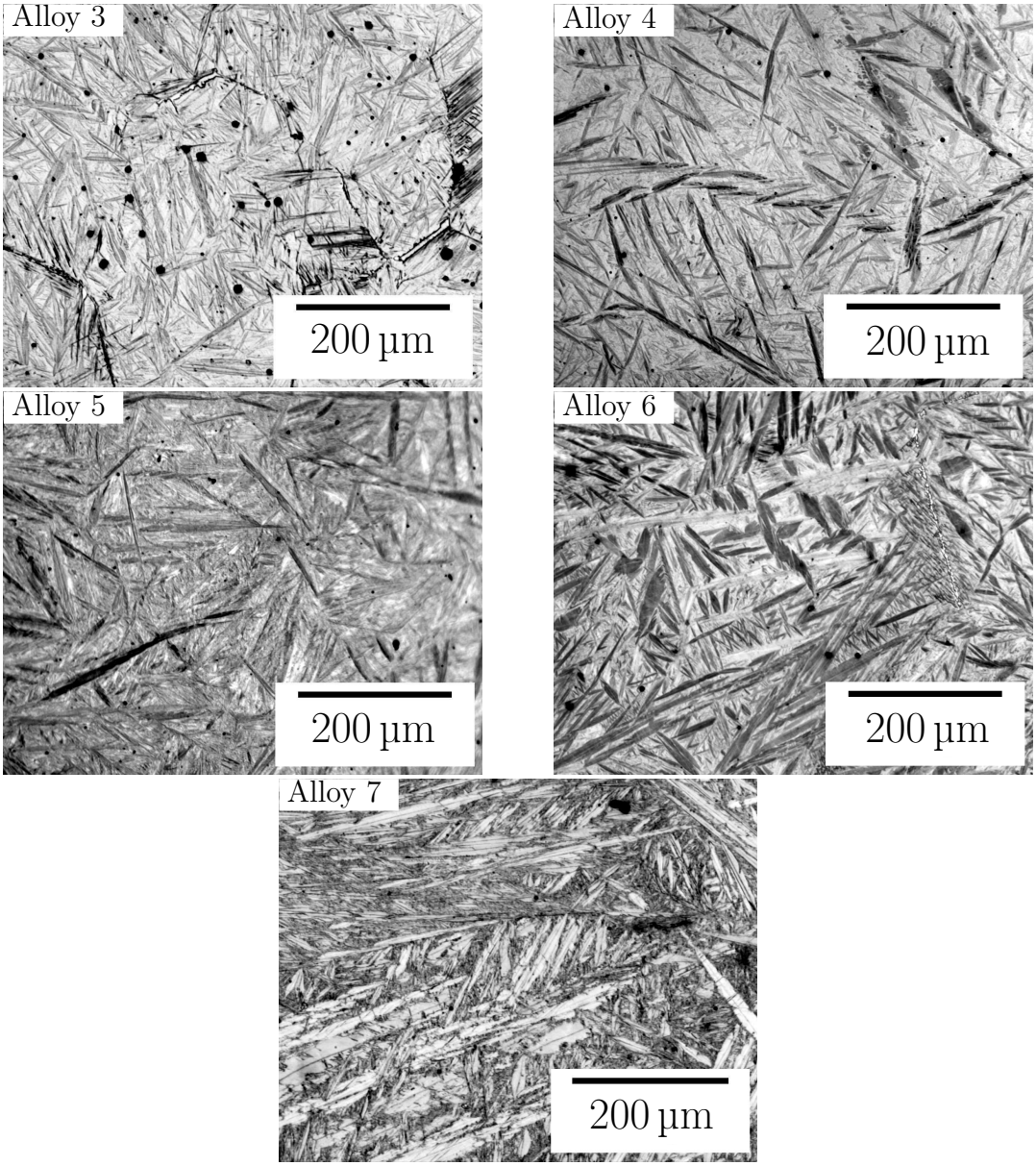

Figure 5.10: Optical micrographs of novel alloys after homogenisation treatment at 1250 ℃ for 72 hours. Microstructures appear homogeneous, consistent with the homogenisation heat treatment.

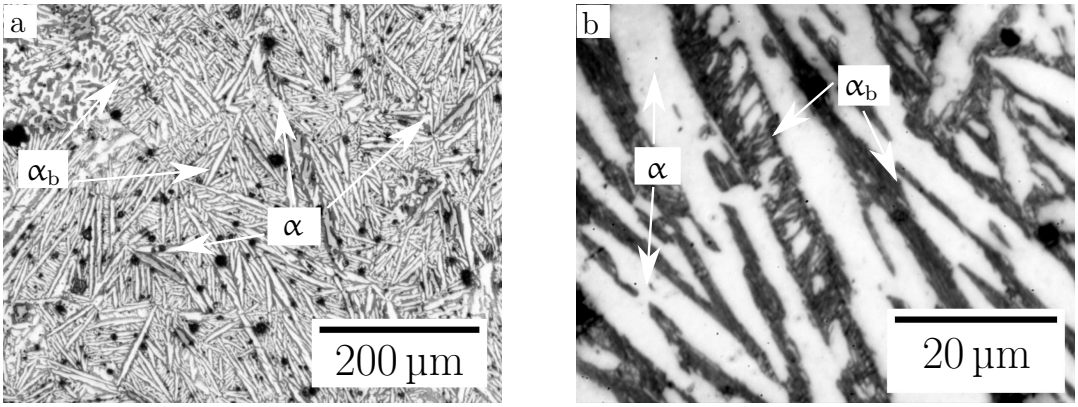

Figure 5.11: Alloy 3 after austenitisation at 950 °C and isothermal holding at 250 °C for 3 days. The microstructure consists of both fine bainite and large grains of ferrite, suggesting that the sample was not fully austenitised before transformation.

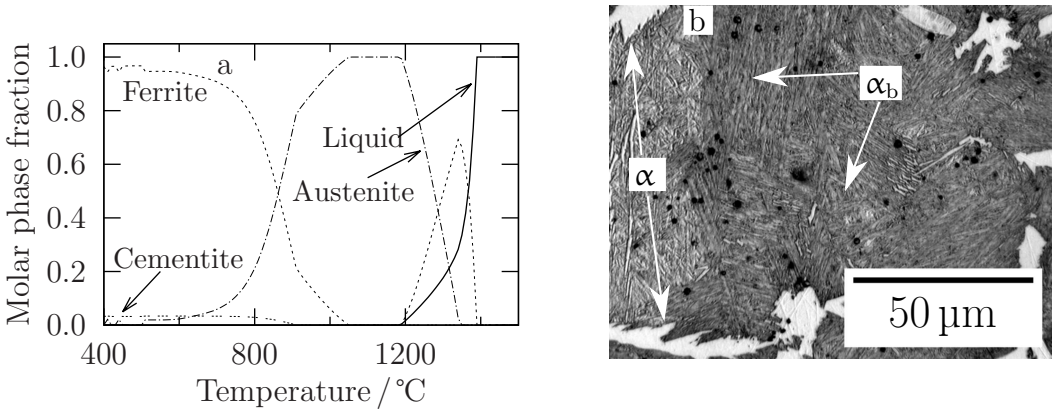

Figure 5.12: (a) Phase fractions as a function of temperature in Alloy 3, calculated using MTData version 4.73 with the TCFE version 1.0 database (equivalent to version 5.0 for Thermo-Calc). The temperature range over which the alloy is calculated to be fully austenitic is significantly smaller and at higher temperature than when calculated using Thermo-Calc. (b) repeating the austenitisation and bainite transformation using the new temperatures gives a predominantly bainitic structure.

phase is clearly bainite (figure 5.13(b)). This may indicate a lack of sufficient hardenability, in spite of calculations (table 5.3).

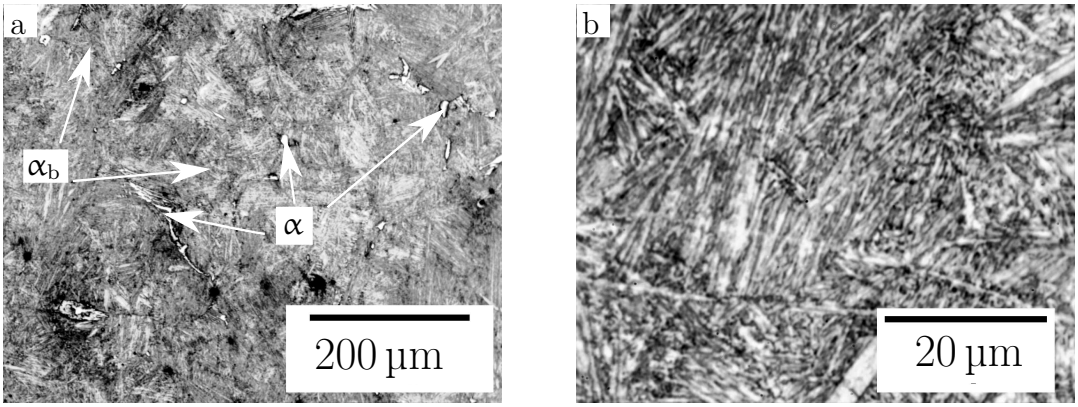

Figure 5.13: Optical micrographs of Alloy 4 after heat treatment at 250 °C for 3 days.

Alloy 6 was successfully austenitised,with no allotriomorphic ferrite (figure 5.14), though large lenticular martensite has formed. This indicates that M_s was greater than the isothermal transformation temperature used, 250 °C as martensite clearly formed before bainite upon cooling to 250 °C. This renders Alloy 6 unsuitable for the generation of nanocrystalline bainite, as a high temperature is required to allow the bainite transformation to proceed. High transformation temperatures are associated with coarse bainite plate size. Measurement of the lineal intercept of bainite sub-unit width from optical and scanning electron microscopy resulted in a value of 640 ± 70 nm.

After austenitisation at 1100 °C for 30 min and isothermal holding at 250 °C for 3 d, Alloy 5 and Alloy 7 do not exhibit ferrite (figure 5.15 and 5.16). Isothermal transformation at 250 °C results in bainite interspersed amongst large lenticular martensite plates, again indicating $M_s \geq 250$ °C and rendering both alloys unsuitable for the formation of nanocrystalline bainite.

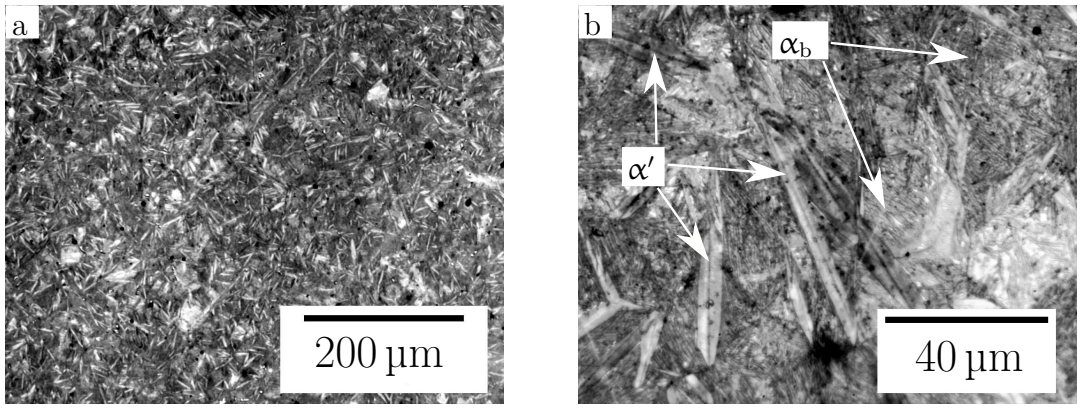

Figure 5.14: Optical micrographs of Alloy 6 after heat treatment at 250 °C for 3 days. The structure consists of large martensite plates with fine bainite in between.

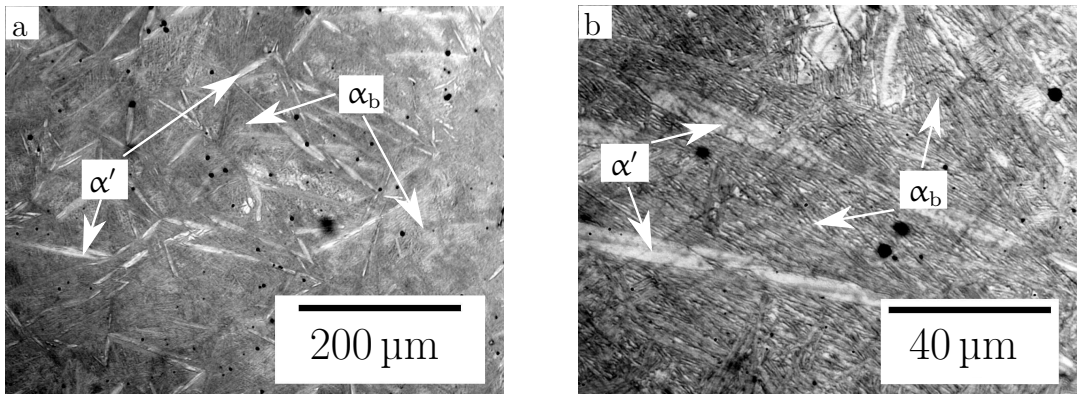

Figure 5.15: Optical micrographs of Alloy 5 after heat treatment at 250 °C for 3 days. The structure consists of large martensite plates with fine bainite in between.

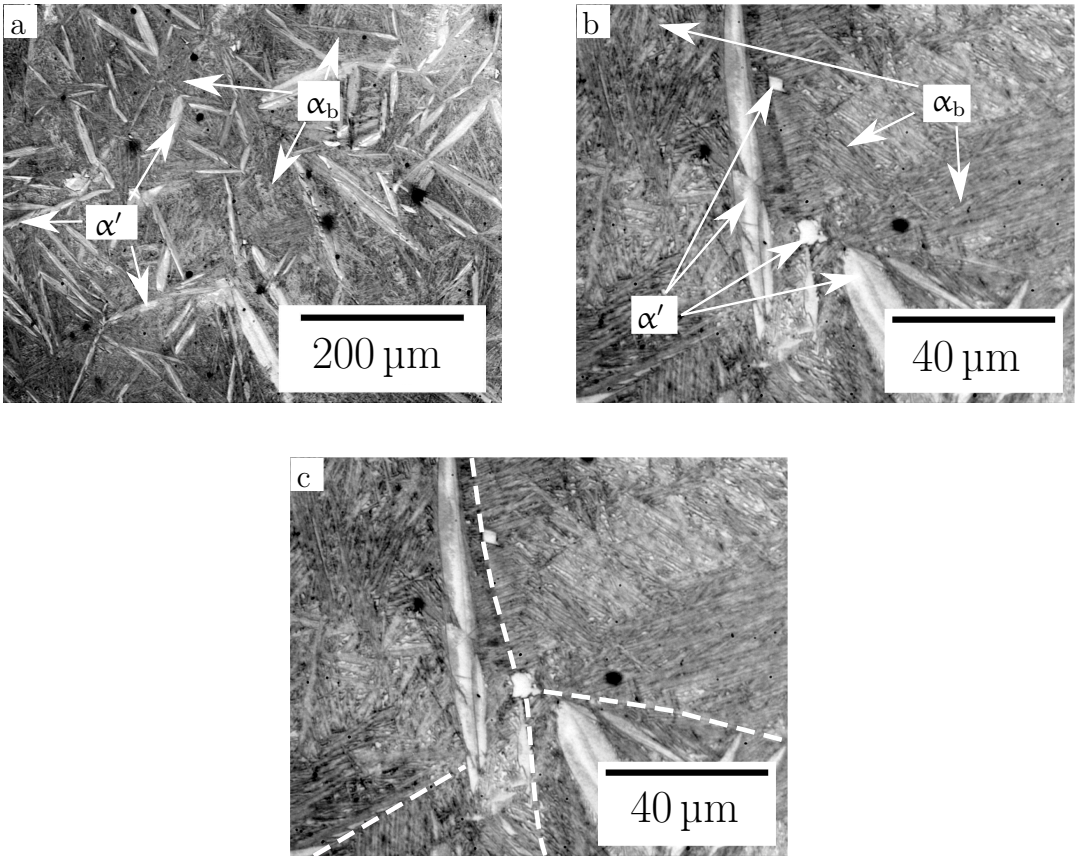

Figure 5.16: Optical micrographs of Alloy 7 after heat treatment at 250 ℃ for 3 days. The structure consists of large martensite plates with fine bainite in between. (c) prior austenite grain boundaries highlighted. Martensite plates extend up to the prior austenite grain boundaries, so they almost certainly formed before bainite.

5.3 Hardness of novel alloys

The experimental casts produced are not large enough to allow comprehensive mechanical tests to be performed, but the hardness of each heat-treated alloy may be tested. Hardnesses were measured using a calibrated Vickers hardness testing machine set to exert the load of 30 kgf. The results quoted in table 5.6 are an average of at least five data.

	Alloy 3	Alloy 4	Alloy 6	Alloy 5	Alloy 7
Vickers Hardness / HV50	402 ± 4	551 ± 6	538 ± 3	490 ± 4	514 ± 6

Table 5.6: Measured Vickers hardnesses for the novel alloys investigated.

The hardnesses are consistent with the observed microstructures. Alloy 3 is the softest due to the large fraction of ferrite. When heat treated to avoid the ferrite, the hardness of Alloy 3 increased to 520 ± 20 HV50. Alloy 4 is the hardest, despite the fact that Alloys 5–7 form martensite, due to the fine bainite it contains Both Alloys 3 and 4 are therefore viable candidates for future nanostructured bainitic alloys.

5.4 Conclusions

Only Alloys 3 and 4 were able to form bainite following transformation at 250 °C, while avoiding coarse ferrite, but the allotriomorphs observed in Alloy 4 suggest that it has insufficient hardenability.

Alloy 3 has been demonstrated to produce the desired microstructure under identical processing conditions to the others and to transform into a hard structure making it the best candidate for engineering applications.

Chapter 6

Alloys optimised for thermal stability

Based on alloys studied previously, two new alloys were designed and cast with the aim of further improving the resistance to thermal decomposition. One alloy, Alloy 8, is an optimised derivative of Alloy 4, incorporating more of silicon, aluminium and nickel to provide favourable transformation kinetics and resistance to cementite precipitation. Alloy 9 is based on the different concept that carbides will precipitate during prolonged holding at 500 °C but that retained austenite may be stabilised to survive the loss of carbon associated with this precipitation. The surviving austenite could then continue to provide toughness and ductility.

6.1 Alloy design

6.1.1 Alloy 8

Alloy 1 demonstrated that incorporating large quantities of silicon and aluminium can improve thermal stability of bainite (figure 4.17) and Alloy 4 showed that that nanocrystalline bainite can be produced when nickel is used in place of manganese. Alloy 4 is now optimised for large-scale production. A small amount of manganese is introduced to combine with sulphur (section 2.3.6) and molybdenum to mitigate

any phosphor embrittlement.

Manganese aids the precipitation of cementite [183], so the minimum required to remove the sulphur was added. The sulphur level in the cast was not expected to exceed 0.01 wt% and so 0.02 wt% manganese was added (figure 6.1). The composition is given in table 6.1).

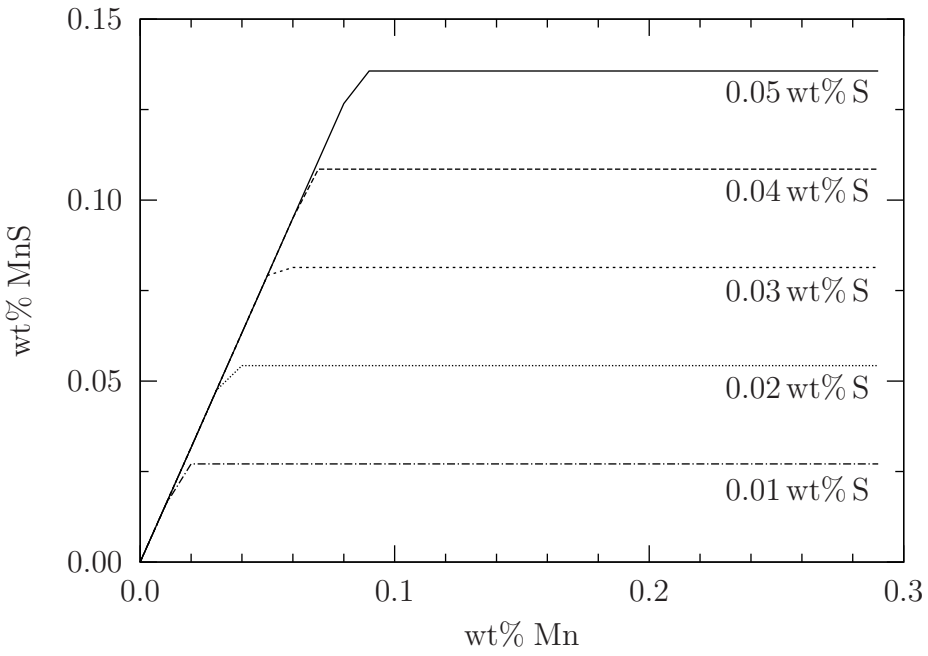

Figure 6.1: Calculated amount of manganese sulphide (MnS) as a function of manganese content for various sulphur contents [199, 254].

C	Ni	Al	Si	Mn	Mo
0.7	3.3	1.4	4.0	0.02	0.25

Table 6.1: Designed composition of Alloy 8. All quantities in wt% and balance is Fe.

6.1.2 Alloy 9

The alloys designed thus far are designed to preserve austenite during tempering, although its decomposition must occur eventually (section 4.3), as demanded by equilibrium. The decomposition of austenite is preceded by cementite precipitation. The question then arises: can cementite be allowed to precipitate while the carbon-depleted austenite is stabilised through some mechanism other than carbon in solid solution?

Substitutional solutes such as manganese, copper and nickel stabilise austenite [12, page 148]. While manganese is the most powerful common substitutional austenite stabiliser it both promotes the precipitation of cementite and greatly increases the time required to form bainite, both of which make it undesirable in large quantities. Upon the advice of the expected level of sulphur in the cast from the steel producer, 0.3 wt% manganese was added to remove sulphur while minimising its ability to promote cementite. Copper stabilises austenite [12, page 148] and is insoluble in cementite, thus contributing to its thermal stability by suppressing precipitation. However, precipitation of ε copper reduces its ability to prevent cementite precipitation. Nickel has little effect on carbide precipitation and stabilises austenite.

Aluminium is necessary to accelerate transformation and suppress cementite but raises the possibility of nickel aluminides (NiAl, Ni_3Al) forming during tempering [298–301]. Cobalt also accelerates transformation [110, 181, 302], does not form carbides, but is expensive. It must be used in this case to reduce the bainite transformation to practicable times, since the amount of aluminium that may be added is limited in order to avoid Al_2O_3 during casting.

The overall design philosophy is illustrated by figure 6.2.

Thermal stability

The response to thermal exposure was modelled for the composition of retained austenite associated with the bainite transformation at 200 °C. This retained austenite was allowed to form an equilibrium mixture of austenite, ferrite and cementite at 600 °C, corresponding to the conditions used in experiments described in sec-

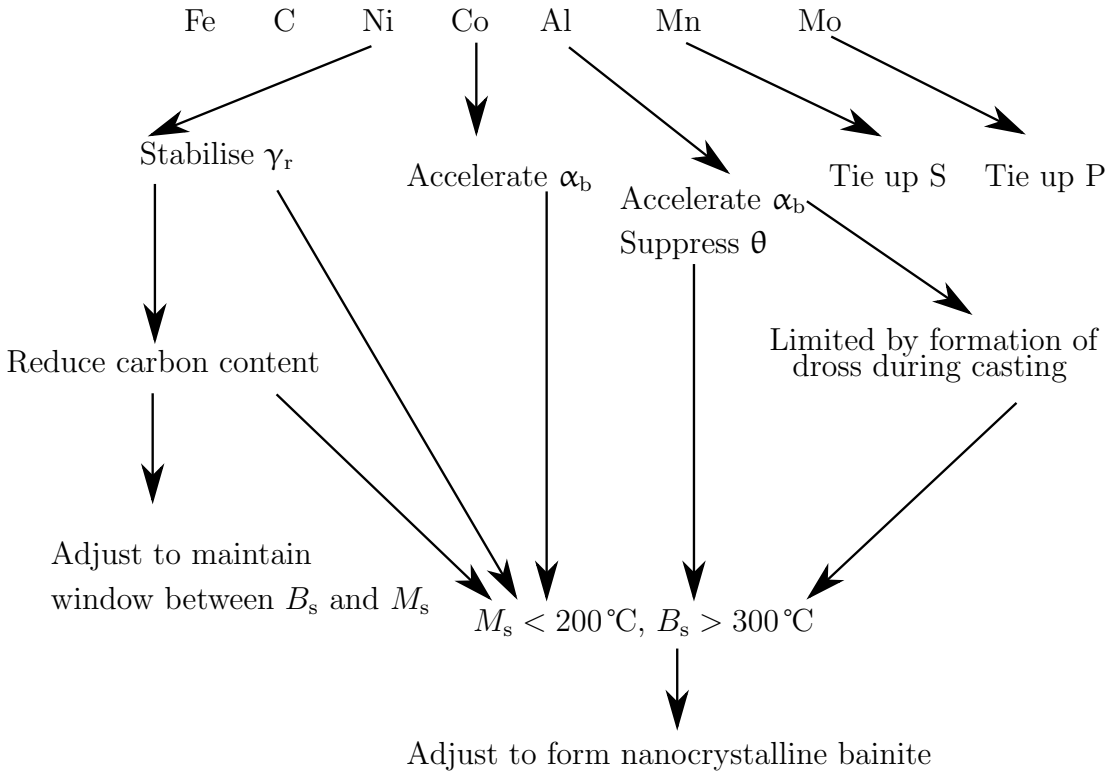

Figure 6.2: Design philosophy for Alloy 9.

tion 8.1.2. This depletes the austenite of carbon, thus increasing the driving force for the martensite transformation on cooling to ambient temperature. The M_s of the carbon-depleted austenite was predicted by the neural network (section 3.1.5) to be $300 \pm 30\,°C$. The driving force for martensite formation at ambient temperature is around -2 kJ mol^{-1}, less than half that for a conventional nanocrystalline bainite. Thus, the equilibrium austenite is more likely to survive the heat treatment and subsequent cooling to ambient temperature.

Composition

Thermodynamic modelling indicated a carbon content $\geqslant 0.4$ wt% to maintain the gap between B_s and M_s. The temperature range over which the alloy is fully austenitic is at least 100 °C (figure 5.5). Cobalt was set to $\leqslant 4$ wt%, to avoid excessive alloying costs. Concentrations of manganese and molybdenum were set as discussed previously.

The final composition thus derived is Fe–0.4 C–13.0 Ni–2.5 Al–4.0 Co–0.15 Mo–

0.3 Mn (wt%). The alloy is fully austenitic at temperatures between 900 °C and 1200 °C (figure 6.3(a)). The predicted B_s and M_s were 370 °C and 90 °C, respectively [259]. The corresponding T_0 and T_0' lines are depicted in figure 6.3(b). The selected composition lies outside the range of mucg83 [241], predictions were nevertheless made: $B_s = 340$ °C and $M_s = 263$ °C with the predicted TTT curve given in figure 6.3(c). An artificial neural network (section 3.1.5) predicted $M_s = 160 \pm 30$ °C. Although the carbon concentration is lower than in conventional nanocrystalline bainitic steel, but the greatest strengthening is expected from the fine scale of the structure (equation 2.25).

6.2 Cast production

6.2.1 As-cast Alloy 8

A total of 54 kg of Alloy 8 was supplied by ATI Allvac of Monroe, North Carolina, U. S. A. as two bars, cast using a vacuum induction melting – vacuum arc remelting (VIM/VAR) process and then forged with a 7:1 reduction ratio to produce bars with a cross-section 57 mm × 83 mm. Compositions, taken at both the top and the bottom of the cast are given in table 6.2.

	C	Si	Ni	Al	Mo	Mn	others (top and bottom)
Top	0.72	3.88	3.39	1.37	0.20	0.02	Co, Cr, W < 0.01 P < 0.003 B < 90 ppm
Bottom	0.71	3.87	3.40	1.39	0.21	0.02	S < 30 ppm, N 2 ppm

Table 6.2: Measured composition of Alloy 8. Unless otherwise specified, values are in wt%.

The calculated transformation behaviour of Alloy 8, calculated using the average of the measured compositions of the top and bottom of the cast are given

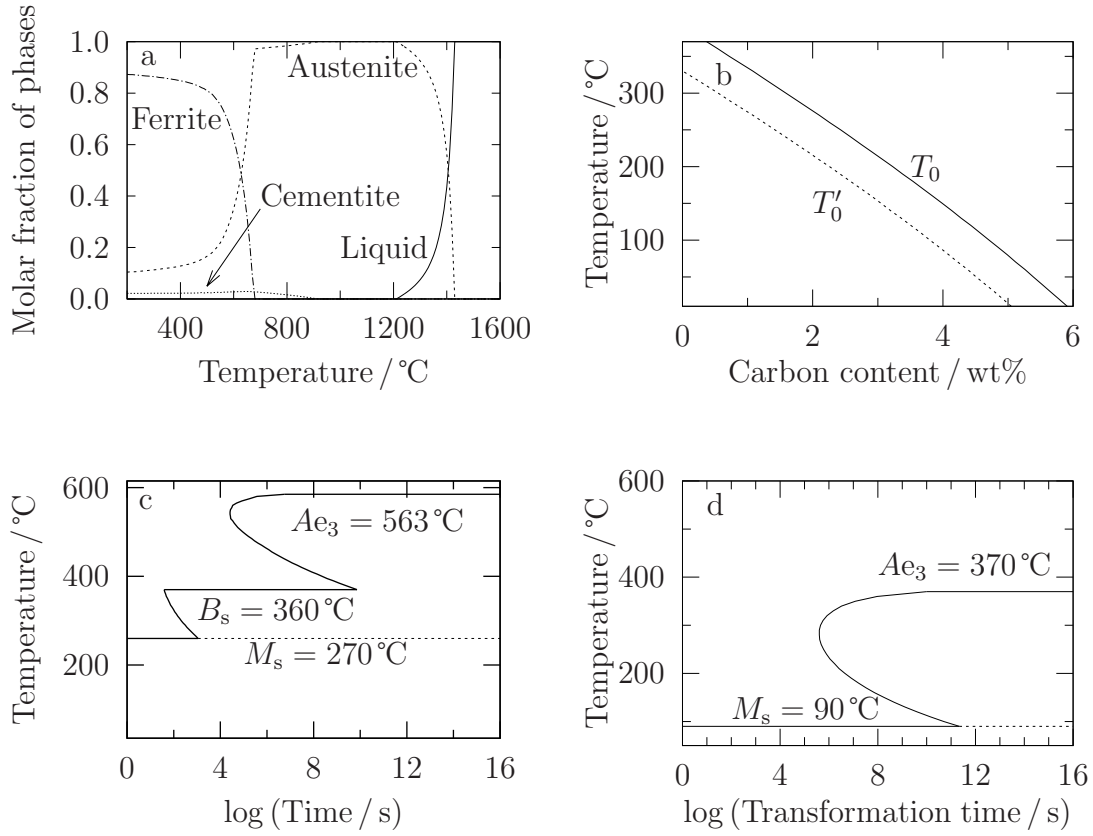

Figure 6.3: (a) calculated equilibrium phase fractions calculated using MTData [26, 199]; (b) T_0 and T_0' lines calculated using MTTTData [199, 254, 259]; and TTT diagrams, calculated using (c) mucg83 [241] and (d) MTTTData for the designed composition of Alloy 9.

in figure 6.4. MTTTData predicts that Alloy 8 is ideal for forming nanostructured bainite, with sufficient hardenability and appropriate B_s and M_s. mucg83. however, predicts that martensite will form below 242 ℃ and the artificial neural network predicts $M_s = 40 \pm 60$ ℃. There is no apparent explanation for this discrepancy and Alloy 8 lies within the composition limits of mucg83 (table 3.1 and there is no reason to be more confident in any one model over the others. M_s will be determined experimentally.

The material was supplied with a microstructure that is a mixture of pearlite and allotriomorphic ferrite (figure 6.5). Sections in various orientations in the as-received bar revealed the microstructure to be visually isotropic. The coarse regions of pearlite probably formed at the early stages of cooling, followed by fine pearlite at lower temperatures. The hardness, averaged over ten points, was 453 ± 5 HV30.

6.2.2 As-cast Alloy 9

A vacuum induction melted alloy was produced by TATA Steel U. K. and was supplied as both plates (120 mm × 20 mm × 600 mm) and rods (≈ 25 mm diameter, 600 mm length), the composition determined at the foundry after production is given in table 6.3. The calculated equilibrium phase fractions for the measured composition, including an ordered BCC phase to represent NiAl, are given in figure 6.6(a). The calculated transformation properties of the composition of the cast are given in figure 6.6(b) and 6.6(c).

C	Mn	Ni	Al	Mo	Co	N	Others > 0.01 wt%
0.45	0.15	13.20	2.63	0.3	3.99	23 ppm	0.06 Cu, 0.03 Si

Table 6.3: Composition of Alloy 9. Unless stated, values are wt%.

The as-received microstructure is martensitic (figure 6.7). EDX performed using a FEI Nova NanoSEM with an accelerating voltage of 20 keV revealed that the bright regions were solute enriched (table 6.4). The solute-deficient dark regions probably formed first during casting, rejecting solute into the remaining melt. The

solute-rich region has a predicted M_s 50 °C lower than the solute-deficient regions [265, 269], thus giving a retained austenite content of 83 vol.%, according to the Koistinen-Marburger relation [303]. The solute-deplete regions are calculated to possess 70 vol.% retained austenite. The hardness, measured using an ATM Qness 30+ automatic indenter and averaged over five indents in each type of region, was measured to be in the 677 ± 7 HV1 dark areas and 663 ± 8 HV1 in the bright, consistent with a higher fraction of martensite in the former.

	Al	Co	Ni	M_s / °C
Bulk	2.63	13.20	3.99	
Bright	2.70 ± 0.16	4.59 ± 0.16	13.5 ± 0.4	130 ± 40 °C
Dark	2.43 ± 0.14	4.69 ± 0.15	11.8 ± 0.3	180 ± 30 °C

Table 6.4: Compositions (wt%) of bright-etching and dark-etching (observed by optical microscopy) regions in as-received Alloy 9. All solutes are enriched in the bright-etching regions, but nickel is significantly more enriched than aluminium and cobalt. This suppresses M_s and results in larger retained austenite grains, giving the brighter appearance.

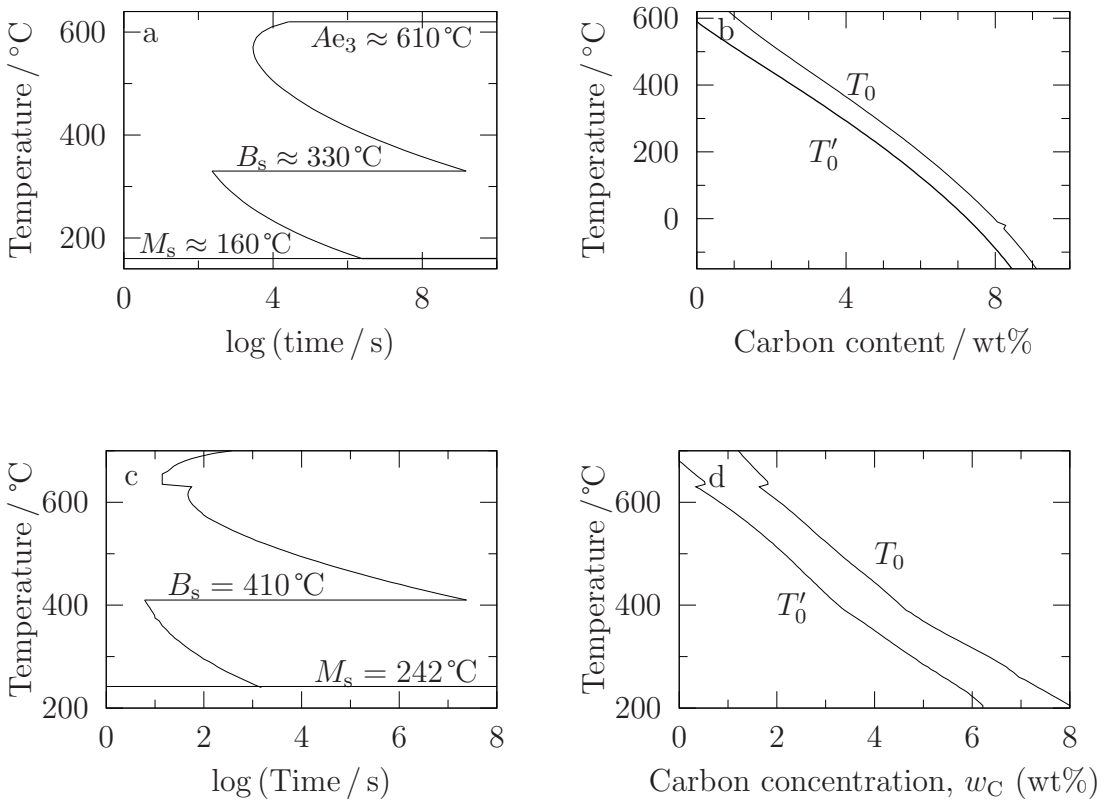

Figure 6.4: Calculated transformation properties for the composition of as-received Alloy 8 cast: (a) TTT and (b) T_0 curves calculated using MTTTData [199, 254, 259] — the calculations predict that bainite will form in the desired range of 200 °C – 300 °C and that bainite will form without the need for rapid cooling. (c) TTT and (d) T_0 curves calculated using mucg83 [241] — he calculations predict that martensite will form below 242 °C and that reconstructive transformations could begin after ~ 10 s.

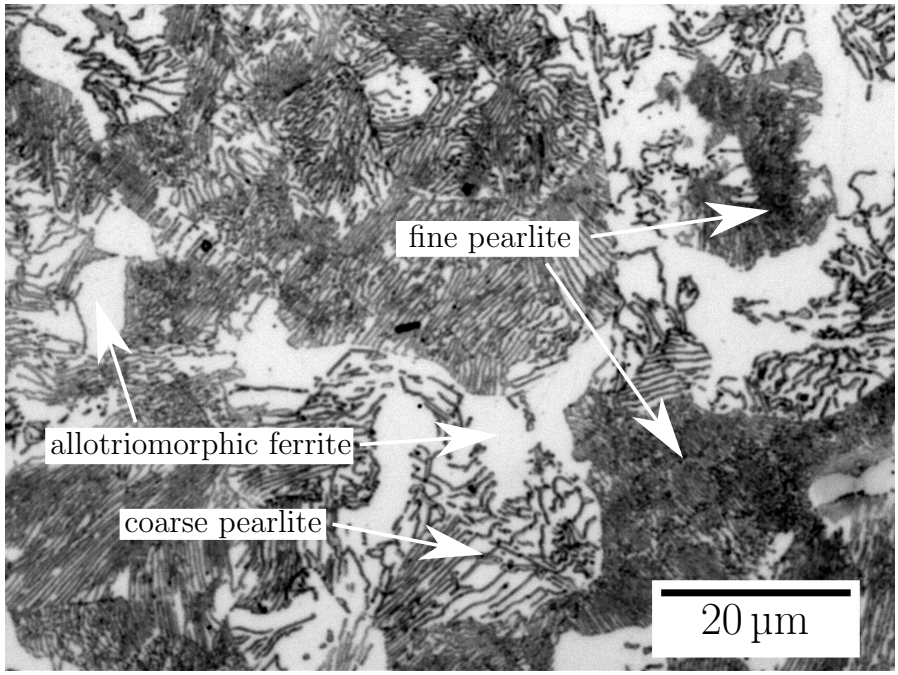

Figure 6.5: Alloy 8 in the as-received condition. The bright areas are allotriomorphic ferrite, which presumably formed first during final cooling, followed by pearlite.

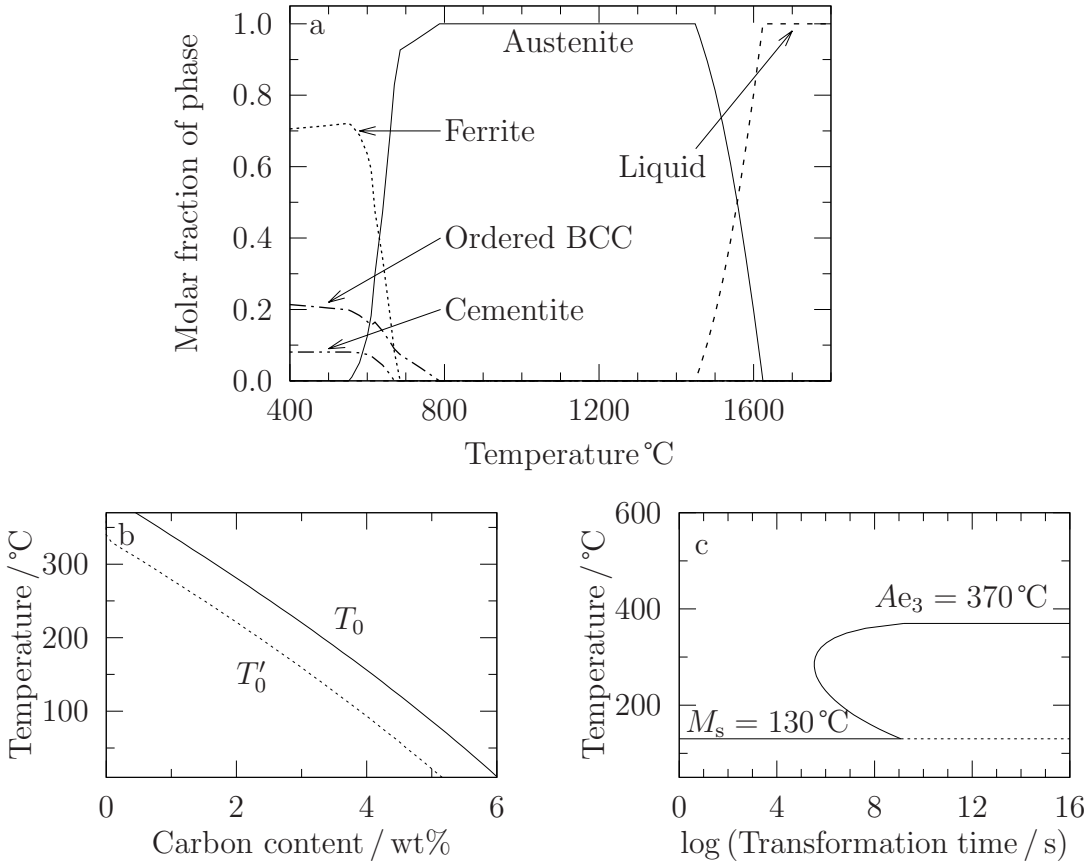

Figure 6.6: (a) equilibrium phase fractions calculated using MatCalc [247, 293]; (b) T_0 and T_0' lines and (c) TTT curve calculated using MTTTData [199, 254, 259] for the experimentally-measured composition of the Alloy 9 cast.

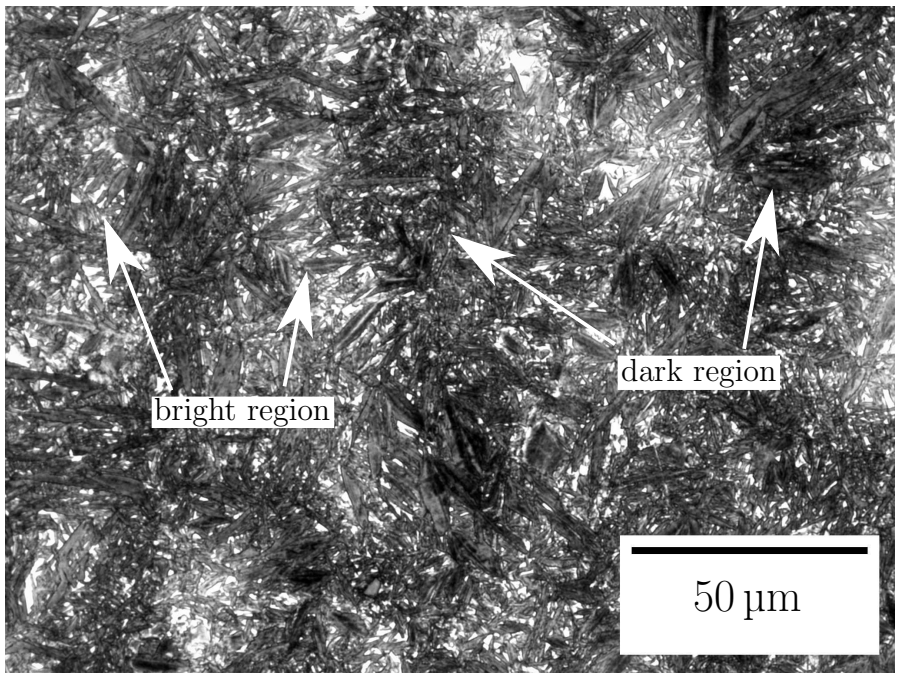

Figure 6.7: Optical micrograph of Alloy 9 in the as-received condition. The structure is fully martensitic but displays two distinct types of region, one dark and one bright.

Chapter 7

Phase transformations of optimised alloys

Experiments were performed to assess the transformation characteristics of Alloys 8 and 9.

7.1 Initial experiments

Samples measuring approximately 70 mm × 30 mm × 8 mm were separately heated to 1000 °C for 30 min in a tube furnace containing an argon atmosphere. Following austenitisation, the samples were isothermally transformed at 300 °C, predicted to lead to bainite formation. Three different cooling rates to the transformation temperature were investigated:

- Samples wrapped in stainless steel foil ("foil cooled");
- Bare samples ("free-air cooled");
- Bare samples agitated in air ("force cooled").

The resulting cooling profiles are given in figure 7.1. Examination of the foil-wrapped samples revealed a mixture of allotriomorphic ferrite and pearlite

(figure 7.2) whereas the free-cooled sample showed a predominantly bainitic microstructure with a small amount of allotriomorphic ferrite (figure 7.3. There was no significant difference between free air-cooled and force-cooled samples, consistent with the similar cooing rates (figure 7.1).

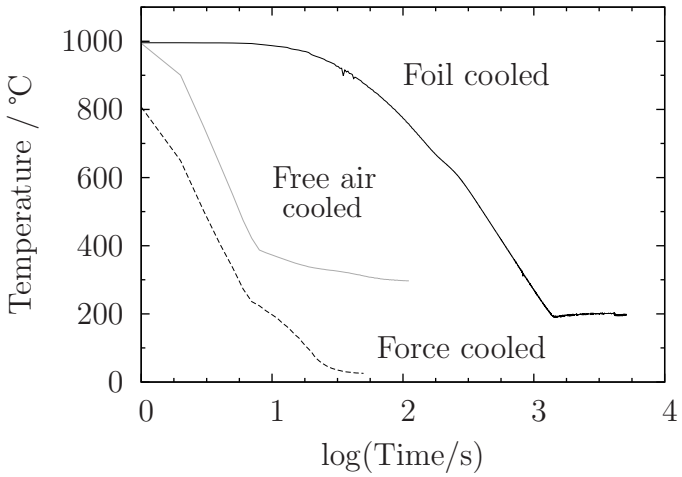

Figure 7.1: Comparison of cooling rates achieved in Alloy 8 using different cooling methods. The cooling rate is very similar in both the "free air cooled" and "force cooled" samples but is orders of magnitude slower in the foil-wrapped sample.

Comparison of the measured cooling curves with the calculated TTT curves for Alloy 8 suggests that mucg83 provides more accurate predictions than MTTTData (figure 7.4[1]). The calculations of mucg83 suggest that the cooling curve for a wrapped sample intersects the upper C-curve of the TTT diagram, whereas that for a free cooled sample does not. MTTTData, however, incorrectly indicates that cooling in foil could form bainite.

Alloy 9 should have a greater hardenability than Alloy 8 (figure 6.6(c) cf. figure 6.4(a)), consistent with the observation that a wrapped sample of the former did not exhibit reconstructive transformation products (figure 7.5). The microstructure after transformation at 200 °C for 10 d consists of large regions of

[1] Superposition of the measured cooling curves onto TTT curves is an approximation. Strictly, the cooling data should be overlaid onto CCT curves.

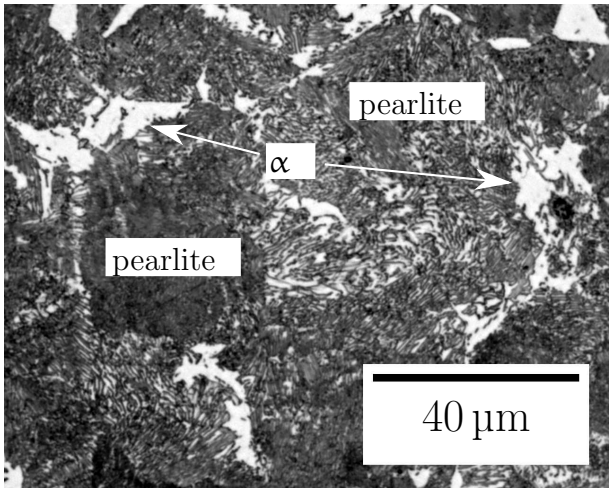

Figure 7.2: Mixture of allotriomorphic ferrite and pearlite formed by cooling Alloy 8 from 1000 ℃ in stainless steel foil.

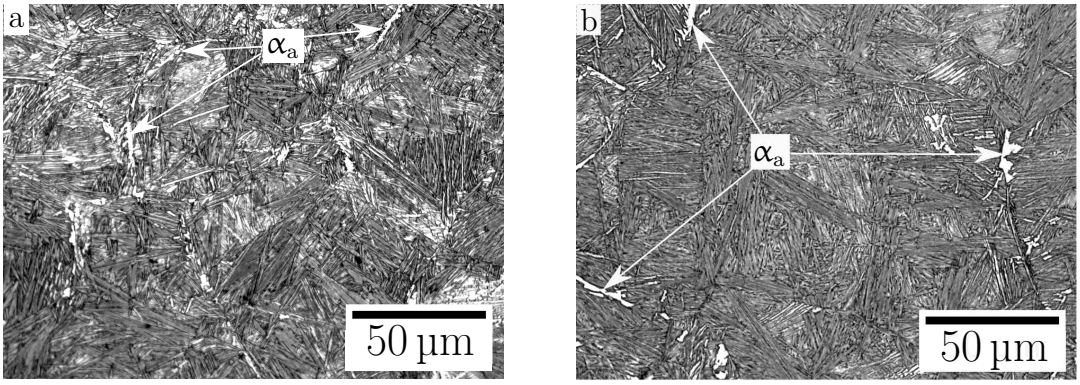

Figure 7.3: Microstructures of Alloy 8 after austenitisation at 1000 ℃ and (a) "free-air cooling" and (b) "force cooling" to an isothermal hold at 300 ℃. Both exhibit a largely bainitic microstructure with a small amount of allotriomorphic ferrite (α_a) at prior austenite grain boundaries.

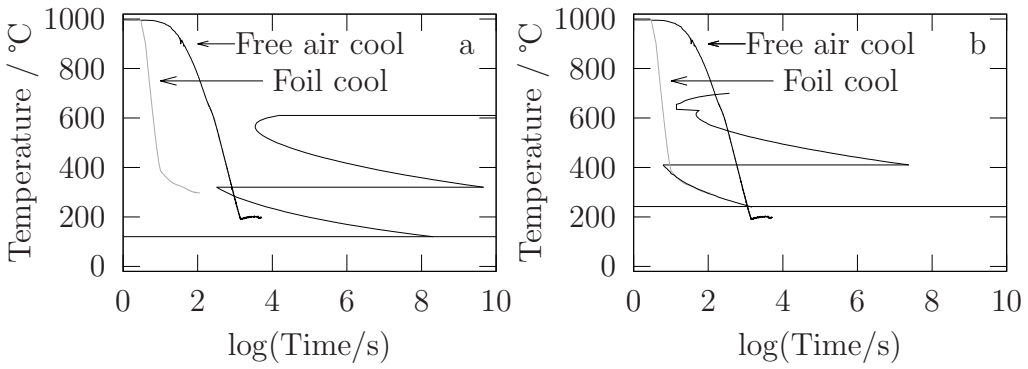

Figure 7.4: Comparison of measured cooling curves and TTT-diagrams calculated by (a) MTTTData and (b) mucg83.

bainite with small regions of martensite in between, formed from the untransformed blocky austenite (figure 7.5) it is evident that martensite forms in between the bainite plates, in what was blocky austenite during the isothermal hold. Thus, M_s in Alloy 9 is below 200 °C.

The instability of the austenite blocks to martensite formation indicates that little carbon enrichment has occurred. This is consistent with the large nickel content of Alloy 9 and is reflected in the predicted $x_{T_0'}$: ≈ 2 wt% at 200 °C (figure 6.6). For comparison, the same quantity in Alloy 8 is ≈ 5 wt%.

7.1.1 M_s temperature

An experiment in which Alloy 8 was austenitised and force cooled to ambient temperature revealed a change in gradient of the temperature profile at around 240 °C (figure 7.6), corresponding to the martensitic transformation (figure 7.7). This is in excellent agreement with the predicted $M_s = 242$ °C using mucg83.

7.1.2 Transformation kinetics of Alloy 8

Samples of Alloy 8 were austenitised at 1000 °C for 30 min, cooled in air and transformed at 300 °C, 250 °C or 200 °C for various times and exhibited the hardness

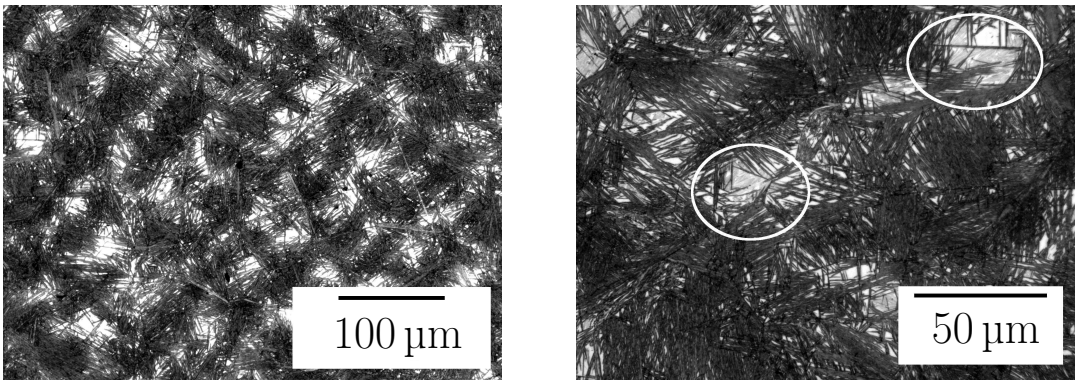

Figure 7.5: Bainitic structure formed in a wrapped sample of Alloy 9 after austenitisation and isothermal holding at 200 °C for 10 d. Highlighted regions contain martensite plates.

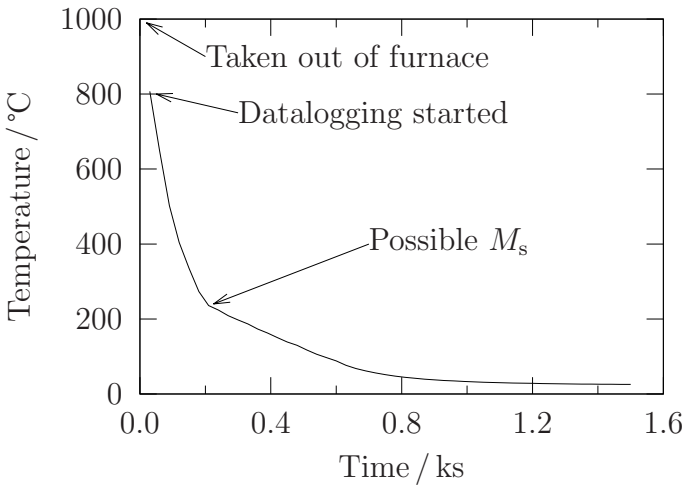

Figure 7.6: Temperature-time profile for sample cooled in air after austenitisation, showing a sudden change in gradient at approximately 240 °C.

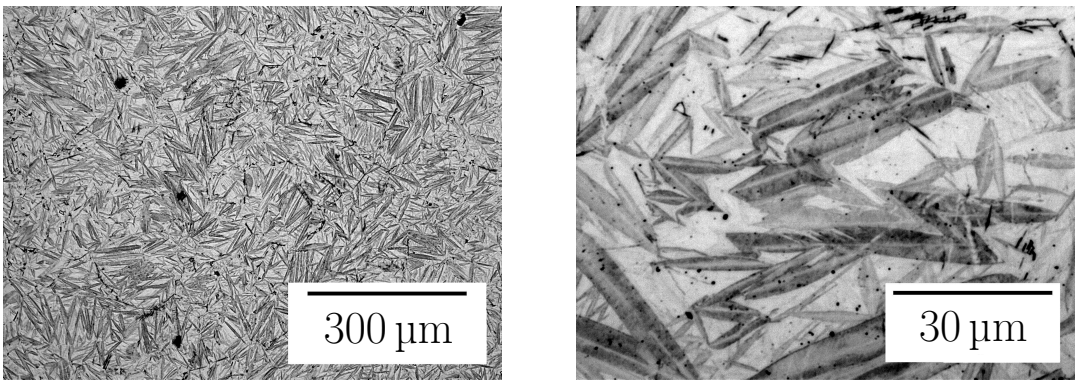

Figure 7.7: Martensitic structure formed in Alloy 8 cooled in air from 1000 ℃ to ambient temperature.

presented in figure 7.8. The hardness becomes constant after no more than 1 d at all temperatures, implying that the microstructure stops evolving. Lower transformation temperatures lead to higher hardness, consistent with a finer bainitic structure.

The samples transformed at 250 ℃ and 300 ℃ exhibited the expected mixture of bainitic ferrite and retained austenite (figure 7.9). The samples transformed at 200 ℃, however, consisted of a mixture of large martensite plates and bainite. The martensite plates are much larger than the bainite and have formed in classical self-accommodating zig-zag arrangements (figure 7.10). Many martensite plates extend to the prior austenite grain boundaries, implying that they formed first upon cooling from the austenitising temperature and that bainite subsequently grew between them. 200 ℃ must therefore be below M_s. Repeating this transformation yielded identical results. Therefore 200 ℃ $< M_s <$ 250 ℃, consistent with the recalescence observed during cooling (figure 7.6) and the predictions of mucg83 (figure 6.4(c)).

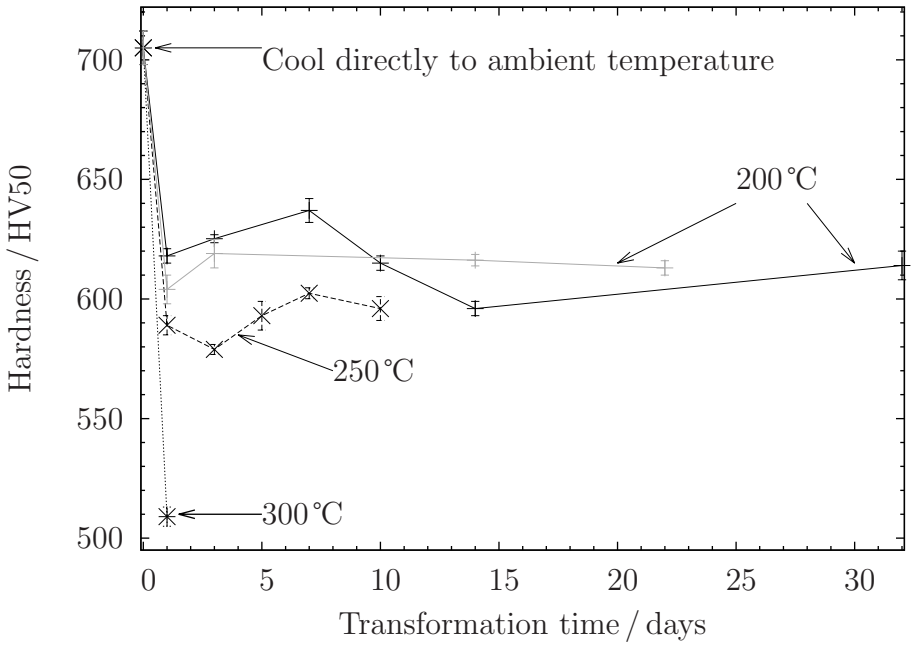

Figure 7.8: Hardness evolution in Alloy 8 after austenitisation at 1000 °C for 30 min and cooling in air without foil or agitation.

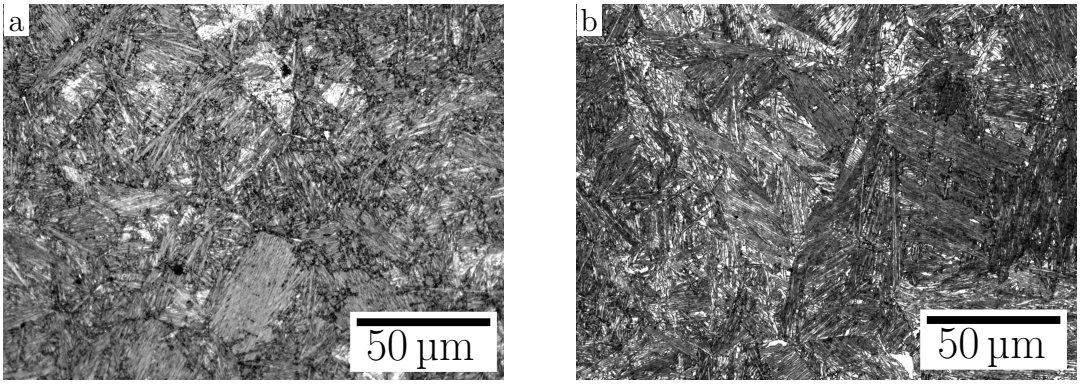

Figure 7.9: Microstructures in Alloy 8 after austenitisation at 1000 °C for 30 min and forced cooling to isothermal holding for 24 h at (a) 250 °C and (b) 300 °C. Both temperatures result in bainitic microstructures.

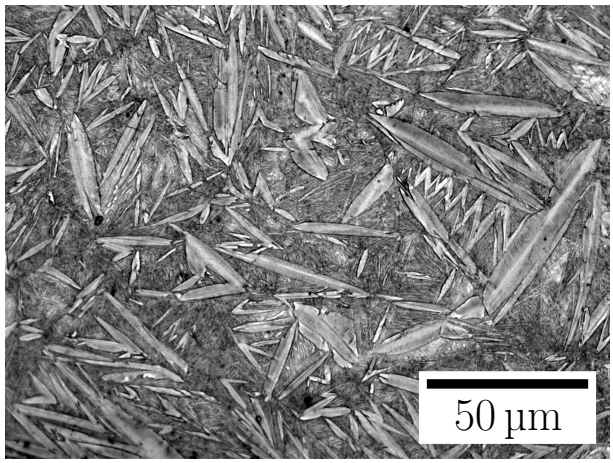

Figure 7.10: Microstructure in ALLVAC after austenitisation at 1000 °C for 30 min and forced cooling to isothermal holding at 200 °C for 24 h. There are large martensite plates with bainite between. The martensite plates clearly form first.

7.2 Dilatometric study of phase transformations

A thorough study of the phase transformations in both Alloy 8 and Alloy 9 was performed in a Thermecmastor-Z thermomechanical simulator, using cylindrical samples of 8 mm diameter and 12 mm length. Any surface oxide was removed using silicon carbide paper. Specimens were heated under vacuum and the temperature was measured using a R-type thermocouple spot-welded onto the sample surface. The sample diameter was continuously measured using a laser accurate to approximately ±5 µm.

All samples were identically heated at 10 °C s^{-1} to 1000 °C where they were held for 30 min. This was followed by either isothermal transformation or continuous cooling to ambient temperature, as listed in table 7.1. Based on figure 7.8, isothermal transformations were assumed to finish within 24 h. This was ultimately found to be correct. Cooling was achieved using (>99.9%) helium gas.

Alloy 8								
Temperature / °C	800	750	700	650	600	650	600	550
Hold time / h	4.5	3.0	3.0	5.0	5.5	6.5	5.25	6.5
Temperature / °C	500	450	400	350	320	300	275	250
Hold time / h	3.5	12.0	12.0	12.0	4.0	12.0	6.0	12.0
Temperature / °C	20	20	20	20				
Cooling rate / °C s^{-1}	20	10	5	2				
Alloy 9								
Temperature / °C	600	450	350	300	250	250		
Hold time / h	10.0	14.0	18.5	18.0	18.0	120		
Temperature / °C	20							
Cooling rate / °C s^{-1}	10							

Table 7.1: Transformation conditions implemented in dilatometry experiments.

7.2.1 Experimental determination of martensite start temperature

An experiment using a Linseis DIL805A/D dilatometer with cryogenically-cooled helium as a quenching medium in which Alloy 8 was austenitised and then cooled to determine, using the offset method [288], $M_s = 246\,℃$ for cooling at both $10\,℃\,s^1$ and $50\,℃\,s^1$. This is in good agreement of the prediction of mucg83. Due to the noise in subsequent measurements taken using the Thermecmastor-Z thermomechanical simulator, a volume fraction of 0.05 was used to identify the onset of non-martensitic phase changes in Alloy 8 (section 7.3). For consistency with these data, the M_s was also derived assuming this detection limit and is 233 ℃. Cooling at $10\,144℃\,s^{-1}$ results in the formation of martensite only while cooling at lower cooling rates also leads to the formation of allotriomorphic ferrite. (figure 7.12).

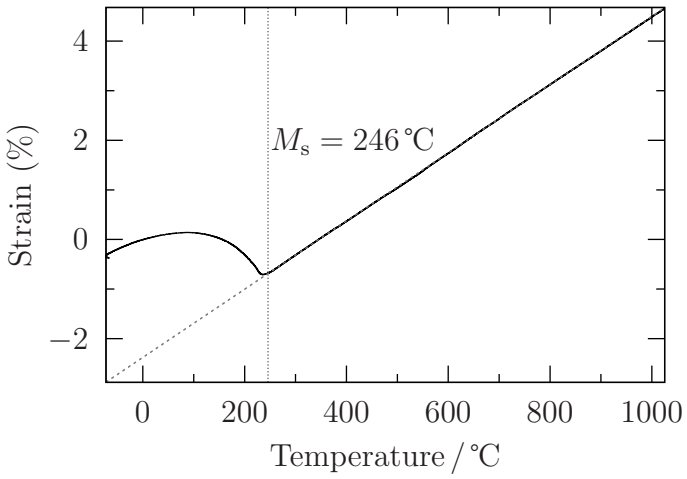

Figure 7.11: Dilatational strain in Alloy 8 cooled at $10\,℃\,s^{-1}$ in a TA Instruments DIL805A/D dilatometer with M_s according to the offset method with 5 vol.% transformation [288].

Austenitising Alloy 9 and cooling at $10\,℃\,s^{-1}$ avoids reconstructive transformations and leads to $M_s = 144\,℃$ using the offset method (figure 7.13).

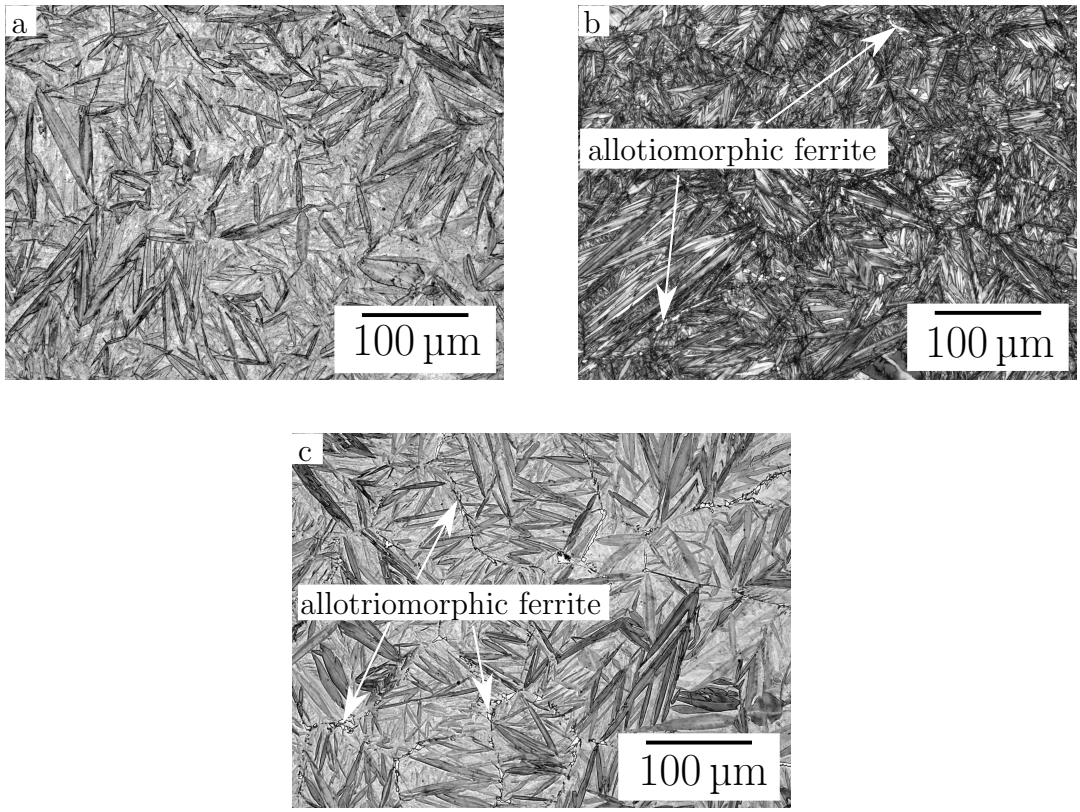

Figure 7.12: Martensitic structure formed in Alloy 8 cooled to ambient temperature at (a) $10\,^{\circ}\mathrm{C\,s^{-1}}$, (b) $5\,^{\circ}\mathrm{C\,s^{-1}}$ and (c) $2\,^{\circ}\mathrm{C\,s^{-1}}$. Cooling at $10\,^{\circ}\mathrm{C\,s^{-1}}$ results in no visible allotriomorphic ferrite. Allotriomorphic ferrite does form at the lower cooling rates.

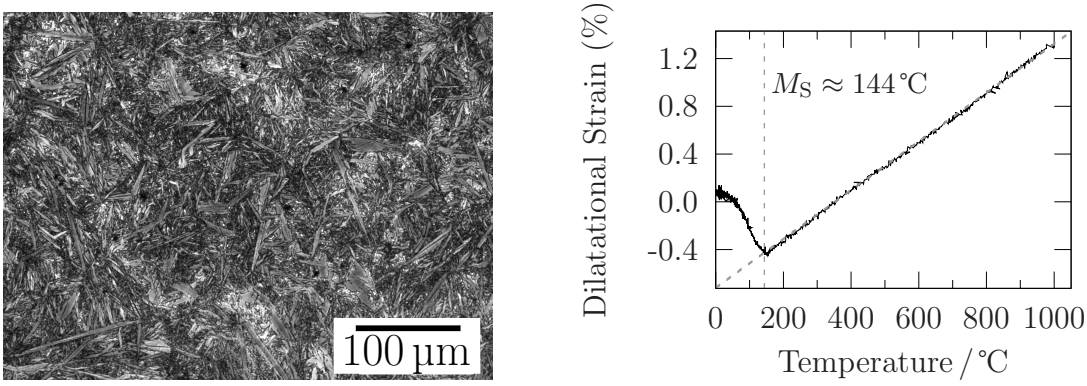

Figure 7.13: (a) microstructure and (b) dilatational strain profile of Alloy 9 austenitised and then cooled at $10\,℃\,s^{-1}$ to ambient temperature. Reconstructive transformations are avoided and the structure is martensitic.

7.3 Dilatometric assessment of transformation kinetics

Samples were heated in the Thermecmastor-Z thermomechanical simulator at $10\,℃\,s^{-1}$ to 1000 ℃ for 30 min, cooled at $10\,℃\,s^{-1}$ to a target temperature and allowed to isothermally transform, according to the conditions in table 7.1. Figures 7.12(a) and 7.13(a) show that reconstructive transformations are avoided under these conditions.

To determine a transformation start time, the dilatational strain of each sample was analysed and the transformation was taken to start when the strain had increased by 5% of the net change during the isothermal hold (figure 7.14). This time represents the onset of transformation on the TTT diagram. The time is set to zero when the isothermal transformation temperature is reached.

The derived transformation start times for Alloy 8 are given in figure 7.15. Transformations measured in Alloy 8 are rapid: an order of magnitude shorter than previous bulk nanocrystalline bainitic steels [e.g. 1, 107, 108]. This is due to the lack of manganese, which reduces transformation driving force. Figure 7.16(a) shows that mucg83 predicts a shorter transformation time than is measured exper-

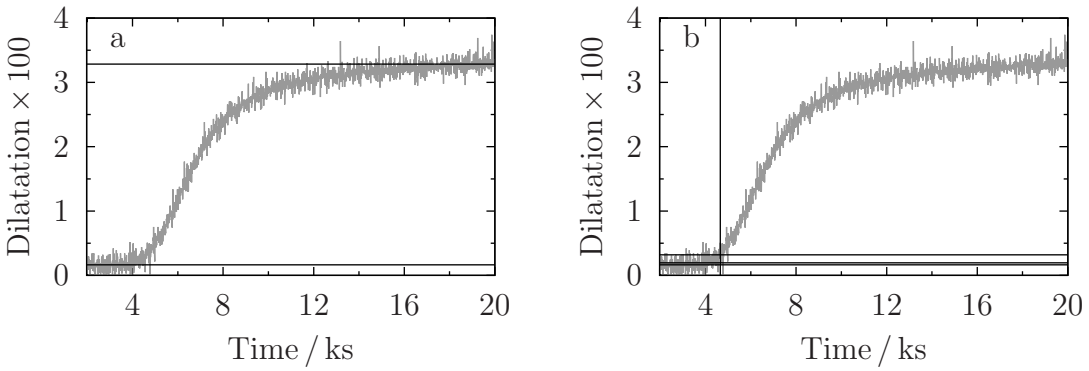

Figure 7.14: Alloy 8 cooled to 250 ℃ after austenitisation. (a) horizontal lines are fitted to the beginning and end of the dataset and (b) intersection of the 5% horizontal lines with the data allow the transformation start time to be estimated to reasonable accuracy.

imentally. MTTTData predicts transformation times many orders of magnitude longer than are measured.

Alloy 9 was found to have slower transformation kinetics than Alloy 8, consistent with calculations (figure 6.6 cf. figure 7.15). Due to the slower kinetics and the narrower temperature range over which transformations were predicted to occur (figure 6.3(a)), fewer isothermal transformation temperatures were investigated. Comparisons of measured data with a TTT diagram calculated using MTTTData is given in figure 7.16(b).

7.4 Transformation microstructures

7.4.1 Alloy 8

Experimental assessments of the transformation products in Alloy 8 are presented in figure 7.17, 7.19 and table 7.2.

X-ray diffraction samples were prepared as optical microscopy samples, but after initial polishing to 1 µm were etched lightly in nital and then repolished with

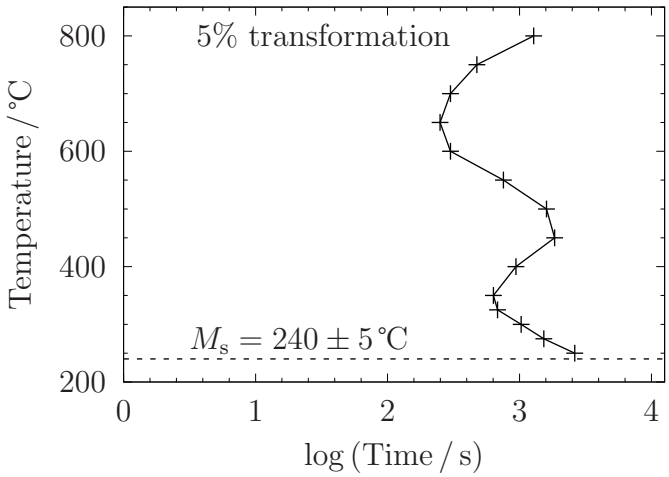

Figure 7.15: Assessed TTT diagram for Alloy 8 based on the times required for the transformation at each temperature to proceed to 5% of maximum.

1 µm diamond paste. This etch-and-polish was repeated three times with progressively gentler polishing and etching. This minimises any strain present in the surface layer. This is vital as X-rays from a copper target (K_α transitions, photon energy ≈ 8 keV) penetrate less than 10 µm into the surface of steel (figure 7.20).

X-ray diffraction experiments used a Bruker DaVinci D9 diffractometer equipped with a variable-width slit to ensure illumination across 10 mm of the sample surface throughout the entire experiment. The sample was rotated at 30 rpm about an axis normal to its surface. The diffracted X-rays were measured using a Lynx-Eye position-sensitive detector with 192 channels covering a range of 3.4° in 2θ. The detector was scanned through a range of $35° < 2\theta < 130°$ with a step size of 0.01° and a dwell time of 0.5 s. An energy discriminator was used to select only X-rays of energy $0.210 \leq E\,/\,\text{eV} \leq 0.226$. This greatly reduces the signal of X-ray fluorescence from iron and nickel atoms and substantially reduces background noise.

The data were converted to simulate a fixed beam size using Bruker DIFFRAC.SUITE EVA software. Fixed sample illumination ensures that the same area is measured at all angles, but necessarily results in a larger total flux of X-rays being incident on the sample at higher angles than if the beam has constant size. As a consequence,

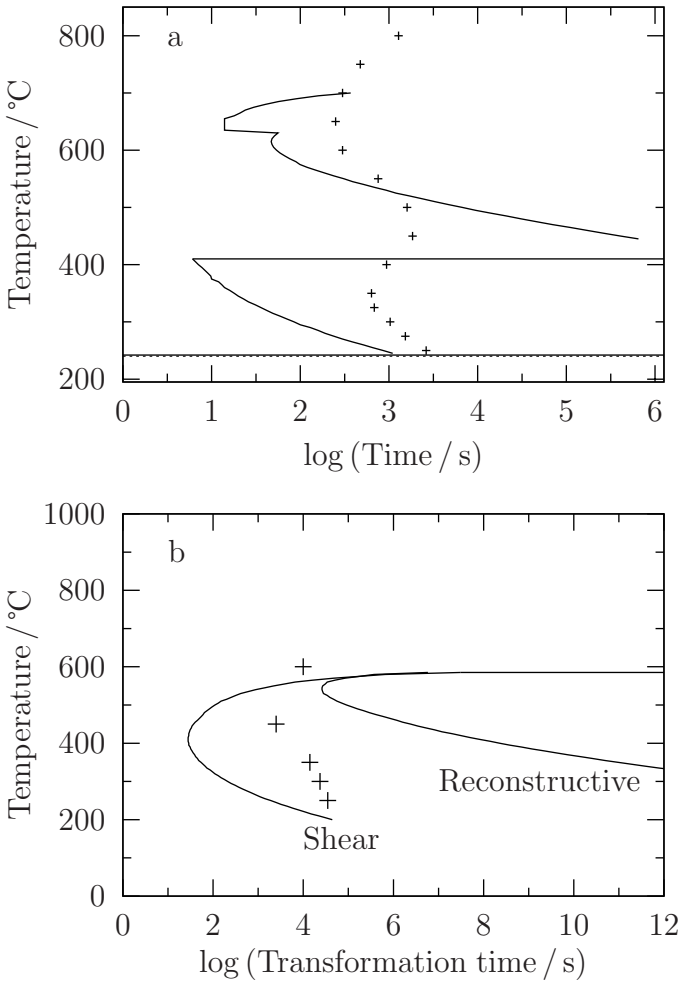

Figure 7.16: Comparison of experimentally-measured transformation start times (points) and those calculated (lines) for (a) Alloy 8 compared to predictions of mucg83 and (b) Alloy 9 compared to the predictions of MTTTData. No B_s is predicted for Alloy 9, so both reconstructive and shear curves are shown for all temperatures for comparison to the measured data.

both background and diffraction peaks are stronger at higher angles. Rietveld analysis was performed, as described in section 4.3. Instrument broadening was calibrated using a NIST 660 LaB_6 standard [304].

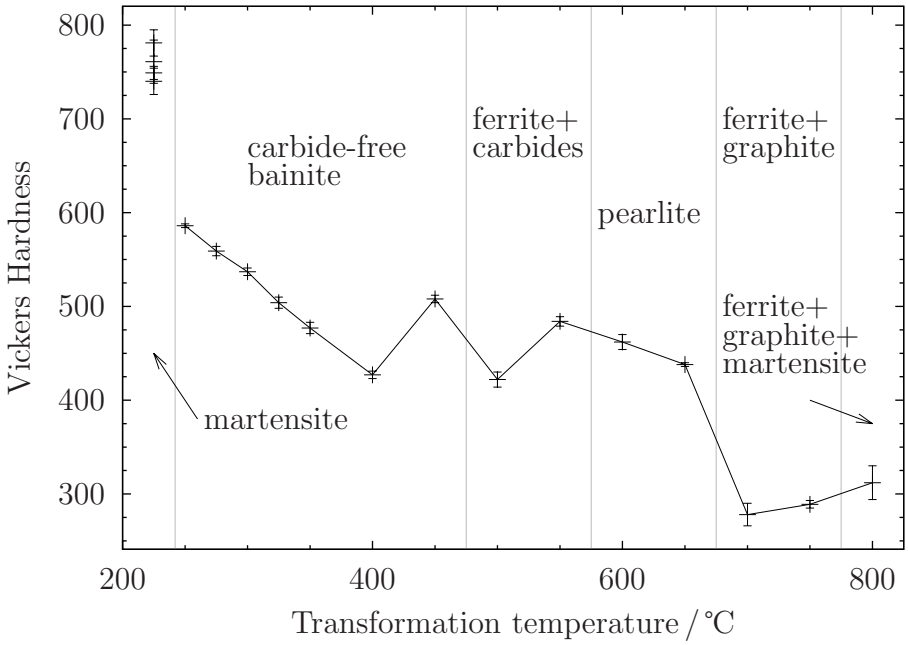

Figure 7.17: Hardness and assessed microstructure for isothermal transformation of Alloy 8. The points in the "martensite" region were from samples that had been quenched in water to room temperature.

Temperature / ℃	Transformation Start Time / s	Microstructure	Hardness HV30
800	1280	Ferrite, graphite, martensite	297 ± 13
750	475	Ferrite, graphite	289 ± 4
700	300	Ferrite, graphite	272 ± 55
650	250	Ferrite, cementite	429 ± 2
600	300	Ferrite, cementite	464 ± 8
550	755	Ferrite, cementite, ε	481 ± 2
500	1600	Bainite, austenite, cementite, ε	414 ± 11
450	1845	Bainite, austenite, cementite, ε	508 ± 4[2]
400	940	Bainite, retained austenite	420.8 ± 1.9
350	635	Bainite, retained austenite	476 ± 2
325	680	Bainite, retained austenite	504.6 ± 1.5
300	1030	Bainite, retained austenite	537 ± 5
275	1530	Bainite, retained austenite	552 ± 5
250	2625	Bainite, retained austenite	582 ± 3
$2\,℃\,s^{-1}$	N/A	Martensite, allotriomorphic ferrite	720 ± 9[3]
$5\,℃\,s^{-1}$	N/A	Martensite, allotriomorphic ferrite	700 ± 10
$10\,℃\,s^{-1}$	N/A	Martensite	720 ± 15
$20\,℃\,s^{-1}$	N/A	Martensite	741 ± 2

Table 7.2: Overall microstructures formed in Alloy 8 and associated hardness data. The microstructure was assessed using a combination of optical and electron microscopy and X-ray diffractometry. All hardness data are the average of five points and the standard deviation in the hardness data are quoted a the uncertainties.

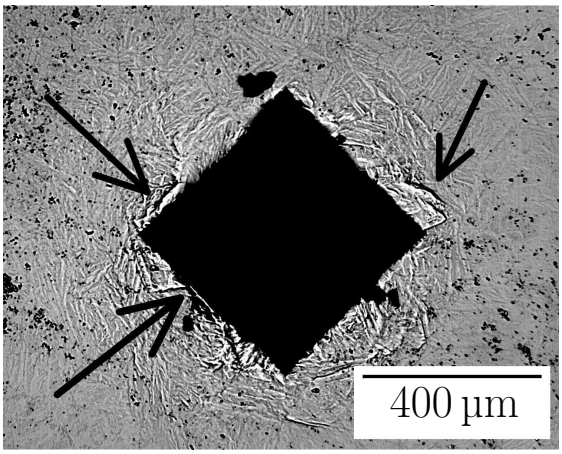

Figure 7.18: Surface cracks around indent during Vickers hardness testing with 30 kg applied load. This led to the exclusion of these data from the analysis of the microstructure and the hardness measured by applying 10 kg, which did not cause cracking, was used instead.

800 °C

Figures 7.21(a) and 7.21(b) show large equiaxed ferrite grains, together with (dark) spheroidal graphite and martensite. The latter forms from the austenite which is stable at equilibrium with the ferrite and graphite at 800 °C. The large X-ray peaks in figure 7.22(a) are due to both $CuK_{\alpha 1}$ and $CuK_{\alpha 2}$ X-rays, the peaks at 40°, 58°, 73° to CuK_{β} radiation. Rietveld analysis indicates (84 ± 6) vol.% ferrite and (16 ± 6) vol.% martensite. This is consistent with the thermodynamic equilibrium calculations that suggest 76 at.% ferrite, 21 at.% austenite and 3 at.% graphite. It was not possible to detect graphite using X-ray diffractometry, but the microstructural appearance is consistent with graphite observed in cast iron (figure 7.22(b)).

750 °C and 700 °C

Transformation at either 750 °C and 700 °C produced ferrite grains containing a small amount of graphite (figure 7.23(a)), along with pearlite near the edges of

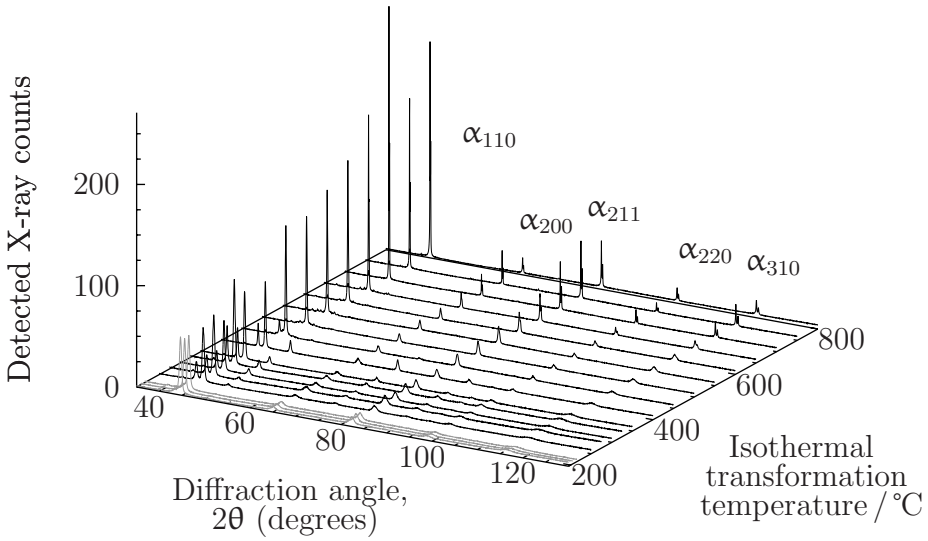

Figure 7.19: X-ray diffractograms of Alloy 8 after isothermal transformation. For clarity, austenite and other peaks are not labelled, but may be seen in figure 7.28.

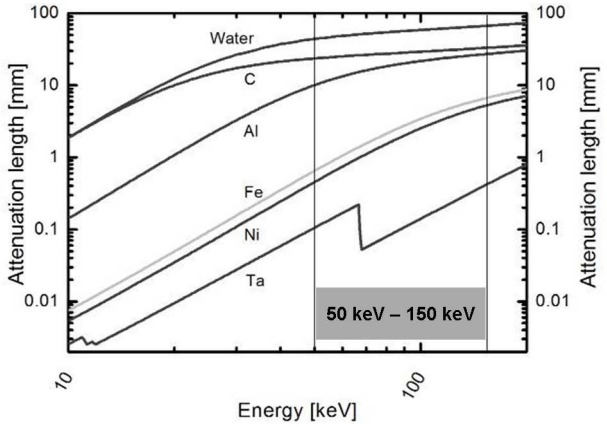

Figure 7.20: Calculated distance for the intensity of X-rays to fall by a factor of e (*attenuation length.*) in common metals [305].

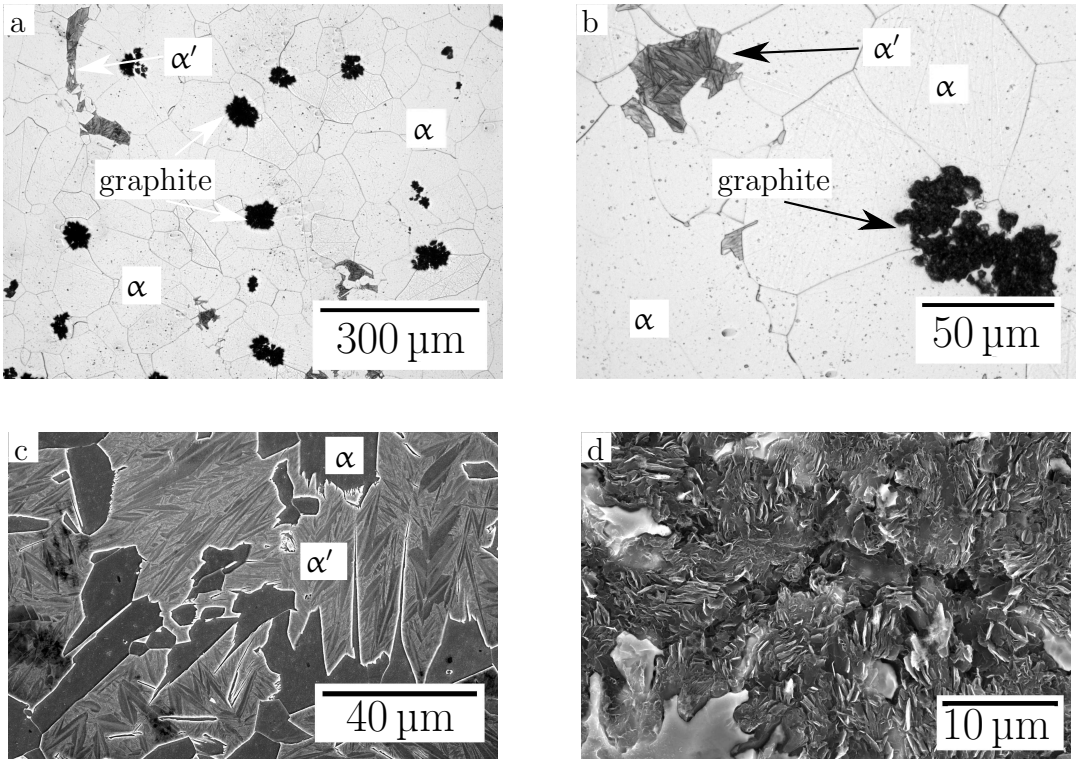

Figure 7.21: Alloy 8 after isothermal transformation at 800 °C for 4.5 h. (a) and (b) optical micrographs. (c) scanning electron micrograph of martensite plates in ferrite and (d) a graphite nodule.

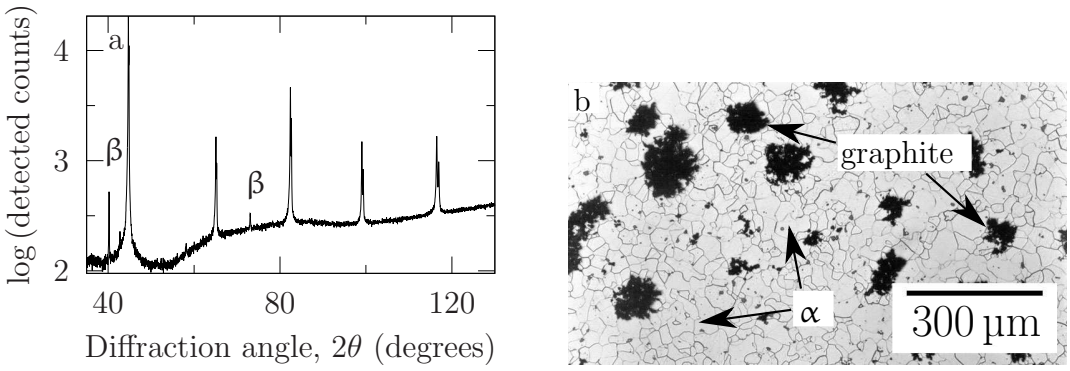

Figure 7.22: (a) XRD data for Alloy 8 transformed at 800 °C, with peaks due to $CuK_{\alpha 1}$, $CuK_{\alpha 2}$ and CuK_{β} radiation. (b) graphite in Fe–2.4 C–1.1 Si–1.1 Mn held at 900 °C for several days to grow graphite nodules [14, micrograph 368].

the sample (figures 7.23(c) and 7.23). Thermodynamic modelling using MTData predicts that cementite can form at temperatures up to 850 °C (figure 5.4), however when graphite is permitted to exist, the calculations predict 3 at.% [26, 199] graphite and cementite is eliminated as a stable phase.

650 °C

Transformation at 650 °C leads to a mixture of pearlite with a small quantity of allotriomorphic ferrite (figure 7.24). If graphite is not included in the calculations, the only phases predicted from thermodynamic modelling are 88 at.% ferrite, 12 at.% cementite and 0.15 at.% molybdenum carbide, Mo_2C. The latter was not detected by XRD or during microscopy, however, it may be that the precipitates are too fine to be readily observed. The diffusion of molybdenum is much slower than carbon and so Mo_2C is unlikely to form during this heat treatment. XRD indicated 11.2 ± 0.3 vol.% cementite with a residue of ferrite, consistent with calculations.

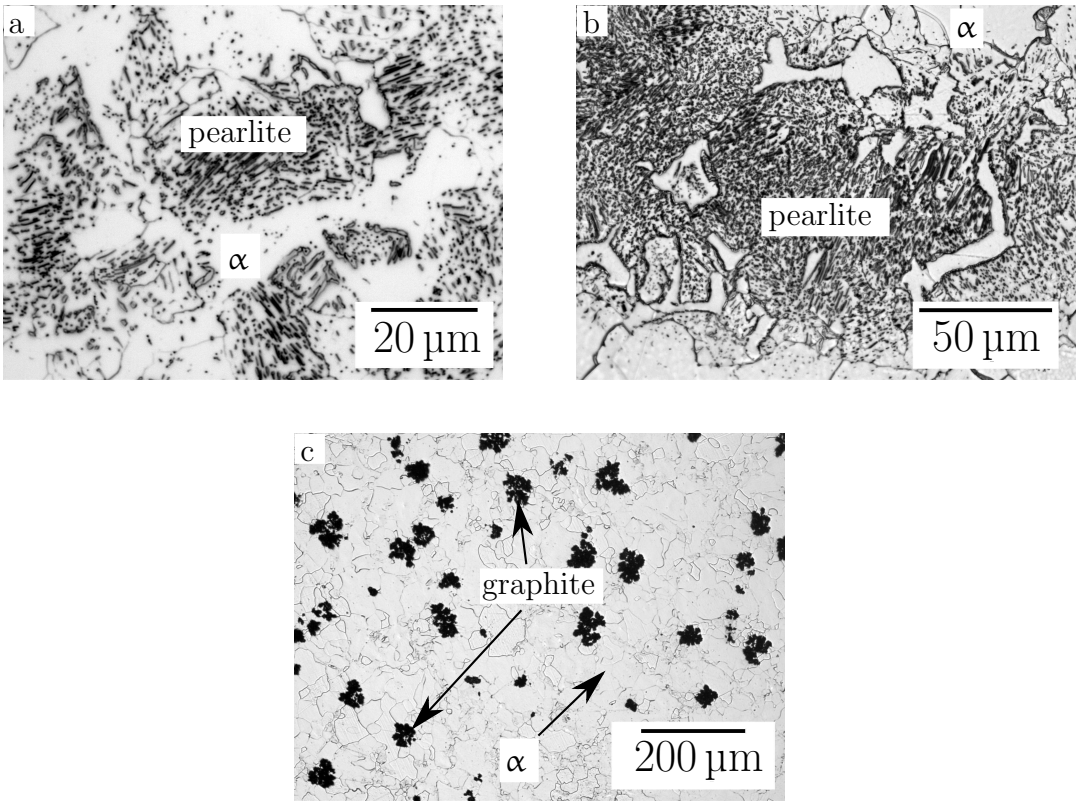

Figure 7.23: Grains near the edge of Alloy 8 isothermally transformed for 3 h at (a) 700 °C and (b) 750 °C. The grain interiors contain pearlite while the grain boundaries are decorated with allotriomorphic ferrite. (c) typical grain near the centre of the samples containing graphite and ferrite. This is presumably due to the slower cooling in the sample interior.

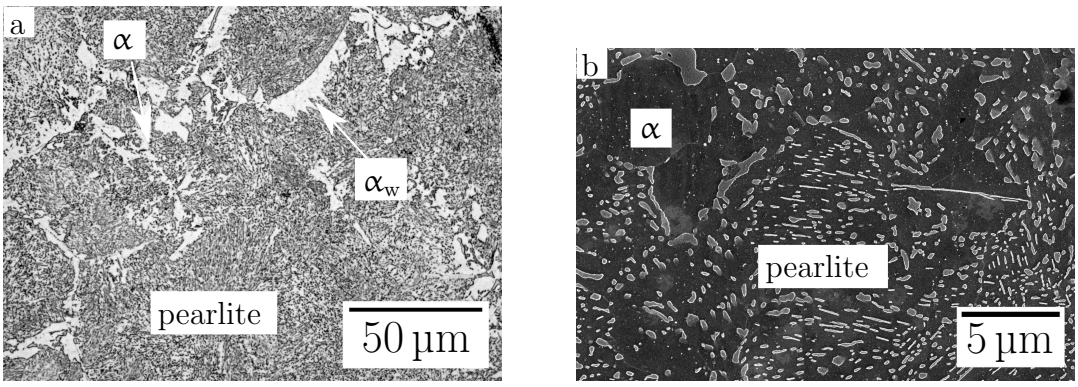

(a) (b)

Figure 7.24: Alloy 8 after isothermal transformation at 650 °C for 5 h. The microstructure consists predominantly of pearlite with Widmanstätten ferrite at prior austenite grain boundaries.

600 °C and 550 °C

A dramatic change occurs when the transformation temperature is reduced to 600 °C (figures 7.25(a) and (b)) or 550 °C (figures 7.25(c) and (d)). Thermodynamic calculations indicate that a small amount of austenite should remain untransformed at both 600 °C and 550 °C, but this is not detected using XRD.

The samples transformed at 600 °C and 550 °C both exhibit similarities to martensite, consisting of spheroidised cementite in ferrite [306]. The ferrite grows from austenite grain boundaries, untransformed austenite transforms to martensite upon cooling from the transformation temperature (figure 7.26). Retained austenite is not expected following holding at either 550 °C or 600 °C. In addition, the phase fractions of cementite and ferrite following Rietveld analysis of XRD data are consistent with those calculated in figure 5.4 with around 88 vol.% ferrite in both cases [4]. The dilatational strain does not become constant before the end of the isothermal hold (figure 7.27(a)), consistent with a transformation in progress. Subsequent isothermal transformation of Alloy 8 at 600 °C for 10 h resulted in a

[4] In this measurement, "ferrite" is the combined fraction of ferrite and martensite, as martensite peaks will coincide with ferrite due to the very similar lattice parameters and crystal structure.

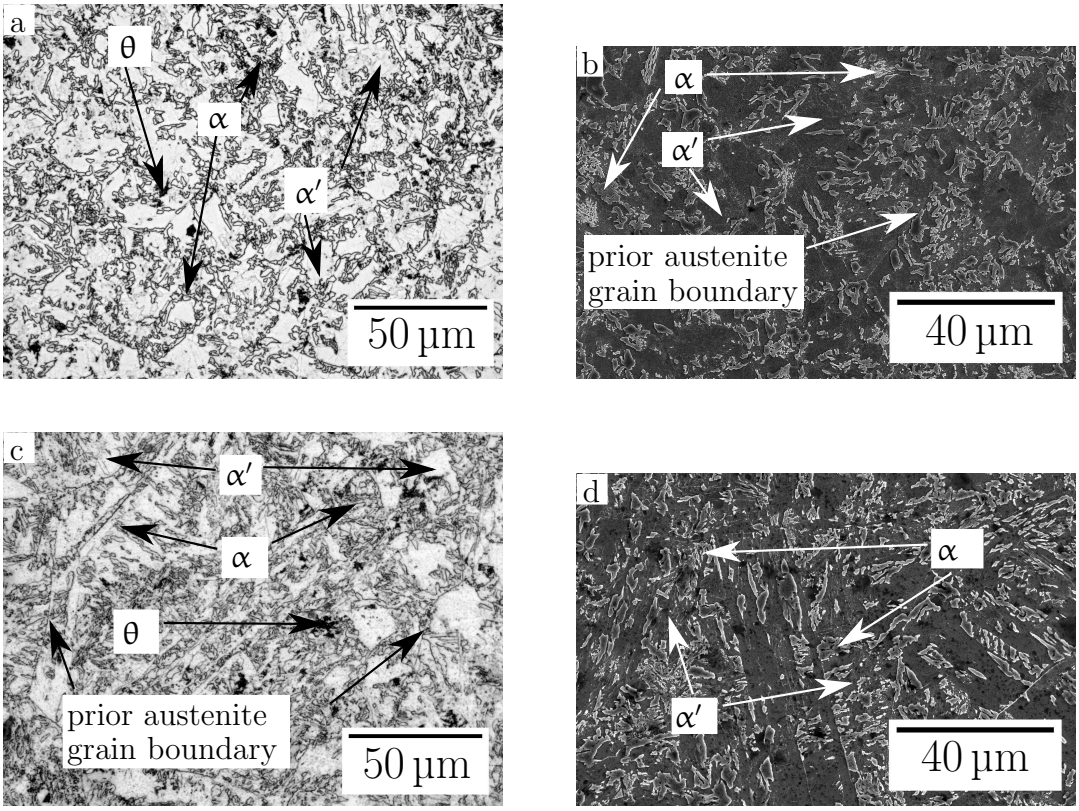

Figure 7.25: Alloy 8 transformed at (a) and (b) 600 °C for 5.5 h; (c) and (d) 550 °C for 6.5 h. The microstructure consists of large ferrite grains formed on prior austenite grain boundaries interspersed with regions of martensite and smaller dark regions of cementite or possibly pearlite.

pearlitic structure with allotriomorphic ferrite at prior austenite grain boundaries (figure 7.27(b)).

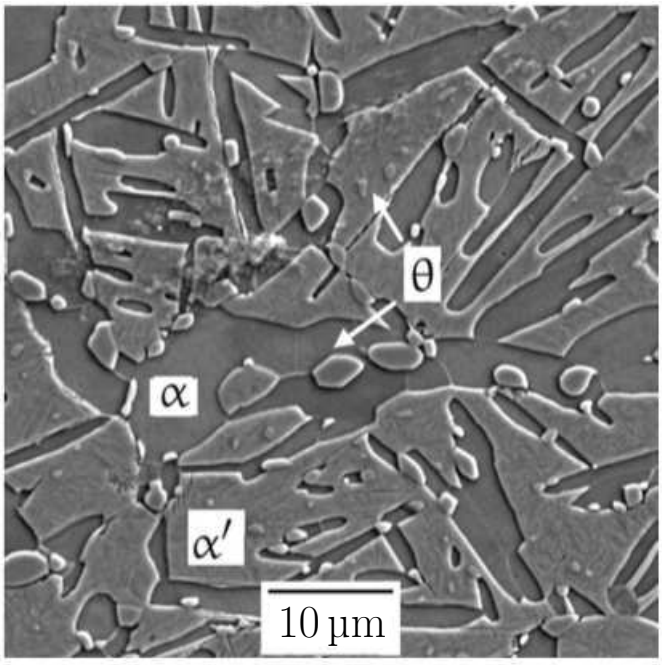

Figure 7.26: Fe–0.78 C–2.02 Mn–1.01 Cr–3.87 Co–1.37 Al–1.6 Si (wt%) tempered at 753 ℃ for 20 d[307, figure 4c]. The morphology of ferrite and martensite grains is similar to that observed in Alloy 8 isothermally heat treated at 550 ℃ and 600 ℃.

500 ℃ – 400 ℃

Transformation between 500 ℃ and 400 ℃ produces plate-shaped ferrite consistent with displacive transformation (figure 7.29). Cementite precipitation is inhibited as the transformation temperature is reduced due to the presence of silicon and aluminium that are increasingly unable to partition [e.g. 78, 162, 171, 308]. Carbon rejected from the transforming austenite is therefore dissolved in untransformed austenite, stabilising it with respect to ferrite. Some austenite is then retained to ambient temperature (figure 7.28). This effect is complete below 450 ℃.

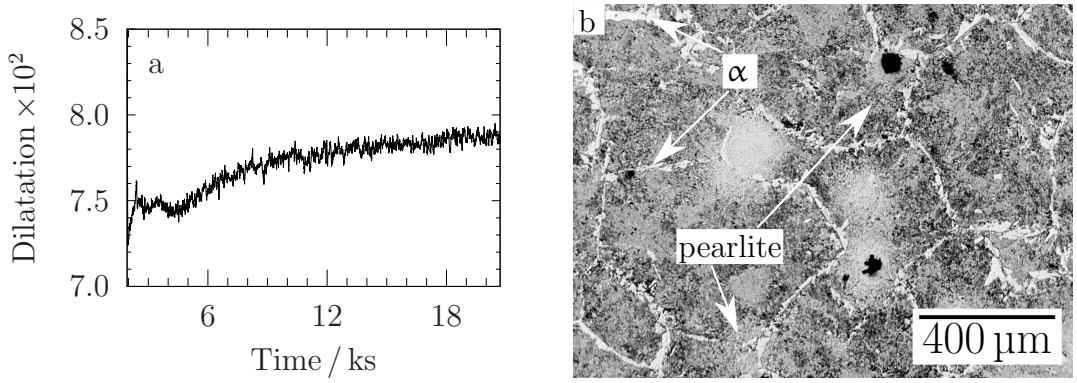

Figure 7.27: (a) dilatational strain measured during isothermal holding of Alloy 8 at 600 ℃ for 5.5 h— the strain does not become horizontal before the end of the isothermal hold,consistent with a transformation in progress at the time of quenching; (b) microstructure formed after 24 h at 600 ℃. The dilatational strain was found to become horizontal before the end the isothermal hold, suggesting the transformation had ceased before quenching, consistent with a mixture of ferrite and pearlitic

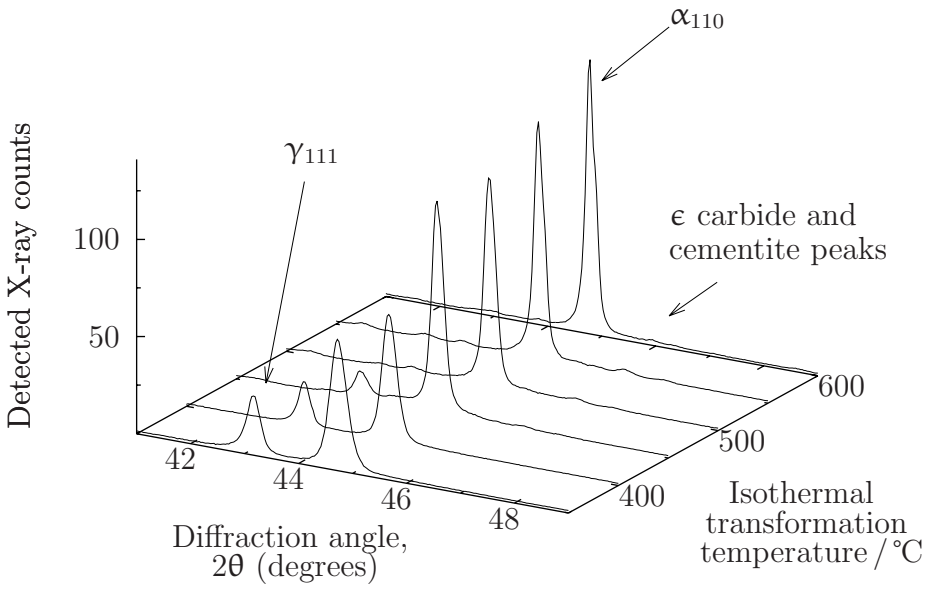

Figure 7.28: XRD peaks in Alloy 8 after isothermal transformation at and below 600 ℃. The peaks attributable to retained austenite increases in height as transformation temperature decreases, while carbide peaks become smaller and then disappear for transformation at or below 400 ℃.

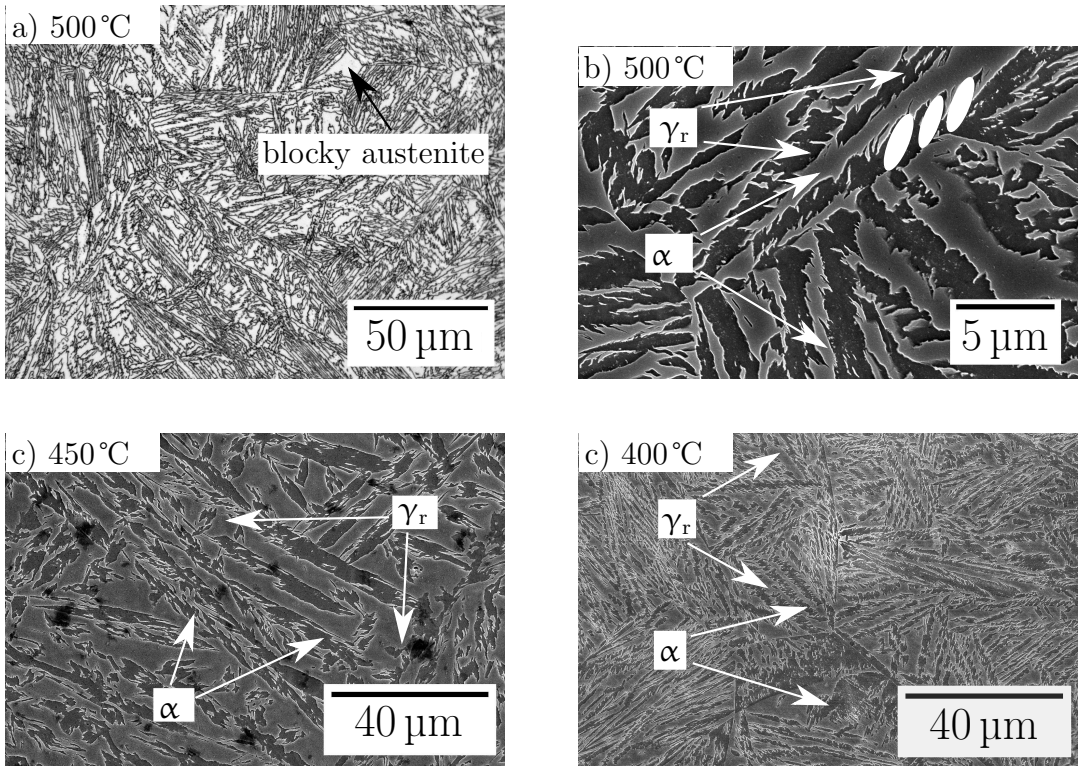

Figure 7.29: Alloy 8 transformed at the temperatures indicated. The dark regions in (c) are artefacts — the microstructure may be seen to continue unchanged through the dark regions. Lenticular shapes may be observed in ferrite, highlighted in figure 7.29(b), indicative of displacive transformation.

Below 400 °C

Isothermal transformations $< 400\,^{\circ}\mathrm{C}$, leads to ferrite plates separated by films or blocks of retained austenite (figures 7.30–7.32). The absence of any other phases was confirmed by XRD (figure 7.28). The amount of retained austenite remains constant as the transformation temperature is reduced from 400 °C to 325 °C, but then decreases for lower transformation temperatures (figure 7.33). The concept of $x_{T_0'}$ predicts that retained austenite can be more enriched in carbon at lower transformation temperatures (figure 6.4(b)), consistent with the austenite lattice parameter measured using XRD. This is expected to lead a greater proportion of the austenite transforming before the bainite reaction stops. Dilatometry indicates that all reactions had ceased in all cases, so there is no apparent explanation for the observed constant retained austenite volume fractions, but the most likely explanation is artefacts in Rietveld analysis. In all cases the volume fraction of retained austenite is consistent with good mechanical properties [92, 103, 104, 181, 192, 282, 309, 310].

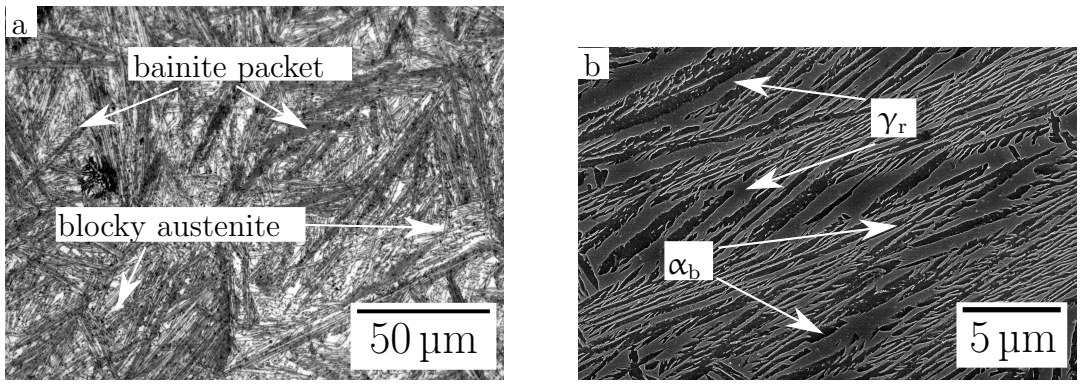

Figure 7.30: Alloy 8 transformed at 350 °C for 3 h. The microstructure consists of packets of alternating films of ferrite and retained austenite with larger regions of blocky austenite.

Reducing the transformation temperature results in grain refinement (figure 7.34). The controlling length scale is the bainite plate widths (i.e. normal to the sub-unit growth direction). Using calibrated scanning electron micrographs, the grain width

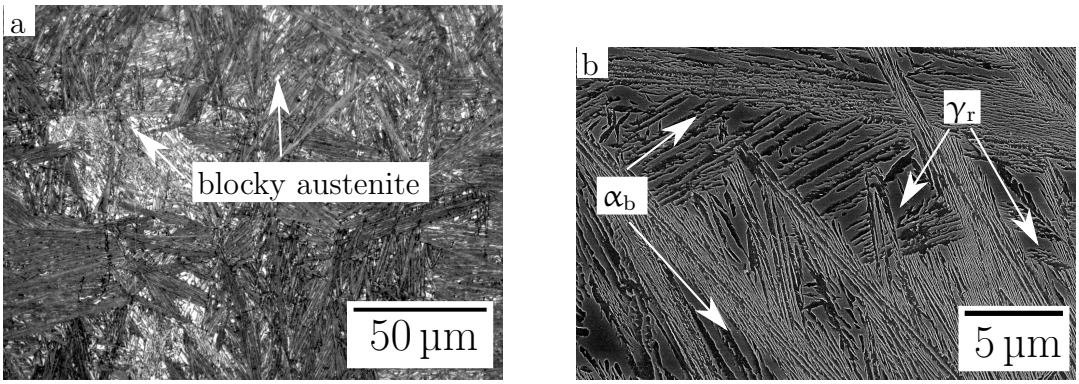

Figure 7.31: Alloy 8 transformed at 300 °C for 3 h. Although finer, the microstructure is very similar to that formed by transformation at 350 °C (figure 7.30)

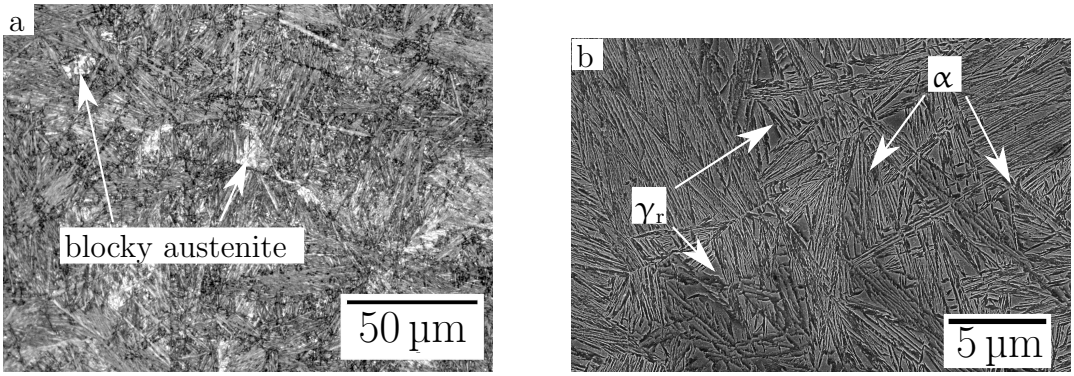

Figure 7.32: Alloy 8 transformed at 250 °C for 5 h. No blocks of retained austenite are visible using optical microscopy, consistent with the greater extent of transformation at the lower transformation temperature, although fine austenite blocks are visible using scanning electron microscopy (b).

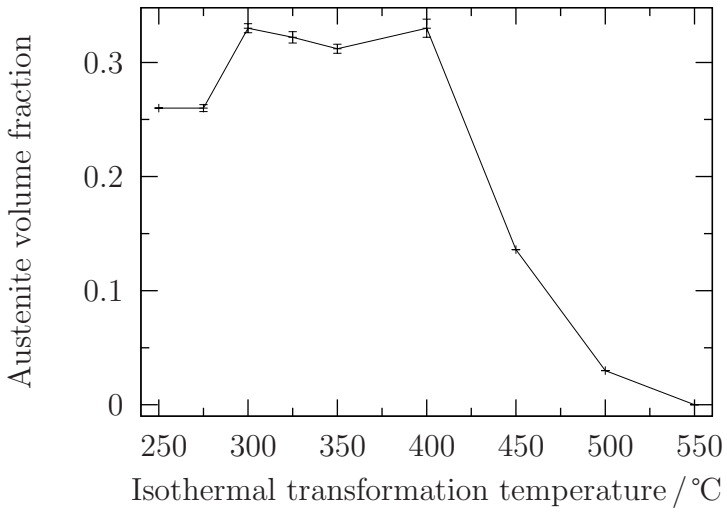

Figure 7.33: Retained austenite volume fraction assessed using Rietveld refinement of XRD data. The volume fraction of retained austenite increases as the transformation temperature decreases below 550 ℃, due to the increased suppression of cementite by the presence of silicon and aluminium. Carbon therefore remains in solution and stabilises austenite.

(distance perpendicular to the long axis of the films) was measured (figure 7.34). The hardness of the bainitic microstructure increases as the inverse of the measured grain width (figure 7.35), as predicted by Langford and Cohen [90, 91] for very fine grains where the expansion of dislocation loops is limiting. The hardness of the material is found to follow $(426 \pm 15) + (6.8 \pm 1.0)\,\bar{L_\gamma}^{-1}$ HV with respect to the austenite, where $\bar{L_\gamma}$ is the mean lineal intercept grain size of retained austenite in micrometres. The austenite grain size is used for comparison since austenite is the more ductile phase and will deform before ferrite.

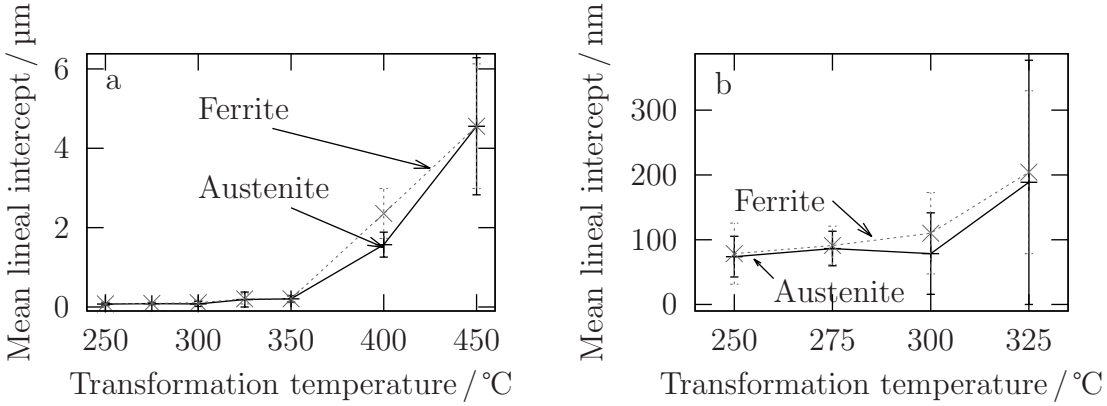

Figure 7.34: Stereologically-corrected [93] mean lineal intercept grain width (perpendicular to long axis of films) of film austenite and bainitic ferrite in Alloy 8 after isothermal transformation. Error bars taken as one standard deviation over at least ten values.

7.4.2 Alloy 9

600 °C and 450 °C

There was no detectable dilatation during isothermal holding at at 600 °C, even after 10 h. This is consistent with predictions that austenite is stable with respect to ferrite at 600 °C. However, grain boundaries were decorated with pearlite (figure 7.36). The structure was otherwise martensitic. Austenitisation and isothermal holding at 450 °C leads to a similar structure, although austenite grain boundaries

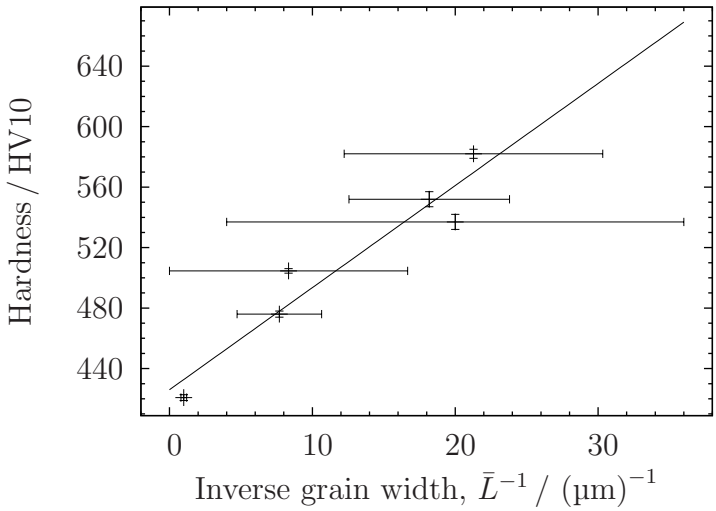

Figure 7.35: Grain refinement strengthening in Alloy 8 is found to be inversely proportional to the mean lineal intercept grain width, consistent with the findings of Langford and Cohen [90].

do not contain any transformation products (figure 7.36(c)).

350 °C

Isothermal transformation of Alloy 9 at 350 °C for 18.5 h produces a microstructure consisting of a mixture of fine bainite plates, large regions of martensite and smaller regions of retained austenite (figure 7.37). Dilatation indicates that the transformation started after 2×10^4 s and was ongoing at the end of the isothermal transformation period, consistent with the microstructure. The larger of these austenite blocks will be less enriched with carbon and then transform to martensite upon cooling. Smaller austenite blocky are both stabilised with respect to martensite by their small size [216] and can retained to ambient temperature. Samples transformed at 350 °C for 24 h contain much smaller austenite blocks (figure 7.37(c) as the bainite transformation had more time to occur and thus more bainite was formed, subdividing the austenite blocks.

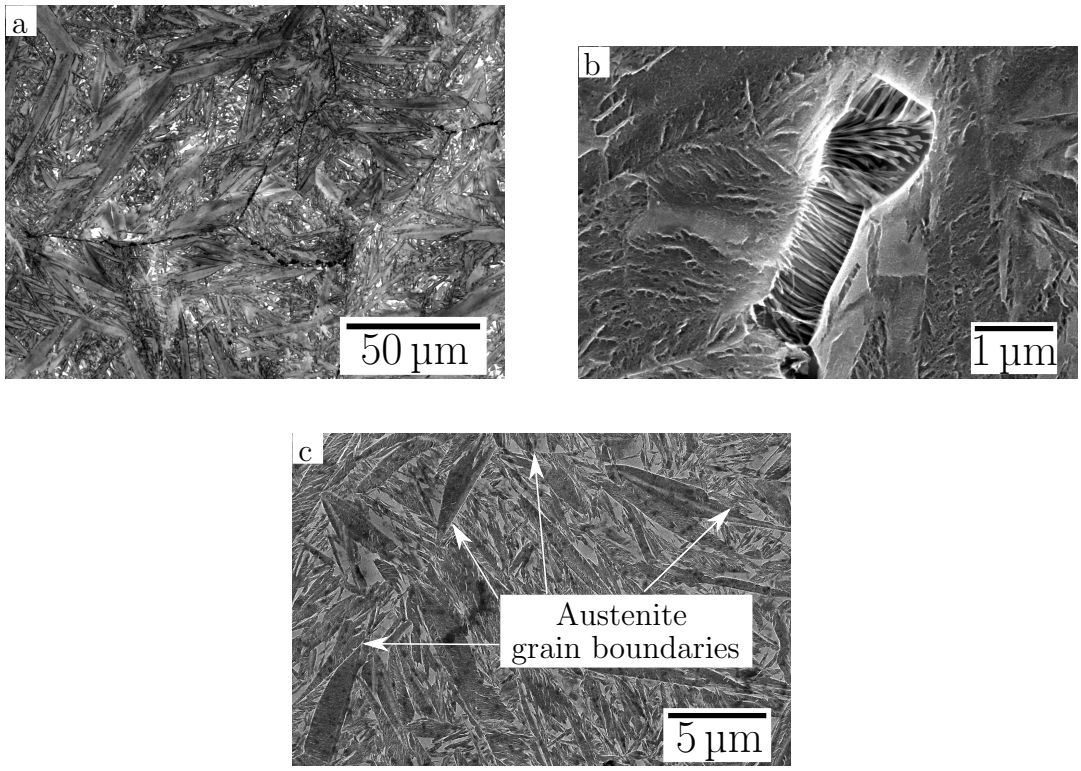

Figure 7.36: In Alloy 9 transformed at 600 °C for 10 h: (a) austenite grain boundaries appear to be decorated with a dark-etching phase and (b) lamellae at dark-etching features, which are presumably pearlite. (c) Alloy 9 transformed at 450 °C for 14 h, consists of large martensite plates spanning prior austenite grains and no dark-etching features at prior austenite grain boundaries.

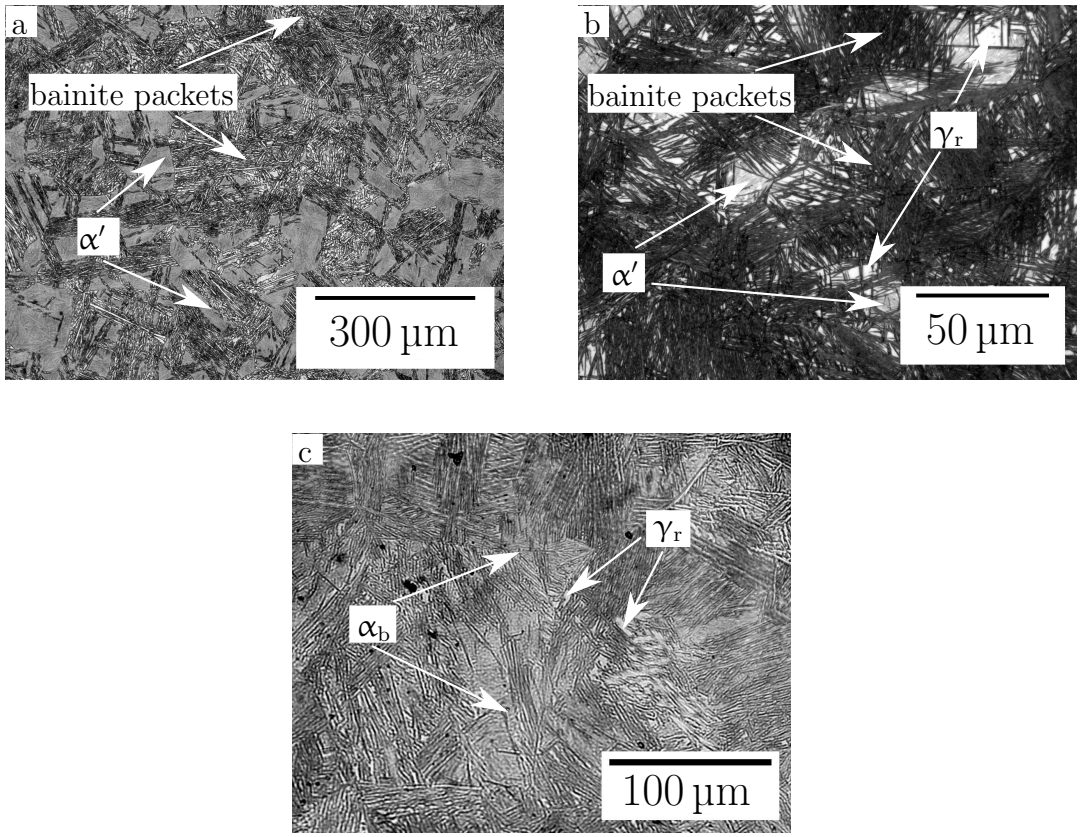

Figure 7.37: Alloy 9 austenitised and held at 350 °C for: (a) and (b) 18.5 h. The microstructure consists of regions of fine platelets and larger regions of martensite and retained austenite; (c) 24 h. The bainite reaction has proceeded further than in (a), as demonstrated by the absence of large regions of martensite and the presence of retained austenite.

300 °C

Transformation at 300 °C for 18.5 h showed similar results to transformation at 350 °C with an incubation period of approximately 3×10^4 s and the transformation still in progress at the end of the isothermal treatment, with remaining large blocks of austenite transform to martensite upon cooling. The bainitic microstructure is finer than after transformation at 350 °C (figure 7.38(a) cf. 7.37(b)). This is to be expected since a lower temperature requires the plastic deformation of stronger parent austenite and more rapid work hardening, stifling the bainitic sub-units earlier. It was found during synchrotron XRD experiments (section 8.1.1) that 3 d at 300 °C is sufficient to allow the bainite transformation to proceed to the extent that no martensite forms during subsequent cooling to room temperature.

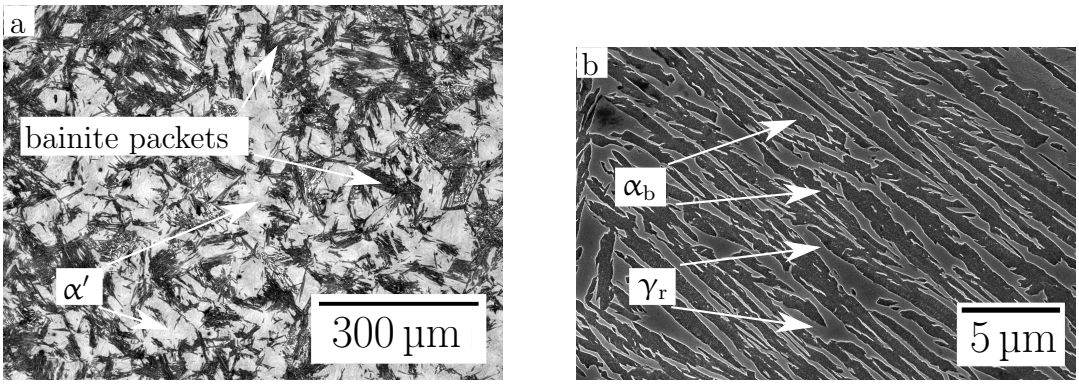

Figure 7.38: Alloy 9 after austenitisation and isothermal holding at 300 °C for 18.5 h. The microstructure consists of regions of fine platelets and large regions of martensite. The platelets are finer than those formed during isothermal transformation at 350 °C.

250 °C

Two samples were transformed at 200 °C: one for 18.5 h and another for 120 h. Figure 7.39 shows that only after 120 h is the transformation close to terminating. After 18 h (0.65×10^5 s), transformation has barely started.

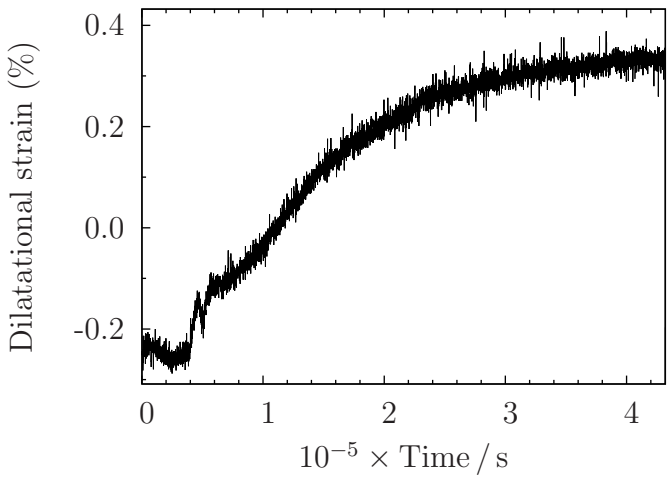

Figure 7.39: Dilatational strain Alloy 9 held at 250 °C. The initial strain is negative, consistent with the change from (as-received) martensite to austenite. After 18.5 h (0.65×10^5 s), the dilatational strain has hardly changed from the initial value and after 120 h, the transformation appears to be stopping.

After 18.5 h, the microstructure exhibits predominantly martensite, with only a small number of regions at austenite grain boundaries showing the early stages of bainite formation (figure 7.40(a)), consistent wit the measured dilatation.

After 120 h, the sample is predominantly a mixture of bainitic ferrite and retained austenite (figure 7.41(a)). The packets are finer than those formed in Alloy 9 transformed at higher temperatures. The austenite blocks are $\sim 10\,\mu$m in size, several times larger than those formed after similar transformation in Alloy 8 (c.f. figure 7.32(a)), but are smaller than those that form in Alloy 9 following isothermal transformation at higher temperatures. These observations are consistent with calculations (section 6.1.2).

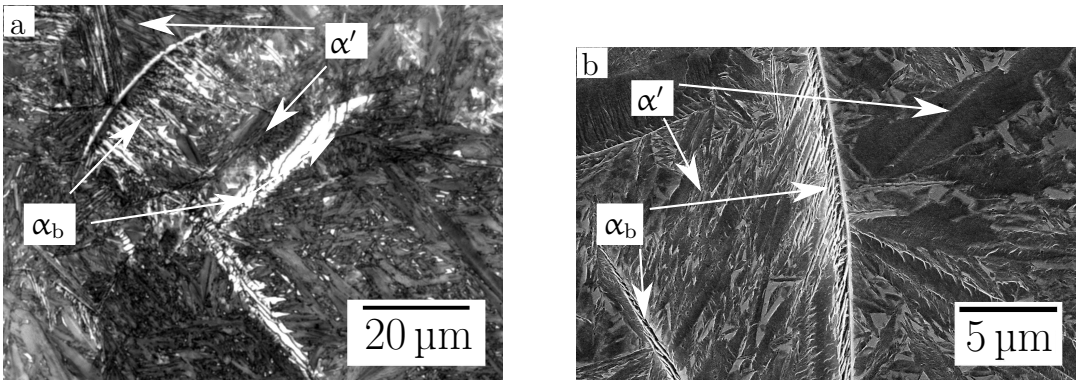

Figure 7.40: Alloy 9 after austenitisation and isothermal holding at 250 ℃ for 18 h. The features in the middle of each micrograph are situated at prior austenite grain boundaries and are presumably the first products of the bainite reaction.

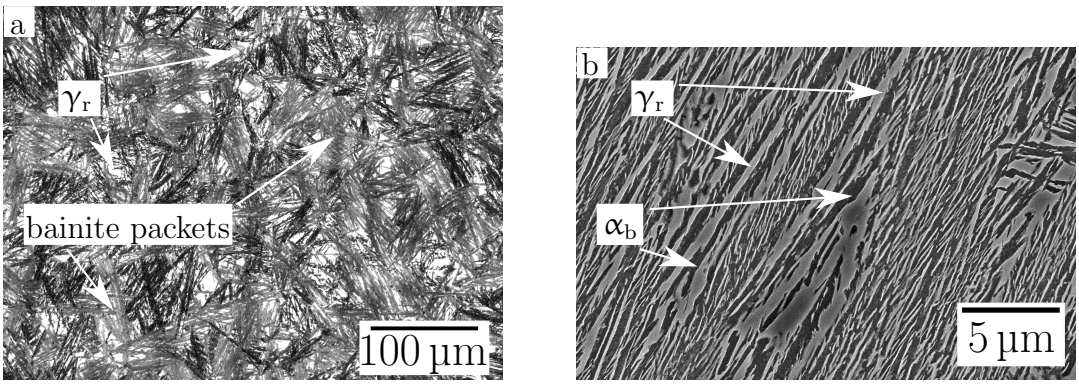

Figure 7.41: Alloy 9 after austenitisation and isothermal holding at 250 ℃ for 120 h. (a)fine platelets and small regions of retained austenite. (b) the film morphology in a bainite packet.

Chapter 8

Thermal stability in optimised alloys: synchrotron X-ray and neutron diffraction

8.1 Synchrotron XRD experimental method

The thermal stability of both Alloy 8 and Alloy 9 were assessed using time-resolved synchrotron XRD with *in-situ* heating, as in section 4.3. Experiments were performed at beamline I12 at Diamond Light Source, Didcot, U. K. 3 mm diameter rods were sealed into glass ampoules filled with argon. They were austenitised at 1000 °C for 30 min and transformed to bainite at 250 °C, 300 °C or 350 °C. Alloy 8 samples were transformed for 24 h and those of Alloy 9 for the times indicated in table 8.1.

In-situ tempering was performed using a bespoke furnace with X-ray transparent windows (figure 8.1). The temperature was controlled using a thermocouple on the surface of the sample close to the X-ray beam. The windows for the diffracted beam had a diameter of 10 mm and were approximately 100 mm from the centre of the sample. X-rays that did not pass through the windows were heavily attenuated. 2θ was thus limited to $\approx 5.7°$. A beam energy of 120 keV was therefore chosen to ensure enough peaks were detected to allow Rietveld refinement to be

performed. Furthermore, 120 keV photons are able to penetrate 3 mm of steel.

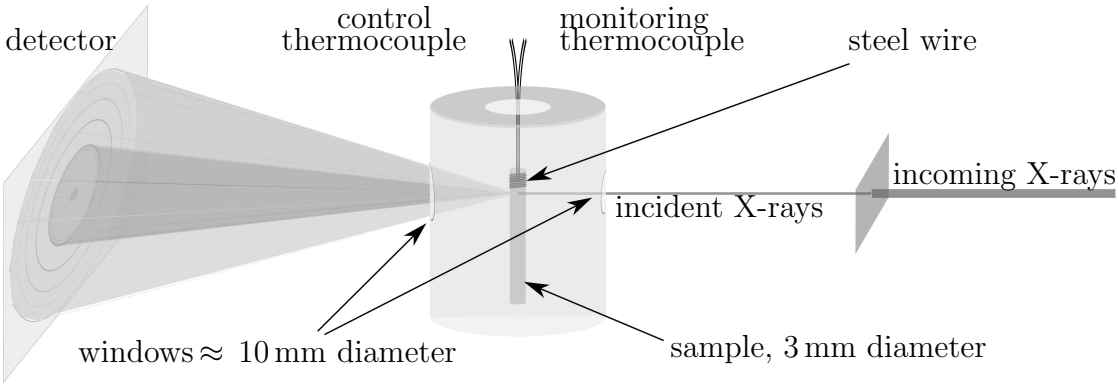

Figure 8.1: Experimental setup for experiments at Diamond Light Source.

X-ray detection was by a Thales Pixium RF4343 large-area 2D detector with pixels 148 µm × 148 µm positioned perpendicular to the X-ray beam. It was determined that a sample-detector distance of 1500 mm allowed the largest possible diffraction ring ($2\theta = 5.7°$) to fill all available space on the detector (figure 8.2) and was used for all experiments.

The X-ray beam size was optimised to 0.5 mm × 0.5 mm. This gives sufficient angular resolution to resolve all peaks while maintaining the maximum possible detected intensity, so allowing data to be recorded every 4 s. The X-ray beam incident on the sample is shown in figure 8.3.

Samples were heated from ambient temperature to 500 °C at 10 °C min^{-1}. The temperature was maintained until it was deemed that no further change in diffraction rings was likely. The samples were then allowed to cool in air to ambient temperature at 10 °C s^{-1}.

The line broadening behaviour of the beamline was calibrated using a ceria standard. Calibrations were performed at both the beginning and end of the experiment after Hart et al. [311].

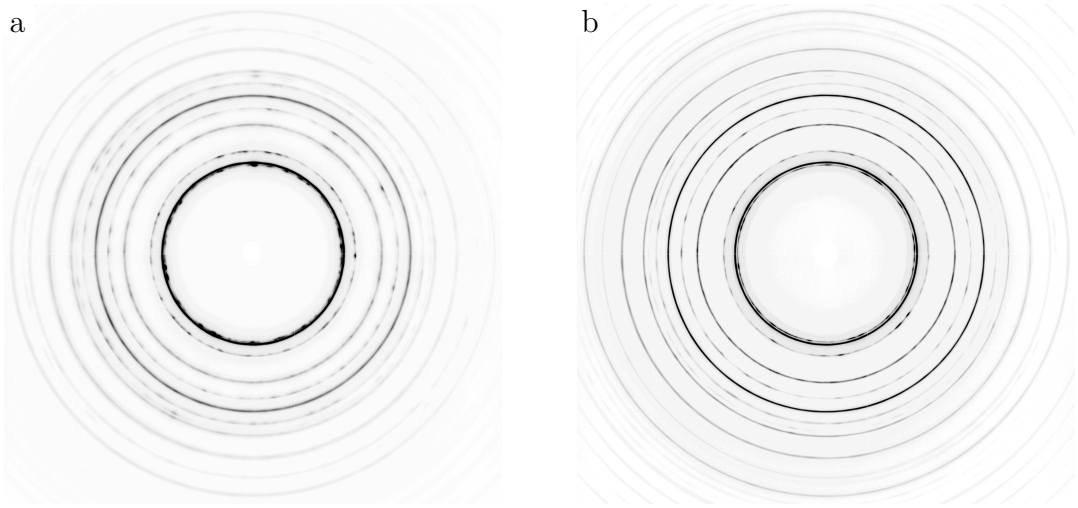

Figure 8.2: Diffraction rings observed during the experiments at Diamond Light Source in a sample of Alloy 8 transformed at 250 °C (a) before and (b) after heating. White indicates no detected X-rays; black indicates the maximum number of detected X-rays in each given frame. Each image is approximately 43 cm square at the detector.

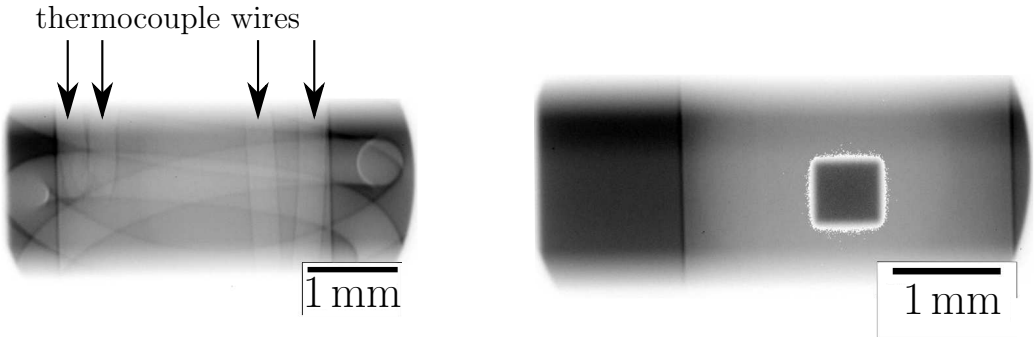

Figure 8.3: X-ray photograph of Alloy 8 in the synchrotron beamline. Left: sample with thermocouple on both edges and stainless steel wire wrapped around the top of the sample; right: the site 2 mm lower used for data collection.

8.1.1 Synchrotron XRD assessment of Alloy 8 thermal stability

Figures 8.4 and 8.5 show that all peaks initially shift to lower diffraction angle, consistent with thermal expansion. Austenite peaks then shift to higher diffraction angles before disappearing suddenly while ferrite peaks become correspondingly more intense, consistent with carbide precipitation and transformation to ferrite (section 4.3 and [116]).

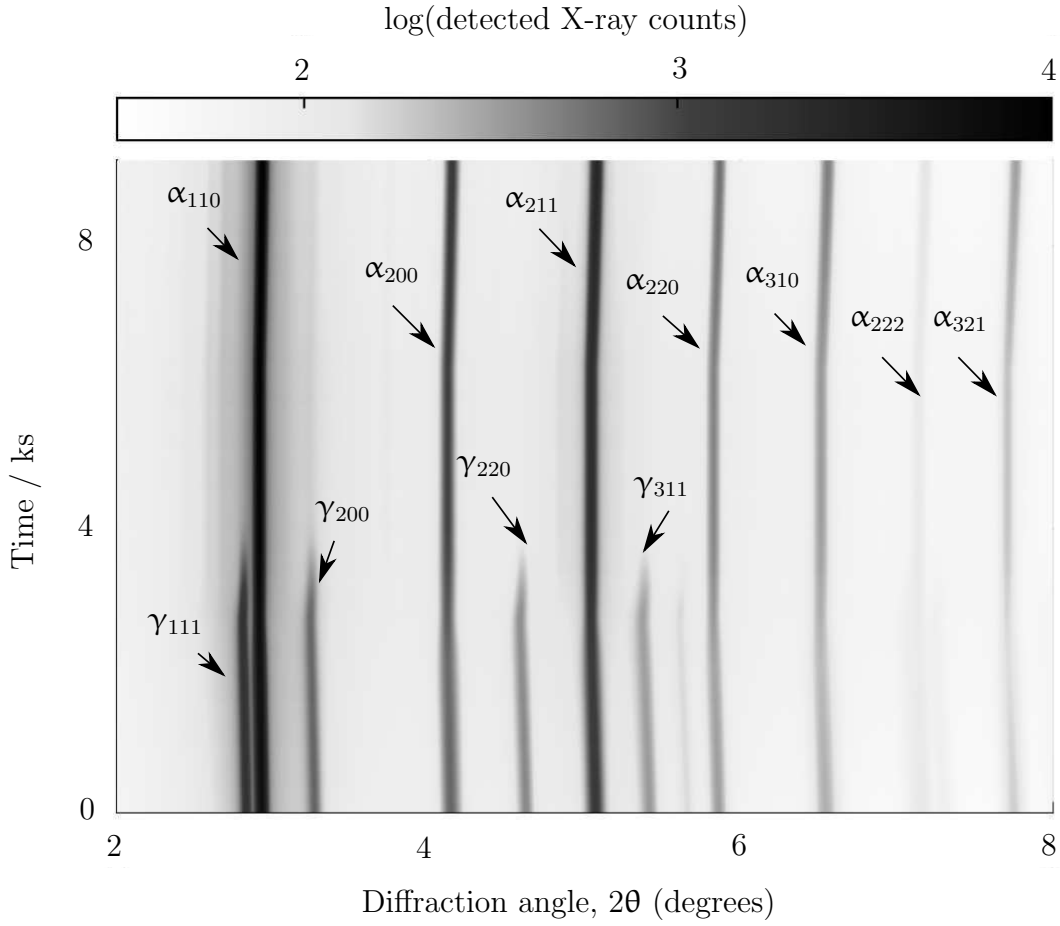

Figure 8.4: Time-resolved plot of synchrotron X-ray diffraction data for Alloy 8 transformed at 250℃, with austenite and ferrite peaks labelled.

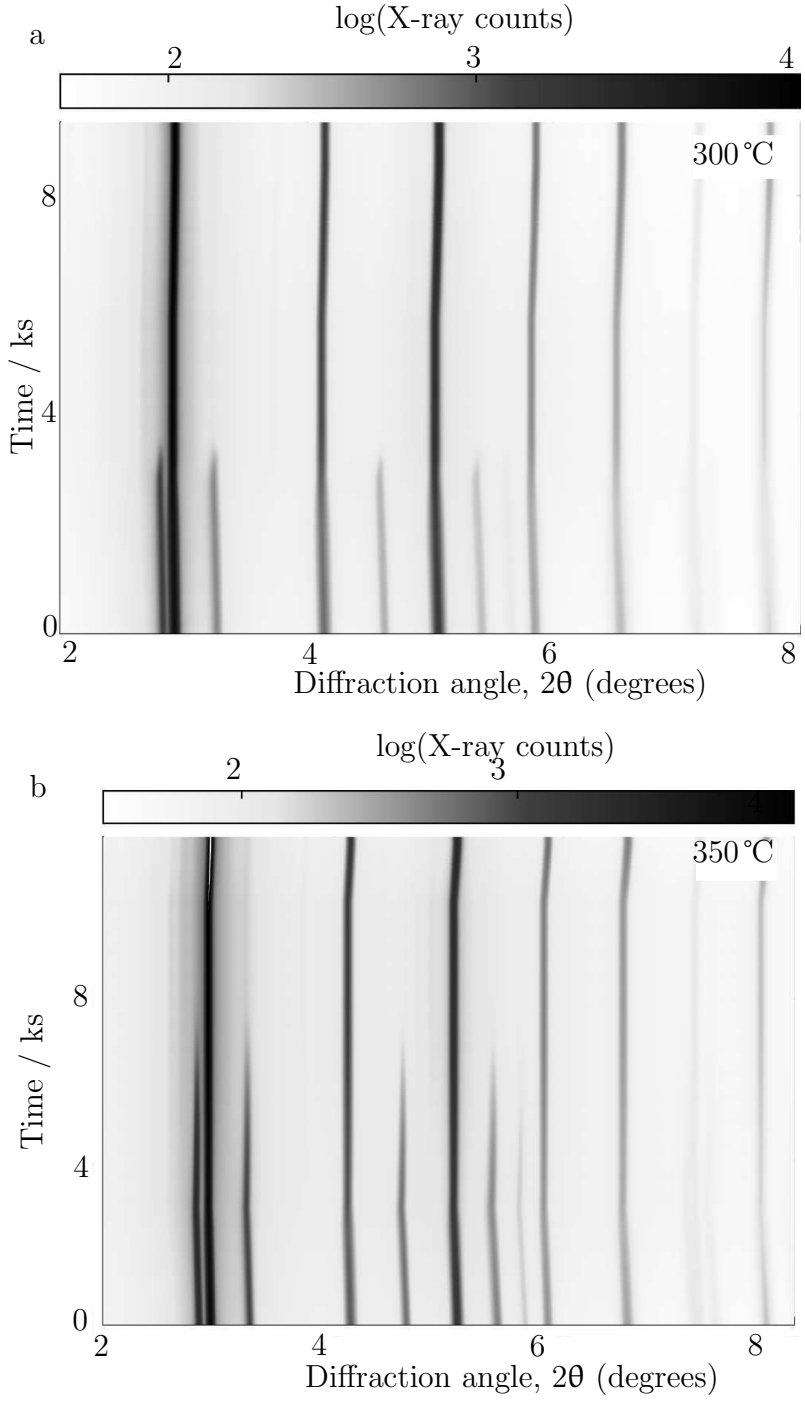

Figure 8.5: Time-resolved synchrotron X-ray diffraction results for Alloy 8 transformed at (a) 300 °C and (b) 350 °C.

Figures 8.4–8.5 indicate that austenite retained after transformation at higher temperatures is more thermally stable: the retained austenite peaks in figure 8.4 disappear abruptly at around 3.5 ks, but those in figure 8.5(b) persist up to 7 ks despite the identical heat treatments. The calculated carbon content in retained austenite is given by the T_0' line in figure 6.4(b) which shows that the expected carbon content of retained austenite in Alloy 8 is $\approx$ 4 wt% for transformation at 250 °C and $\approx$ 2.5 wt% at 350 °C. This increased carbon content renders the retained austenite more susceptible to the precipitation of carbides and subsequent transformation to ferrite.

Figures 8.6(a)–8.8(a) show that the loss of austenite is almost simultaneous with the reduction in austenite lattice parameter. This is in contrast with the equivalent decomposition in Alloy 1 (figure 4.23), which shows a delay of several minutes between the lattice contraction and the loss of austenite. This confirms the findings of Saha Podder [134, page 161] that retained austenite decomposition in nickel-containing steels is faster than in an equivalent manganese-containing steel. Since previous synchrotron experiments used a tempering temperature of 450 °C or 500 °C (section 4.3) and the current tempering was done at 600 °C (necessary to accelerate decomposition and allow all experiments to be completed during the allocated beamtime), no direct comparison may be made between the relative stabilities of Alloy 1 and Alloy 8. However, the fact that Alloy 8 decomposes while being held at 600 °C for less than 3 h suggests that it is not sufficiently thermally stable for long-term use at elevated temperatures.

Figures 8.6(b), 8.7(b) and 8.8(b) show that, just as in Alloy 1, there was no change in ferrite lattice parameter during the isothermal hold, save for a slight initial contraction at the same time as the austenite lattice parameter contracts. Within ferrite, carbon is either trapped at defects or is otherwise reluctant to leave solid solution. This phenomenon has been noted previously [53, 76, 169, 226, 312, 313] and will be explored in detail in chapter 10, where the possibility of non-cubic symmetry in ferrite will be presented. To simplify the analysis of the thermal stability, all ferrite will be assumed to be body-centred cubic in the current chapter.

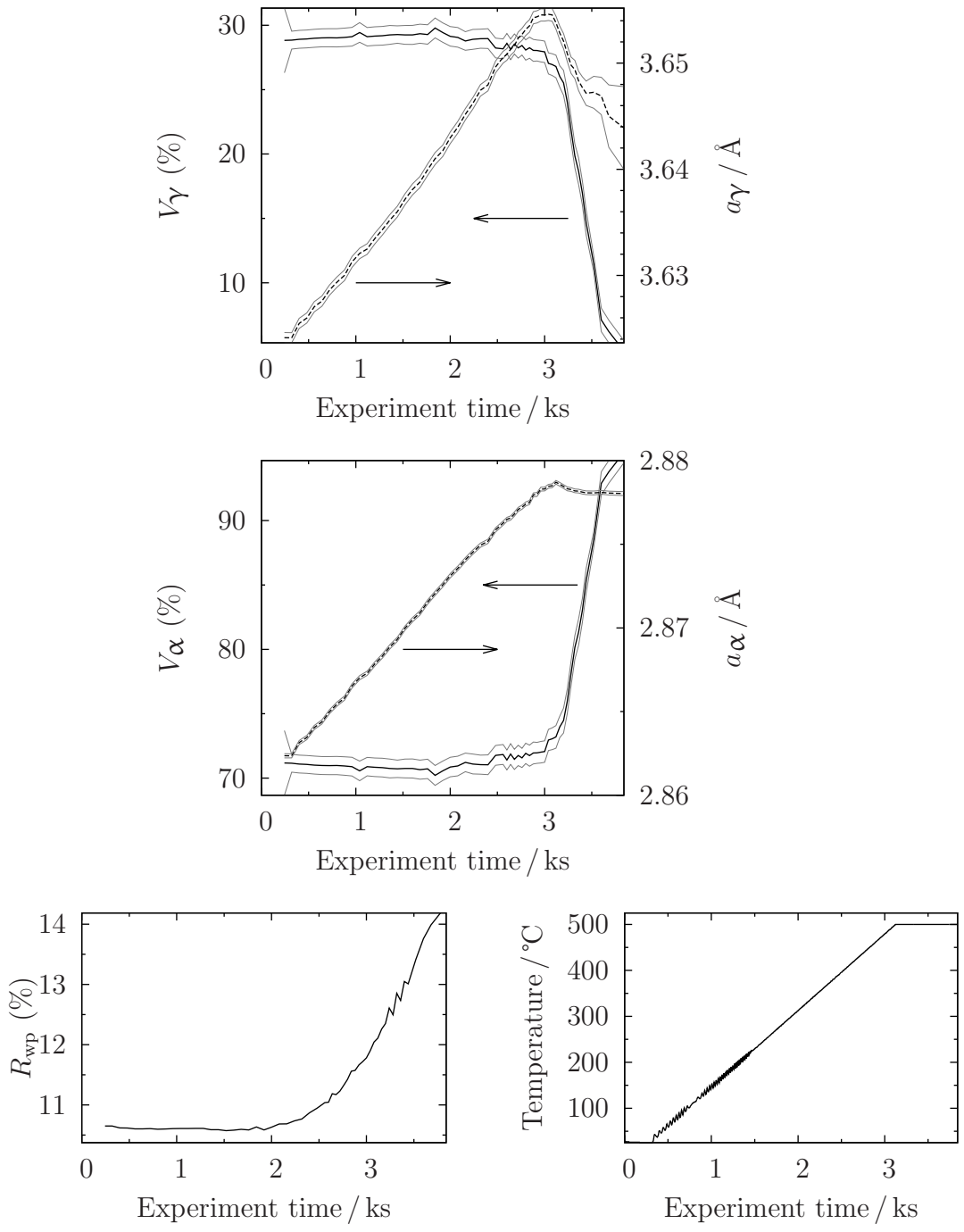

Figure 8.6: Rietveld refinement results for Alloy 8 transformed at 250 °C and investigated using synchrotron XRD with *in-situ* heating. Grey lines represent ± the standard error for each measurement.

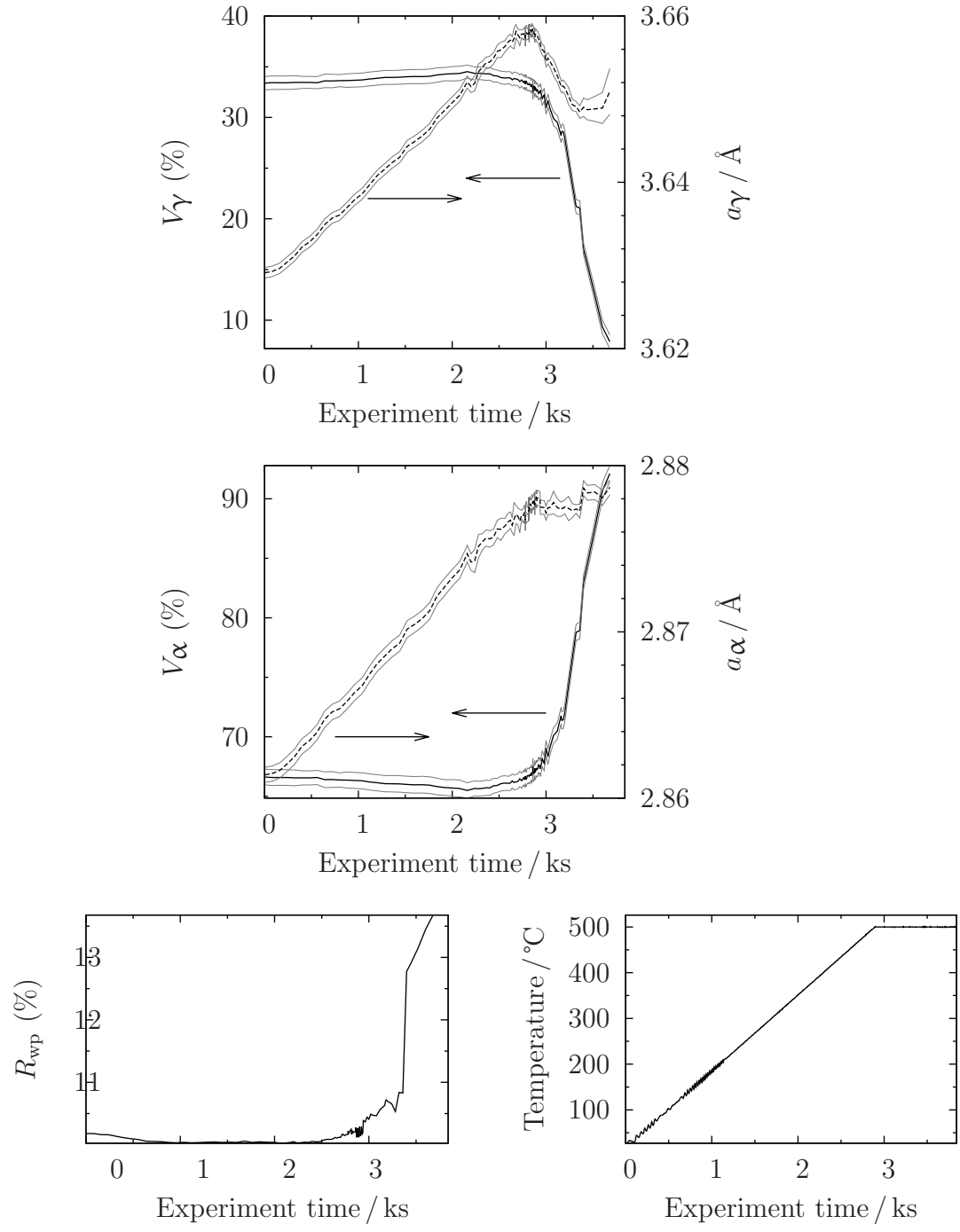

Figure 8.7: Rietveld refinement results for Alloy 8 transformed at 300 °C and investigated using synchrotron XRD with *in-situ* heating. Grey lines represent ± the standard error for each measurement.

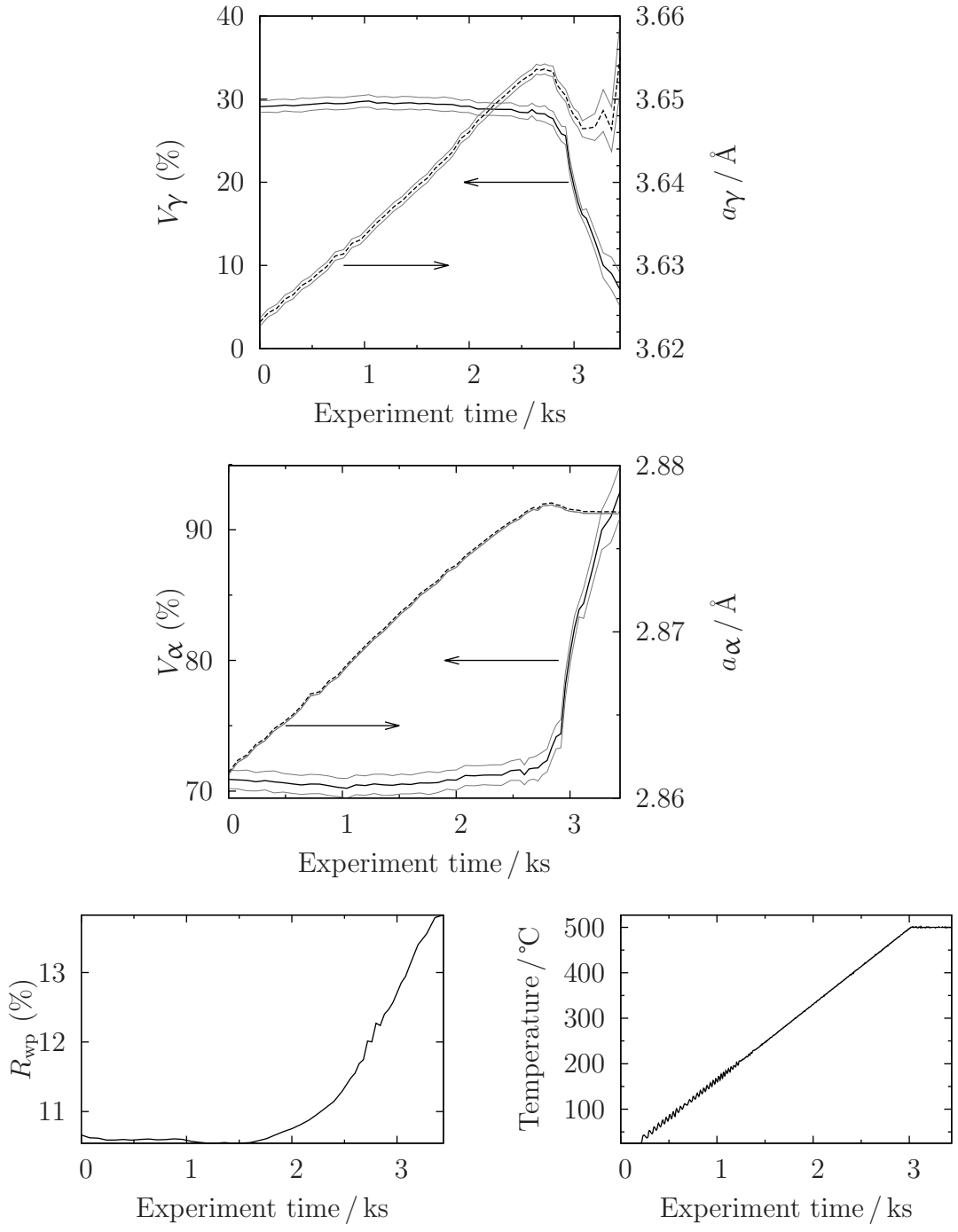

Figure 8.8: Rietveld refinement results for Alloy 8 transformed at 350 °C and investigated using synchrotron XRD with *in-situ* heating. Grey lines represent ± the standard error for each measurement.

Examination of the microstructures of Alloy 8 before and after thermal exposure at Diamond Light Source shows that the austenite films are completely destroyed (figure 8.9).

The hardness of Alloy 8 transformed at 250 °C was found to reduce from 586 ± 2 HV10 to 530 ± 15 HV30 after the heat treatment. The loss of the strengthening contributions of grain refinement due to the austenite films and carbon in solid solution outweigh the strengthening due to the precipitates, consistent with the vast majority of studies into the tempering of martensite and nanocrystalline bainite, [e.g. 75, 134, 143, 150, 226, 307].

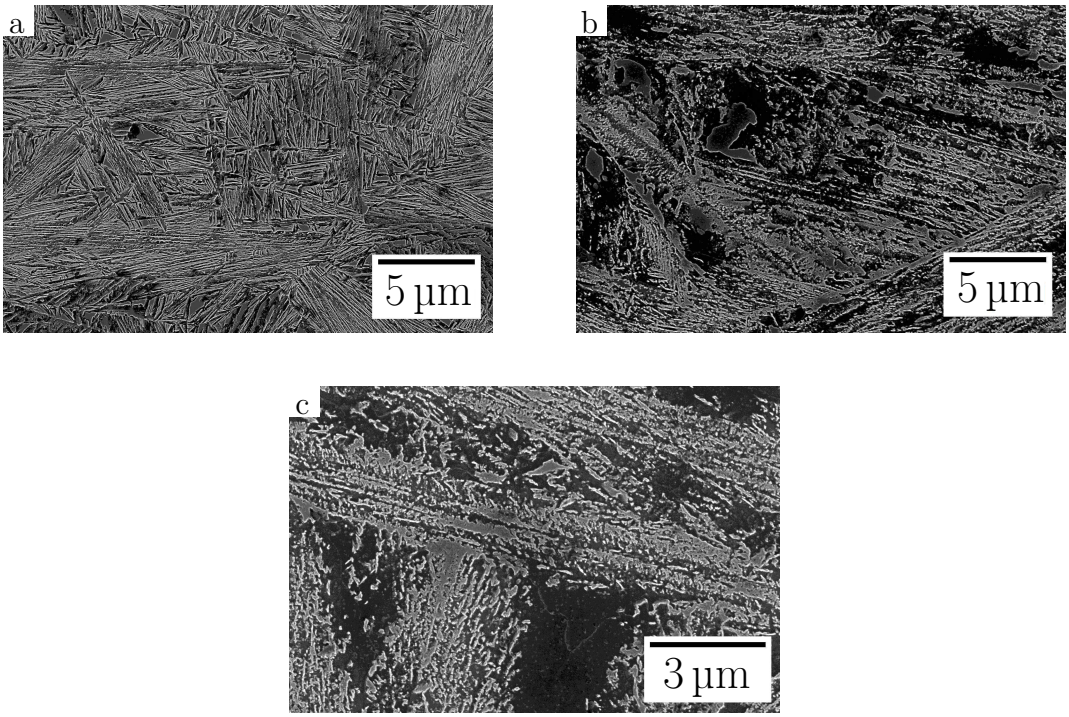

Figure 8.9: Scanning electron micrographs of Alloy 8, transformed at 250 °C (a) before and (b) and (c) after tempering experiment at Diamond Light Source. The mottled appearance is consistent with the carbide precipitation implied by the appearance of additional XRD peaks, transformation of austenite to ferrite and contraction of lattice parameters observed after tempering.

8.1.2 Synchrotron XRD assessment of Alloy 9 thermal stability

The thermal stability of Alloy 9 samples transformed according to table 8.1 was assessed using the same set-up as in section 8.1.1. Due to time constraints, all experiments involving Alloy 9 used a final cooling rate of 20 °C min^{-1} and the samples transformed at 275 °C and 300 °C were heated at 20 °C min^{-1}. This is not expected to significantly affect thermal stability.

Transformation temperature / °C	225	250	275	300
Transformation Time / d	21	14	10	5

Table 8.1: Transformation conditions for Alloy 9 studied using synchrotron X-ray diffraction with *in-situ* heating following austenitisation at 1000 °C for 30 min prior to transformation.

Figure 8.10 shows that austenite persists throughout the entire heat treatment. Figures 8.11(a)–8.14(a) show that although there is a partial loss of austenite at 500 °C concurrent with a contraction in the austenite lattice parameter, the volume fraction stabilises and subsequently survives cooling to ambient temperature.

8.1.3 Tempering precipitates

The contraction in the austenite lattice parameter at 600 °C suggests depletion of carbon in austenite and thus precipitation of carbides. Calculated cementite peaks have excellent correspondence to measured XRD data (figure 8.15(a)) and all peaks bar one can be identified using austenite, ferrite and cementite. The formation of cementite is consistent with the lack of silicon in Alloy 9 and the persistence of austenite at a constant volume fraction after cementite formation vindicates the design philosophy in section 6.1.2.

Figure 8.15(a) contains an unidentified peak at around $2\theta = 2^\circ$ that is not explained by cementite. This is in the position of a notional 100 peak for ferrite and is consistent with β-NiAl, which has a primitive cubic CsCl crystal structure with

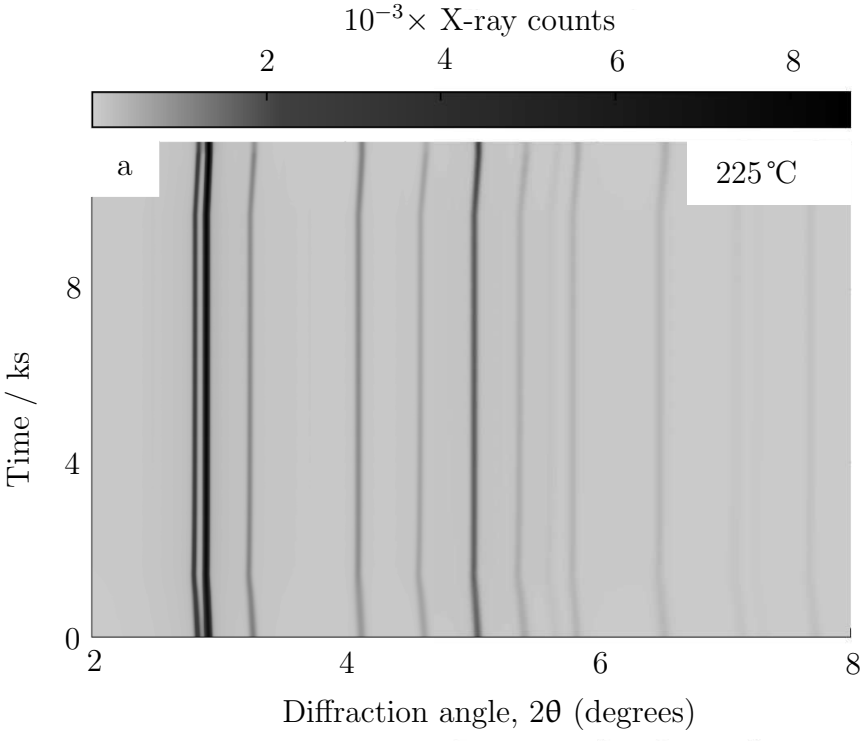
$10^{-3}\times$ X-ray counts
2
4
6
8
a
225 °C
Time / ks
0
4
8
2
4
6
8
Diffraction angle, 2θ (degrees)

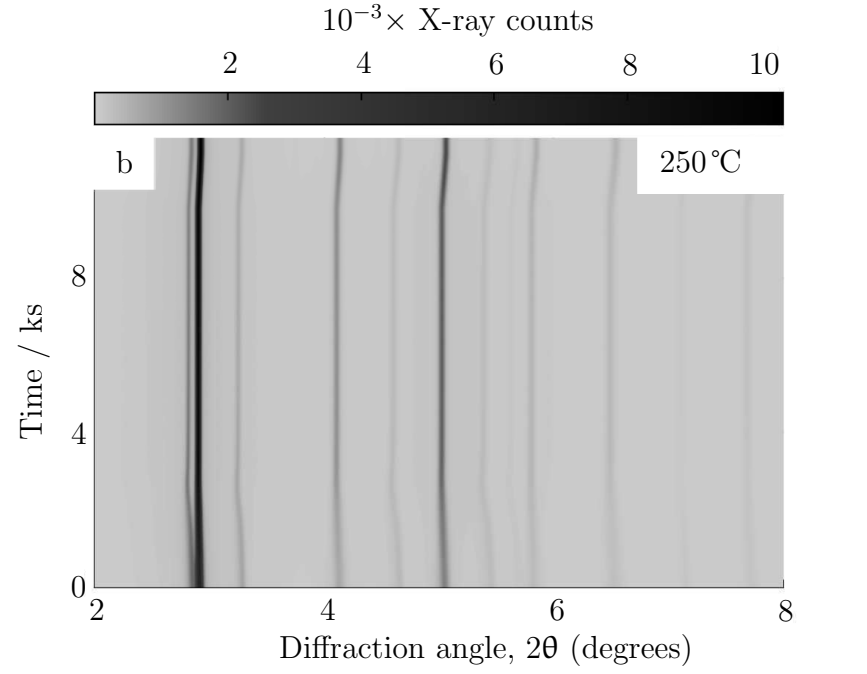
$10^{-3}\times$ X-ray counts
2
4
6
8
10
b
250 °C
Time / ks
0
4
8
2
4
6
8
Diffraction angle, 2θ (degrees)

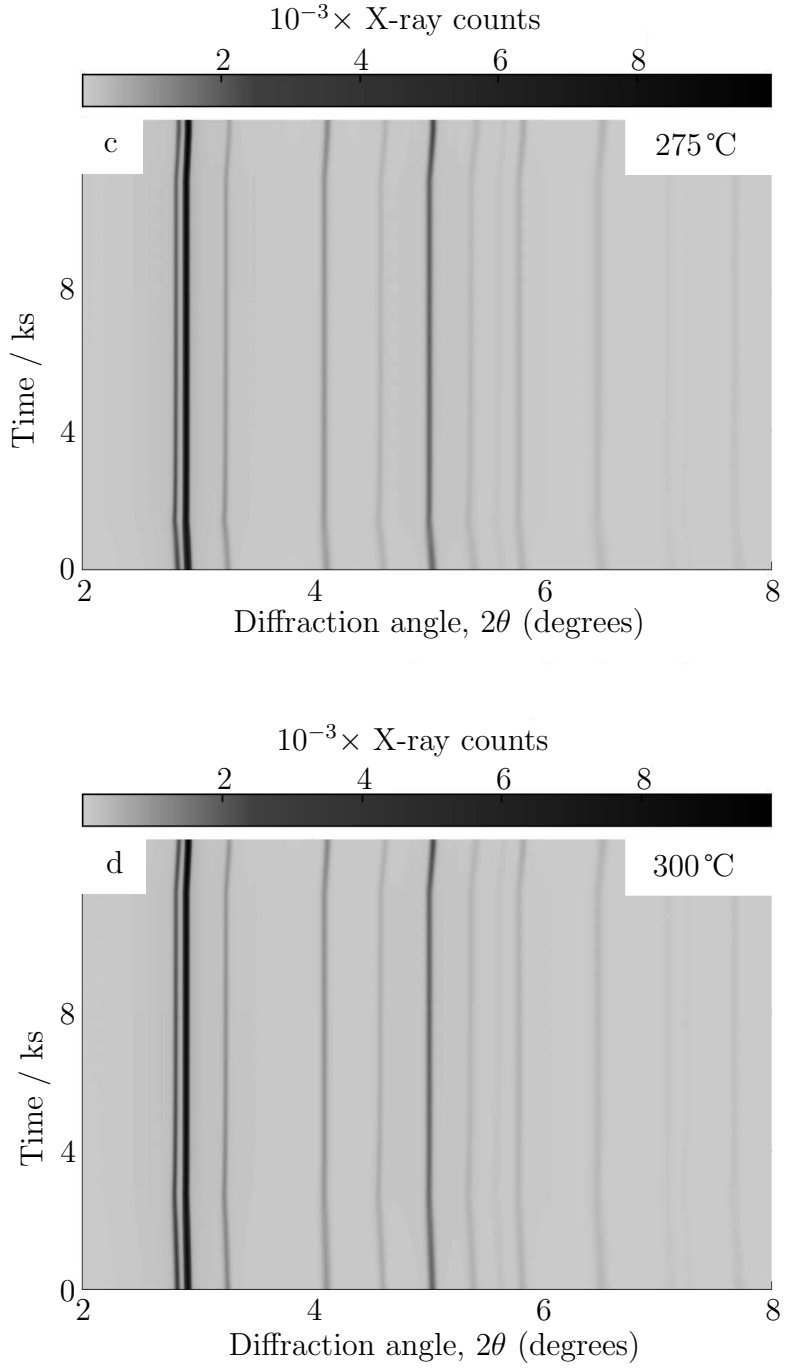

Figure 8.10: Time-resolved synchrotron X-ray diffraction results for Alloy 9 transformed at the temperature indicated on each figure.

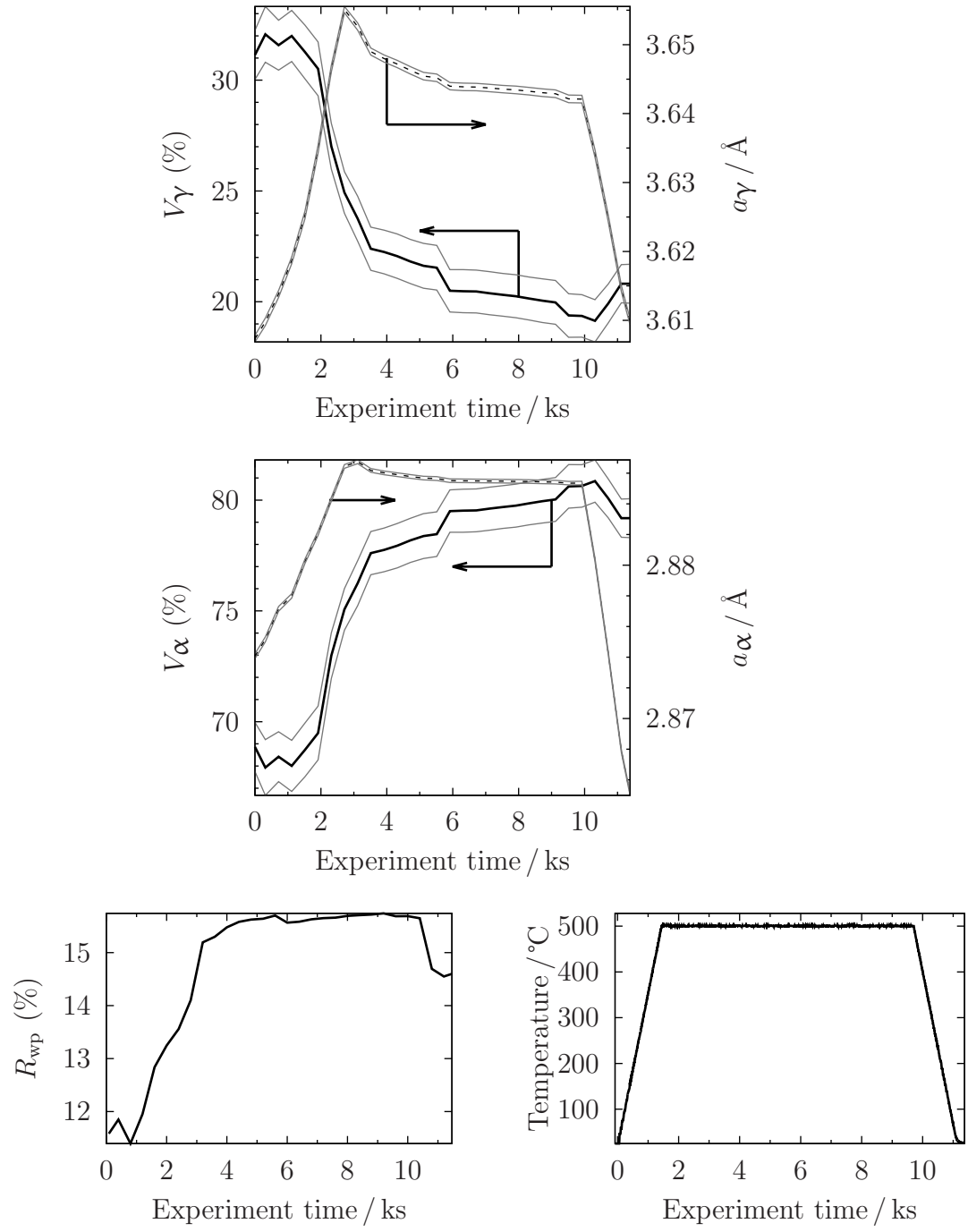

Figure 8.11: Rietveld analysis results for time-resolved synchrotron X-ray diffraction with *in-situ* tempering of Alloy 9 transformed at 225 ℃. Grey lines represent ± one standard error. Arrows indicate the the relevant axis for each dataset.

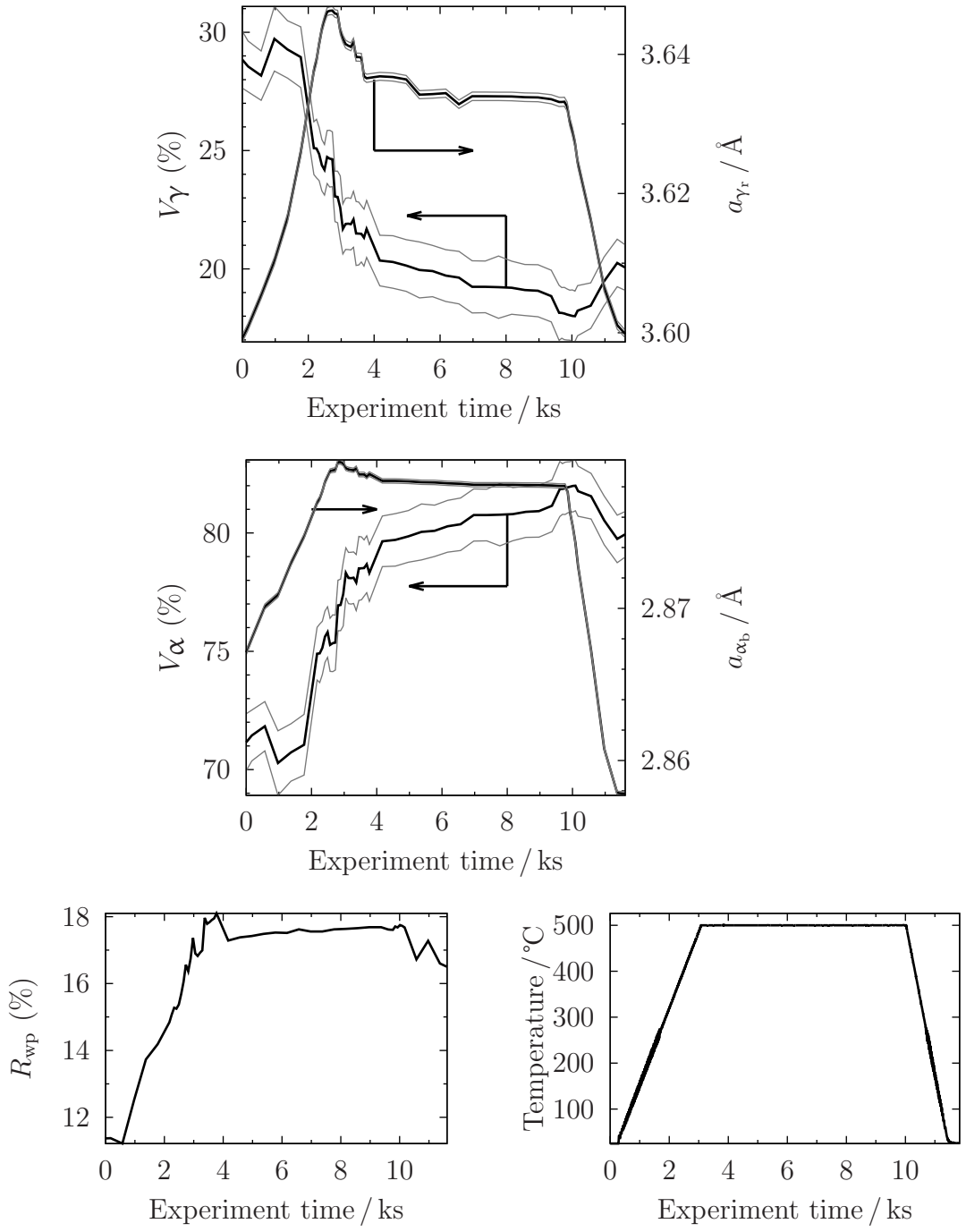

Figure 8.12: Rietveld refinement results for tempering Alloy 9 transformed at 250 °C. Grey lines represent ± one standard error. Arrows indicate the the relevant axis for each dataset.

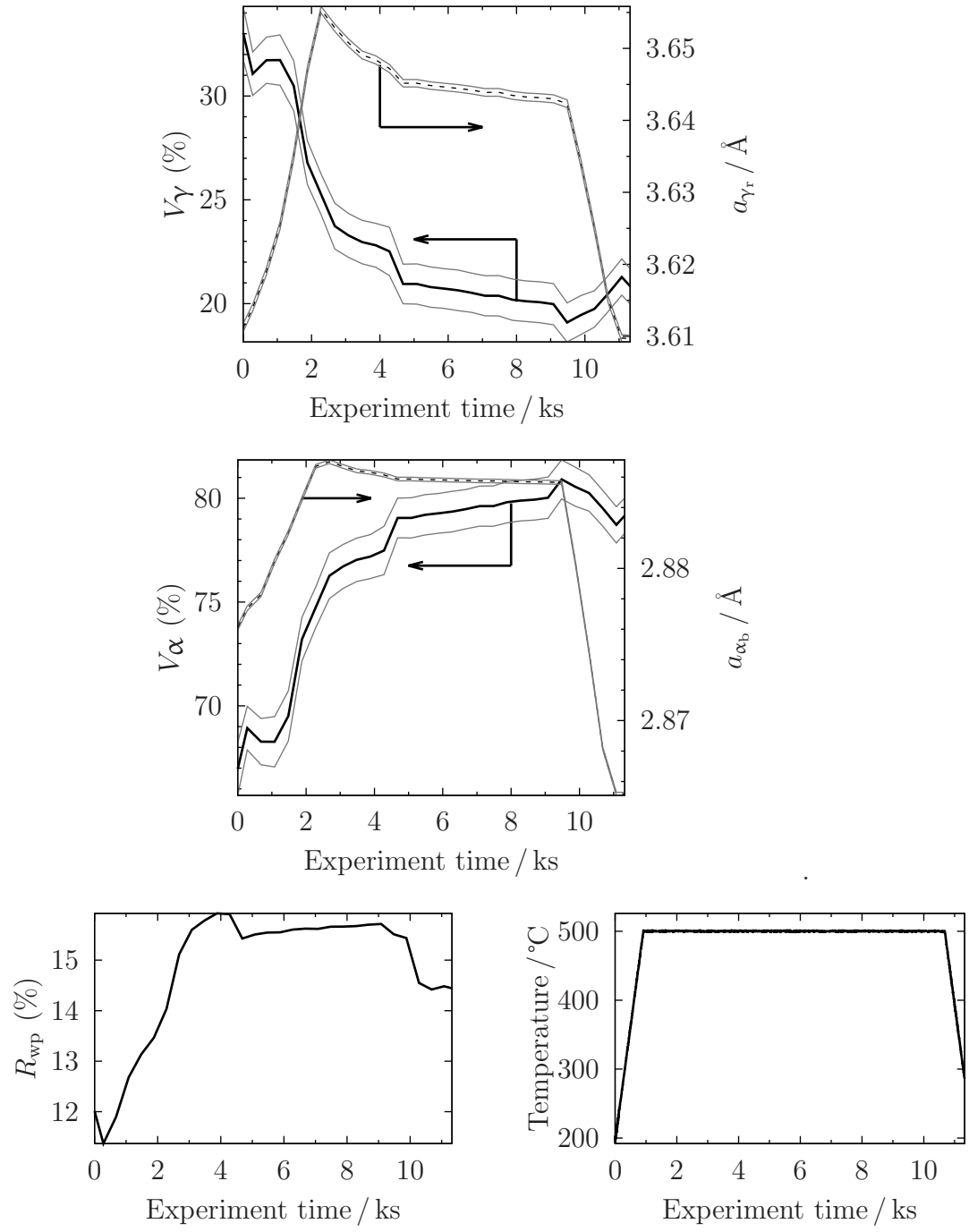

Figure 8.13: Rietveld analysis results for time-resolved synchrotron X-ray diffraction with *in-situ* tempering of Alloy 9 transformed at 275 ℃. Grey lines represent ± one standard error. Arrows indicate the the relevant axis for each dataset.

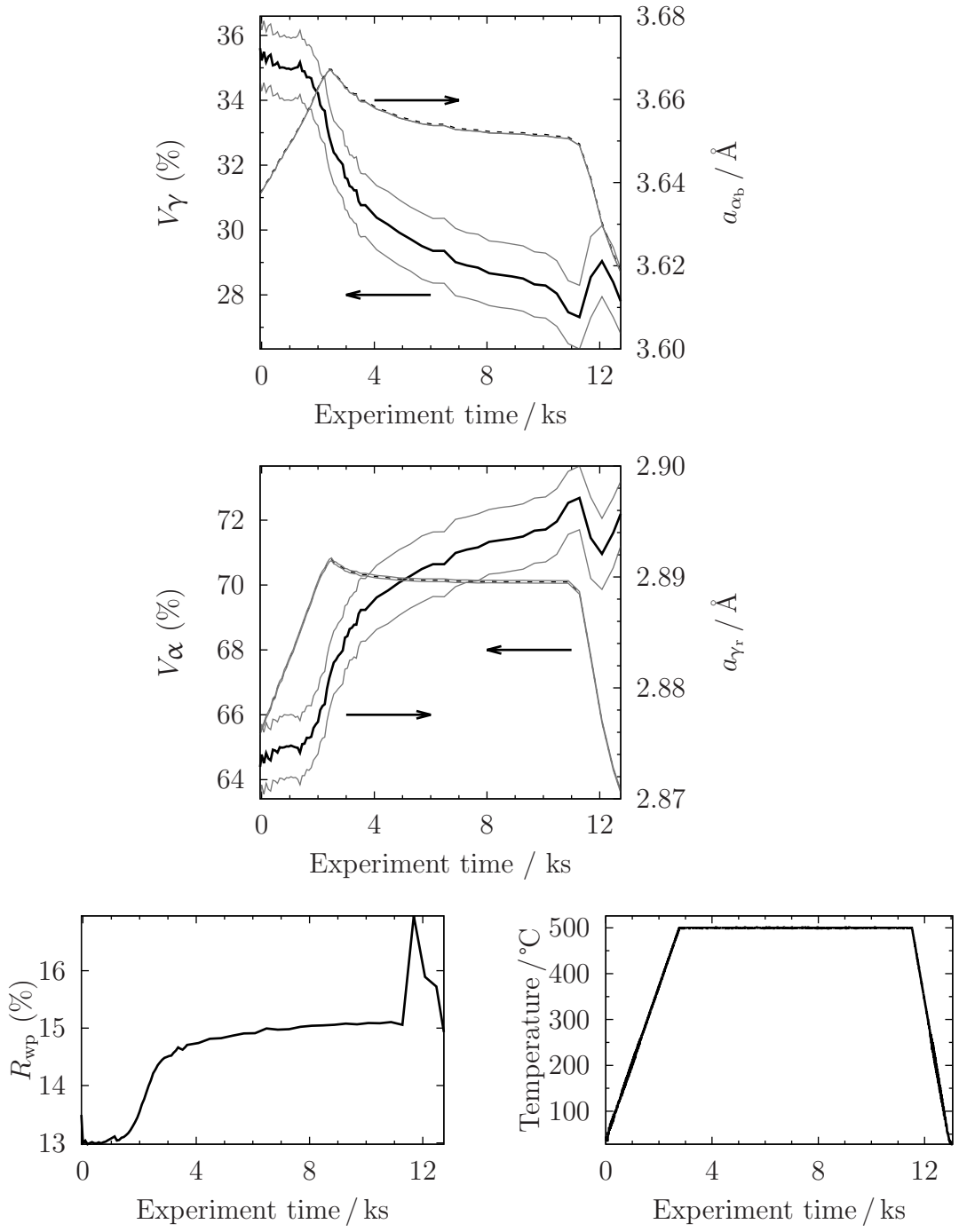

Figure 8.14: Rietveld refinement results for tempering Alloy 9 transformed at 300 ℃. Grey lines represent ± one standard error. Arrows indicate the the relevant axis for each dataset.

a lattice parameter of 2.881 Å [314]. With a large amount of nickel and aluminium present, it is reasonable that β-NiAl could form at 600 ℃ (figure 6.6(a)). This result is entirely consistent with that of Teng et al., made using neutron diffraction of Fe–13.0 Ni–18.9 Al.9.8 Cr–1.8 Mo (at.%), however, no micrographic evidence of β-NiAl could be found.

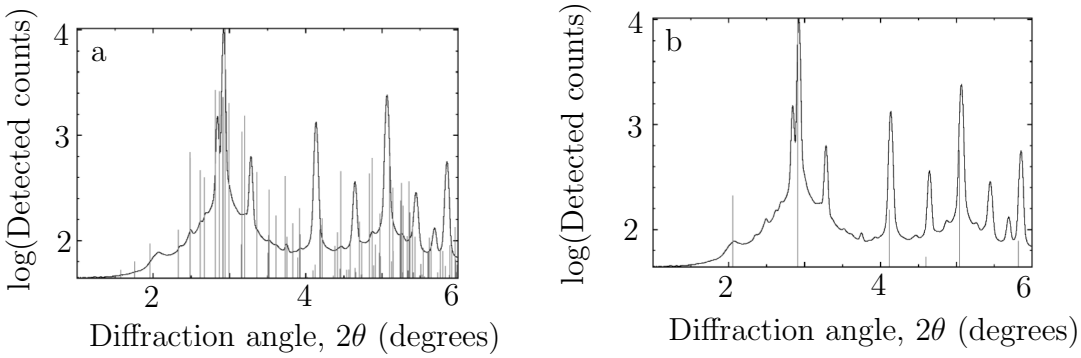

Figure 8.15: Synchrotron X-ray diffraction data of Alloy 9 after tempering at 600 ℃ for ≈ 1 h overlaid with calculated peaks for (a) cementite and (b) β-NiAl.

Figure 8.16 shows microstructural features of Alloy 9 that was transformed at 225 ℃ and tempered at 600 ℃ for ≈ 1 h. The microstructure appears virtually identical to the as-transformed condition, apart form the presence of martensite plates in some retained austneite films (figure 8.16(a) cf. figure 7.41). Before tempering, the as-transformed microstructure of a sample of Alloy 9 transformed at 250 ℃ was measured to be 613 ± 3 HV10 and after exposure was found to be 580±6 HV10. This is consistent with the retention of ductile austenite and the loss of carbon from solid solution, which is not fully compensated for by precipitation of cementite and β-NiAl.

These results were confirmed by neutron diffraction experiments conducted on Alloy 9 at the HRPD beamline at ISIS neutron diffraction facility, Didcot, U. .K. Austenite persists after a tempering treatment at 600 ℃ (figure 8.17(a) (note that the order of the peaks is reversed relative to synchrotron X-ray diffraction results). As expected, an identical experiment on a conventional nanocrystalline bainite, Alloy 10 (composition in table 8.2), which has not been designed to improve thermal

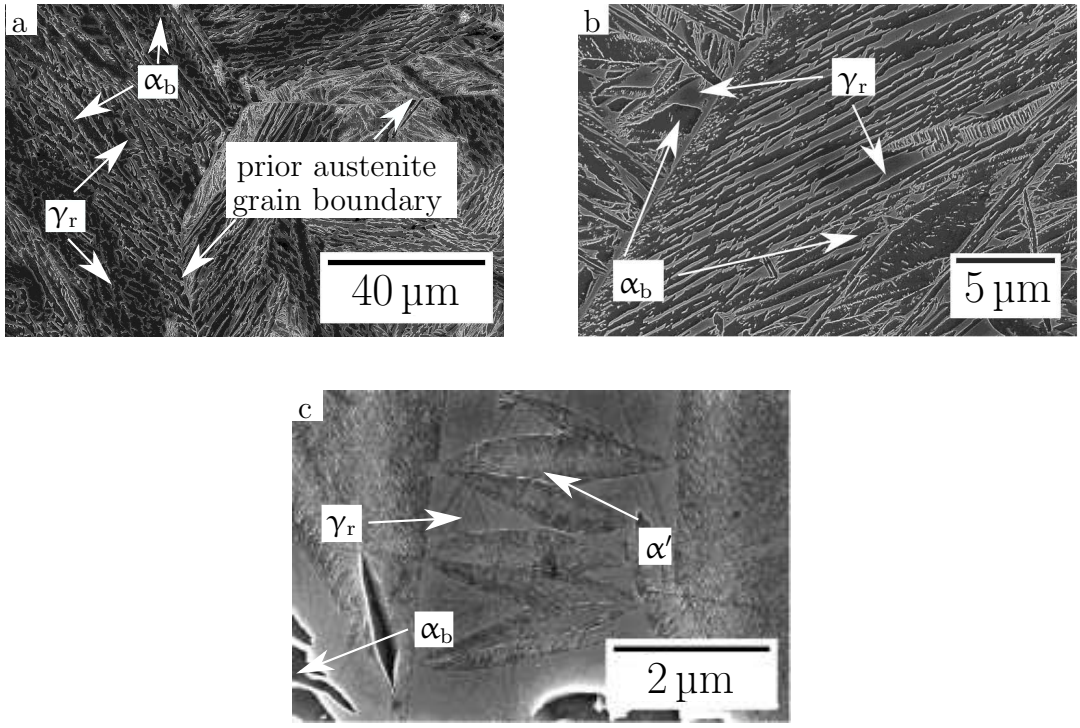

Figure 8.16: Film structure of Alloy 9 after transformation at 225 ℃ and tempering at 600 ℃ for 1 h. The microstructure is largely unaffected by tempering, apart from the development of martensite plates in the retained austenite films.

stability shows that austenite does not survive tempering (figure 8.17(b)).

C	Mn	Si	Cr	Co	Al	Mo
0.78	1.95	1.49	0.97	1.60	0.99	0.24

Table 8.2: Composition of Alloy 10 used in neutron diffraction experiments (wt%).

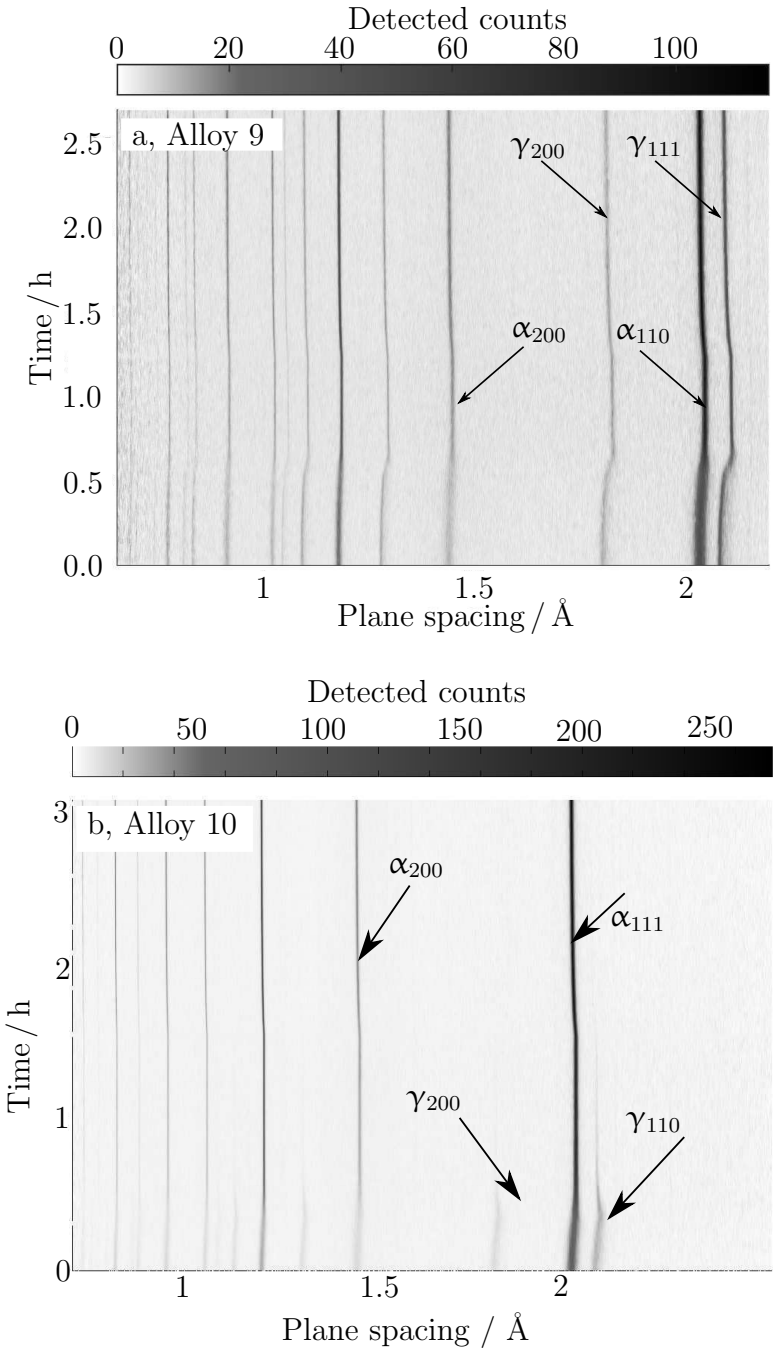

Figure 8.17: Results of neutron diffraction experiments on samples transformed at 200 ℃ and tempered at 600 ℃.

Chapter 9

Mechanical properties of optimised alloys

Alloy 8 and Alloy 9 were subjected to tensile, fracture toughness, fatigue and creep tests at both ambient temperature and at 450 °C. No creep data has ever been published for nanocrystalline steels and very little fatigue data is available, with the exceptions of [201, 225, 315–317]. The data in this chapter therefore represent a significant addition to literature.

Tests were performed on samples in the as-transformed condition and after additional tempering (table 9.1) by Incotest Ltd., Hereford, U. K. and Westmoreland Mechanical Research and Testing Ltd., Banbury, U. K, respectively. The tempering treatment is expected to simulate the worst-case scenario for thermal exposure during the service life of aeronautic gas turbine engine components that may utilise nanocrystalline steels [318]. Each testpiece was transformed and, if necessary, tempered as a blank that was larger than the mechanical testpiece dimension and one testpiece was machined from the centre of each blank. This prevents decarburisation in the final testpieces.

	Austenitisation	Transformation	Tempering
Temperature / ℃	1000	250	480
Time	30 min	24 h (Alloy 8) 5 d (Alloy 9)	8 d

Table 9.1: Transformation conditions for mechanical testpiece blanks.

9.1 Tensile tests

Tensile tests were conducted on cylindrical samples according to ASTM E21-09 and following industry standards of geometry (figure 9.1) and test conditions. A constant crosshead speed of $0.006\,\mathrm{min}^{-1}$ was used and all tests were run to failure.

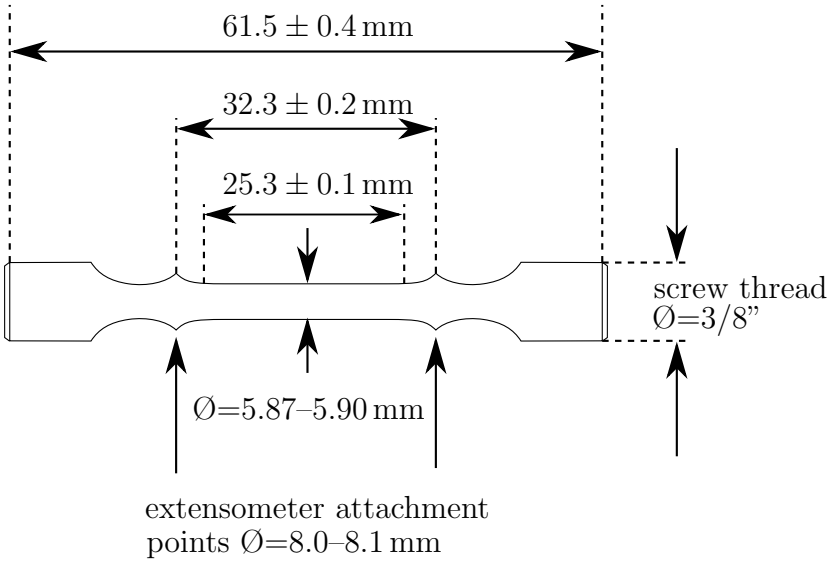

Figure 9.1: Sample geometry for tensile tests. All testpieces were machined from blanks after heat treatment to a maximum surface roughness of 3 mm in the gauge volume and 5 µm elsewhere.

Results are are given in table 9.2. Alloy 8 consistently exhibits a higher strength than Alloy 9 exposed to the same heat treatment, consistent with its higher car-

bon content and smaller grain size. Tempering also increases the 0.2% proof stress and ultimate tensile strength of both alloys, consistent with the transformation of austenite to the less-ductile ferrite and the precipitation of cementite. The measured ambient temperature proof stress and ultimate tensile strength of Alloy 8 are consistent with other nanocrystalline steels reported in literature (table 2.2), as is the elongation at failure compared to a nanostructured steel with 3 wt% silicon [106]. The alloy design of Alloy 8 to improve thermal stability has, therefore, not compromised mechanical properties. Alloy 9 has lower strength than the nanocrystalline steels reported in table 2.2, consistent with its lower carbon content. The reduction of area to failure is, however, greater than that reported by García-Mateo et al. [106] in a conventional nanocrystalline steel, consistent with the higher retained austenite content of Alloy 9, which accommodates deformation, by allowing dislocation motion and potentially by the TRIP effect. García-Mateo et al. noted that 15% retained austenite remained close to the fracture surface following tensile tests. This is above the percolation threshold (approximately 10% [92, 103–106, 192, 261, 282, 309, 310]), implying that failure occurred before austenite percolation was lost. The same study also found that raising the transformation temperature from 200 °C to 250 °C increases in the reduction of area at failure from 7% to 32%. The authors surmised that this was because the sample transformed at 250 °C had less carbon in the austenite and a wider distribution of blocky austenite grain sizes and carbon contents, leading to a wider distribution of austenite strengths and carbon contents. In the current experiments, this is analogous to the move from Alloy 8 to Alloy 9.

Fractographs of both alloys tested in the as-received condition showed extensive ductile cleavage. The appearance of both alloys was very similar to that in Hull [319, figure 8.18] depicting ductile cleavage in Fe–0.2 C–1.4 M (wt%). Alloy 8 showed ductile cleavage across almost all the fracture surface, which was predominantly flat. By contrast, only the central region of Alloy 9 showed cleavage, with a large proportion of the surface lying at 45°to the tensile axis in a classic cup-and-cone fracture (c.f. [319, figure 8.17]). This is consistent with the higher σ_{UTS} of Alloy 8, delaying final fracture until cracks had consumed a large proportion of

Alloy	Temper	Test temp.	0.2% proof stress / MPa	σ_{UTS} / MPa	Failure elong. (%)	Red./ of area (%)
Alloy 8	×	ambient	1432	1737	6.7	19.5
			1540	1838	6.6	21.2
Alloy 8	×	450 °C	972	1139	27.5	88.1
			1035	1170	27.5	84.6
Alloy 9	×	ambient	1015	1435	10.5	34.9
			1006	1429	11.9	42.6
			990	1446	12.5	45.4
			996	1437	12.1	43.8
Alloy 9	×	450 °C	791	894	23.5	81.9
			766	859	29.2	85.3
Alloy 8	✓	ambient	1767	1795	0.4	1.8
			N/A	1717	0.4	1.6
Alloy 9	✓	ambient	1615	1941	1.4	3.0
			1591	1893	1.2	3.0

Table 9.2: Tensile test results for Alloy 8 and Alloy 9 in as-transformed and tempered conditions. All tests performed at a constant crosshead speed of $0.002\,\mathrm{mm\,min^{-1}}$.

the cross sectional area while comparatively small proportion of the cross-sectional area had to be cracked to obtain failure of Alloy 9.

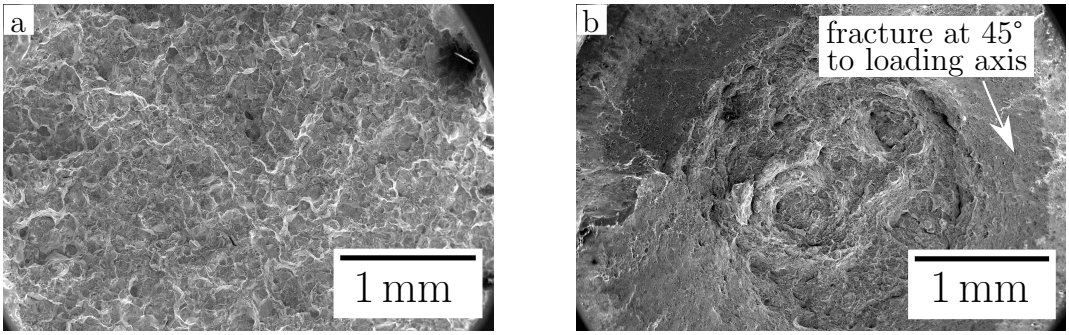

Figure 9.2: Fracture surfaces of (a) Alloy 8 and (b) Alloy 9 after tensile testing in the as-transformed condition. The region labelled as lying at 45° is involved in cup-and-cone failure.

Tempering at 480 °C for 8 d results in both alloys becoming stronger and less ductile. Stress-strain curves for each alloy are given in figure 9.3. This is consistent with the decomposition of austenite to cementite and ferrite [104, 226]. The loss of carbon from solid solution does not lead to a loss of strength as the high density of interfaces dominates the strength in the as-transformed steel. The loss of ductility in Alloy 9 is surprising, given that ≥ 20 vol.% austenite persists after tempering, but is consistent with the perceived change in failure mode to quasi cleavage (figure 9.4(b)). No evidence was found of martensite at or below the fracture surface at any stage of the current study. However, it was found that the austenite lattice parameter decreased due to tempering (figures 8.11–8.14). This implies that carbon had left solid solution and precipitated as cementite (figure 8.15(a)). This cementite could restrict ductility and reduce strength, and it is noticeable that the fracture surface contains a significant amount of intergranular cleavage (figure 9.4(b)), which is indicative of reduced strength and toughness compared to a fracture surface that exhibits entirely ductile cleavage (c.f figure 9.2(b)).

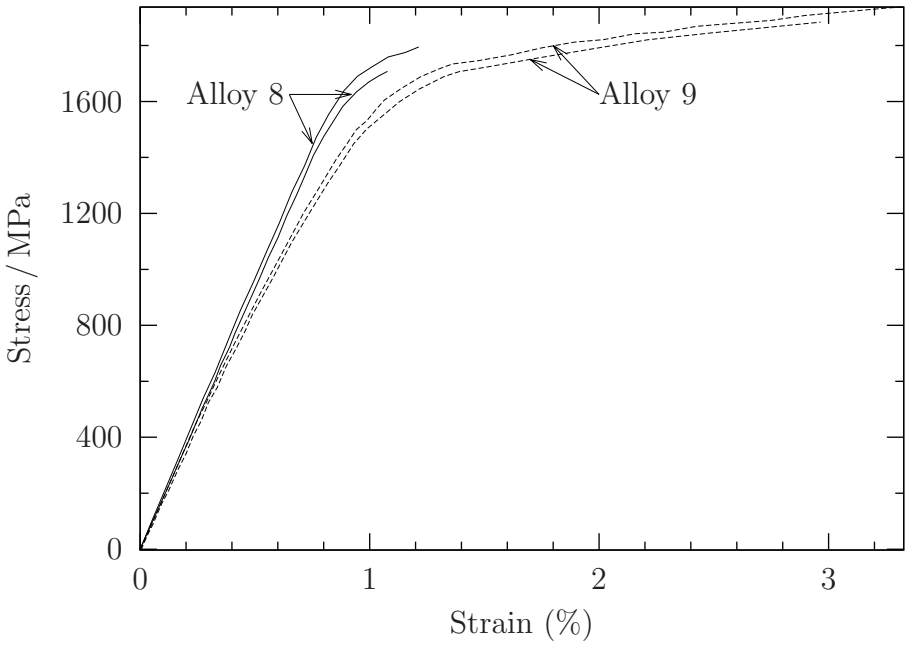

Figure 9.3: Stress-strain curves measured during tensile tests of two samples each of Alloy 8 and Alloy 9 after tempering at 480 ℃ for 8 d.

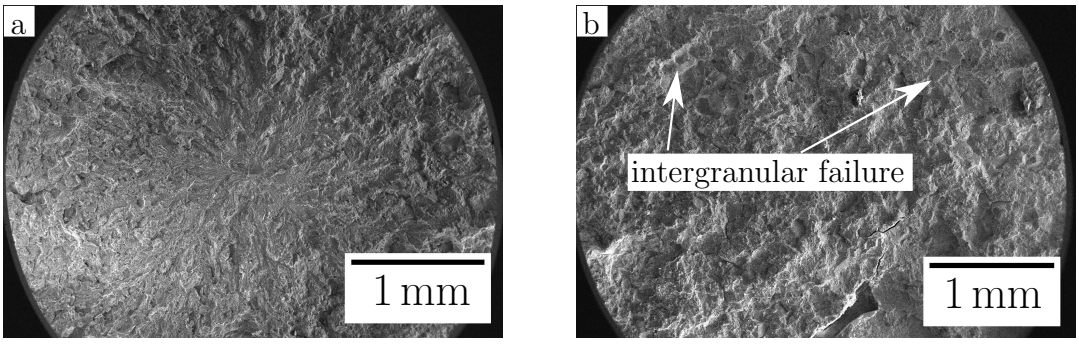

Figure 9.4: Fracture surfaces of (a) Alloy 8 and (b) Alloy 9 tempered at 480 ℃ for 8 d after tensile testing. The failure in Alloy 8 appears to have initiated very close to the centre of the sample. Tempering appears to have changed the failure mode of Alloy 9 from ductile cleavage to to quasi-cleavage.

9.2 Fracture toughness

Fracture toughness was measured using crack-tip opening displacement (CTOD) according to standard ASTM E399-12E3 and using the sample geometry in figure 9.5. Load was applied with a ratio of minimum stress to maximum stress, $R = 0.1$. Following Dieter [320, page 358], the following dimensions apply to the samples tested here: $a = 10.5\,\text{mm}$, $W = 26\,\text{mm}$ and $B = 13\,\text{mm}$, (figure 9.5). Failure was deemed to have occurred when the crack-tip opening displacement crossed the 95% secant of the initial linear region of the data (figure 9.6). To form a valid measurement of K_{Ic}, conditions must be satisfied as described in the standard ASTM E399-12E3, to ensure plane strain at the crack tip during failure. If these conditions are not met, the measured toughness is designated K_{Q} and is not a material property, but does allow comparison between samples.

$$K_{\text{Q}} = \frac{P_{\text{Q}}}{W^{1/2}B}\left[29.6\left(\frac{a}{W}\right)^{1/2} - 185.8\left(\frac{a}{W}\right)^{3/2} + 655.7\left(\frac{a}{W}\right)^{5/2} - 1017.0\left(\frac{a}{W}\right)^{7/2} + 638.9\left(\frac{a}{W}\right)^{9/2}\right] \tag{9.1}$$

All measured fracture toughness values are given in table 9.3. Alloy 8 exhibits a toughness significantly higher than previously-reported values of bulk nanocrystalline bainitic steels of similar strength (cf. table 2.2). It is clear that the large quantity of silicon in Alloy 8 has not led to embrittlement. This may be explained by the lower carbon content of Alloy 8 compared to the alloys listed in table 2.2, which all contained $\geq 0.78\,\text{wt}\%$ carbon. The austenite in Alloy 8 is therefore able to deform more readily and extensively as dislocations are less pinned by Cottrell atmospheres. This increase in high-stress deformation represents an energy-absorbing mechanism and will contribute to toughness.

It is also evident that as-transformed Alloy 9 is extremely tough. No valid measurements of K_{Ic} were possible due to the unexpectedly-high toughness. Budget constraints prevented retesting with larger testpieces. However, the comparison with the K_{Q} measurement of Alloy 8 suggests that Alloy 9 is significantly tougher, as is expected given the lower bulk carbon content, much higher level of nickel and

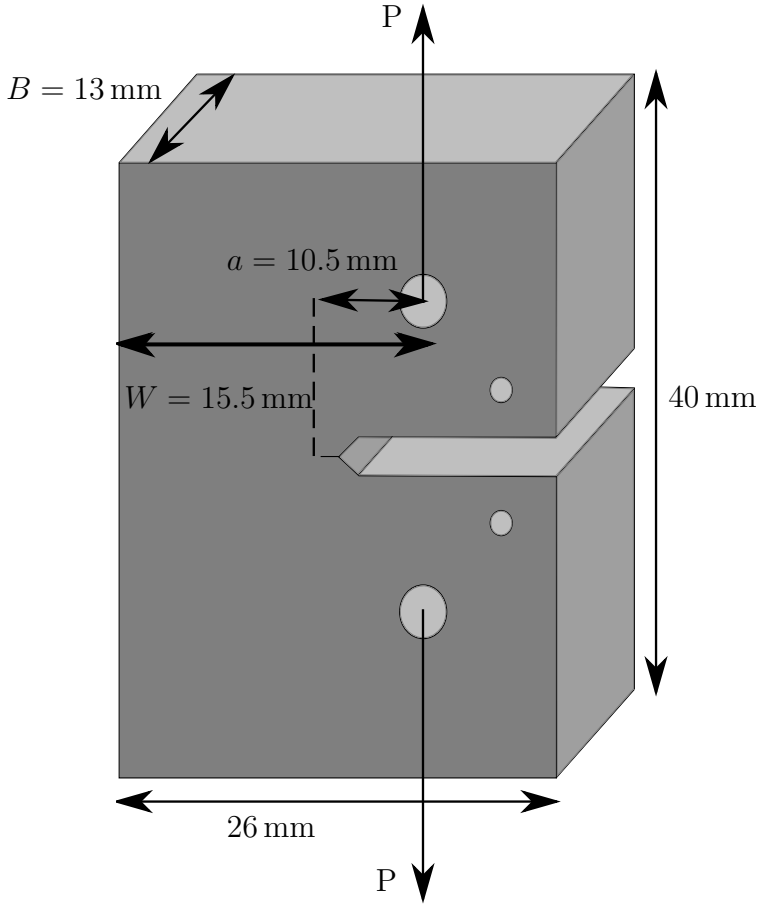

Figure 9.5: Schematic drawing of a compact tension testpiece tested under a stress, P. The labels a, B and W refer to the measurements used in Dieter [320, equations 11-19].

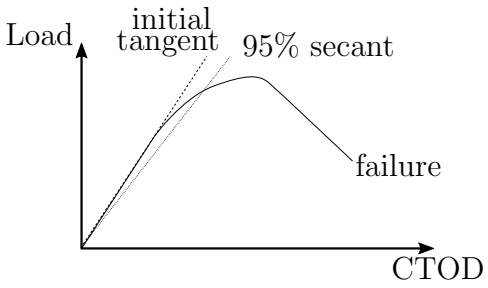

Figure 9.6: Schematic CTOD test data for Alloy 8, showing 95% secant and point of failure.

higher content of retained austenite. Should Alloy 9 meet strength requirements for a given application, its improved thermal stability and impressive toughness make it a very good candidate material.

Alloy	Tempered	Test temperature / ℃	K_Q / MPa m$^{\frac{1}{2}}$	K_{Ic} / MPa m$^{\frac{1}{2}}$
Alloy 8	×	ambient	60.2	69.0
Alloy 9	×	ambient	105.6 101.9	
Alloy 8	×	150	106.0 126.0	
Alloy 9	✓	ambient	19.8	

Table 9.3: Compact tension results for Alloy 8 and Alloy 9. Tempering was at 480 ℃ for 8 d. Alloy 8 tested after tempering and Alloy 9 tested at 150 ℃ failed during pre-cracking and so no data may be presented.

Two samples each of both Alloy 8 and Alloy 9 tempered at 480 ℃ for 8 d were sent for fracture toughness testing. All but one sample failed during pre-cracking. It was not possible to repeat the tests due to budget constraints. It was therefore decided to perform Charpy V-notch tests to gauge the toughness of the tempered alloys as a cost-effective alternative that was likely to produce results. The single fracture toughness measurement obtained for tempered Alloy 9 of 19 MPa m$^{\frac{1}{2}}$f, is close to the fracture toughness of conventional nanocrystalline steels in the as-transformed condition (cf. table 2.2), demonstrating the excellent potential of Alloy 9 for high-temperature applications. The residual toughness of Alloy 9 is likely due to the persistence of ductile austenite and the presence of nickel within that austenite, which raises the stacking fault energy. This allows easier dislocation glide and therefore mechanically stabilises the austenite [251, 321, 322].

9.3 Charpy impact

Charpy tests were performed on tempered samples of both Alloy 8 and Alloy 9 with the geometry given in figure 9.7. The results are summarised in table 9.4.

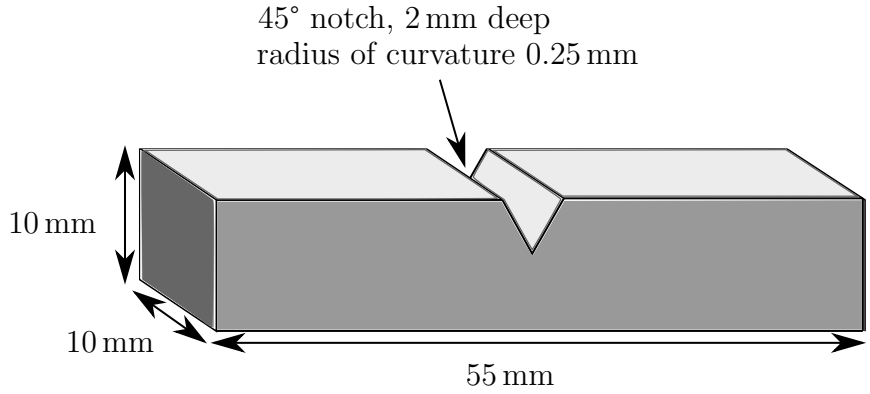

Figure 9.7: Schematic drawing of sample geometry for Charpy impact tests performed on tempered Alloy 8 and Alloy 9.

Alloy	Impact energy / J^{-2}
Alloy 8	11.5
	11.5
Alloy 9	46.8
	49.5

Table 9.4: Ambient temperature Charpy impact results for Alloy 8 and Alloy 9 tested after tempering at 480 °C for 8 d.

There are several equations that may be used to compare Charpy V-notch impact test results to fracture toughness data [323]. Of these, the Rolfe-Novak-Barsom equation (equation 9.2, where C_V is the Charpy V-notch impact energy in Joules and other symbols have their usual meanings) provides a straightforward and well-tested conversion [324–327]. It is only possible to convert from Charpy impact energy to fracture toughness above the ductile-brittle transition tempera-

ture (DBTT). This is because fracture toughness tests are performed such that the sample fails with plane strain and in a ductile manner. If impact testing measures the absorbed energy for brittle failure, different processes occur during failure and there is no correspondence between the tests. For ductile failures during impact testing, both tests are causing similar fractures to occur and so a conversion is possible. There are further restrictions on the use of the Barsom-Rolfe-Novak equation that the yield stress of the material satisfies $270 < \sigma_{\mathrm{y}} \,/\, \mathrm{MPa} < 1700$ and the measured Charpy V-notch impact energy must lie in the range $4 < \mathrm{CVN} \,/\, \mathrm{J} < 82$ [323]. Both of these conditions are met for both alloys so a comparison with the fracture toughnesses of the as-transformed specimens is possible. An alternative relationship is Robert's lower bound (equation 9.3), which provides a more conservative estimate of K_{Ic}. The calculated fracture toughness values are given in table 9.5, using Young's moduli calculated from the elastic loading of samples prior to creep tests. Both conversions predict that the toughness has decreased significantly after tempering, consistent with the loss of austenite.

$$K_{\mathrm{Ic}} = \left(0.228 E C_{\mathrm{V}}^{\frac{3}{2}}\right)^{\frac{1}{2}} \tag{9.2}$$

$$K_{\mathrm{Ic}} = 8.47 C_{\mathrm{V}}^{0.63} \tag{9.3}$$

$$\tag{9.4}$$

9.4 Fatigue

Fatigue tests were conducted on as-transformed samples in accordance with ASTM E466-07. Due to budget constraints, tests were limited to six per alloy, each to a maximum of 50,000 cycles. The sample geometry is given in figure 9.8 and the schematic stress cycle is shown in figure 9.9. Test were performed at both ambient temperature and 450 ℃ for both alloys. The number of cycles to failure are plotted against peak applied stress in figures 9.10 and 9.13. Also plotted are the measured ultimate tensile strengths (σ_{UTS}) in the as-transformed condition (table 9.2) and curves fitted to the modified Basquin equation (equation 9.5, where σ_{max} is the

Alloy	C_V / J	E / GPa	K_{Ic} / MPa m$^{\frac{1}{2}}$ (Rolfe-Novak-Barsom)	K_{Ic} / MPa m$^{\frac{1}{2}}$ (Robert's lower bound)
Alloy 8	8.5	190	33	29
	8.5	190	33	29
Alloy 9	34.5	170	89	58
	36.5	170	92	60

Table 9.5: Fracture toughness estimates based on Charpy V-notch impact energies and converted using the Rolfe-Novak-Barsom equation and Robert's lower bound. Young's moduli were derived from the elastic loading of samples at the beginning of creep tests.

peak stress, N is the number of cycles to failure and a and b are fitted constants) [328, 329, equation 7.1] using Marquardt-Leverberg linear regression. The fitting parameters for each condition are given in table 9.6. It was assumed that when the peak stress exceeded σ_{UTS}, the failure would not be due to fatigue and the effective number of cycles to failure would be 1.

$$\sigma_{max} = a\,(2N)^{-b} \tag{9.5}$$

The results of fatigue tests on Alloy 8 are shown in figure 9.10. No fatigue limit was detected, although Peet et al. [201] recorded a fatigue limit of 855 MPa in a similar nanocrystalline steel using the same waveform and ratio of peak to minimum stress, R and further tests at lower peak applied stresses may detect such a limit in the current alloys. The peak stresses used here were those that were considered most relevant to potential engineering applications.

The consistency in the number of cycles to failure between each pair of Alloy 8 samples suggests that failure was not being initiated at occasional large flaws, which would cause variations in fatigue life, but rather flaws which are consistent within the microstructure. This is expected for the (VIM/VAR) processing route, which results in a very clean steel with few defects. The subsequent hot-rolling

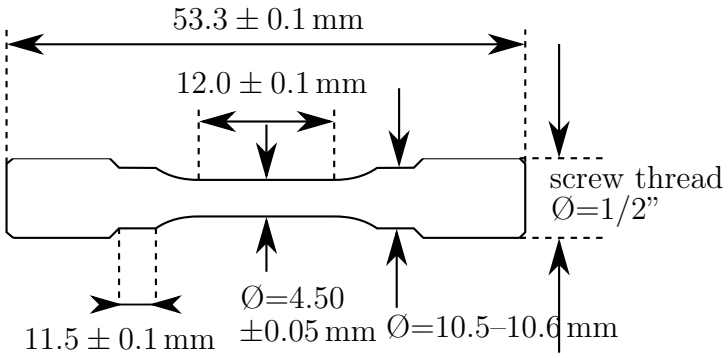

Figure 9.8: Schematic drawing of a fatigue specimen used in the current study. The screw threads of each sample were shot peened to prevent failure outside the gauge length.

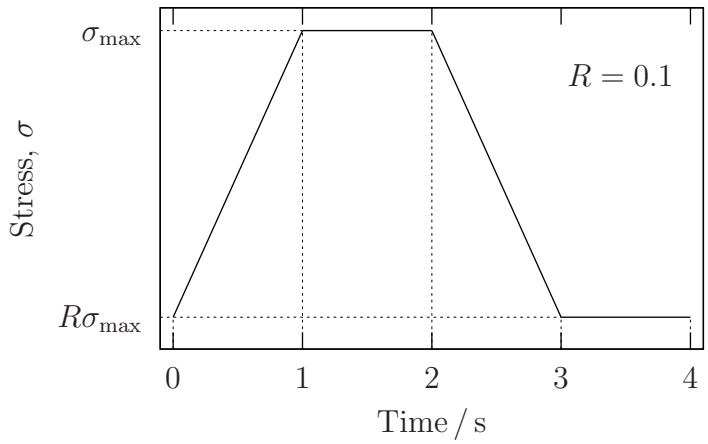

Figure 9.9: Waveform of one stress cycle for all fatigue tests performed in this study. This waveform is commonly referred to as a “1-1-1-1 trapezoid”.

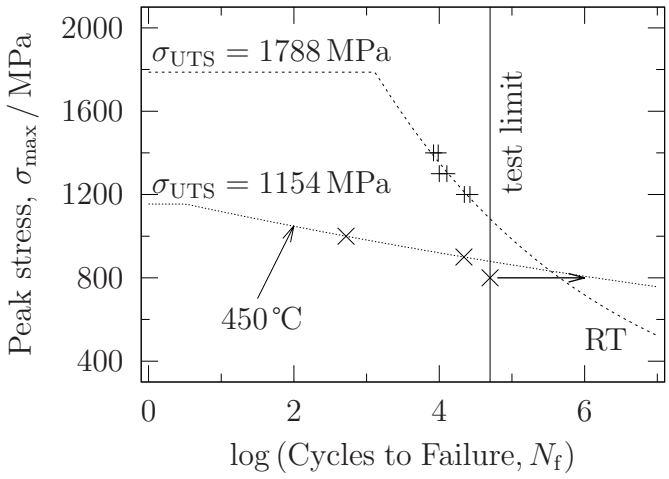

Figure 9.10: Fatigue results for Alloy 8 showing data at ambient temperature ("RT", +) and 450 ℃ (×). The horizontal lines are the measured σ_{UTS} at the relevant temperature (section 9.1 and the curves are fitted to the data according to the modified Basquin equation (equation 9.5).

with a reduction ratio of 7:1 will remove any pores. The less clean processing route for Alloy 9 is one possible explanation for the greater difference in measured fatigue lives for a given stress in Alloy 9 (figure 9.13).

In most cases, examination of the fracture surfaces revealed no obvious initiation site. Where a likely initiation site could be identified, no sample exhibited obvious flaws such as pores, inclusions or precipitates visible at or near the site, although it is always possible that particular flaws did initiate fatigue failures and these particles dropped out during failure. The fracture surface (figure 9.11) of a sample of Alloy 8 tested at 450 ℃ shows predominantly ductile cleavage, with regions at the edges that are typical of fast fracture, the surfaces of which lie at approximately 45°to the rest of the fracture surface. These regions were the last to fail during testing. The region immediately around the initiation site shows no evidence of striations or beach marks and is ≈ 100 µm wide, consistent with the observations of Peet et al. (see [table 1 201]). Samples tested at ambient temperature with lower other peak stresses showed similar ductile cleavage, consistent with the work of García-Mateo et al., but none of them showed discernable initiation

sites.

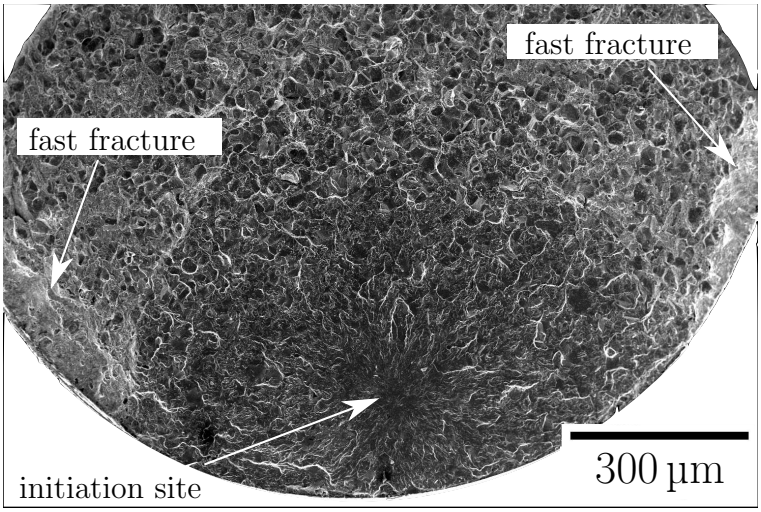

Figure 9.11: Fractograph of failed sample of Alloy 8 after fatigue testing at 450 °C with a peak stress of 900 MPa. The initiation site is surrounded by a dark, flat region. Outside this, the fracture surface is mottled, consistent with ductile rupture. The regions labelled "fast fracture" are brighter than the ductile region to the naked eye and the surface is at 45°to the rest of the fracture surface.

The rapid failure of the samples of Alloy 8 tested at 450 °C with a peak stress of 1000 MPa is not surprising as the peak stress exceeds the yield stress (cf. table 9.2) and hence leads to rapid damage accumulation. The resistance to fatigue failure at 450 °C with a peak stress of 800 MPa suggests that little damage is being accumulated. Since the test is performed with peak stresses close to the yield stress, it is likely that dislocations are being created. However, since the homologous temperature is ≈ 0.4, recovery is likely to occur, which will reduce the rate of net damage accumulation and hence extend fatigue life.

It was not possible to achieve a fatigue failure in Alloy 9 at 450 °C within the limit of 50000 cycles. The peak stress used, 800 MPa, was close to the ultimate tensile strength which was assessed to be as low as 859 MPa at 450 °C (table 9.2) and so it was not possible to raise the peak stress to induce failure without the risk of exceeding σ_{UTS}. Failure in this case would be tensile rather than fatigue.

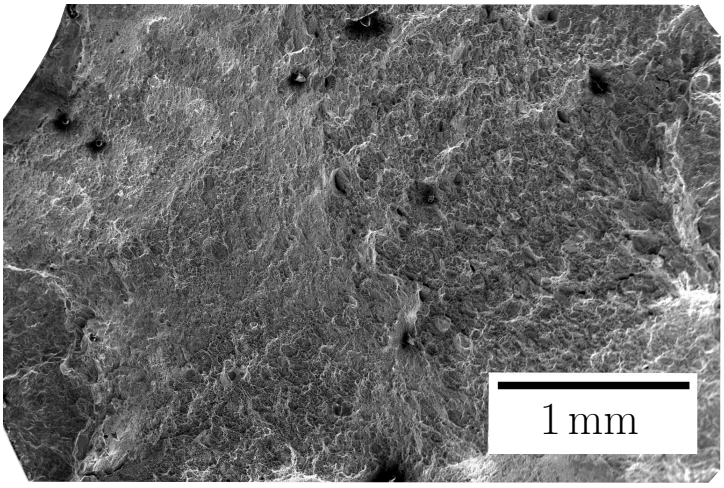

Figure 9.12: Fractograph of Alloy 8subjected to fatigue testing at ambient temperature with a peak stress of 1400 MPa. No initiation site could be observed anywhere on the fracture surface of either half of the failed sample.

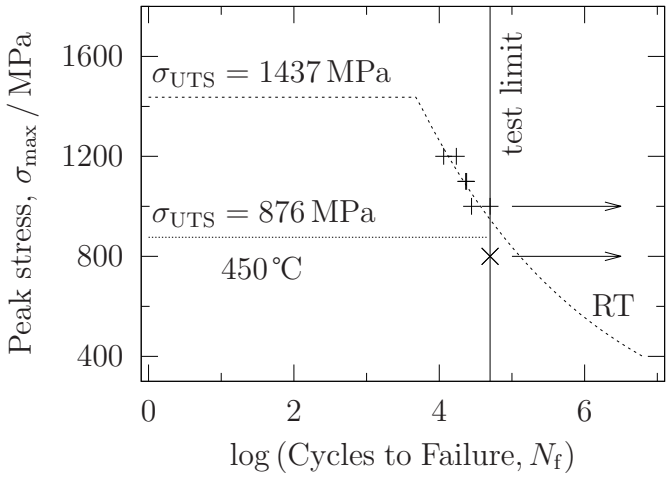

Figure 9.13: Fatigue test results for Alloy 9. Data are shown for tests performed at both ambient (+) and unit[450]℃ (×). Tests marked with an arrow did not fail with in the 50,000 cycle limit. No S–N curve is shown for tests conducted at 450 ℃ as no test resulted in a fatigue failure.

The fracture surface of a fatigue sample of Alloy 9 shows largely ductile cleavage (figure 9.14(a)), with some areas of fast fracture that failed last, as in Alloy 8. It was not possible to identify initiation sites in all samples, also similar to Alloy 8. In this fractograph, river lines are discernable radiating out across the zone immediately around the initiation site, which is around 200 µm across. The initiation site contains a string of pores extending from the surface to a depth of approximately 100 µm (figure 9.14(b)). At the end of these pores a particle, about 10 µm, which was identified as silica using EDX. The fracture surfaces of samples tested at 450 MPa and with other peak stresses were not significantly different to that shown in figure 9.14 and initiation sites were only found on a small number of samples.

Alloy	Test temperature / °C	a / MPa	b
Alloy 8	ambient	5280	0.138
	450 °C	12210	0.028
Alloy 9	ambient	3696	0.178

Table 9.6: Parameters of the modified Basquin equation (equation 9.5) fitted to fatigue life data. Tests where the samples did not fail were not included in the fitting.

Zhang et al. [317] examined low-cycle (i.e. strain-controlled) fatigue of bainitic steels and found that nanocrystalline bainite (called "low temperature bainite" in Zhang et al. [317]) exhibited slower fatigue crack growth than lower and upper bainite formed in the same alloy, which was attributed to a finer grain size and larger misorientation between adjacent grains, measured by EBSD. These factors lead to more rapid blunting of fatigue cracks and slower crack growth.

Peet et al. [201] obtained a longer fatigue life than either of the current alloys (figure 9.15), consistent with a higher σ_{UTS} [201, 225]. Both of the current alloys exhibited large-scale ductile rupture, as was noted by García-Mateo et al. [225] in high-carbon steel. The consensus in literature is that the fatigue properties of nanostructured steel are promising and the current study has found that the

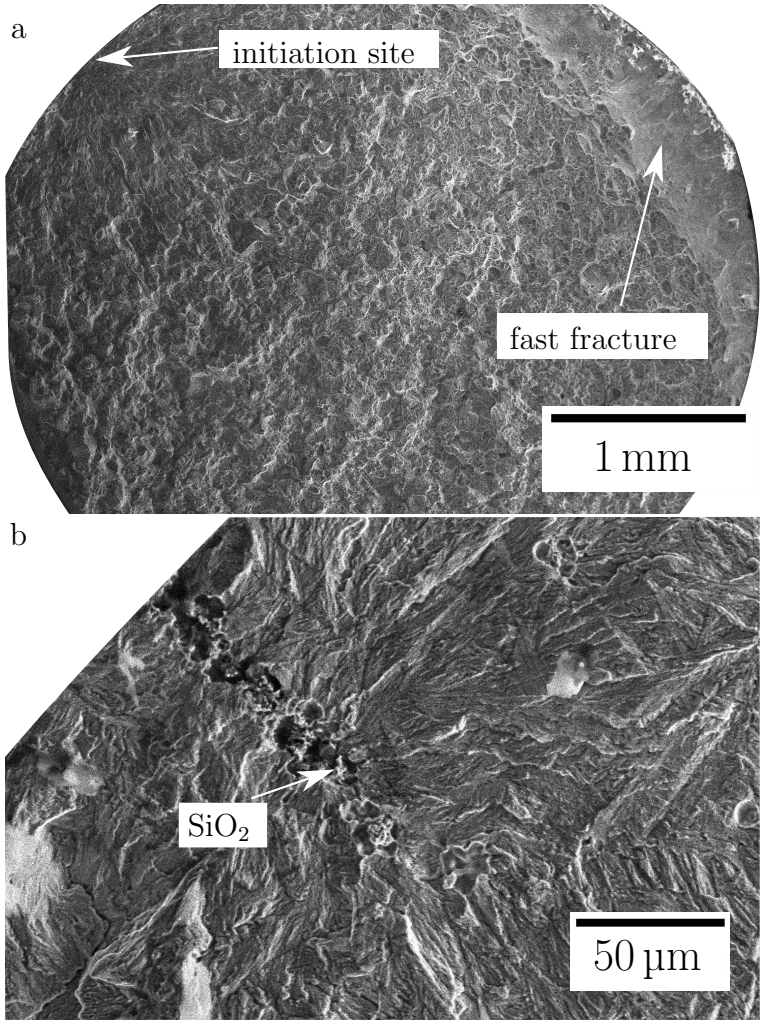

Figure 9.14: Fracture surface of a sample of Alloy 9 subjected to fatigue testing at ambient temperature with a peak stress of 1100 MPa. The fracture surface consists mostly of ductile cleavage with an initiation site and some areas of fast fracture that failed at the very final stages of testing. The initiation site contains a string of pores extending in from the surface. A silica particle lies at the end of this string of pores.

fatigue lives of the current alloys are consistent with those previously reported.

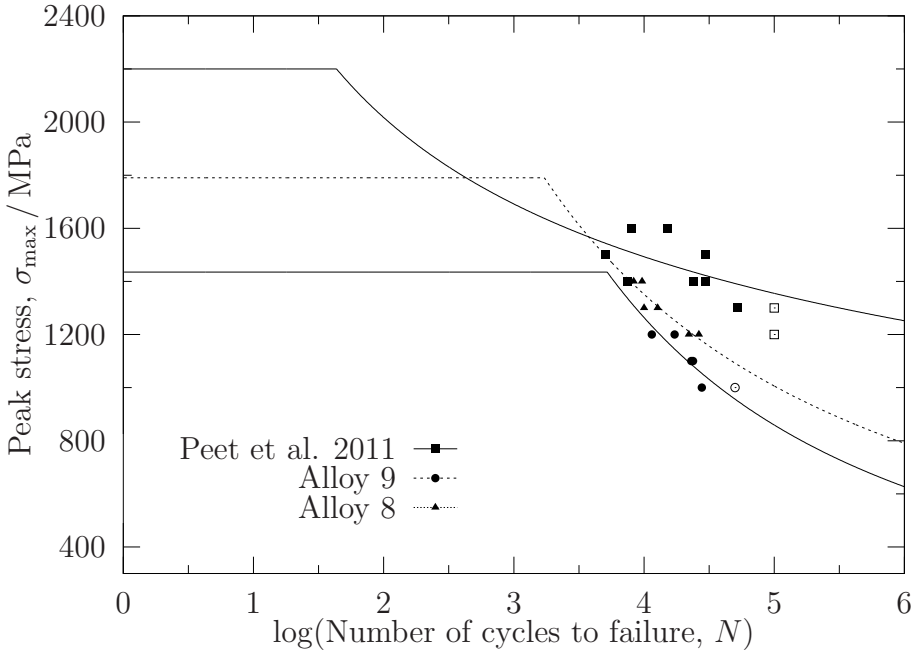

Figure 9.15: Assessed fatigue lives for Alloy 8, Alloy 9 and the alloy studied by Peet et al. [201]. The data are fitted with the modified Basquin relation (equation 9.5) and are limited to the reported σ_{UTS}. The fatigue lives of samples studied by Peet et al. were greater than the current alloys, consistent with the higher σ_{UTS} of the former. Open symbols represent samples that ran out without failure.

9.5 Creep

There are no reported creep results for nanocrystalline bainitic steels. This is because they were not originally intended for elevated temperature service. It is only with the production of more thermally-stable alloys such as Alloy 9 that creep data may be usefully assessed.

Creep tests were performed using the samples schematically drawn in figure 9.16, tested in accordance with ASTM 139-11 at 450 °C under 700 MPa constant stress. Both alloys showed good creep resistance.

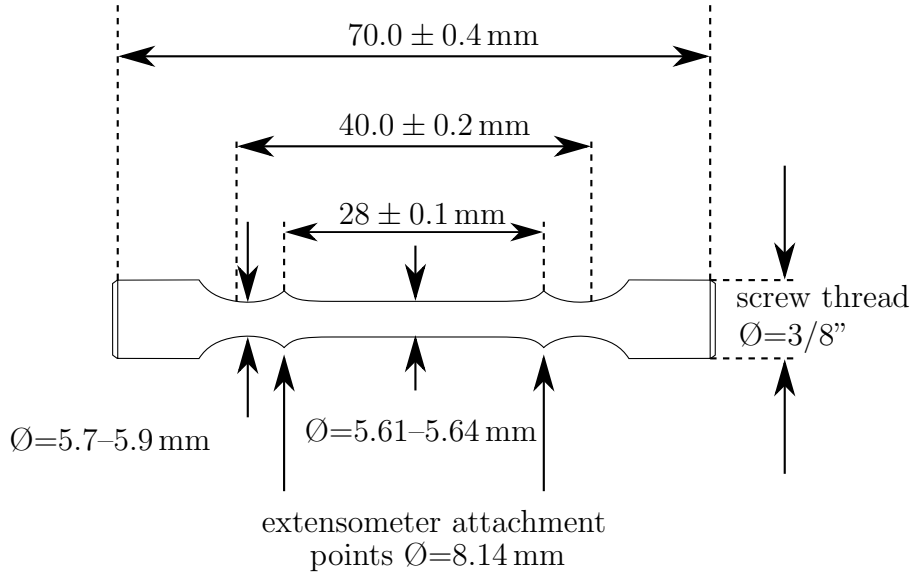

Figure 9.16: Schematic drawing of creep specimen.

Creep data for both the current alloys is given in figure 9.17. Two tests were carried out for each alloy, giving similar results in both cases. Alloy 8 exhibits better resistance to creep deformation than Alloy 9, although both alloys compare favourably to existing steels. For example, Jitsukawa et al. [330] collated an extensive database of 9 Cr–1 Mo (wt%) steels and reduced-activation martensitic steels for nuclear pressure vessels and found that stress levels of approximately 400 MPa corresponded to a creep life consistent with a Larson-Miller parameter of 20.5 (evaluated as $0.001T\,(26.4 + \log t_\mathrm{r})$ where T is the test temperature in Kelvin and t_r is the creep rupture time). The current alloys exhibit the same Larson-Miller parameter at a stress level of 700 MPa (figure 9.18). The ASM handbook on heat-resistant materials lists common classes of steel and selected other materials (figure 9.19) [331]. The current alloys survive approximately 100 h at 450 °C (823 K) under a constant stress of 700 MPa. This is competitive with 12 wt% Cr steels and is only outperformed by nickel alloys and maraging steels. Both of these alloy systems are orders of magnitude more expensive than nanocrystalline bainitic steel [12, 109, 332]

The form of figure 9.17 suggests that both Alloy 8 and Alloy 9 undergo primary

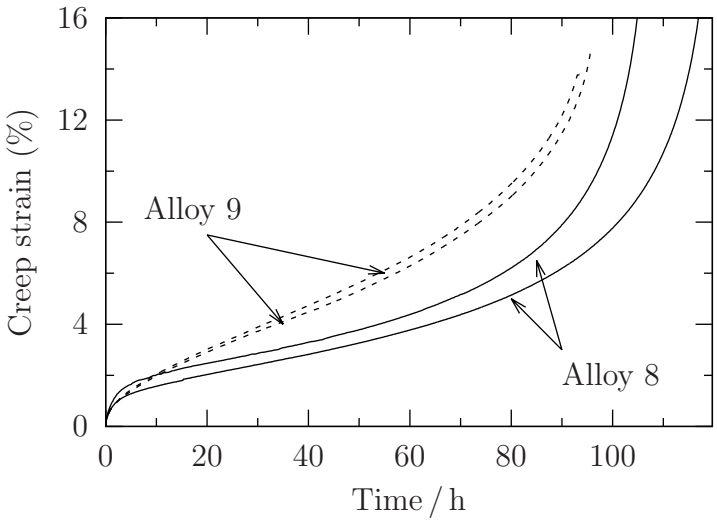

Figure 9.17: Measured creep data for two samples each of Alloy 8 and Alloy 9 under 700 MPa constant stress at 450 °C. The creep curve shows that creep is extensive in both time and strain after the minimum strain rate occurs.

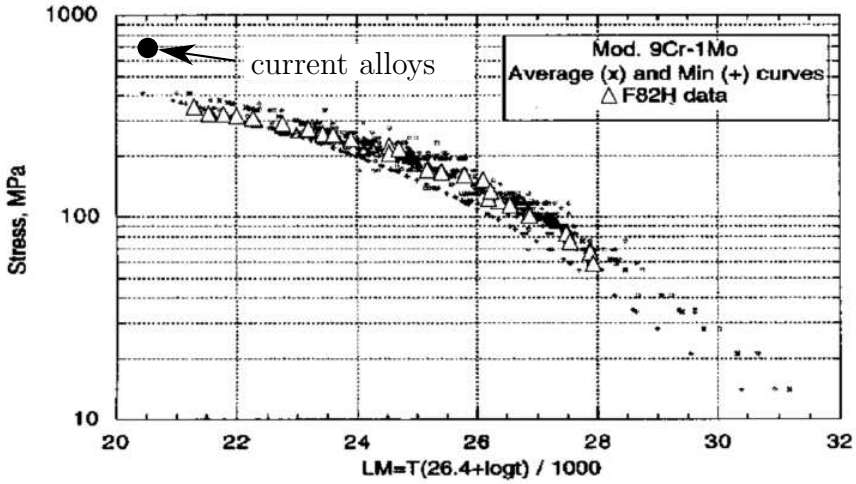

Figure 9.18: Comparison of current alloys to data for 9 Cr–1 Mo (wt%) (small crosses) and reduced-activation martensitic steel (triangles) collated by Jitsukawa et al. [330]. The current alloys outperform those studied by Jitsukawa et al. Figure reproduced with permission of Elsevier B. V.

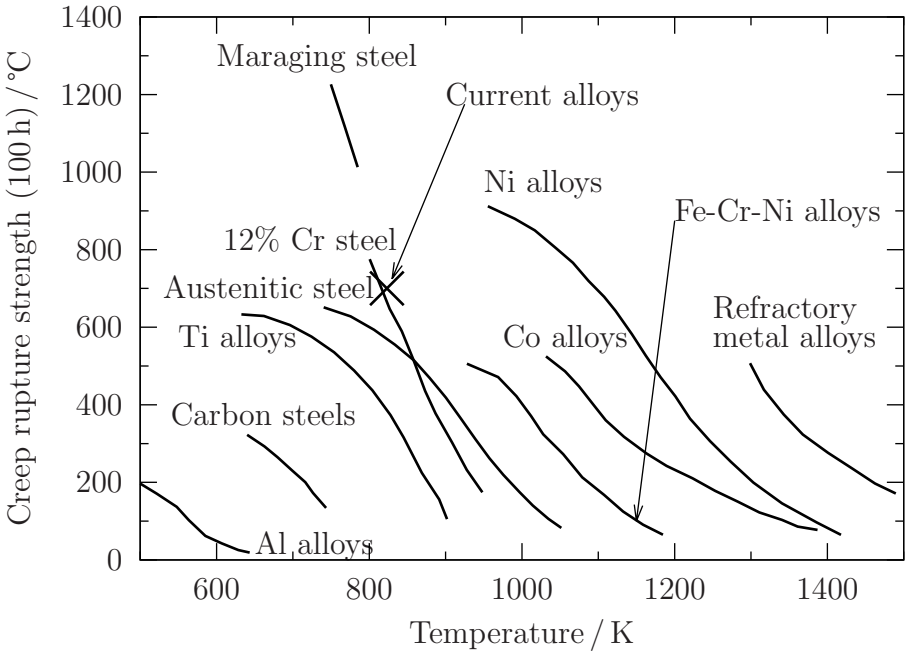

Figure 9.19: Comparison of typical creep performance of various steel grades and selected other materials [after 331] and comparison with the current alloys. Only maraging steels and nickel alloys outperform Alloy 8 and Alloy 9.

Alloy	Creep rupture life / h
Alloy 8	120
	107
Alloy 9	95.9
	93.6

creep which is complete within 10 h of the start of the test. Shortly after this, both alloys exhibit the minimum creep strain rates: at approximately 20 h in Alloy 9 and 30 h in Alloy 8. However, the time between the minimum creep rate and failure is markedly prolonged in both alloys, consistent with creep-resistant martensitic steels [333]. Nabarro and de Villiers [334] describe primary creep as consisting of grain boundary sliding and/or plastic deformation of grains with high Schmidt factors, resulting in work hardening and a redistribution of load to other less-favourably oriented grains. In this case, the vast majority of the grain boundaries are between bainitic ferrite and untransformed parent austenite, which are semi-coherent. The atomic correspondence across the interface makes grain boundary sliding extremely unlikely. It may, however, be possible for the incoherent interfaces at prior austenite grain boundaries to slide. At the test temperature (450 °C), the applied stress (700 MPa) is approximately 70% of the 0.2% proof stress of Alloy 8 and 90% of that for Alloy 9 (table 9.2). This suggests that the favourably-oriented grains could plastically deform, but since this initial deformation is likely to be confined to the ductile austenite, and the grain size is small, strain will be localised and work hardening is liable to be rapid.

Nabarro and de Villiers note that fine grain sizes are detrimental to both grain boundary sliding and diffusional creep [334, section 8.5.6]. However, in nanostructured bainite, the vast majority of grain boundaries are between retained austenite films and bainitic ferrite. These are semi-coherent boundaries and contain a well-ordered array of misfit dislocations. These boundaries will not act as efficient sources or sinks of vacancies as is the case for incoherent boundaries. Prior austenite grain boundaries are incoherent and can contribute to creep, but these are found infrequently in the structure, at a density associated with conventional grain sizes. Thus it is possible to obtain the strengthening from a fine grain structure without the penalties associated with short diffusion paths and easy grain boundary sliding. While the temperature and stress used in the current tests make it very likely that dislocation creep will be the dominant mechanism, vacancy flux is still required to allow the dislocations to overcome obstacles and mediate deformation. The use of semi coherent and coherent boundaries to pin dislocations in creep-resistant "co-

herent hierarchical precipitate" strengthened ferritic steels was reported by Song et al. [335] and is discussed in the case of TiAl/Ti_3Al by Nabarro and de Villiers [334, page 359–361], who note that semi-coherent boundaries contain networks of dislocations. These misfit dislocations could act as sources and sinks for vacancies due to climb of their edge components, but this is only significant for the late stages of deformation, with the dislocations anchored at the interfaces during the initial stages of creep to maintain the semi-coherent nature of the boundary. This gives rise to one possible explanation for the extensive creep life after the minimum strain rate occurs: the creep strain rate gradually increases as deformation occurs and progressively more misfit dislocations begin to undergo climb.

The appearance of a section of failed creep testpieces of both Alloy 9 and Alloy 8 contains severely elongated grain structure near the fracture surface, together with large numbers of voids. The voids in Alloy 9 lie predominantly perpendicular to the tensile axis and follow prior austenite grain boundaries (figures 9.20(a) and 9.20(b)). The voids in figure 9.20(c) do not obviously follow grain boundaries, as is seen in Alloy 9, but are otherwise typical of creep failure [e.g. 334, figure 8.22].

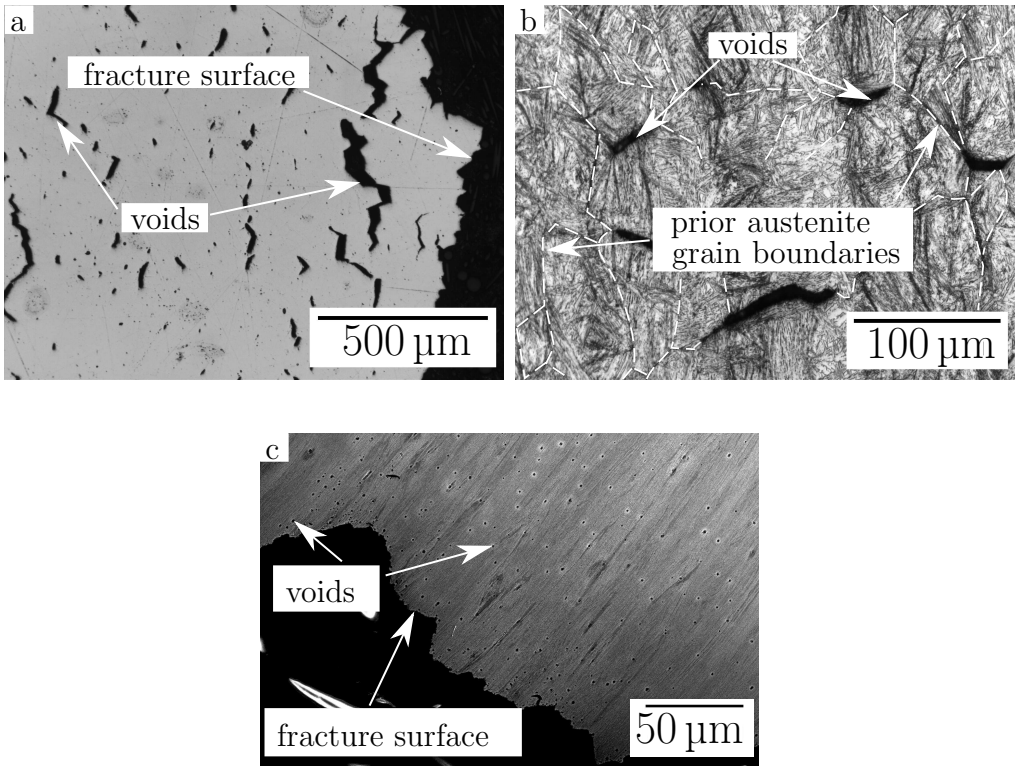

Figure 9.20: Voids formed during creep testing under 700 MPa at 450 °C of (a) immediately below the fracture surface of Alloy 9, appearing to follow austenite grain boundaries; (b) ≈ 1 cm below the fracture surface of Alloy 9 with austenite grain boundaries highlighted, creep applied in the vertical direction; (c) Alloy 8.

Chapter 10

Tetragonal bainitic ferrite

Cohen [236] determined that the crystal structure of martensite is body-centred cubic (BCC) when carbon is absent, but body-centred tetragonal (BCT) otherwise. The degree of tetragonality is indicated by the ratio of the lattice parameters c and a and is related to the dissolved carbon content by equation 10.1 where w_{C} is the carbon content in wt%. The phenomenon is discussed in detail in section 2.4 and also in Cohen [236] for martensite and Jang et al. [237] for bainite. Before the current study, the loss of lattice symmetry due to the presence of carbon had never before been observed in bainite. In non-nanostructured bainite, the transformation temperature is sufficiently high to ensure that carbon is able to partition immediately following transformation. However, the lower temperatures used in the formation of bulk nanocrystalline bainitic steels leads to retention of carbon in the bainitic ferrite. This is possible despite there being sufficient time for carbon to diffuse and escape from the bainitic ferrite. The reduction in symmetry from BCC to BCT provides lower energy regular interstitial sites in bainitic ferrite, greatly increasing the solubility of carbon in the bainitic ferrite [237].

$$\frac{c}{a} = 1 + 0.045 w_{\mathrm{C}} \tag{10.1}$$

The data collected in this project using high-resolution diffraction techniques was examined to investigate the symmetry of the bainitic ferrite in bulk nanocrystalline steels. Initial investigations involved the sample of Alloy 2 investigated at

DESY during the experiments detailed in section 4.3. The sample was heated using the same hot gas blower detailed in section 4.3 and the XRD data were recorded using the same method and similar parameters to those detailed in section 4.3. These data were compared to laboratory X-ray diffraction results. Subsequent neutron diffraction investigations were performed on samples of Alloy 9 and another conventional bulk nanocrystalline bainite, Alloy 10.

10.1 Weighted profile R factor

Rietveld refinement was used to derive physical properties from the X-ray diffraction data. The goodness-of-fit may be quantified in various ways, the simplest useful method being the weighted sum of the squares of the errors, S, as outlined in equation 10.2, where n is the total number of data points, x_i is the observed number of X-ray counts, y_i is the number of counts expected for a given set of physical properties and σ_i is the standard uncertainty in the i^{th} datapoint. The physical properties are refined, the expected diffractogram calculated and compared to the measured data. Since the detection of diffracted X-rays involves a number of discrete events in a given time, Poisson statistics apply and $\sigma_i = \sqrt{x_i}$ [336, 337]. Equation 10.2 may therefore be rewritten as equation 10.3 [285, 338].

$$S = \sum_{i=1}^{n} \left(\frac{x_i - y_i}{\sigma\left[y_i\right]} \right)^2 \tag{10.2}$$

$$= \sum_{i=1}^{n} \frac{\left(x_i - y_i\right)^2}{x_i} \tag{10.3}$$

The sum of squares of errors is not independent of the absolute value of the measurements, since the numerator of equation 10.3 will increase as the square of the measured values whereas the denominator will increase in linear proportion. To remove the effect of the magnitude of the measurements, the *weighted profile R-factor*, R_{wp} is commonly used to assess the goodness-of-fit of Rietveld refinements [336, 339]. The weighted sum of squared errors is divided by the weighted square of the observed number of counts (equation 10.4). The weighting factor is

the inverse of the uncertainty, which is equal to the observed number of counts according to Poisson statistics (equation 10.6). This provides a meaningful, relative measurement of the discrepancy between calculated and measured intensities, independent of the absolute scale of the measurements.

$$R_{\text{wp}} = \left(\frac{\sum_{i=1}^{n} w_i \left(x_i - y_i \right)^2}{\sum_{i=1}^{n} w_i x_i^2} \right)^{1/2} \tag{10.4}$$

$$w_i = \frac{1}{\sigma^2 \left[x_i \right]} \tag{10.5}$$

$$= \frac{1}{x_i} \tag{10.6}$$

If a model is a perfect physical description of the material being investigated, discrepancy is expected to be due solely to statistical deviations (i.e. noise), so $\left(x_i - y_i \right)^2 = \sigma_i^2$. In this case, the best achievable value of $w_i \left(x_i - y_i \right)^2$ is 1 and the contribution to R_{wp} from each data point is approximately $\left(w_i x_i^2 \right)^{-1} = \left(x_i \right)^{-1}$. For N degrees of freedom (defined as the difference between the number of data points and the number of refined parameters), the corresponding value of R_{wp} is known as the *expected R-factor*, R_{exp} [339], and is given as follows:

$$R_{\text{exp}} = \frac{N}{\sum_{i=1}^{N} x_i} \tag{10.7}$$

Given the large number of datapoints, the change in the number of refined parameters has only a negligible effect on R_{exp} and so the fit to a dataset is only expected to improve if fitting more parameters is a more accurate physical description of the sample.

10.2 Cubic and tetragonal ferrite in Alloy 2

During the Rietveld analysis conducted in earlier chapters to determine lattice parameters and phase fractions, ferrite is assumed to have a BCC structure given by space group $\text{Im}\bar{3}\text{m}$. An alternative space group may be used to describe BCT ferrite: $\text{I}\frac{4}{\text{m}}\text{mm}$. Assuming a body-centred tetragonal crystal structure for ferrite will

lead to one more refined variable: the c lattice parameter. In order to investigate whether any further loss of symmetry was possible, a body-centred orthorhombic (BCO) crystal structure was also tested, with the space group I222. There is no mechanism for the formation of orthorhombic ferrite directly from austenite, but there is evidence that a lattice with orthorhombic characteristics may form if a proportion of the carbon atoms are shuffled into different sites via slip or twinning [340]. The space group initially used for austenite was $Fm\bar{3}m$ (FCC), but a face-centred orthorhombic crystal structure (space group F222) was also tested to check whether this led to any significant improvement in the fit. To simplify analysis, all carbide peaks were ignored and samples were assumed to consist only of austenite and ferrite. This is not expected to significantly affect results since carbide peaks are much weaker than those of austenite and ferrite.

A sample of Alloy 2 transformed 215 °C for 10 d was heated at 5 °C s^{-1} and the resulting data were analysed assuming each of cubic, tetragonal and orthorhombic ferrite. Figure 10.1(a) shows that reducing the symmetry of the ferrite from cubic to tetragonal causes a large drop in R_{wp}, suggesting that a body-centred tetragonal crystal is a better physical description of the ferrite than body-centred cubic. Allowing the ferrite to be body-centred orthogonal provides a slight reduction in R_{wp}, but the difference is substantially less than between the cubic and tetragonal cases.

The reduction in $c_{\mathrm{t}}/a_{\mathrm{t}}$ during tempering (figure 10.1(b)) is indicative of carbon leaving the ferrite. Prolonged heating is required for any change to be observed, as Jang et al. [237] predicted for carbon in the regular octahedra in body-centred tetragonal ferrite. Comparison of figures 10.1(b) and 10.1(d) shows that the rapid loss of austenite coincides with the rapid reduction in ferrite asymmetry after approximately 5500 s. The initial $c_{\mathrm{t}}/a_{\mathrm{t}}$ ratio measured was 1.0086. Using this value in equation 10.1 suggests a solid solution carbon content in the ferrite of 0.19 wt%, which is consistent with results obtained using atom probe tomography on steels of similar composition and thermal history [54, 56]. The same convergence of lattice parameters is observed in the case of orthorhombic ferrite (figure 10.1(c)).

To ensure any measured asymmetry was not an artefact of the flat-plate de-

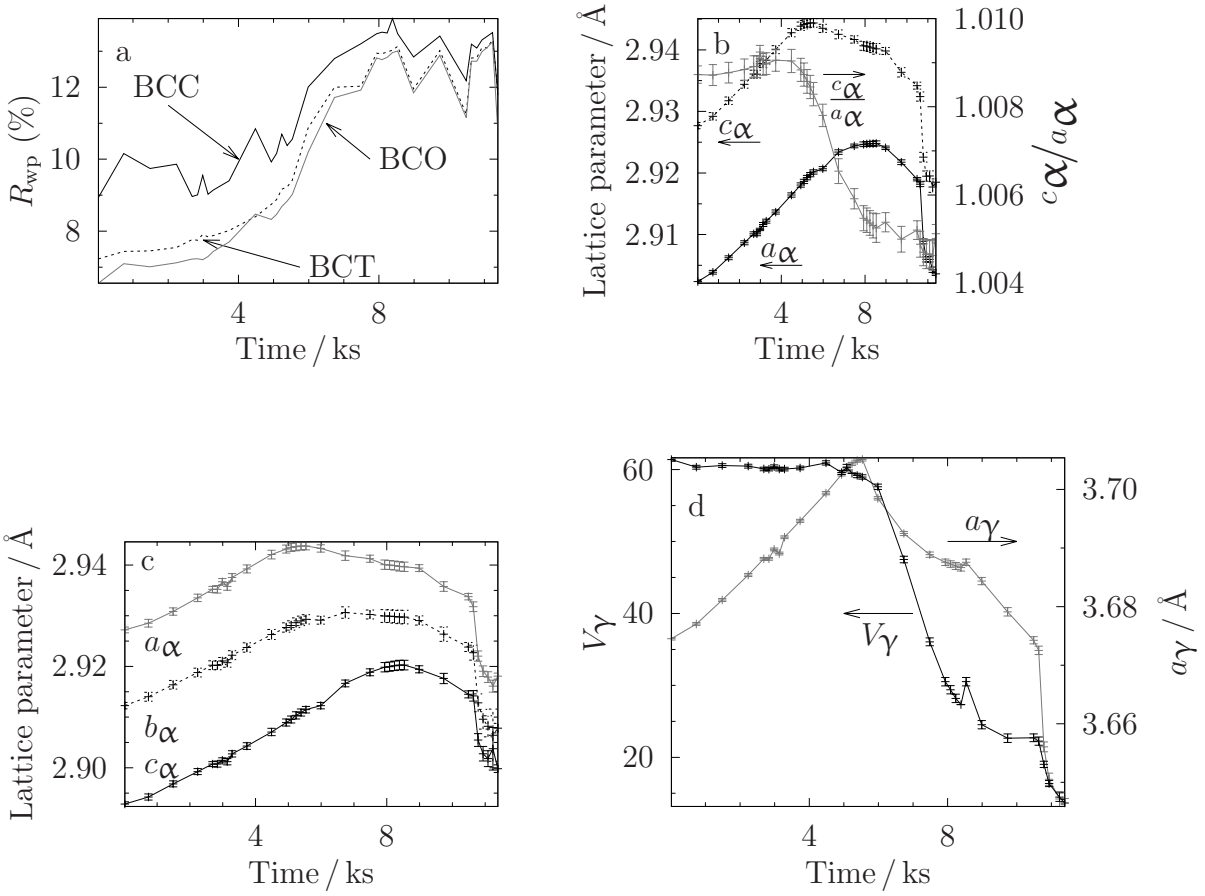

Figure 10.1: (a) R_{wp}, (b) lattice parameters in body-centred tetragonal ferrite, (c) lattice parameters in body-centred orthorhombic ferrite, (d) austenite volume fraction and lattice parameter for Alloy 2 during heating at $5\,^{\circ}\mathrm{C\,s^{-1}}$. The results are all consistent with a starting crystal structure of BCT in ferrite, which is lost during prolonged tempering. Error bars on the points represent one standard error.

tector geometry, the diffractometer was calibrated using a NIST silicon standard. After this calibration, the detector data were taken for a (cubic) ceria standard and were found to be well-matched to a predicted pattern. In addition, the austenite in the sample is well-fitted using a face-centred cubic space group. As may be seen in figure 10.2, there is almost no difference between the fits obtained for austenite assuming either FCC or face-centred orthorhombic space groups.

To confirm the findings from the synchrotron, experiments were repeated using laboratory-based XRD using a Phillips PW1820 diffractometer to give the results in table 10.1. The diffractometer produces Cu K_α radiation and utilises a graphite monochromator, a divergence slit of 10 mm width, a 0.2° receiving slit and a 0.5° anti-scatter slit. The diffractometer was calibrated using a NIST silicon standard. The results are similar to those obtained using synchrotron XRD, but do not agree to within the fitting errors of the Rietveld refinements.

	Cubic	Tetragonal	Orthorhombic
R_{wp}	23.05	22.08	20.98
V_γ	26.5 ± 0.3	28.0 ± 0.2	27.7 ± 0.2
a_γ /Å	3.6143 ± 0.0002	3.6146 ± 0.0002	3.6145 ± 0.0002
a_α /Å	2.86343 ± 0.00009	2.8560 ± 0.0002	2.8449 ± 0.0003
b_α /Å	—	—	2.86910 ± 0.00010
c_α /Å	—	2.8769 ± 0.0005	2.8747 ± 0.00011
c_α/a_α	—	1.0073 ± 0.0002	1.0101 ± 0.0004
b_α/a_α	—	—	1.0085 ± 0.0004

Table 10.1: Results obtained from laboratory-based X-ray diffraction of Alloy 2. The results are very similar to those obtained using synchrotron XRD (cf. figure 10.1) but do not agree within one standard error.

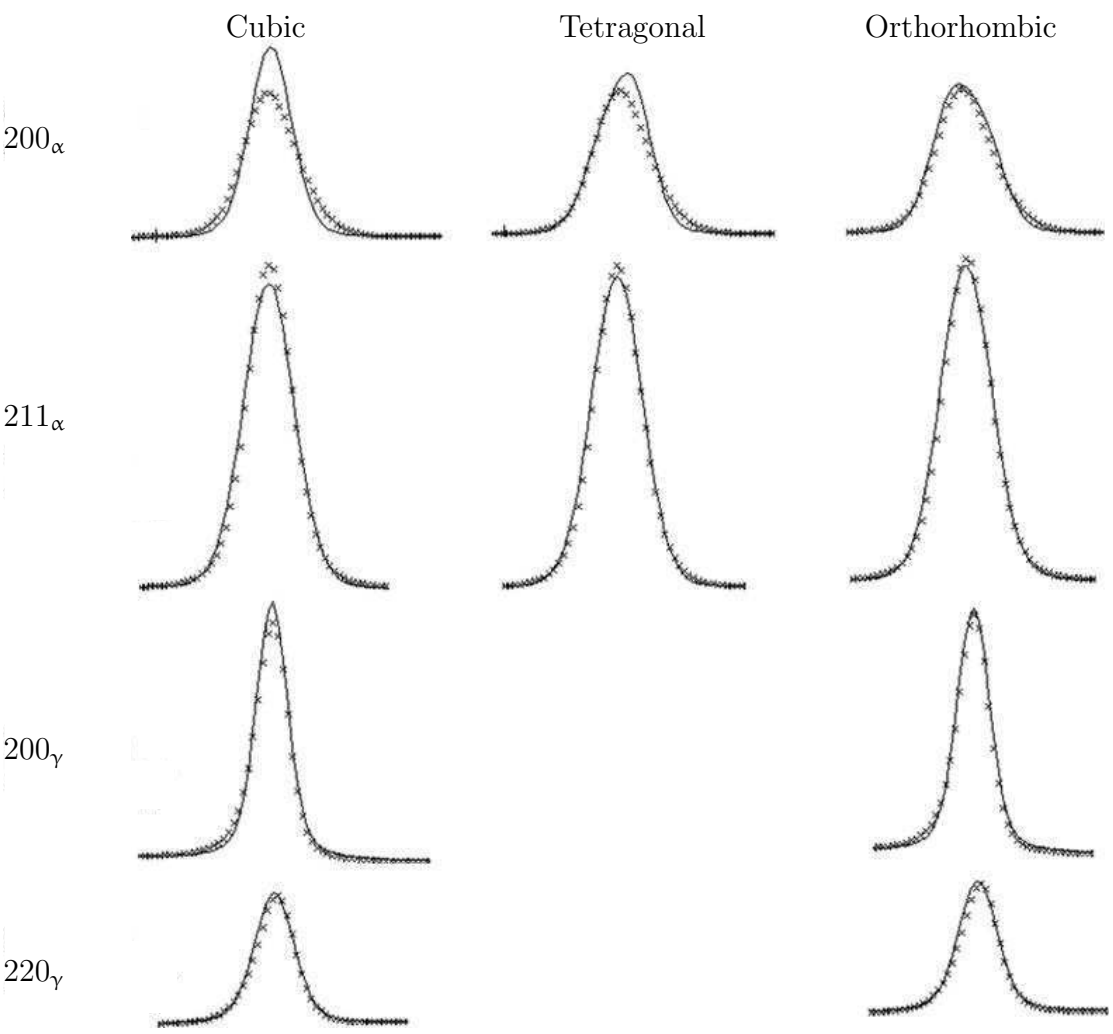

Figure 10.2: Peak profiles calculated in MAUD for the 200_α and 211_α peaks and austenite 200_γ and 220_γ peaks using cubic, tetragonal and orthorhombic space groups. Austenite is equally well-fitted by a face-centred cubic or a face-centred orthorhombic lattice. There is a significant improvement in the fit of ferrite from a body-centred cubic lattice to body-centred tetragonal. Reproduced with permission of Elsevier B. V.

10.3 Ferrite symmetry in Alloy 1

In order to test whether the findings of non-cubic symmetry in ferrite were specific to Alloy 2, another experiment was conducted using laboratory XRD on Alloy 1 transformed at 250 °C. The experiment was identical to that described in section 10.2. The full findings are listed in table 10.2 and show that tetragonality may be measured in bainitic ferrite. The dissolved carbon content was derived to be 0.16 wt%. This is lower than that found in Alloy 2, consistent with the higher transformation temperature used for this sample of Alloy 1.

	Cubic	Tetragonal	Orthorhombic
R_{wp}	20.18	19.96	19.62
v_{γ}	0.214 ± 0.007	0.218 ± 0.008	0.2298 ± 0.0005
a_{γ} /Å	3.6346 ± 0.00013	3.64403 ± 0.00013	3.63712 ± 0.00012
a_{α} /Å	2.86465 ± 0.00010	2.8586 ± 0.0003	2.8478 ± 0.0005
b_{α} /Å	—	—	2.872 ± 0.0003
c_{α} /Å	—	2.876 ± 0.00076	2.874 ± 0.003
c_{α}/a_{α}	—	1.0063 ± 0.0003	1.0093 ± 0.0011
b_{α}/a_{α}	—	—	1.0085 ± 0.0011

Table 10.2: Results obtained from laboratory-based X-ray diffraction of Alloy 1. The ratio of ${}^{c}\alpha/{}_{a}\alpha$ is consistent with tetragonal ferrite with a lower carbon content than was measured in Alloy 2.

The data collected from Alloy 1 in section 4.3 transformed at 200 °C and 300 °C were also analysed using the same procedure as in section 10.2.

Figures 10.3(b) and 10.4(b) show that transformation at 200 °C causes more tetragonality than that at 300 °C. The as-transformed carbon contents inferred from the data are 0.221 ± 0.005 wt% and 0.192 ± 0.007 wt%. In both samples, the fitting error, R_{wp} is smaller in the body-centred tetragonal case than if body-centred cubic symmetry is used.

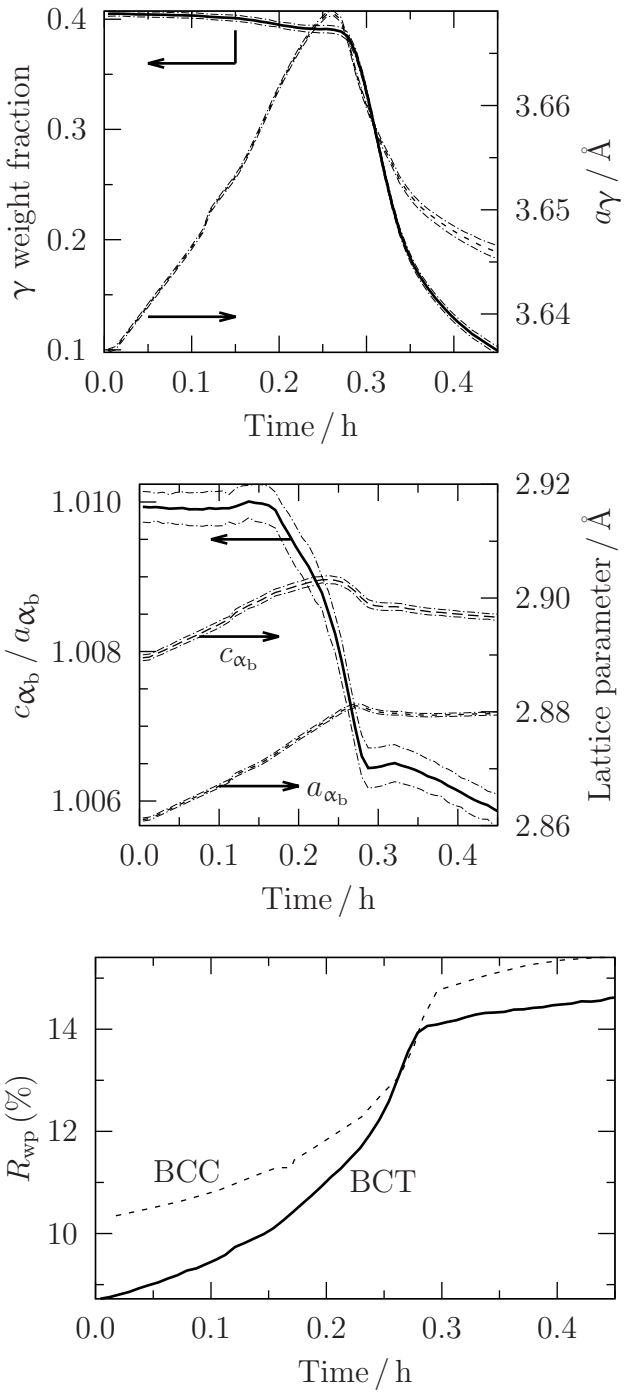

Figure 10.3: Lattice parameter and volume fraction of (a) austenite, (b) ferrite and (c) R_{wp} in Alloy 1 transformed at 200 °C. The results are entirely consistent with tetragonal bainitic ferrite. The thin dashed lines represent the data ± one standard error.

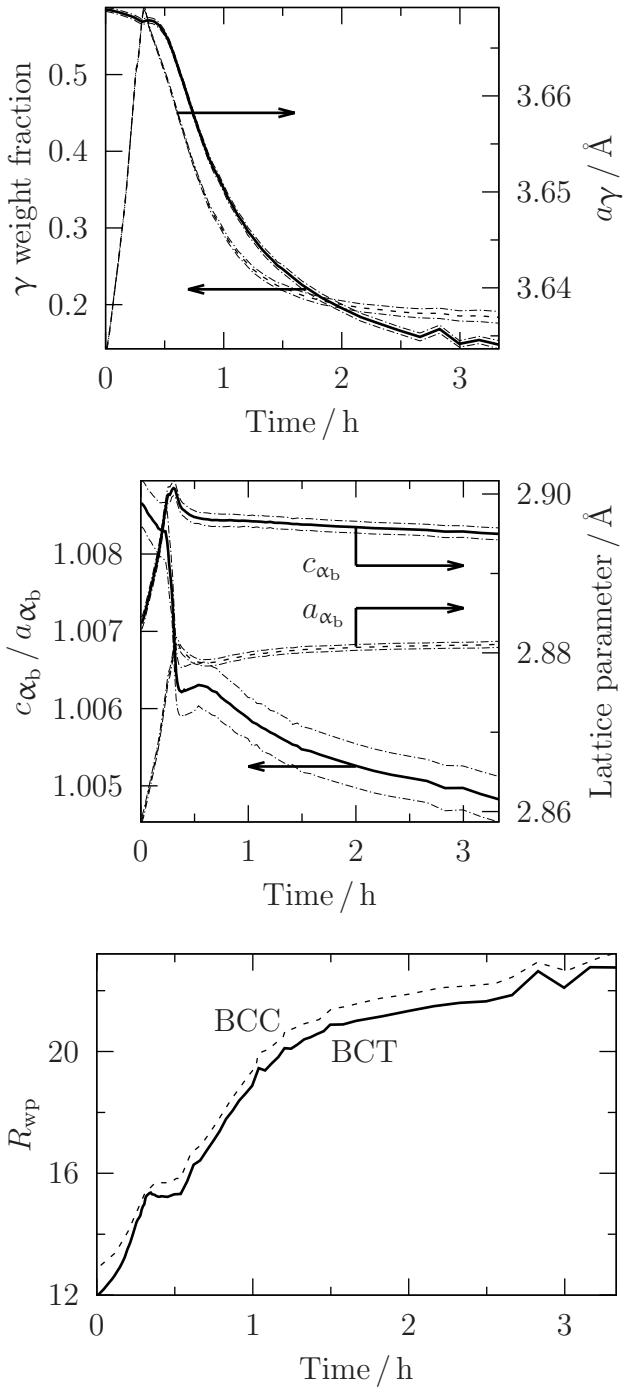

Figure 10.4: Lattice parameter and volume fraction of (a) austenite, (b) ferrite and (c) R_{wp} in Alloy 1 transformed at 300℃. The results are entirely consistent with tetragonal bainitic ferrite and the lower initial value of $c_{\alpha_{\mathrm{b}}} / a_{\alpha_{\mathrm{b}}}$ than is seen in figure 10.4 suggests a lower dissolved carbon content than is seen following transformation at 200℃. Thin dashed lines represent ± one standard error.

10.4 Ferrite symmetry in Alloy 9 and Alloy 10

Samples of Alloy 9 and another conventional nanostructured steel, Alloy 10 (compositon given in table 10.3), transformed according to table 10.4 to produce nanocrystalline bainite. The samples were then investigated at the High Resolution Powder Diffraction (HRPD) beamline at the ISIS neutron diffraction facility, Didcot, U. K. This beamline uses a long ($\sim 100\,\mathrm{m}$) flight path to allow excellent plane spacing resolution [341]. Heating was performed using a vacuum furnace with neutron-transparent vanadium windows. Data were recorded using the detector banks at $2\theta = 90^\circ$ to the incident beam.

C	Mn	Ni	Al	Si	Mo	Cu	Co	Cr
0.78	1.95	0.00	0.99	1.49	0.24	0.00	1.61	0.97

Table 10.3: Composition of Alloy 10 (wt%).

	200 °C	250 °C	300 °C
Alloy 9	10 d	5 d	3 d
Alloy 10	10 d	3 d	1 d

Table 10.4: Transformation conditions for samples used in neutron diffraction experiments. All samples were austenitised at 1000 °C for 30 min before isothermal holding.

The numbers of detected counts were recorded as a function of plane spacing. The instrument parameters are well-calibrated and freely available online [1] as files that are compatible with the program "General Structure Analysis Software" (GSAS) [342]. A background profile was fitted using a Chebyschev polynomial of the first kind with 16 refined coefficients [342, page 129]. The incident neutron intensity, phase fractions, thermal broadening factors and lattice parameters and

[1] http://www.isis.stfc.ac.uk/instruments/hrpd/data-analysis/hrpd-data-analysis4442.html

parameters related to microstrain and crystallite size of each phase were refined. Full Rietveld refinement results are given in Appendix B.

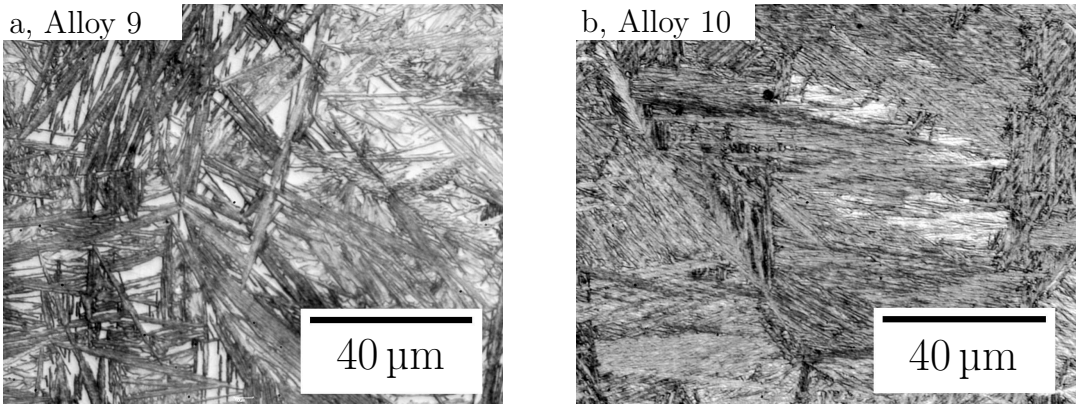

Figure 10.5: Optical micrographs of Alloy 9 and Alloy 10 as transformed at 250 °C. There is no evidence of either allotriomorphs or non-metallic precipitates. Both images are consistent with the micrographs in section 7.

It is expected that the degree of asymmetry will increase as transformation temperature decreases, as demonstrated in Caballero et al. [56] and that the degree of tetragonality will be higher in Alloy 10 than in Alloy 9, due to the lower bulk carbon content and the high level of nickel in Alloy 9, which will limit the degree of carbon enrichment in the austenite before the bainite transformation ceases, i.e. reduce $x_{T_0'}$.

As expected Alloy 10 exhibits greater asymmetry than Alloy 9. However, the tetragonality does not show a strong temperature dependence in either alloy (figure 10.6). It is not immediately obvious why this is the case, especially since no evidence of carbides has been found in any microscopic study on as-transformed samples of either alloy. García-Mateo et al. [187] detected that both the carbon content of bainitic ferrite and the dislocation density increase with decreasing transformation temperature and postulated that this led to more carbon being trapped at dislocation cores as the transformation temperature is reduced. Although it has never been explicitly shown, it is possible that the concentration of carbon in solid solution in ferrite in a nanostructured bainitic steel is approximately

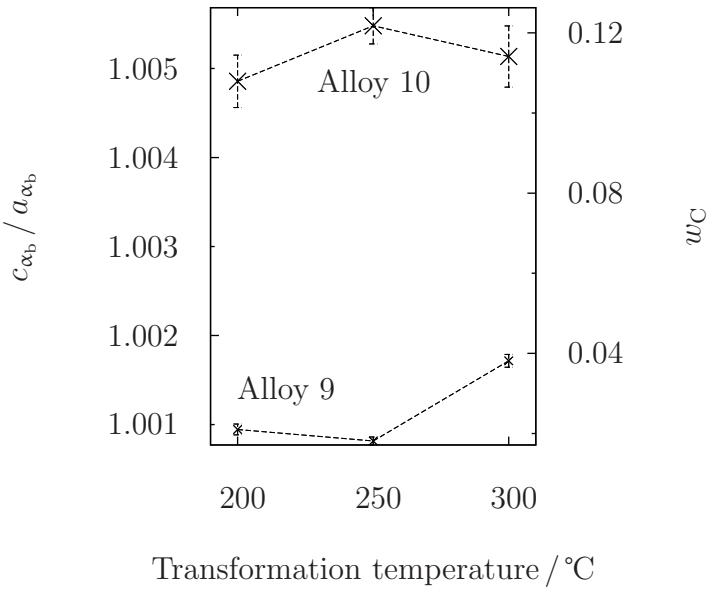

Figure 10.6: c_t/a_t in Alloy 9 and Alloy 10. The values follow the expectation that Alloy 10 will display more tetragonality than Alloy 9, but the temperature dependence of both alloys is not as expected.

constant and the additional carbon in ferrite transformed at lower temperature is accommodated in dislocation cores.

During tempering at 600 °C, the measured tetragonality of Alloy 10 decreases to the point at which the predicted carbon content is below that expected at full equilibrium at 600 °C (figure 10.7 cf. figure 2.1). Upon cooling to room temperature, the measured tetragonality increases (figure 10.7). Saha Podder and Bhadeshia [116] suggested that this is due to the transformation of small amounts of austenite to martensite upon cooling, although no such transformation was observed in micrographs of either alloy taken after the heat treatment.

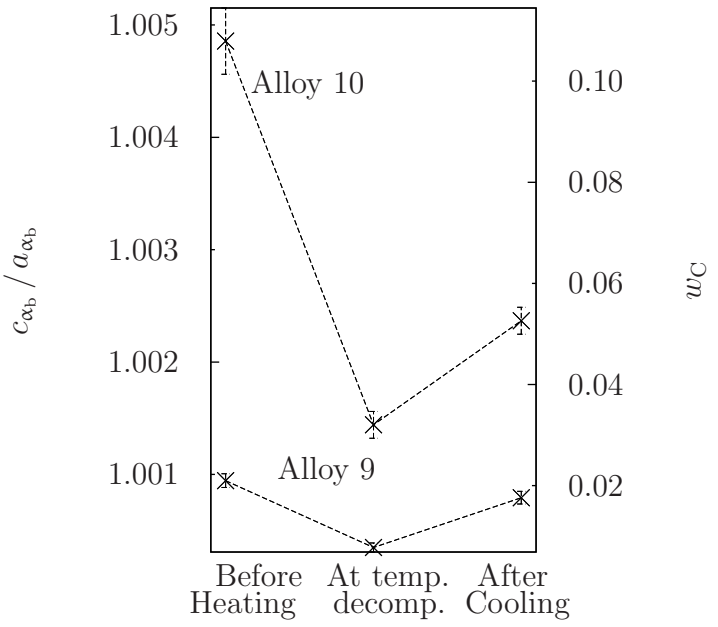

Figure 10.7: c_t/a_t in Alloy 9 and Alloy 10 transformed at 200 °C, measured using neutron diffraction

10.5 Conclusions

It has been shown using synchrotron X-ray, laboratory and neutron diffraction that nanocrystalline bainitic ferrite exhibits a body-centred tetragonal crystal structure. This is consistent with a diffusionless transformation mechanism for bainite and literature concerning the carbon content of nanostructure bainitic ferrite. The amount of carbon suggested to be in solid solution by the tetragonality results is consistent with atom probe tomography measurements of similar steels [47, 52–54, 169]. Although the evidence amassed in this project is encouraging, and has been supported by other contemporary work considering anisotropic thermal expansivity of textured bainitic steels [343] and high resolution transmission electron microscopy [47], further data are required to prove the existence of tetragonal bainitic ferrite beyond reasonable doubt. These data could include more results based on X-ray and neutron diffraction for a wider range of carbon contents and transformation temperatures. These results would be pivotal if they could show non-cubic bainitic ferrite forming in real time during the bainite transformation. Other potential sources of information could be atomic resolution TEM, similar to that undertaken by Caballero et al. [47]. Again, if corroborating evidence could be obtained using high resolution TEM during the bainite transformation, the evidence would be definitive.

General Conclusions & Future Work

"I confess that I have been blind as a mole, but it is better to learn wisdom late than never to learn it at all."

Sherlock Holmes in *The Man with the Twisted Lip* by Sir Arthur Conan Doyle

The main goal of this work was to develop alloys that form a nanocrystalline bainitic structure and are resistant to thermal decomposition. An alloy developed before the start of the project was assessed using synchrotron X-ray diffractometry with *in-situ* heating to track the changes in phase fraction and was found to outlast a conventional nanocrystalline steel tested in identical conditions at 500 °C. Refinements were made to this alloy using theoretical calculations to ensure the correct structure was formed while incorporating alloying additions likely to postpone thermal decomposition. Two alloys were selected and approximately 50 kg of each was cast. One of these alloys featured a high concentration of silicon (Alloy 8) and the other a very large nickel content, high aluminium content and a lower carbon content than existing nanocrystalline steels (Alloy 9). These new alloys were investigated using synchrotron X-ray diffractometry and neutron diffractometry. The former was found to decompose during tempering at 600 °C while the latter was observed to precipitate cementite while austenite consistently persisted throughout the experiments, even down to room temperature. This represents the first ever nanocrystalline steel that is able to withstand prolonged heating without the complete loss of austenite. This material has the potential to be used in high-temperature applications and to be subjected to high-temperature processing

such as galvanising.

Both optimised alloys showed an impressive combination of strength and toughness at ambient temperature. The thermally stabilised alloy showed exceptionally high fracture toughness ($K_{\mathrm{Q}} \approx 100\,\mathrm{MPa\,m^{-\frac{1}{2}}}$) and good strength ($\sigma_{0.2\%\,\mathrm{proof}} \approx 1000\,\mathrm{MPa}$, $\sigma_{\mathrm{UTS}} \approx 1400\,\mathrm{MPa}$). The high-silicon alloy showed an impressive combination of strength and toughness ($\sigma_{0.2\%\,\mathrm{proof}} \approx 1500\,\mathrm{MPa}$, $\sigma_{\mathrm{UTS}} \approx 1800\,\mathrm{MPa}$, $K_{\mathrm{IC}} \approx 69\,\mathrm{MPa\,m^{\frac{1}{2}}}$). All of these properties, as well as the measured fatigue life in both alloys, are consistent with previous nanocrystalline bainitic alloys. This proves that thermal stability has been achieved without compromising mechanical properties to an unacceptable degree. While the strengths of both alloys was found to decrease after thermal exposure at 480 °C for 8 d, both show good ambient temperature impact toughness — a property not often found in nanocrystalline bainite. Bearing in mind the persistence of austenite during heat treatment, the mechanical tests show the high-nickel alloy (Alloy 9) as a potential candidate for future high-temperature engineering applications.

The first ever creep data of nanocrystalline steel have been recorded. Both alloys were subjected to 700 MPa constant stress at 450 °C. The alloys have superior creep lives to common engineering alloys with the exception of maraging steels and nickel superalloys. These excellent creep properties are likely to be related to the low number density of incoherent interfaces, which only occur at prior austenite grain boundaries. The semi-coherent boundaries between bainitic ferrite and retained austenite are not able to contribute to creep as they contain misfit dislocations strongly fixed in place and unable to undergo climb to absorb or emit vacancies.

Throughout this project, investigations using high-resolution diffractometry at both synchrotron and neutron sources allowed the symmetry of the bainitic ferrite lattice to be investigated. It was found that the diffraction data were routinely described better by a body-centred tetragonal lattice. This is consistent with the diffusionless theory of the bainite transformation, previously-observed carbon contents of bainite ferrite and related *ab-initio* calculations.

Future work

While the alloys and theories summarised in this thesis represent a major advance in the capabilities of nanocrystalline steels, a far greater body of work is required before these alloys may be used for high-temperature engineering applications:

- Further refinements to the composition may yield nanostructured steels with superior thermal stability. For example, the inclusion of silicon into Alloy 9, in which austenite survives heat treatment, may further minimise cementite precipitation and thereby lead to improved thermal stability.

- Further assessments of thermally stability over a range of temperatures should be conducted, preferably using *in-situ* methods. The effects of repeated heating and cooling should also be established.

- Further mechanical tests should be performed on all alloys, especially to establish fatigue and creep data over a wider range of temperatures and stresses. Toughness measurements should be made from ambient temperature to any candidate service temperature to establish whether a ductile-brittle transition occurs and its effect on properties.

- During any future mechanical tests, evidence of TRIP should be searched for to establish whether or not this effect is significant in the current alloys and to establish its consequences for toughness. Although searched for, no evidence for TRIP was found in the current study.

- More thorough investigation of ferrite lattice symmetries of high-carbon bainitic alloys should be performed to confirm and quantify tetragonality. High resolution transmission electron microscopy may be used to complement the diffraction data already accrued and any arising from future experiments.

Appendix A

Alloy compositions

Alloy	C	Mn	Ni	Al	Si	Mo	Cu	B_s / °C	M_s / °C
Alloy 3	0.7	0.0	3.30	1.4	4.0	0.25	0.00	350	160 ± 50
Alloy 4	0.7	0.0	4.50	2.0	2.0	0.25	0.00	300	110 ± 40
Alloy 5	0.7	0.0	7.50	3.0	2.0	0.25	0.00	100	—
Alloy 6	0.7	0.0	4.00	2.0	2.0	0.25	2.00	230	130 ± 50
Alloy 7	0.7	0.0	7.00	3.0	2.0	0.25	2.00	100	—
Alloy 8	Made to the composition of Alloy 3							—	—
Alloy 9	0.4	0.3	13.0	2.5	0.0	0.15	0.0	370	90

Table A.1: Compositions of new alloys, as determined by thermodynamic modelling and predicted bainite and martensite start temperatures. B_s predicted by MTTTData and M_s predicted by artificial neural network. Alloys used for comparison purposes and not designed in this project are not included in this table.

Alloy	C	Mn	Ni	Al	Si	Mo	Cu	> 0.01
Alloy 1	1.037	1.97	0.00	1.43	3.89	0.24	0.00	—
Alloy 2	0.84	2.26	0.04	0.04	1.78	0.25	0.10	1.55 Co, 1.47 Cr
Alloy 3	0.622	0.00	3.35	1.29	3.40	0.27	< 0.01	0.016 W
Alloy 4	0.572	0.00	4.55	4.3	1.70	0.03	< 0.01	0.019 W
Alloy 5	0.522	0.00	7.64	7.5	1.55	0.03	< 0.01	—
Alloy 6	0.544	0.00	4.10	4.7	1.68	0.03	2.01	0.030 W
Alloy 7	0.420	0.00	7.27	6.7	1.58	0.04	2.04	0.116 W
Alloy 8	0.72	0.02	3.40	1.38	3.88	0.20	0.00	—
Alloy 9	0.45	0.15	13.20	2.63	0.03	0.30	0.06	3.99 Co
Alloy 10	0.78	1.95	0.00	0.99	1.49	0.24	0.00	1.61 Co, 0.97 Cr

Table A.2: Experimentally measured composition of alloys studied. All measurements are from commercial testing houses except for the aluminium contents of Alloy 3–Alloy 7 which are measured using EDX. Uncertainties are omitted from this table for clarity, but are given where available when the composition of each alloy is discussed in the main body of this document.

Appendix B

Rietveld analysis of neutron diffraction data

The following tables detail the full results obtained from Rietveld refinement of data collected during neutron diffraction experiments at the High Resolution Powder Diffraction (HRPD) beamline at the ISIS pulsed neutron source at the Rutherford Appleton Laboratory near Didcot, Oxfordshire, U.K. Data were analysed using the General Structure Analysis Software (GSAS) [342, 344] using freely-available calibration data for the beamline [1]. During analysis, the "Peak-shape function #4" calibration data were used, consistent with the incident intensity function "ITYP 4" in GSAS and the background signal was well-fitted to a Chebyschev Polynomial of the first kind (background function #1 in GSAS).

[1] http://www.isis.stfc.ac.uk/instruments/hrpd/data-analysis/hrpd-data-analysis4442.html

Trans.	200			225	250	275	300		
Temp / ℃	before	at temperature	after				before	at temperature	after
$f_{\gamma_{\text{film}}}$	0.185 ± 0.018	0.235 ± 0.003	0.224 ± 0.005	0.248 ± 0.011	0.241 ± 0.007	0.181 ± 0.006	0.169 ± 0.011	0.240 ± 0.003	0.228 ± 0.005
$f_{\gamma_{\text{blocky}}}$	0.083 ± 0.017	N/A	N/A	0.044 ± 0.019	0.099 ± 0.006	0.111 ± 0.005	0.151 ± 0.011	N/A	N/A
$f_{\alpha_{\text{b}}}$	0.732 ± 0.018	0.7651 ± 0.0024	0.776 ± 0.005	0.708 ± 0.011	0.660 ± 0.006	0.708 ± 0.005	0.679 ± 0.010	759 ± 0.003	0.772 ± 0.005
$w_{\gamma_{\text{film}}}$	0.184 ± 0.014	0.2349 ± 0.0019	0.225 ± 0.004	0.247 ± 0.008	0.222 ± 0.005	0.181 ± 0.004	0.169 ± 0.009	0.2392 ± 0.0020	228 ± 0.004
$w_{\gamma_{\text{blocky}}}$	0.083 ± 0.016	N/A	N/A	0.044 ± 0.011	0.092 ± 0.005	0.113 ± 0.005	0.153 ± 0.009	N/A	N/A
$w_{\alpha_{\text{b}}}$	0.732 ± 0.021	0.7651 ± 0.019	0.7749 ± 0.0041	0.708 ± 0.013	0.685 ± 0.007	0.706 ± 0.007	0.677 ± 0.013	0.7608 ± 0.0020	0.772 ± 0.004
$a_{\gamma_{\text{film}}}$ / Å	3.6251 ± 0.0013	3.64666 ± 0.00003	3.6166 ± 0.00008	3.6260 ± 0.0009	3.6195 ± 0.0004	3.6141 ± 0.0006	3.6147 ± 0.0011	3.64410 ± 0.00004	3.61466 ± 0.00008
$a_{\gamma_{\text{blocky}}}$ / Å	3.6066 ± 0.0011	N/A	N/A	3.6059 ± 0.0003	3.59921 ± 0.00016	3.59557 ± 0.00006	3.5981 ± 0.0001	N/A	N/A
$a_{\alpha_{\text{b}}}$ / Å	2.869957 ± 0.000013	2.888897 ± 0.000007	2.870758 ± 0.000017	2.873499 ± 0.000009	2.869114 ± 0.000010	2.868843 ± 0.000006	2.870058 ± 0.000016	2.887912 ± 0.000008	2.870248 ± 0.000018
$d_{\gamma_{\text{film}}}$ / nm	47 ± 32	120 ± 60	100 ± 10	483 ± 24	272 ± 10	22 ± 7	21 ± 10	110 ± 570	85 ± 7
$d_{\gamma_{\text{blocky}}}$ / nm	260 ± 180	N/A	N/A	350 ± 570	72 ± 37	170 ± 40	140 ± 40	N/A	N/A
$d_{\alpha_{\text{b}}}$ / nm	117 ± 3	129 ± 19	108 ± 3	149 ± 4	108.4 ± 2.2	95.3 ± 1.6	104.2 ± 3.2	121.7 ± 1.8	96.7 ± 2.5
R_{wp}	2.43	2.1	4.91	2.56	2.78	2.33	2.3	2.24	4.67
R_{p}	3.13	2.85	7.03	3.31	3.52	3.22	3.01	3.06	7.31
R_{wp} no bg	1.69	1.4	3.7	1.75	1.97	1.45	1.57	1.52	3.11
R_{p} no bg	2.73	2.36	6.04	2.69	3.01	2.41	2.45	2.48	5.64

Table B.1: Overall results for HS3 with cubic bainitic ferrite

Trans.	200			225	250	275	300		
Temp / ℃	before	at temperature	after				before	at temperature	after
$f_{\gamma_{\text{film}}}$	0.133 ± 0.016	0.257 ± 0.004	0.241 ± 0.005	0.273 ± 0.014	0.217 ± 0.006	0.194 ± 0.020	0.182 ± 0.010	0.251 ± 0.003	0.247 ± 0.005
$f_{\gamma_{\text{blocky}}}$	0.050 ± 0.006	N/A	N/A	0.0108 ± 0.0006	0.02713 ± 0.0008	0.033 ± 0.003	0.051 ± 0.003	N/A	N/A
$f_{\alpha_{\text{b}}}$	0.82 ± 0.10	0.743 ± 0.012	0.759 ± 0.016	0.72 ± 0.04	0.756 ± 0.021	0.77 ± 0.08	0.76 ± 0.04	0.749 ± 0.009	0.753 ± 0.015
$w_{\gamma_{\text{film}}}$	0.160 ± 0.009	0.2559 ± 0.0027	0.241 ± 0.004	0.264 ± 0.010	0.201 ± 0.005	0.177 ± 0.007	0.161 ± 0.007	0.2504 ± 0.0022	0.247 ± 0.004
$w_{\gamma_{\text{blocky}}}$	0.160 ± 0.011	N/A	N/A	0.038 ± 0.013	0.092 ± 0.005	0.110 ± 0.016	163 ± 0.007	N/A	N/A
$w_{\alpha_{\text{b}}}$	0.723 ± 0.016	0.744 ± 0.003	0.758 ± 0.004	0.696 ± 0.016	0.706 ± 0.007	0.713 ± 0.021	0.676 ± 0.011	0.7496 ± 0.022	0.7529 ± 0.0038
$a_{\gamma_{\text{film}}}$ / Å	3.6305 ± 0.0010	3.64664 ± 0.00005	3.61661 ± 0.00009	3.6255 ± 0.0010	3.6200 ± 0.0004	$3.6264pm0.0012$	3.6159 ± 0.0009	3.64403 ± 0.00004	3.61453 ± 0.00009
$a_{\gamma_{\text{blocky}}}$ / Å	3.6120 ± 0.0009	N/A	N/A	3.6059 ± 0.0005	3.5992 ± 0.0001	3.6079 ± 0.0011	3.59815 ± 0.00008	N/A	N/A
$a_{\alpha_{\text{b}}}$ / Å	2.86919 ± 0.00007	2.88864 ± 0.00004	2.87017 ± 0.00006	2.87290 ± 0.00006	2.86845 ± 0.00005	2.869183 ± 0.00007	2.86882 ± 0.00008	2.8861 ± 0.0003	2.8673 ± 0.0003
$c_{\alpha_{\text{b}}}$ / Å	2.8719 ± 0.00016	2.8897 ± 0.00011	2.872445 ± 0.00015	2.8750 ± 0.0013	2.87079 ± 0.00012	2.87190 ± 0.00018	2.87312 ± 0.00019	2.8919 ± 0.0006	2.8766 ± 0.0006
$\frac{c}{a}$	1.00093 ± 0.00006	1.00036 ± 0.00004	1.00080 ± 0.00006	1.0007 ± 0.0004	1.00082 ± 0.00005	1.00094 ± 0.00006	1.00150 ± 0.00007	1.0020 ± 0.0002	1.00322 ± 0.00022
w_{C} / wt%	0.0207 ± 0.0014	0.0081 ± 0.0008	0.0177 ± 0.0012	0.015 ± 0.010	0.0181 ± 0.0010	0.0210 ± 0.0015	0.0333 ± 0.0016	0.045 ± 0.005	0.071 ± 0.005
$d_{\gamma_{\text{film}}}$ / nm	35 ± 3	97 ± 5	81 ± 7	49.7 ± 2.4	28.0 ± 1.0	43 ± 3	22.0 ± 0.9	87 ± 4	57 ± 3
$d_{\gamma_{\text{blocky}}}$ / nm	260 ± 110	N/A	N/A	N/A	67 ± 13	160 ± 60	170 ± 40	N/A	N/A
$d_{\alpha_{\text{b}}}$ / nm	174 ± 9	390 ± 30	228 ± 14	233 ± 8	159 ± 6	200 ± 12	153 ± 8	118 ± 3	88.5 ± 2.4
R_{wp}	2.18	2.93	4.08	2.51	2.52	2.44	1.95	2.58	4.47
R_{p}	2.91	3.58	6.56	3.27	3.26	3.05	2.68	3.52	7.33
R_{wp} no bg	1.45	2.11	2.61	1.71	1.73	1.68	1.11	1.29	2.51
R_{p} no bg	2.39	3.36	5.06	2.59	2.62	2.6	1.85	2.4	5.23

Table B.2: Overall results for HS3 with tetragonal bainitic ferrite

Trans.	200			225	250			Trans.	275	300		
Temp / ℃	before	at temperature	after		before	at temeprature	after	Temp / ℃		before	at temperature	after
f_γ	0.240 ± 0.006	0	0	0.2749 ± 0.0027	0.2481 ± 0.0029	0	0	f_γ	0.241 ± 0.005	0.227 ± 0.005	0	0
f_{α_b}	0.760 ± 0.006	1	1	0.7251 ± 0.0027	0.2481 ± 0.0029	1	1	f_{α_b}	0.7589 ± 0.0023	0.7727 ± 0.0023	1	1
w_γ	0.239 ± 0.005	0	0	0.2726 ± 0.0019	0.2463 ± 0.0022	0	0	w_γ	0.240 ± 0.004	0.227 ± 0.004	0	0
w_{α_b}	0.761 ± 0.005	1	1	0.7274 ± 0.019	0.7537 ± 0.0022	1	1	w_{α_b}	0.760 ± 0.004	0.773 ± 0.004	1	1
a_γ / Å	3.62344 ± 0.00018	N/A	N/A	3.62719 ± 0.00006	3.62227 ± 0.00008	N/A	N/A	a_γ / Å	3.62629 ± 0.00014	3.61194 ± 0.00017	N/A	N/A
a_{α_b} / Å	2.87052 ± 0.00003	2.887559 ± 0.000006	2.870135 ± 0.000011	2.867715 ± 0.000013	2.865609 ± 0.000014	2.887439 ± 0.000004	2.866227 ± 0.000007	a_{α_b} / Å	2.870443 ± 0.000022	2.867092 ± 0.000019	2.887219 ± 0.000006	2.867275 ± 0.000012
d_γ / nm	19.1 ± 0.7	N/A	N/A	28.8 ± 0.6	24.2 ± 0.5	N/A	N/A	d_γ / nm	18.9 ± 0.5	19.7 ± 0.9	N/A	N/A
d_{α_b} / nm	92 ± 4	147 ± 20	140 ± 40	95.5 ± 2.1	81.5 ± 1.7	139.8 ± 1.1	126.5 ± 1.6	d_{α_b} / nm	90 ± 3	82.8 ± 2.5	140 ± 190	139 ± 4
R_{wp}	3.63	1.77	3.37	3.02	3.37	2.04	3.66	R_{wp}	2.84	2.18	1.7	3.3
R_p	5	3.28	6.99	3.97	4.12	3.49	7.24	R_p	3.55	2.91	2.98	6.53
R_{wp} no bg	2.57	1.09	2.25	2.25	2.67	1.54	2.83	R_{wp} no bg	2.3	1.6	1.16	2.27
R_p no bg	3.76	2.11	4.76	3.54	3.85	2.71	5.43	R_p no bg	3.12	2.36	1.94	4.33

Table B.3: Overall results for SP10 with cubic bainitic ferrite

Trans.	200			225	250			Trans.	275	300		
Temp / ℃	before	at temperature	after		before	at temeprature	after	Temp / ℃		before	at temperature	after
f_γ	0.22 ± 0.11	0	0	0.27 ± 0.05	0.28 ± 0.11	0	0	f_γ	0.22 ± 0.09	0.22 ± 0.11	0	0
f_{α_b}	0.78 ± 0.11	1	1	0.72 ± 0.05	0.72 ± 0.12	1	1	f_{α_b}	0.77 ± 0.09	0.78 ± 0.11	1	1
w_γ	0.221 ± 0.004	0	0	0.2751 ± 0.0016	0.280 ± 0.004			w_γ	0	0	0.228 ± 0.003	0.223 ± 0.004
w_{α_b}	0.778 ± 0.004	1	1	0.7249 ± 0.0016	0.720 ± 0.004	1	1	w_{α_b}	0.772 ± 0.003	0.777 ± 0.004	1	1
a_γ / Å	3.62389 ± 0.00017	N/A	N/A	3.62714 ± 0.00005	3.61774 ± 0.00010	N/A	N/A	a_γ / Å	3.62345 ± 0.00012	3.61234 ± 0.00015	N/A	N/A
a_{α_b} / Å	2.86638 ± 0.00027	2.88624 ± 0.00017	2.86801 ± 0.00017					a_{α_b} / Å	2.8663 ± 0.0003	2.8627 ± 0.0004	2.88617 ± 0.00009	2.8666 ± 0.0003
c_{α_b} / Å	2.8803 ± 0.0008	2.8904 ± 0.0003	2.8748 ± 0.0003	2.87298 ± 0.00016	2.8806 ± 0.0005	2.88868 ± 0.00006	2.86817 ± 0.00008	c_{α_b} / Å	2.8804 ± 0.0006	2.8774 ± 0.0009	2.88921 ± 0.00018	2.8694 ± 0.0005
$\frac{c}{a}$	1.0048 ± 0.0003	1.00144 ± 0.00013	1.00236 ± 0.00013	1.00259 ± 0.00006	1.00548 ± 0.00022	1.000560 ± 0.000020	1.00091 ± 0.000029	$\frac{c}{a}$	1.00493 ± 0.00022	$1.0051 \pm 0.0003\pm$	1.00105 ± 0.00007	1.00098 ± 0.00020
w_C / wt%	0.108 ± 0.006	0.031 ± 0.003	0.052 ± 0.003	0.0577 ± 0.0013	0.122 ± 0.005	0.0124 ± 0.0004	0.0202 ± 0.0006	w_C	0.109 ± 0.005	0.114 ± 0.008	0.0234 ± 0.0015	0.022 ± 0.005
d_γ / nm	23.2 ± 1.3	N/A	N/A	31.0 ± 1.2	57.4 ± 2.1	N/A	N/A	d_γ / nm	22.1 ± 0.1	19.4 ± 0.9	N/A	N/A
d_{α_b} / nm	99 ± 5	151 ± 23	136 ± 3	143 ± 5	88 ± 3	N/A	390 ± 200	d_{α_b} / nm	97 ± 5	84 ± 4	139 ± 19	125 ± 3
R_{wp}	2.96	1.6	3.11	2.42	3.38	3.19	3.85	R_{wp}	2.68	2.74	1.63	2.94
R_p	4.51	3.1	6.68	3.35	4.27	5.17	7.67	R_p	3.05	3.06	2.92	6.01
R_{wp} no bg	1.65	0.87	1.98	1.56	1.88	2.22	3.02	R_{wp} no bg	1.96	1.97	1.1	1.94
R_p no bg	2.9	1.77	4.33	2.49	3.21	4.11	5.91	R_p no bg	2.45	2.41	1.88	3.91

Table B.4: Overall results for SP10 with tetragonal bainitic ferrite

Bibliography

[1] H. K. D. H. Bhadeshia. Hard bainite. *The Minerals, Metals and Materials Society*, 1:469–484, 2005.

[2] Rolls-Royce. *The Jet Engine*. Derby, 5th edition, 1986.

[3] J. M. Allwood, J. M. Cullen, M. A. Carruth, D. R. Cooper, M. McBrien, L. Milford, Rachel, M. C. Moynihan, and A. C. H. Patel. *Sustainable Materials With Both Eyes Open*. 2012.

[4] World Steel Association. Crude steel production, 1980-2012. Technical report, World Steel Association, 2012.

[5] F.-W. Wellmer and J. D. Becker-Platen. Global Nonfuel Mineral Resources and Sustainability. Technical report, 2007.

[6] D. J. C. Mackay. *Sustainable Energy without the hot air*. Cambridge, U. K., 2009.

[7] H. Okamoto. The C-Fe (carbon-iron) system. *Journal of Phase Equilibria*, 13:543–565, 1992.

[8] H. Ohtani, M. Hasebe, and T. Nishizawa. Calculation of Fe-C, Co-C and Ni-C phase diagrams. *Transactions of the Iron and Steel Institute of Japan*, 24:857–864, 1984.

[9] J. Chipman. Thermodynamics of liquid Fe-C solutions. *Metallurgical Transactions*, 1:2163–2168, 1970.

[10] *ASM Handbook Volume III: Alloy Phase diagrams*. ASM International, 1992.

[11] H. K. D. H. Bhadeshia. *Bainite in Steels: Theory and Practice*. Maney Publishing, Leeds, U.K., 3rd edition, 2015.

[12] H. K. D. H. Bhadeshia and R. W. K. Honeycombe. *Steels*. Elsevier Ltd, Cambridge, 3rd edition, 2006.

[13] E. C. Bain and H. W. Paxton. *Alloying Elements in Steel*. ASM, Metals Park, Ohio, USA, 2nd edition, 1966.

[14] DoITPoMS - Micrograph Library. Avaible from `http://www.doitpoms.ac.uk/miclib/index.php`, University of Cambridge, 2015.

[15] M. Hillert. The formation of pearlite. In V. F. Zackay and H. I. Aaronson, editors, *The decomposition of austenite by diffusional processes*, pages 197–247. NY Interscience, New York, N. Y., U. S. A., 1962.

[16] R. J. Dippenaar and R. W. K. Honeycombe. The crystallography and nucleation of pearlite. *Proceedings of the Royal Society A: Mathematical and Physical Sciences*, 333:455–467, 1973.

[17] M. a. Mangan and G. J. Shiflet. The pitsch-petch orientation relationship in ferrous pearlite at small undercooling. *Metallurgical and Materials Transactions A*, 30:2767–2781, 1999.

[18] D. N. Shackleton and P. M. Kelly. The crystallography of cementite precipitation in the bainite transformation. *Acta Metallurgica*, 15:979–992, 1967.

[19] K. W. Andrews. The structure of cementite and its relation to ferrite and epsilon carbide. *Acta Metallurgica*, 12:921–929, 1964.

[20] S. Chattopadhyay and C. M. Sellars. Quantitative measurements of pearlite spheroidization. *Metallography*, 10:89–105, 1977.

[21] N. V. Luzginova, L. Zhao, and J. Sietsma. The Cementite Spheroidization Process in High-Carbon Steels with Different Chromium Contents. *Metallurgical and Materials Transactions A*, 39:513–521, 2008.

[22] E. D. Hyam and J. Nutting. The Tempering of Plain Carbon Steels. *Journal of the Iron and Steel Institute*, 184:148–, 1956.

[23] J. W. Christian. Thermodynamics and Kinetics of Martensite. In G. B. Olson, editor, *International Conerence on the Martensitic Transformations*, page 222, Cambridge, MA, USA, 1979.

[24] A. Ali and H. K. D. H. Bhadeshia. Nucleation of Widmanstatten ferrite. *Materials Science and Technology*, 6:781–784, 1990.

[25] R. H. Davies, A. T. Dinsdale, J. A. Gisby, J. A. J. Robinson, and S. M. Martin. MTData thermodynamic modelling software, 2001.

[26] SGTE thermodynamic Database for steels, version 4.2, 2006.

[27] J. D. Watson and P. G. McDougall. The crystallography of Widmanstätten ferrite. *Acta Metallurgica*, 21:961–973, 1973.

[28] P. G. McDougall. Comment on "The Watson-McDougall shear: proof that Widmanstatten ferrite cannot grow martensitically". *Scripta Metallurgica*, 9:713–715, 1975.

[29] H. Miyaji and E.-I. Furubayashi. Transformation Texture Analysis of BCC and BCT Ferrous Martensite. *Textures and Microstructures*, 22:43–51, 1993.

[30] T. Maki, S. Shimooka, S. Fujiwara, and I. Tamura. Formation Temperature Thin Plate Martensite and Growth Behavior of in Fe-Ni-C Alloys. *Transactions of the Japan Instuitute of Metals*, 16:35–41, 1975.

[31] S. M. C. Van Bohemen, M. J. M. Hermans, and G. den Ouden. Monitoring of martensite formation during welding by means of acoustic emission. *Journal of Physics D: Applied Physics*, 34:3312–3317, 2001.

[32] F. Foerster and E. Scheil. Akustische Untershung der Bildung von Martensitnadeln. *Zeitschrift für Metallkunde*, 9:245–247, 1936.

[33] H. K. D. H. Bhadeshia. *Steels* - University of Cambridge course lecture notes, available from `http://www.msm.cam.ac.uk/phase-trans/2010/M21.pdf`. Cambridge, U. K., 2015.

[34] G. V. Kurdjumov and G. Sachs. Over the mechanisms of steel hardening. *Zeitschrift für Physik*, 64:325–343, 1930.

[35] G. Wasserman. Einflusse der alpha-gamma-umwandlung eines irreversiblen nickelstahls auf kristallorientierung und zugfestkeit. *Arch. Eisenhuettenwes*, 6:347–351, 1933.

[36] Z. Nishiyama. X-ray investigation of the mechanism of the transformation from face centered cubic lattice to body centered cubic. *Science Repository of Tohoku Imperial University*, 23:637–664, 1934.

[37] A. R. Troiano and A. B. Greninger. The marteniste transformation. *Metal Progress*, 50:303–307, 1946.

[38] H. K. D. H. Bhadeshia and D. V. Edmonds. The Mechanism of Bainite Formation in Steels. *Acta Metallurgica*, 28:1265–1273, 1980.

[39] E. S. Davenport, E. C. Bain, and N. J. Kearny. Transformation of Austenite at Constant Subcritical Temperatures. *Transactions of the American Intsitute of Metallurgical Engineers*, 90:117–154, 1930.

[40] M. Hillert and A. Borgenstam. Centennial of the diffusionless paradigm of bainite. *Metallurgical and Materials Transactions A: Physical Metallurgy and Materials Science*, 43:4487–4495, 2012.

[41] E. C. Bain. The Nature of Martensite. *Transactions of the American Intsitute of Metallurgical Engineers*, 70:25–46, 1924.

[42] A. Hultgren. Isothermal Transformation of Austenite. *Transactions of the American Society of Materials*, 39:915–989, 1947.

[43] R. F. Hehemann, K. R. Kinsman, and H. I. Aaronson. A debate on the bainite reaction. *Metallurgical Transactions*, 3:1077–1094, 1972.

[44] M. Hillert, A. Borgenstam, and J. Ågren, John. Do bainitic and Widmanstätten ferrite grow with different mechanisms? *Scripta Materialia*, 62:75–77, 2010.

[45] E. Swallow and H. K. D. H. Bhadeshia. High resolution observations of displacements caused by bainitic transformation. *Materials Science and Technology*, 12:121–125, 1996.

[46] H.-Y. Li and X.-J. Jin. Determination of Dislocation Density in Nano structured Bainitic Steels. *Journal of Shanghaijiaotong University*, 44:613–616, 2010.

[47] F. G. Caballero, H.-W. Yen, M. K. Miller, J.-R. Yang, J. Cornide, and C. García-Mateo. Complementary use of transmission electron microscopy and atom probe tomography for the examination of plastic accommodation in nanocrystalline bainitic steels. *Acta Materialia*, 59:6117–6123, 2011.

[48] F. G. Caballero, M. K. Miller, and C. García-Mateo. Atom Probe Tomography Analysis of Precipitation during Tempering of a Nanostructured Bainitic Steel. *Metallurgical and Materials Transactions A*, 42:3660–3668, 2011.

[49] C. García-Mateo, F. G. Caballero, C. Capdevila, and C. G. D. Andres. Estimation of dislocation density in bainitic microstructures using high-resolution dilatometry. *Scripta Materialia*, 61:855–858, 2009.

[50] H. J. Stone, M. J. Peet, H. K. D. H. Bhadeshia, P. J. Withers, S. S. Babu, and E. D. Specht. Synchrotron X-ray studies of austenite and bainitic ferrite. *Proceedings of the Royal Society A: Mathematical, Physical and Engineering Sciences*, 464:1009–1027, 2008.

[51] H. Matsuda and H. K. D. H. Bhadeshia. Kinetics of the bainite transformation. *Proceedings of the Royal Society A: Mathematical, Physical and Engineering Sciences*, 460:1707–1722, 2004.

[52] F. G. Caballero, M. K. Miller, and C. García-Mateo. Carbon supersaturation of ferrite in a nanocrystalline bainitic steel. *Acta Materialia*, 58:2338–2343, 2010.

[53] F. G. Caballero, M. K. Miller, A. J. Clarke, and C. García-Mateo. Examination of carbon partitioning into austenite during tempering of bainite. *Scripta Materialia*, 63:442–445, 2010.

[54] F. G. Caballero, M. K. Miller, C. García-Mateo, and J. Cornide. New experimental evidence of the diffusionless transformation nature of bainite. *Journal of Alloys and Compounds*, 577:S626–S630, 2013.

[55] C. García-Mateo, F. G. Caballero, M. K. Miller, and J. A. Jimenez. On measurement of carbon content in retained austenite in a nanostructured bainitic steel. *Journal of Materials Science (full set)*, 47:1004–1010, 2012.

[56] F. G. Caballero, M. K. Miller, C. García-Mateo, J. Cornide, and M. J. Santofimia. Temperature dependence of carbon supersaturation of ferrite in bainitic steels. *Scripta Materialia*, 67:846–849, 2012.

[57] F. G. Caballero, C. García-Mateo, and M. K. Miller. Design of Novel Bainitic Steels: Moving from UltraFine to Nanoscale Structures. *Jom*, 2014.

[58] H. Yada, M. Enomoto, and T. Sonoyama. Lengthening Kinetics of Bainitic Plates in Iron-Nickel-Carbon Alloys. *ISIJ International*, 35:976–981, 1995.

[59] D. Quidort and Y. J. M. Brechet. Isothermal growth kinetics of bainite in 0.5% C steels. *Acta Materialia*, 49:4161–4170, 2001.

[60] H. Hu, G. Xu, Y. Zhang, Z. Xue, and M. Zhou. Dynamic observation of bainite transformation in a Fe-C-Mn-Si superbainite steel. *Journal of Wuhan University of Technology-Mater. Sci. Ed.*, 30:818–821, 2015.

[61] H.-S. Fang, J. B. Yang, Z. G. Yang, and B. Z. Bai. The mechanism of bainite transformation in steels. *Scripta Materialia*, 47:157–162, 2002.

[62] H.-S. Fang, B. Xiang-Zheng, and J.-J. Wang. A Model for Surface Reliefs Formation in Bainite Transformation Mechanism. *Materials Transactions*, 39:1264–1271, 1998.

[63] A. Borgenstam, M. Hillert, and J. Ågren. Metallographic evidence of carbon diffusion in the growth of bainite. *Acta Materialia*, 57:3242–3252, 2009.

[64] M. Kang, M. X. Zhang, and M. Zhu. In situ observation of bainite growth during isothermal holding. *Acta Materialia*, 54:2121–2129, 2006.

[65] G. V. Smith and R. F. Mehl. Lattice Relationships in Decomposition of Austenite to Pearlite, Bainite, and Martensite. *Transactions of the American Intsitute of Metallurgical Engineers*, 150:211–226, 1942.

[66] N. Udompongsanon and D. W. Borland. Note on the transition from Lath to Plate Martensite. *Journal of the Australian Institute of Metals*, 19:56–58, 1974.

[67] F. G. Caballero, H. K. D. H. Bhadeshia, K. J. A. Mawella, D. G. Jones, and P. M. Brown. Very strong low temperature bainite. *Materials Science and Technology*, 18:279–284, 2002.

[68] B. P. J. Sandvik. The Bainite Reaction in Fe-Si-C Alloys: The Primary Stage. *Metallurgical Transactions A*, 13:777–787, 1982.

[69] P. Yan and H. K. D. H. Bhadeshia. Mechanism and kinetics of solid-state transformation in high-temperature processed linepipe steel. *Metallurgical and Materials Transactions A: Physical Metallurgy and Materials Science*, 44:5468–5477, 2013.

[70] P. J. Withers and H. K. D. H. Bhadeshia. Residual stress. Part 2 Nature and origins. *Materials Science and Technology*, 17:366–375, 2001.

[71] H. K. D. H. Bhadeshia and D. V. Edmonds. The bainite transformation in a silicon steel. *Metallurgical Transactions A*, 10A:895–907, 1979.

[72] G. R. Speich. Growth Kinetics of Bainite in a Three Per Cent Chromium Steel. In V. F. Zackay and H. I. Aaronson, editors, *Decomposition of Austenite by Diffusional Processes*, pages 353–367. 1962.

[73] K. Shimizu, T. Ko, and Z. Nishiyama. Transmission Electron Microscope Observation of the Bainite of Carbon Steel. *Transactions of the Japan Instuitute of Metals*, 5:225–230, 1964.

[74] L. C. Chang and H. K. D. H. Bhadeshia. Microstructure of lower bainite formed at large undercoolings below martensite start temperature. *Materials Science and Technology*, 12:233–236, 1996.

[75] P. M. Brown and D. P. Baxter. Hyper-strength Bainitic steels. Technical report, Porton Down / Qinetiq, Salisbury / Farnborough, 2004.

[76] H. K. D. H. Bhadeshia and A. R. Waugh. Bainite: an atom probe study of the incomplete reaction phenomenon. *Acta Metallurgica*, 30:775–784, 1982.

[77] F. Hu and K. M. Wu. Isothermal Transformation of Low Temperature Super Bainite. *Advanced Materials Research*, 146-147:1843–1848, 2010.

[78] E. Kozeschnik and H. K. D. H. Bhadeshia. Influence of silicon on cementite precipitation in steels. *Materials Science and Technology*, 24:343–347, 2008.

[79] K. J. Irvine and F. B. Pickering. High-carbon bianitic steels. Technical report, Iron and Steel Institute, 1965.

[80] K. J. Irvine, F. B. Pickering, W. C. Heselwood, and M. Atkins. The Physical MeIetallurgy of Low-carbon, Low-alloy Steels containing Boron. *Journal Of The Iron And Steel Institute*, 186:54–67, 1957.

[81] T. Angel. Formation of martensite in austenitic stainless steels-effects of deformation, temperature, and composition. *Journal Of The Iron And Steel Institute*, 177:165, 1954.

[82] V. F. Zackay. The enhancement of ductility in high-strength steels. *ASM Transactions Quaterly*, 60:252–259, 1967.

[83] G. B. Olson and M. Azrin. Transformation behavior of TRIP steels. *Metallurgical and Materials Transactions A*, 9A:713–721, 1978.

[84] P. J. Jacques, Q. Furnémont, A. Mertens, and F. Delannay. On the sources of work hardening in multiphase steels assisted by transformation-induced plasticity. *Philosophical Magazine A*, 81:1789–1812, 2001.

[85] D. Webster. Effect of Grain Refinement on the Microstructure and Mechanical Properties of 4340M. *Metallurgical Transactions*, 4:1972–1974, 1973.

[86] J. Eshelby, F. Frank, and F. Nabarro. XLI. The equilibrium of linear arrays of dislocations. *The London, Edinburgh, and Dublin Philosophical Magazine and Journal of Science*, 42:351–364, 2010.

[87] E. O. Hall. The Deformation and Ageing of Mild Steel: III Discussion of Results. *Proceedings of the Royal Physical Society B*, 64:747–753, 1951.

[88] N. J. Petch. The cleavage strength of polycrystals. *Journal Of The Iron And Steel Institute*, 174:25–28, 1953.

[89] A. Cracknell and N. J. Petch. Frictional forces on dislocation arrays at the lower yield pint of iron. *Acta Metallurgica*, 3:186–189, 1955.

[90] G. Langford and M. Cohen. Strain hardening of iron by severe plastic deformation. *Transactions of the American Society of Materials*, 62:623–638, 1969.

[91] G. Langford and M. Cohen. Calculation of Cell-Size Strengthening of Wire-Drawn Iron. *Metallurgical Transactions*, 1:1478–1480, 1970.

[92] H. K. D. H. Bhadeshia. Nanostructured bainite. *Proceedings of the Royal Society A: Mathematical, Physical and Engineering Sciences*, 466:3–18, 2009.

[93] C. Mack and M. S. Bartlett. On clumps formed when convex laminae or bodies are placed at random in two or three dimensions. *Mathematical Proceedings of the Cambridge Philosophical Society*, 52:246, 1956.

[94] K. Miyata, M. Wakita, S. Fukushima, M. Eto, T. Sasaki, and T. Tomida. Ultrafine Grained Steels due to Super Short Interval Multi-Pass Rolling in Stable Austenite Region. *Materials Science Forum*, 539-543:4698–4703, 2007.

[95] S. Ferrasse, V. M. Segal, K. T. Hartwig, and R. E. Goforth. Development of a submicrometer-grained microstructure in aluminum 6061 using equal channel angular extrusion. *Journal of Materials Research*, 12:1253–1261, 2011.

[96] D. H. Shin, K.-T. Park, and Y.-S. Kim. Formation of fine cementite precipitates in an ultra-fine grained low carbon steel. *Scripta Materialia*, 48: 469–473, 2003.

[97] A. Kostka, K. Tak, R. Hellmig, Y. Estrin, and G. Eggeler. On the contribution of carbides and micrograin boundaries to the creep strength of tempered martensite ferritic steels. *Acta Materialia*, 55:539–550, 2007.

[98] H. Beladi, G. L. Kelly, and P. D. Hodgson. Ultrafine grained structure formation in steels using dynamic strain induced transformation processing. *International Materials Reviews*, 52:14–28, 2007.

[99] R. Ueji, N. Tsuji, Y. Minamino, and Y. Koizumi. Ultragrain refinement of plain low carbon steel by cold-rolling and annealing of martensite. *Acta Materialia*, 50:4177–4189, 2002.

[100] N. Tsuji, R. Ueji, Y. Minamino, and Y. Saito. A new and simple process to obtain nano-structured bulk low-carbon steel with superior mechanical property. *Scripta Materialia*, 46:305–310, 2002.

[101] R. Ueji, N. Tsuji, Minamino, and Y. Koizumi.

[102] H. Kitahara, R. Ueji, N. Tsuji, and Y. Minamino. Crystallographic features of lath martensite in low-carbon steel. *Acta Materialia*, 54:1279–1288, 2006.

[103] H. K. D. H. Bhadeshia. Properties of fine-grained steels generated by displacive transformation. *Materials Science and Engineering A*, 481-482:36–39, 2008.

[104] M. J. Peet. *Transformation and tempering of low-temperature bainite*. PhD thesis, University of Cambridge, 2010.

[105] L. C. D. Fielding, E. J. Song, D. K. Han, H. K. D. H. Bhadeshia, and D.-W. Suh. Hydrogen diffusion and the percolation of austenite in nanostructured bainitic steel. *Proceedings of the Royal Society A*, 470:1–32, 2014.

[106] C. García-Mateo, F. G. Caballero, T. Sourmail, M. Kuntz, J. Cornide, V. Smanio, and R. Elvira. Tensile behaviour of a nanocrystalline bainitic steel containing 3 wt% silicon. *Materials Science and Engineering A*, 549: 2–9, 2012.

[107] C. García-Mateo, F. G. Caballero, and H. K. D. H. Bhadeshia. Low Temperature Bainite. *Journal de Physique IV*, 112:285–288, 2003.

[108] F. G. Caballero and H. K. D. H. Bhadeshia. Very strong bainite. *Current Opinion in Solid State and Materials Science*, 8:251–257, 2004.

[109] C. García-Mateo, F. G. Caballero, T. Sourmail, V. Smanio, and C. G. de Andres. Industrialised nanocrystalline bainitic steels. Design approach. *International Journal of Materials Research*, 105:725–734, 2014.

[110] C. García-Mateo, F. G. Caballero, and H. K. D. H. Bhadeshia. Acceleration of Low-temperature Bainite. *ISIJ International*, 43:1821–1825, 2003.

[111] C. García-Mateo and F. G. Caballero. Ultra-high-strength Bainitic Steels. *ISIJ International*, 45:1736–1740, 2005.

[112] F. G. Caballero, M. J. Santofimia, C. García-Mateo, J. Chao, and C. G. de Andres. Theoretical design and advanced microstructure in super high strength steels. *Materials & Design*, 30:2077–2083, 2009.

[113] M. Zhang, T. S. Wang, Y. Wang, J. Yang, and F. C. Zhang. Preparation of nanostructured bainite in medium-carbon alloysteel. *Materials Science and Engineering A*, 568:123–126, 2013.

[114] M. J. Peet and H. K. D. H. Bhadeshia. Surface Relief Due to Bainite Transformation at 473 K (200 celsius). *Metallurgical and Materials Transactions A*, 42:3344–3348, 2011.

[115] H. K. D. H. Bhadeshia. A rationalisation of shear transformations in steels. *Acta Metallurgica*, 29:1117–1130, 1981.

[116] A. Saha Podder and H. K. D. H. Bhadeshia. Thermal stability of austenite retained in bainitic steels. *Materials Science and Engineering A*, 527:2121–2128, 2010.

[117] K. H. Jack. Structural Transformations in the Tempering of High-Carbon Martensitic Steels. *Journal of the Iron and Steel Institute*, 169:26–36, 1951.

[118] J. van Aswegen, R. W. K. Honeycombe, and D. Warrington. Precipitation on stacking faults in Cr-Ni austenitic steels. *Acta Metallurgica*, 12:1–13, 1964.

[119] J. M. Gray. Effect of niobium (columbium) on transformation and precipitation process in high-strength low-alloy steels. In *Proceeding of Heat Treatment 73*, pages 12–13, 1973.

[120] N. Fujita and H. K. D. H. Bhadeshia. Modelling precipitation of niobium carbide in austenite: multicomponent diffusion, capillarity, and coarsening. *Materials Science and Technology*, 17:403–408, 2001.

[121] W. M. Rainforth, M. P. Black, R. L. Higginson, E. J. Palmiere, C. M. Sellars, I. Prabst, P. Warbichler, and F. Hofer. Precipitation of NbC in a model austenitic steel. *Acta Materialia*, 50:735–747, 2002.

[122] B. Dutta, E. J. Palmiere, and C. M. Sellars. Modelling the kinetics of strain induced precipitation in Nb microalloyed steels. *Acta Materialia*, 49:785–794, 2001.

[123] E. Courtois, T. Epicier, and C. Scott. EELS study of niobium carbo-nitride nano-precipitates in ferrite. *Micron*, 37:492–502, 2006.

[124] M. Perez, E. Courtois, D. Acevedo, T. Epicier, and P. Maugis. Precipitation of niobium carbonitrides in ferrite: chemical composition measurements and thermodynamic modelling. *Philosophical Magazine Letters*, 87:645–656, 2007.

[125] A. T. Davenport and R. W. K. Honeycombe. The Secondary Hardening of Tungsten Steels. *Metal Science*, 9:201–208, 1975.

[126] H. J. Goldschmidt. A New Carbide in Chomium Steels. *Nature*, 162:855–856, 1948.

[127] A. Melander and P. Ölund. Detrimental effect of nitride and aluminium oxide inclusions on fatigue life in rotating bending of bearing steels. *Materials Science and Technology*, 15:555–562, 1999.

[128] S. Murphy and J. A. Whiteman. The Kinetics of Mo_2C Precipitation in Tempered Martensite. *Metal Science*, 4:58–62, 1970.

[129] J. B. Lupton. The Kinetics of Mo2C Precipitation in Tempered Martensite. *Metal Science*, 5:160–160, 1971.

[130] K. J. Kurzydłowski and W. Zieliński. $Mo_2C \rightarrow Mo_6C$ carbide transformation in low alloy Cr-Mo ferritic steels. *Metal Science*, 18:223–224, 1984.

[131] E. Smith. An investigation of secondary hardening of a 1% vanadium - 0.2% carbon steel. *Acta Metallurgica*, 14:583–593, 1966.

[132] S. Yamasaki and H. K. D. H. Bhadeshia. Modelling and characterisation of V_4C_3 precipitation and cementite dissolution during tempering of Fe-C-V martensitic steel. *Materials Science and Technology*, 19:1335–1343, 2003.

[133] A. L. Bowman, G. P. Arnold, E. K. Storms, and N. G. Nereson. The crystal structure of $Cr_{23}C_6$. *Acta Crystallographica Section B Structural Crystallography and Crystal Chemistry*, 28:3102–3103, 1972.

[134] A. Saha Podder. *Tempering of a Mixture of Bainite and Retained Austenite*. Phd, University of Cambridge, 2011.

[135] R. T. Downs and M. Hall-Wallace. The American Mineralogist crystal structure database. *American Mineralogist*, 88:247–250, 2003.

[136] S. Graulis, D. Chateigner, R. T. Downs, A. F. T. Yokochi, M. Quirós, L. Lutterotti, E. Manakova, J. Butkus, P. Moeck, and A. Le Bail. Crystallography Open Database - An open-access collection of crystal structures. *Journal of Applied Crystallography*, 42:726–729, 2009.

[137] S. Gražulis, A. Daškevič, A. Merkys, D. Chateigner, L. Lutterotti, M. Quirós, N. R. Serebryanaya, P. Moeck, R. T. Downs, and A. Le Bail. Crystallography Open Database (COD): An open-access collection of crystal structures and platform for world-wide collaboration. *Nucleic Acids Research*, 40:420–427, 2012.

[138] S. B. Hendricks. XXXVI. The Crystal Structure of Cementite. *Zeitschrift für Kristallographie - Crystalline Materials*, 74:535–545, 1930.

[139] S. Nagakura. Study of Metallic Carbides by Electron Diffraction PartIII. Iron Carbides. *Journal of the Physical Society of Japan*, 14:186–195, 1958.

[140] D. Kalish and M. Cohen. Structural changes and strengthening in the strain tempering of martensite. *Materials Science and Engineering*, 6:156–166, 1970.

[141] K. H. Jack. Results of Furher X-ray Structural Investigations of the Iron-Carbon and Iron-Nitrogen Systems and of Related Intersititial Alloys. *Acta Crystallographica*, 3:392–394, 1950.

[142] B. K. Jha and N. S. Mishra. Microstructural evolution during tempering of a multiphase steel containing retained austenite. *Materials Science and Engineering A*, 263:42–55, 1999.

[143] B. Kim, C. Celada, D. San Martín, T. Sourmail, and P. E. J. Rivera-Díaz-del Castillo. The effect of silicon on the nanoprecipitation of cementite. *Acta Materialia*, 61:6983–6992, 2013.

[144] Y. Hirotsu and S. Nagakura. Crystal structure and morphology of the carbide precipitated from martensitic high carbon steel during the first stage of tempering. *Acta Metallurgica*, 20:645–655, 1972.

[145] I. G. Kim, G. Rahman, J. H. Jang, Y. Y. Song, S. W. Seo, H. K. D. H. Bhadeshia, A. Freeman, and G. B. Olson. A Systematic Study on Iron Carbides from First-Principles. *Materials Science Forum*, 654-656:47–50, 2010.

[146] W. Pitsch. Der Orientierungszusammenhang zwischen Zementit und Austenit. *Acta Metallurgica*, 10:897–900, 1962.

[147] S. W. Thompson and P. R. Howell. The orientation relationship between intragranularly nucleated Widmanstätten cementite and austenite in a commercial hypereutectoid steel. *Scripta Metallurgica*, 21:1353–1357, 1987.

[148] I. B. Timokhina, H. Beladi, X. Y. Xiong, Y. Adachi, and P. D. Hodgson. Nanoscale microstructural characterization of a nanobainitic steel. *Acta Materialia*, 59:5511–5522, 2011.

[149] D. A. Porter, K. E. Easterling, and M. Sherif. *Phase Transformations in Metals and Alloys*. CRC Press, 3rd correc edition, 2009.

[150] G. R. Speich and W. C. Leslie. Tempering of Steel. *Metallurgical Transactions*, 3:1043–1054, 1972.

[151] H. Beladi, Y. Adachi, I. B. Timokhina, and P. D. Hodgson. Nano-structured Bainitic Steels: Microstructure Characteristics and Mechanical Properties. *CAMP-ISIJ*, 21:540, 2008.

[152] F. G. Caballero, M. K. Miller, and C. Capdevila. Phase Transformation Theory : Advanced Steels. *Solid State Phase Transformations*, 60:16–21, 2008.

[153] T. Bell and B. C. Farnell. The Isothermal Decomposition of Nitrogen Austenite to Bainite. pages 282–287, 1968.

[154] N. Nakada, N. Fukuzawa, T. Tsuchiyama, S. Takaki, T. Koyano, T. Iwamoto, and Y. Omori. Isothermal Transformation in Fe-N Hypereutectoid Alloy. *ISIJ International*, 53:139–144, 2013.

[155] D. Jiao, C. Luo, J. Liu, and G. Zhang. Morphology and crystallographic orientation relationship in isothermally transformed Fe-N austenite. *Materials Characterization*, 88:52–57, 2014.

[156] Y. Wang, Y. Rong, X. Chen, and G. Hu. Characterization of γ-Fe4N precipitates in a compound layer formed by austenitic nitrocarburizing treatment. *Materials Characterization*, 34:213–216, 1995.

[157] H. A. Wriedt, N. A. Gokcen, and R. H. Nafziger. Fe (Iron) Binary Phase Diagrams. In *ASM Metals Handbook, Volume 3 - Alloy Phase Diagrams*, chapter Fe-N. ASM International, 1992.

[158] E. R. Petty. *Physical metallurgy of engineering materials.* American Elsevier Publishing Company, 6th edition, 1968.

[159] R. Elliott. *Cast Iron Technology.* Butterworth & Co. (Publshers) Ltd., 1988.

[160] W. S. Owen. The Effect of Slicon on the Kinetics of Tempering. *Transactions of the American Society of Materials*, 46:812–829, 1954.

[161] J. Deliry. Nouveau carbure de fer. Transformation bainitique dans le aciers au carbone silicium. *Memoires Scientifiques de la Revue de Metallurgie*, 62: 527–550, 1965.

[162] J. Gordine and I. Codd. The influence of silicon up to 1.5 wt% on the tempering characteristics of a spring steel. *Journal of the Iron and Steel Institute*, 207.1:461–468, 1969.

[163] R. M. Hobbs, G. W. Lorimer, and N. Ridley. Effect of Silicon on the Microstructure of Quenched and Tempered Medium-Carbon Steels. *Journal of the Iron and Steel Institute*, 210.2:757–764, 1972.

[164] R. A. Mesquita, C. A. Barbosa, E. V. Morales, and H. J. Kestenbach. Effect of silicon on carbide precipitation after tempering of H11 hot work steels. *Metallurgical and Materials Transactions A: Physical Metallurgy and Materials Science*, 42:461–472, 2011.

[165] S. S. Babu, K. Hono, and T. Sakurai. Atom Probe Field Ion Microscopy Study of the Partitioning of Substitutional Elements during Tempering of a Low-Alloy Steel Martensite. *Metallurgical and Materials Transactions A*, 25:499–508, 1994.

[166] G. Ghosh, C. E. Campbell, and G. B. Olson. An Analytical Electron Microscopy Study of Paraequilibrium Cementite Precipitation in Ultra-High-Strength Steel. *Metallurgical and Materials Transactions A*, 30, 1999.

[167] G. Ghosh and G. B. Olson. Precipitation of paraequilibrium cementite: Experiments, and thermodynamic and kinetic modeling. *Acta Materialia*, 50:2099–2119, 2002.

[168] S. S. Babu, K. Hono, and T. Sakurai. APFIM studies on martensite tempering of Fe-C-Si-Mn low alloy steel. *Applied Surface Science*, 67:321–327, 1993.

[169] F. G. Caballero, M. K. Miller, S. S. Babu, and C. García-Mateo. Atomic scale observations of bainite transformation in a high carbon high silicon steel. *Acta Materialia*, 55:381–390, 2007.

[170] H. K. D. H. Bhadeshia, M. Lord, L. E. Svensson, P. Street, and C. Cb. Silicon Rich Bainitic Steel Welds. 2003.

[171] J. H. Jang, I. G. Kim, and H. K. D. H. Bhadeshia. Substitutional solution of silicon in cementite: A first-principles study. *Computational Materials Science*, 44:1319–1326, 2009.

[172] J. H. Jang, I. G. Kim, and H. K. D. H. Bhadeshia. ϵ-carbide in Alloy Steels : First-principles Assessment. *Scripta Materialia*, 63:121–123, 2010.

[173] D.-H. Huang and G. Thomas. Structure and Mechanical Properties of Tempered Martensite and Lower Bainite in Fe-Ni-Mn-C Steels. *Metallurgical Transactions*, 2:1587–1598, 1971.

[174] J. Liu and C. P. Luo. Precipitation behavior of the lower bainitic carbide in a medium-carbon steel containing Si, Mn and Mo. *Materials Science and Engineering A*, 438-440:153–157, 2006.

[175] W. Song, J. von Appen, P.-P. Choi, R. Dronskowski, D. Raabe, and W. Bleck. Atomic-scale investigation of ϵ and θ precipitates in bainite in 100Cr6 bearing steel by atom probe tomography and ab initio calculations. *Acta Materialia*, 61:7582–7590, 2013.

[176] C. H. Young and H. K. D. H. Bhadeshia. Strength of mixtures of bainite and martensite. *Materials Science and Technology*, 10:209–214, 1994.

[177] H. K. D. H. Bhadeshia. Computational design of advanced steels. *Scripta Materialia*, 70:12–17, 2014.

[178] H. I. Aaronson and H. A. Domian. Partitioning of Alloying Elements Between Austenite and Proeutectoid Ferrite or Bainite. *Transactions Of The Metallurgical Society Of AIME*, 237:781–796, 1966.

[179] M. Soliman and H. Palkowski. Ultra-fine Bainite Structure in Hypo-eutectoid Steels. *ISIJ International*, 47:1703–1710, 2007.

[180] I. Lonardelli, L. Girardini, L. Maines, C. Menapace, A. Molinari, and H. K. D. H. Bhadeshia. Nanostructured bainitic steel obtained by powder metal-

lurgy approach: structure, transformation kinetics and mechanical properties. *Powder Metallurgy*, 55:256–259, 2012.

[181] I. Lonardelli, M. Bortolotti, W. van Beek, L. Girardini, M. Zadra, and H. K. D. H. Bhadeshia. Powder metallurgical nanostructured medium carbon bainitic steel : Kinetics , structure , and in situ thermal stability studies. *Materials Science and Engineering A*, 555:139–147, 2012.

[182] H. Huang, M. Sherif, and P. E. J. Rivera-Díaz-del Castillo. Combinatorial optimization of carbide-free bainitic nanostructures. *Acta Materialia*, 61: 1639–1647, 2013.

[183] W. C. Leslie and G. C. Rauch. Precipitation of Carbides in Low-Carbon Fe-Al-C Alloys. *Metallurgical Transactions A*, 9A:343–349, 1978.

[184] K. R. Kinsman and H. I. Aaronson. Effect of manganese and molybdenum on the kinetics of the ferrite reaction. In *Transformation and hardenability in Steels: symposium, Climax Molybdenum Co.*, page 39, Ann-Arbor, Michigan, U. S. A., 1967.

[185] J. M. Oblak and R. F. Hehemann. Structure and Growth of Widmanstatten Ferrite and Bainite. In *Hardenability of Alloy Steels: symposium: Climax Molybdenum Co.*, pages 15–38, Ann-Arbor, Michigan, U. S. A., 1967.

[186] S. J. Paynter. *Effects On The Hardness Of Super Bainite Through Isothermal Heat-Treatment*. PhD thesis, University of Wolverhampton, 2005.

[187] C. García-Mateo, F. G. Caballero, and H. K. D. H. Bhadeshia. Mechanical properties of low-temperature bainite. *Materials Science Forum*, 500-501: 495–502, 2005.

[188] H. K. D. H. Bhadeshia. Steels for bearings. *Progress in Materials Science*, 57:268–435, 2012.

[189] J. Pacyna, A. Jedrzejewska-Strach, and M. Strach. The effect of manganese and silicon on the kinetics of phase transformations during tempering Con-

tinuous Heating Transformation (CHT) curves. *Journal of Materials Processing Technology*, 64:311–318, 1997.

[190] S. Dinda and W. R. Warke. The Effect of Grain Boundary Segregation on Liquid Metal Induced Embrittlement of Steel. *Materials Science and Engineering*, 24:199–208, 1976.

[191] G. King, R. A. Jarman, and P. Judson. The Effect of Manganese and Nickel on the Room Temperature Tensile Characteristics of Ferritic Weld Metal. Technical report, Thames Polytechnic, London, U. K., 1989.

[192] S. Khare, K. Y. Lee, and H. K. D. H. Bhadeshia. Carbide-Free Bainite: Compromise between Rate of Transformation and Properties. *Metallurgical and Materials Transactions A*, 41:922–928, 2010.

[193] H. Qu, G. M. Michal, and A. H. Heuer. A 3rd Generation Advanced High-Strength Steel (AHSS) Produced by Dual Stabilization Heat Treatment (DSHT). *Metallurgical and Materials Transactions A*, 44:4450–4453, 2013.

[194] R. A. Stevens and P. E. J. Flewitt. The Effects of gamma' Precipitate Coarsening During Isothermal Aging and Creep of the Nickel-Base Superalloy IN-738. *Materials Science and Engineering*, 37:237–247, 1978.

[195] W. M. Garrison. The effect of silicon and nickel additions on the sulfide spacing and fracture toughness of a 0.4 carbon low alloy steel. *Metallurgical Transactions A*, 17:669–678, 1986.

[196] E. Keehan, L. Karlsson, and H.-O. Andrén. Influence of carbon, manganese and nickel on microstructure and properties of strong steel weld metals: Part 1 Effect of nickel content. *Science and Technology of Welding and Joining*, 11:1–8, 2006.

[197] F. G. Caballero, J. Chao, J. Cornide, C. García-Mateo, M. J. Santofimia, and C. Capdevila. Toughness deterioration in advanced high strength bainitic steels. *Materials Science and Engineering A*, 525:87–95, 2009.

[198] R. A. Depaul and A. L. Kitchin. The Role of Nickel, Copper, and Columbium (Niobium) in Strengthening a Low-Carbon Ferritic Steel. *Metallurgical Transactions*, I:389–393, 1970.

[199] R. H. Davies, A. T. Dinsdale, J. A. Gisby, J. A. J. Robinson, and S. M. Martin. MTDATA-thermodynamic and phase equilibrium software from the national physical laboratory. *Calphad*, 26:229–71, 2002.

[200] L. C. D. Fielding. The Bainite Controversy. *Materrials Science and Technology*, 29:383–399, 2013.

[201] M. J. Peet, P. Hill, M. Rawson, S. Wood, and H. K. D. H. Bhadeshia. Fatigue of extremely fine bainite. *Materials Science and Technology*, 27: 119–123, 2011.

[202] H. K. D. H. Bhadeshia. Very Short and Very Long Heat Treatments in the Processing of Steel. *Materials and Manufacturing Processes*, 25:1–6, 2010.

[203] J. Cornide, C. García-Mateo, C. Capdevila, and F. G. Caballero. An assessment of the contributing factors to the nanoscale structural refinement of advanced bainitic steels. *Journal of Alloys and Compounds*, 2011.

[204] D.-Q. Kong, Q. Liu, L. Yuan, and Z. Dong. Low-temperature Bainite in a Low Alloy Steel. *Journal of Basic and Applied Physics*, 2:155–158, 2013.

[205] M. N. Yoozbashi and S. Yazdani. Mechanical properties of nanostructured, low temperature bainitic steel designed using a thermodynamic model. *Materials Science and Engineering A*, 527:3200–3205, 2010.

[206] H. K. D. H. Bhadeshia. *Bainite in Steels*. Institute of Materials, London, 2nd edition, 2001.

[207] M. Sherif. *Characterisation and Development of Nanostructured, Ultrahigh Strength, and Ductile Bainitic Steels*. Phd, University of Cambridge, 2009.

[208] S. K. Putatunda, A. V. Singar, R. Tackett, and G. Lawes. Development of a high strength high toughness ausferritic steel. *Materials Science and Engineering A*, 513-514:329–339, 2009.

[209] M. Kundu, S. Ganguly, S. Datta, and P. P. Chattopadhyay. Simulating Time Temperature Transformation Diagram of Steel Using Artificial Neural Network. *Materials and Manufacturing Processes*, 24:169–173, 2009.

[210] J. Koutsky. Structural Changes in Certain Modified 12% Chromium Steels. *Metal Science and Heat Treatment*, 2:319–328, 1960.

[211] A. A. Chulkina, A. I. Ulyanov, A. V. Zagainov, A. L. Ulyanov, and E. P. Yelsukov. Formation of chromium-alloyed cementite in the process of mechanosynthesis and subsequent annealings. *The Physics of Metals and Metallography*, 116:293–301, 2015.

[212] M. Bouet, J. H. Root, E. Es-Sadiqui, and S. Yue. The Effect of Mo in Si-Mn Nb Bearing TRIP Steels. *Materials Science Forum*, 284:319–326, 1998.

[213] S. J. Lee and Y. K. Lee. Effect of Austenite Grain Size on Martensitic Transformation of a Low Alloy Steel. *Materials Science Forum*, 475-479: 3169–3172, 2005.

[214] P. Brofman and G. Ansell. On the Effect of Fine Grain Size on the Ms Temperature in Fe-27Ni-O.025C Alloys. *Metallurgical and Materials Transactions A*, 14:2–4, 1983.

[215] J. Huang and Z. Xu. Effect of dynamically recrystallized austenite on the martensite start temperature of martensitic transformation. *Materials Science and Engineering A*, 438-440:254–257, 2006.

[216] H. S. Yang and H. K. D. H. Bhadeshia. Austenite grain size and the martensite-start temperature. *Scripta Materialia*, 60:493–495, 2009.

[217] H. K. D. H. Bhadeshia. Thermodynamic analysis of isothermal transformation diagrams. *Metal Science*, 16:159–165, 1982.

[218] A. T. Davenport. The influence of hot deformation on a nas-hot-rolled bainitic steel. In J. B. Ballance, editor, *The Hot Deformation of Austeite*, pages 517–536, 1977.

[219] W. Gong, Y. Tomota, M. S. Koo, and Y. Adachi. Effect of ausforming on nanobainite steel. *Scripta Materialia*, 63:819–822, 2010.

[220] W. Gong, Y. Tomota, Y. Adachi, A. M. Paradowska, J. F. Kelleher, and S. Y. Zhang. Effects of ausforming temperature on bainite transformation, microstructure and variant selection in nanobainite steel. *Acta Materialia*, 61:4142–4154, 2013.

[221] A. A. Shirzadi, H. Abreu, L. Pocock, D. Klobčar, P. J. Withers, and H. K. D. H. Bhadeshia. Bainite orientation in plastically deformed austenite. *International Journal of Materials Research*, 100:40–45, 2009.

[222] M. Zhang, Y. Wang, C. L. Zheng, F. C. Zhang, and T. S. Wang. Effects of ausforming on isothermal bainite transformation behaviour and microstructural refinement in medium-carbon SiAl-rich alloy steel. *Materials & Design*, 62:168–174, 2014.

[223] J. D. H. Paul and N. Ridley. Microstructure-property relationships in tempered low alloy cr-mo-3.5ni-v steel. *Materials Science and Technology*, 9: 1014–1018, 1993.

[224] M. J. Peet, P. Hill, L. C. D. Fielding, A. Al-Hamdany, M. Rawson, and H. K. D. H. Bhadeshia. Strength and toughness of clean nanostructured bainite. 2015.

[225] C. García-Mateo, T. Sourmail, F. G. Caballero, V. Smanio, M. Kuntz, A. Leiro, E. Vuorinen, R. Elvira, and T. Teeri. Nanostructured steel industrialisation: plausible reality. *Materials Science and Technology*, 000: 1–8, 2013.

[226] C. García-Mateo, M. J. Peet, F. G. Caballero, and H. K. D. H. Bhadeshia. Tempering of hard mixture of bainitic ferrite and austenite. *Materials Science and Technology*, 20:814–818, 2004.

[227] J. G. Speer, D. V. Edmonds, F. C. Rizzo, and D. K. Matlock. Partitioning of carbon from supersaturated plates of ferrite, with application to steel processing and fundamentals of the bainite transformation. *Current Opinion in Solid State and Materials Science*, 8:219–237, 2004.

[228] M. Takahashi and H. K. D. H. Bhadeshia. Model for transition from upper to lower bainite. *Materials Science and Technology*, 6:592–603, 1990.

[229] G. R. Speich and P. R. Swann. Yield strength and transformation substructure of quenched iron-nickel alloys. *Journal Of The Iron And Steel Institute*, 203:480–485, 1965.

[230] F. B. Pickering. *Physical metallurgy and the design of steels*. Applied Science Publishers, London, U. K., first edit edition, 1978.

[231] D. T. Llewllyn. *Steels: Metallurgy and Applications*. Butterworth-Heinemann, Oxford, U. K., first edit edition, 1992.

[232] S. B. Singh and H. K. D. H. Bhadeshia. Esitmation of Bainite Plate-Thickness in Low-Alloy Steels. *Materials Science and Engineering A*, 245: 72–79, 1998.

[233] R. Hammond. *Shock and ballistic properties of bainitic steels and tungsten alloys*. PhD thesis, University of Cambridge, 2004.

[234] New armour steel showcased at DSEi. Available from `https://www.gov.uk/government/news/new-armour-steel-showcased-at-dsei`, 2011.

[235] H. K. D. H. Bhadeshia and D. V. Edmonds. Bainite in silicon steels: new compositionproperty approach Part 1. *Metal Science*, 17:420–425, 1983.

[236] M. Cohen. The Strengthening of Steel. *Transactions of the American Intsitute of Metallurgical Engineers*, 224:638–657, 1962.

[237] J. H. Jang, D.-W. Suh, and H. K. D. H. Bhadeshia. Solubility of carbon in tetragonal ferrite in equilibrium with austenite. *Scripta Materialia*, 68: 195–198, 2013.

[238] H. K. D. H. Bhadeshia. Martensite in Steels. Available from `http://www.msm.cam.ac.uk/phase-trans/2000/C9/lectures45.pdf`, 2002.

[239] J. Cermak and L. Kral. Carbon diffusion in carbon-supersaturated ferrite and austenite. *Journal of Alloys and Compounds*, 586:129–135, 2013.

[240] F. G. Caballero, M. K. Miller, C. García-Mateo, C. Capdevila, and S. S. Babu. Redistribution of alloying elements during tempering of a nanocrystalline steel. *Acta Materialia*, 56:188–199, 2008.

[241] M. J. Peet and H. K. D. H. Bhadeshia. mucg83. Available from `http://www.msm.cam.ac.uk/map/steel/programs/mucg83.html`, 2006.

[242] C. Zener. Equilibrium Relations in Medium-alloy Steels. *Transactions of the American Intsitute of Metallurgical Engineers*, 167:513–534, 1946.

[243] J. C. Fisher. The Free Energy Change Accompanying the Martensite Tranformation in Steels. *Metals Transactions*, 185:688–690, 1949.

[244] H. K. D. H. Bhadeshia. Application of first-order quasichemical theory to transformations in steels. *Metal Science*, 16:167–170, 1982.

[245] J. S. Kirkaldy and E. A. Baganis. Thermodynamic Prediction of the Ae3 Temperature of Steels with Additions of Mn, Si, Ni, Cr, Mo, Cu. *Metallurgical Transactions A*, 9A:495–501, 1978.

[246] H. I. Aaronson, H. A. Domian, and G. M. Pound. Thermodynamics of the Austenite $\rightarrow$ Proeutectoid Ferrite Transformation part 1, Fe-C Alloys. *Transactions Of The Metallurgical Society Of AIME*, 236:768–780, 1966.

[247] E. Kozeschnik. MATCALC - a simulation tool for multicomponent thermodynamics, diffusion and phase transformations. In *Fifth International Seminar on the Numerical Analysis of Weldability*, pages 349–361, 1999.

[248] J.-O. Andersson, T. Helander, L. Höglund, P. Shi, and B. Sundman. Thermo-Calc & DICTRA, computational tools for materials science. *CALPHAD*, 26: 273–312, 2002.

[249] B. Sundman, B. Jansson, and J.-O. Andersson. The Thermo-Calc databank system. *CALPHAD*, 9:153–190, 1985.

[250] M. N. Yoozbashi, S. Yazdani, and T. S. Wang. Design of a new nanostructured, high-Si bainitic steel with lower cost production. *Materials & Design*, 32:3248–3253, 2011.

[251] B. Avishan, S. Yazdani, and S. H. Nedjad. Toughness variations in nanostructured bainitic steels. *Materials Science and Engineering A*, 548:106–111, 2012.

[252] H. L. Yi, P. Chen, and H. K. D. H. Bhadeshia. Optimizing the Morphology and Stability of Retained Austenite in a δ-TRIP Steel. *Metallurgical and Materials Transactions A*, 2014.

[253] K. W. Andrews. The Calculation of Transformation Temperatures and Austenite-Ferrite Equilibria in Steels. *Journal of the Iron and Steel Institute*, pages 414–427, 1956.

[254] NPL PLUS thermodynamic database version 3.02, 1993.

[255] TCAB thermodynamic database for steels version 1.0, 2001.

[256] P. Shi and B. Sundman. TCCS (Thermo-Calc Classic Version S) Users' Guide. *Thermo-calc*, 2008.

[257] E. Kozeschnik and B. Buchmayr. Matcalc - a simulation tool for multicomponent thermodynamics, diffusion and phase transformations. *Mathematical Modelling of Weld Phenomena 5*, pages 349–361, 2001.

[258] H. S. Yang and H. K. D. H. Bhadeshia. Designing low carbon, low temperature bainite. *Materials Science and Technology*, 24:335–342, 2008.

[259] T. Okumura and T. Sourmail. MTTTData, http://www.msm.cam.ac.uk/map/steel/programs/MTTTDATA.html, 2004.

[260] W. Xu. *Genetic Design of Ultra High Strength Bainitic Steels*. Phd, Technische Universiteit Delft, 2009.

[261] S. Chatterjee, M. Murugananth, and H. K. D. H. Bhadeshia. δ TRIP steel. *Materials Science and Technology*, 23:819–827, 2007.

[262] H. L. Yi, K. Y. Lee, and H. K. D. H. Bhadeshia. Stabilisation of ferrite in hot rolled δ-TRIP steel. *Materials Science and Technology*, 27:525–529, 2011.

[263] W. H. Press, S. A. Teukolsky, W. T. Vetterling, and B. P. Flannery. *Numerical recipes in FORTRAN*. Cambridge University Press, Cambridge, U. K., 1992.

[264] D. MacKay and D. MacKay. Searching for 'optimal' inputs with an empirical regression model. *University of Cambridge*, 1997.

[265] D. MacKay and D. MacKay. Bayesian non-linear modeling with neural networks. *Mathematical Modelling of Weld Phenomena 3. Institute*, 650:359–389, 1997.

[266] D. J. C. Mackay. Bayesian model comparison and backprop nets.

[267] M. J. Peet. Bayesian Neural Networks as Implemented in Model Manager. pages 1–5, 2014.

[268] T. Sourmail. Neuromat Model Manager. Available from `http://thomas-sourmail.net/neural_networks_model_manager.html`, 2004.

[269] T. Sourmail and C. García-Mateo. MAP martensite start temperature data library. Available from `http://www.msm.cam.ac.uk/map/data/materials/Ms_data_2004.html`, 2004.

[270] C. Capdevila, F. G. Caballero, and C. García de Andrés. Determination of Ms Temperature in Steels. A Bayesian Neural Network Model. *ISIJ International*, 42:894–902, 2002.

[271] C. García-Mateo, T. Sourmail, F. G. Caballero, C. Capdevila, and C. García de Andrés. New approach for the bainite start temperature calculation in steels. *Materials Science and Technology*, 21:934–940, 2005.

[272] L. Gavard, H. K. D. H. Bhadeshia, D. J. C. Mackay, and S. Suzuki. Bayesian neural netword mdel for austenite formation in steels. *Materials Science and Technology*, 12:453–463, 1996.

[273] B. Wimarshana, J. Ryu, and H.-J. Choi. Neural network based material models with Bayesian framework for integrated materials and product design. *International Journal of Precision Engineering and Manufacturing*, 15: 75–81, 2014.

[274] G. A. Cottrell, R. Kemp, H. K. D. H. Bhadeshia, G. R. Odette, and T. Yamamoto. Neural Network Analysis of Charpy Transition Temperatures of Irradiated Low-activation Mertensitic Steels. *Journal of Nuclear Materials*, 367-370:603–609, 2007.

[275] M. A. Yescas. Prediction of the Vickers hardness in austempered ductile irons using neural networks. *International Journal of Cast Metals Research*, 15:513–521, 2003.

[276] A. Al-Hamdany, D. Al Fattal, T. A. Jabbar, and H. K. D. H. Bhadeshia. Estimation of fracture toughness of tempered nanostructured bainite. *Materials Science and Technology*, 28:685–689, 2012.

[277] M. J. Peet and D. J. C. Mackay. MAP database of austenite lattice parameters and compositions. Available from http://www.msm.cam.ac.uk/map/neural/programs/MAP_NEURAL_LATTICE_PARAMETER_AUSTENITE.html, 2002.

[278] M. J. Peet. Bainite for Aeroengine Shafts. Technical report, University of Cambridge, Derby, U.K., 2006.

[279] Carbolite PF60 Technical Specifications. Available from http://www.carbolite.com/products/ovens/standard-laboratory-ovens/pf-peak-series-fan-convection-ovens/models/, 2015.

[280] C. A. Schneider, W. S. Rasband, and K. W. Eliceiri. NIH Image to ImageJ: 25 years of image analysis. *Nature Methods*, 9:671–675, 2012.

[281] H. F. Lan, X. H. Liu, and L. X. Du. Ultra-Hard Bainitic Steels Processed through Low Temperature Heat Treatment. *Advanced Materials Research*, 156-157:1708–1712, 2011.

[282] H. S. Hasan, M. J. Peet, M.-N. Avettand-Fénoël, and H. K. D. H. Bhadeshia. Effect of tempering upon the tensile properties of a nanostructured bainitic steel. *Materials Science and Technology*, 615:1–22, 2014.

[283] D. Graham and D. H. Tomlin. Self-diffusion in iron. *Philosophical Magazine*, 8(93):1581–1585, 1963.

[284] L. Lutterotti, S. Matthies, and H.-R. Wenk. MAUD (Material Analysis Using Diffraction): a user friendly Java program for Rietveld Texture Analysis and more. In *Proceeding of the Twelfth International Conference on Textures of Materials (ICOTOM-12)*, page 159, 1999.

[285] R. A. Young. *The Rietveld Method*. Oxford University Press, Oxford, 1993.

[286] L. B. McCusker, R. B. von Dreele, D. E. Cox, D. Louër, and P. Scardi. Rietveld refinement guidelines. *Journal of Applied Crystallography*, 32:36–50, 1999.

[287] F. G. Caballero, C. García-Mateo, and C. García de Andrés. Dilatometric Study of Reaustenitisation of High Silicon Bainitic Steels: Decomposition of Retained Austenite. *Materials Transactions*, 46:581–586, 2005.

[288] H. S. Yang and H. K. D. H. Bhadeshia. Uncertainties in dilatometric determination of martensite start temperature. *Materials Science and Technology*, 23:556–560, 2007.

[289] P. Kolmskog, A. Borgenstam, M. Hillert, P. Hedström, S. S. Babu, H. Terasaki, and Y. I. Komizo. Direct observation that bainite can grow below MS. *Metallurgical and Materials Transactions A: Physical Metallurgy and Materials Science*, 43:4984–4988, 2012.

[290] H. K. D. H. Bhadeshia, S. A. David, J. M. Vitek, and R. W. Reed. Stress induced transformation to bainite in pressure vessel steel. *Materials Science and Technology*, 7:686–698, 1991.

[291] J. Sun and H. Yu. Microstructure development and mechanical properties of quenching and partitioning (Q&P) steel and an incorporation of hot-dipping galvanization during Q&P process. *Materials Science and Engineering A*, 586:100–107, 2013.

[292] A. R. Marder. Metallurgy of zinc-coated steel. *Progress in Materials Science*, 45:191–271, 2000.

[293] E. Povoden-Karadeniz. MATCALC thermodynamic database for iron v2.021. Technical report, 2014.

[294] J. A. Wasynczuk, R. M. Fisher, and G. Thomas. Effects of copper on proeutectoid cementite precipitation. *Metallurgical Transactions A*, 17:2163–2173, 1986.

[295] R. A. Ricks. A comparative study of precipitation at interphase boundaries in Fe-Cu-Ni and Fe-Au-Ni alloys. *Journal of Materials Science*, 16:3006–3012, 1981.

[296] I. Kirman. United States Patent 4043807, 1977.

[297] J. Fridberg, L. E. Torndahl, and M. Hillert. Diffusion in Iron. *Jernkont. Ann.*, 153:263–276, 1969.

[298] C. Stallybrass, A. Schneider, and G. Sauthoff. The strengthening effect of (Ni,Fe)Al precipitates on the mechanical properties at high temperatures of ferritic Fe-Al-Ni-Cr alloys. *Intermetallics*, 13:1263–1268, 2005.

[299] Z. K. Teng, G. Ghosh, M. K. Miller, S. Huang, B. Clausen, D. W. Brown, and P. K. Liaw. Neutron-diffraction study and modeling of the lattice parameters of a NiAl-precipitate-strengthened Fe-based alloy. *Acta Materialia*, 60:5362–5369, 2012.

[300] Z. Teng, M. Miller, G. Ghosh, C. Liu, S. Huang, K. Russell, M. Fine, and P. Liaw. Characterization of nanoscale NiAl-type precipitates in a ferritic steel by electron microscopy and atom probe tomography. *Scripta Materialia*, 63:61–64, 2010.

[301] S. Zhu, S. Tjong, and J. Lai. Creep behavior of a β(NiAl) precipitation strengthened ferritic FeCrNiAl alloy. *Acta Materialia*, 46:2969–2976, 1998.

[302] H. I. Aaronson, H. A. Domian, and G. M. Pound. Thermodynamics of the Austenite → Proeutectoid Ferrite Transformation part 2 Fe-C-X alloys. *The American Institute of Mechanical Engineers Metal Society Transactions*, 236: 768–781, 1966.

[303] D. Koistinen and R. Marburger. A general equation prescribing the extent of the austenite-martensite transformation in pure iron-carbon alloys and plain carbon steels. *Acta Metallurgica*, 7:59–60, 1959.

[304] NIST. Certificate of Analysis for Standard Reference Material 660 (lanthanum hexaboride), avilable from `https://www-s.nist.gov/srmors/certificates/archive/660.pdf`. Technical report, NIST, 1989.

[305] M. Drakopoulos. Diamond Light Source - I12 - JEEP: Joint Engineering, Environmental and Processing. Available from http://www.diamond.ac.uk/Home/Beamlines/I12.html, 2013.

[306] H. K. D. H. Bhadeshia. Tempered Martensite. Available from http://www.msm.cam.ac.uk/phase-trans/2004/Tempered.Martensite/severe.gif, 2004.

[307] H. S. Hasan, M. J. Peet, and H. K. D. H. Bhadeshia. Severe tempering of bainite generated at low transformation temperatures. *International Journal of Materials Research*, 103:1319–1324, 2012.

[308] P. J. Jacques, E. Girault, T. Catlin, N. Geerlofs, T. Kop, S. van der Zwaag, and F. Delannay. Bainite transformation of low carbon MnSi TRIP-assisted multiphase steels: influence of silicon content on cementite precipitation and austenite retention. *Materials Science and Engineering A*, 273-275:475–479, 1999.

[309] C. García-Mateo and F. G. Caballero. Understanding the Mechanical Properties of Nanostructured Bainite. In *NANOBAIN: Significant Extension of the Bainite Transformation Theory*, pages 35–65. 2015.

[310] B. Avishan, C. García-Mateo, L. Morales-Rivas, S. Yazdani, and F. G. Caballero. Strengthening and mechanical stability mechanisms in nanostructured bainite. *Journal of Materials Science*, 48:6121–6132, 2013.

[311] M. L. Hart, M. Drakopoulos, C. Reinhard, and T. Connolley. Complete elliptical ring geometry provides energy and instrument calibration for synchrotron-based two-dimensional X-ray diffraction. *Journal of Applied Crystallography*, 46:1249–1260, 2013.

[312] M. J. Peet, S. S. Babu, M. K. Miller, and H. K. D. H. Bhadeshia. Three-dimensional atom probe analysis of carbon distribution in low-temperature bainite. *Scripta Materialia*, 50:1277–1281, 2004.

[313] I. B. Timokhina, X. Y. Xiong, H. Beladi, S. Mukherjee, and P. D. Hodgson. Three-dimensional atomic scale analysis of microstructures formed in high strength steels. *Materials Science and Technology*, 27:739–741, 2011.

[314] R. W. G. Wyckoff. *Crystal Structures*, volume 1. Interscience Publishers, New York, N. Y., U. S. A., 2nd edition, 1963.

[315] P. Zhang, F. C. Zhang, Z. G. Yan, T. S. Wang, and L. H. Qian. Rolling Contact Fatigue of a Low Temperature Bainite in Surface Layer of a Low Carbon Steel. *Materials Science Forum*, 675-677:585–588, 2011.

[316] T. Sourmail, F. G. Caballero, C. García-Mateo, V. Smanio, C. Ziegler, M. Kuntz, R. Elvira, A. Leiro, E. Vuorinen, and T. Teeri. Evaluation of potential of high Si high C steel nanostructured bainite for wear and fatigue applications. *Materials Science and Technology*, 29:1166–1173, 2013.

[317] F. C. Zhang, X. Y. Long, J. Kang, D. Cao, and B. Lv. Cyclic deformation behaviors of a high strength carbide-free bainitic steel. 94:1–8, 2016.

[318] P. Hill. Personal Communication, 2016.

[319] D. Hull. *Fractography*. Cambridge University Press, Cambridge, U. K., 1999.

[320] G. E. Dieter. *Mechanical Metallurgy*. McGraw-Hill Book Company (U. K.) Limited, si metric edition, 1988.

[321] L. Vitos, J.-O. Nilsson, and B. Johansson. Alloying effects on the stacking fault energy in austenitic stainless steels from first-principles theory. *Acta Materialia*, 54:3821–3826, 2006.

[322] S. Curtze, V.-T. Kuokkala, A. Oikari, J. Talonen, and H. Hänninen. Thermodynamic modeling of the stacking fault energy of austenitic steels. *Acta Materialia*, 59:1068–1076, 2011.

[323] P. R. Sreenivasan. Estimation of ASTM E-1921 reference temperature from Charpy tests: Charpy energy-fracture toughness correlation method. *Engineering Fracture Mechanics*, 75:5229–5245, 2008.

[324] J. M. Barsom and S. T. Rolfe. Correlations Between K] c and Charpy V-notch Test Results in the Transition-Temperature Range. In *Impact Testing of metals*, pages 281–301. 1970.

[325] J. M. Barsom and S. T. Rolfe. K_{Ic} transition-temperture behavior of a517-f steel. *Engineering Fracture Mechanics*, pages 341–357.

[326] B. Ule, A. Ažman, A. Lagoja, and A. Jesenice. Relationship betvveen Fracture Toughness and mechanical Properties of some Structural Steels. *Kovine, zlitine, technologije*, 27:283–288, 1993.

[327] J. A. Kapp and J. H. Underwood. Correlation between fracture toughness, Charpy V-notch impact energy, and yield strength for ASTM A723 steel. Technical report, US Army Armament Research, Development and Engineering Center: Close Combat Armaments Center, 1992.

[328] S. Suresh. *Fatigue of Materials*. Cambridge University Press, Cambridge, U. K., 2nd edition, 1998.

[329] O. H. Basquin. The exponential law of endurance tests. *Proceedings of the American Society for Testing and Materials*, 10:625–630, 1910.

[330] S. Jitsukawa, M. Tamura, B. Van der Schaaf, R. L. Klueh, a. Alamo, C. Petersen, M. Schirra, P. Spaetig, G. R. Odette, a. a. Tavassoli, K. Shiba, a. Kohyama, and a. Kimura. Development of an extensive database of mechanical and physical properties for reduced-activation martensitic steel F82H. *Journal of Nuclear Materials*, 307-311:179–186, 2002.

[331] J. R. Davis, editor. *ASM Speciality Handbook: Heat-Resistant Materials*. ASM International, Materials Park, Ohio, U. S. A., 1997.

[332] M. Ashby. CES EduPack 2011, 2011.

[333] K. Maruyama, K. Sawada, and J.-i. Koike. Strengthening mechanisms in creep-resistant tempered martensitic steel. *ISIJ International*, 41(6):641–653, 2001.

[334] F. Nabarro and H. L. de Villiers. *The Physics of Creep*. Taylor & Francis, London, U. K., 1995.

[335] G. Song, Z. Sun, L. Li, X. Xu, M. Rawlings, C. H. Liebscher, B. Clausen, J. Poplawsky, D. N. Leonard, S. Huang, Z. Teng, C. T. Liu, M. D. Asta, Y. Gao, D. C. Dunand, G. Ghosh, M. Chen, M. E. Fine, and P. K. Liaw. Ferritic Alloys with Extreme Creep Resistance via Coherent Hierarchical Precipitates. *Scientific Reports*, 5:16327, 2015.

[336] W. I. F. David. Powder diffraction: Least-squares and beyond. *Journal of Research of the National Institute of Standards and Technology*, 109:107, 2004.

[337] E. Prince. *Mathematical techniques in Crystallography and Materials Science*. Springer, New Your, U. S. A., 3rd edition, 2004.

[338] E. Jansen, W. Schaefer, and G. Will. R values in analysis of powder diffraction data using Rietveld refinement. *Journal of Applied Crystallography*, 27: 492–496, 1994.

[339] B. H. Toby. R factors in Rietveld analysis: How good is good enough? *Powder Diffraction*, 21:67–70, 2012.

[340] J. W. Christian. Tetragonal Martensites in Ferrous Alloys - A Critique. *Materials Transactions*, 33:208–214, 1992.

[341] R. M. Ibberson, W. I. F. David, and K. S. Knight. High Resolution Powder Diffractometer (HRPD) at ISIS. A User Guide. (Rutherford-Appleton Laboratory report RAL-92-031). Technical report, Rutherford-Appleton Laboratory, Didcot, U. K., 1992.

[342] A. C. Larson and R. B. von Dreele. General Structure Analysis System (GSAS). Technical report, Los Alamos National Laboratory Report LAUR 86-748, Los Alamos, New Mexico, U. S. A., 1994.

[343] R. K. Dutta, R. M. Huizenga, H. Gao, M. Amirthalingam, A. King, M. J. M. Hermans, and I. M. Richardson. Anisotropy in Thermal Expansion of Bainitic Ferrite. *Metallurgical and Materials Transactions A*, 45:5281–5285, 2014.

[344] S. C. Vogel. gsaslanguage: a GSAS script language for automated Rietveld refinements of diffraction data. *Journal of Applied Crystallography*, 44:873–877, 2011.